UNIVERSITY OF CALIFORNIA

Santa Barbara

Photonic & Epitaxial Design of Bio-Inspired, Structured Surfaces for Optoelectronic Materials and Devices

A dissertation submitted in partial satisfaction of the

requirements for the degree Doctor of Philosophy

in Chemical Engineering

by

Pavel Shapturenka

Committee in charge:

Professor Michael J. Gordon, Chair

Professor Steven P. DenBaars

Professor Todd M. Squires

Professor Phillip Christopher

June 2021

The dissertation of Pavel Shapturenka is approved.

_____

Phillip Christopher

_____

Todd M. Squires

_____

Steven P. DenBaars

_____

Michael J. Gordon, Committee Chair

June 2021

Photonic & Epitaxial Design of Bio-Inspired, Structured Surfaces

for Optoelectronic Materials and Devices

by

Pavel Shapturenka

To my parents, Sergey & Oksana.

Я посвящаю эту работу моим дорогим родителям, Сергею и Оксане.

Acknowledgements

The past five years have been a journey of personal growth like no other in my life. I've come to appreciate how rare and special it is for curious, critically thinking, and empathetic individuals to converge and embark on a path toward deeper scientific understanding, unabated (and in fact motivated) by perpetual challenges, and catalyzed by mutual understanding, respect, and open-mindedness. I am grateful and proud that this fully captures my experiences here at UCSB. Moreover, I carry deep gratitude for those whom I've had the pleasure of sharing this crazy and wonderful ride with.

This is for you all.

I vividly recall my brief chat with Mike Gordon over recruitment weekend, and remember wondering if there will ever be another time that I would resonate so much with someone's scientific perspective and genuine curiosity about the world around them. It was with great excitement and relief that I was welcomed in, after finally gathering enough wit to commit. In turn, Mike nurtured and tamed my own curiosity through patient and methodical guidance and helped me realize the importance of parallelizing over-arching vision and attention to detail in doing impactful science. That said, thank you for entertaining my tangent-prone adventures; I do believe I am all the better for it. Finally, I am humbled by and thankful for your continuous sacrifice and unwavering advocacy on our group's behalf.

Where Mike supplied the fuel for my sometimes-trivial pursuits, Steve DenBaars provided the much-needed spark. From the very start, he has been a source of inspiration, support, and an uncanny eye for the next technologically and scientifically

interesting thing to try. Meeting with Steve was a refreshing and uplifting experience; the poorly documented "post-Steve high" is real, and it was instrumental in keeping me working within my pace and scope, despite the highly dynamic trajectories that many other projects around me seemed to take. Lastly, I will always be grateful for the freedom and wealth of opportunities Steve granted me to explore, learn, and collaborate with the entire SSLEEC community.

I would like to thank Professors Todd Squires and Phil Christopher for their engaging and stimulating presence in my committee, and for the invaluable perspective that helped contextualize my efforts and solidify my unique take on many optoelectronic and materials challenges. Moreover, I'd like to acknowledge Prof. Dan Morse, for his active, warm, and unconditional engagement in my research and continued support in my professional endeavors.

I had the great pleasure and privilege to learn from, and work alongside, the mellow-mercurial and brilliant Chris Pynn. Chris, you taught me everything I know about MOCVD growth, shear-resolved stresses, and good ohmic contacts. Your mentorship was instrumental to my successes, and, while wearing many hats, your mastery of the craft was inspiring. I am proud to call you a mentor and friend, and will always fondly remember our various adventures, both States-side and abroad.

David Hwang is an amazing scientist, mentor, manager, carillonneur, and friend, who also happens to be an absolute machine when it comes to cranking out high-quality LEDs and doing it all while streaming "Curb Your Enthusiasm" in the background. On second thought, his chocolate chip banana bread and blue microLEDs are neck-and-neck,

also pending availability of reduced-fat milk from O'Keefe's. "cork food appreciation" for life.

Lesley – you have been a fantastic mentor, friend, and just plain human being. You've been instrumental to my growth as a scientist and as a person, and I hope to always have you as a friend. If nothing else, I hope to have become a cooler person just by diffusion and proximity.

Ryan – you're my academic fraternal twin, and a great scientist who has a bright future. We were in the crucible right from Baron's class in first year, where you showed by doing, just how bright that future could get. It's been great to have you as a lab- and office-mate, and as a fountain of processing and electronics knowledge.

The Gordon group has evolved over my time here but has always remained a rich and amazingly diverse source of scientific and personal support. Lesley, Sheng-Ping, Ryan, Rich, Katie, Heilman, Pebbles, and Oscar made for a fun and supportive group environment at the outset; I will never forget our 2017 Mammoth snow-in snafu and will cherish countless other outings. The welcome additions of Sasha, Michael H., Graham, Eloise, Sara, and Visoth since then has truly made us Gordon All-Stars, and we're all glad you guys are here.

SSLEEC has always welcomed me with open arms, and more than a few good friendships and collaborations were forged here. Cheyenne, Chris Z., Akhil, and Srinivas, it was great to be able to work with you all and learn alongside one another.

A major thanks goes out to the MOCVD scientists and staff – Stacia Keller, Mike Iza, David Whitlatch, and Brian Carralejo, who were always supportive, instructive, and

great to work with. MO5 crew, past and present: Chris P., Cheyenne, Jared, Yi Chao, Ryan White, SeungGeun, Caroline, Panpan, Vineeta, and Jake – I'm continuously impressed by our ability to remain civil, responsible, and pleasant in the face of the recurring, seemingly insurmountable logistical nightmare that is scheduling. I'm glad all of us shared the unique experience of avoiding all forms of disaster every month or so, with bated breath.

To the great friends and acquaintances made here across departments, sports circles, and hangouts: Kan, Payton, Jocelyn, Ljube, Manny, Grant, Maša, Shona, Richard, Ryan A., Clarke, Alex, Yuning, Tsatsa, Jiamin, Chatarin and Antoine; you are a fantastic crowd of people, and have made being here all the more worth it.

To my New York crew: the CCNY Seenyaz squad (Sneha, Andrew, Neil, Kata, Dimitri, and George), Lanie, Max, Katya, Yevgeniy, Waseem – it's been great staying in touch and reconnecting at various points in our lives. I'm so glad to have all of you on board, all these years later.

To my housemates, Sam and Dezmond – it's been a wonderful three years of sharing our living space, along with great memories of karaoke, volleyball, late night pizza, glow-in-the-dark Jello, and pierced Fig Newtons.

Sheng – whether by complete chance or by some form of incomprehensible providence, we've been on this journey together since the day I came to Santa Barbara. You remain, to this day, the person I've lived with the longest, outside my family. Our lab work truly proceeded 24/7, as our San Clemente apartment, and later Patterson House, would become an experimental space for personal betterment and long conversations

about difficult and curious things in the spiritual, gastronomic, and economic planes. You've kept me sane through some rough stretches, and I am forever grateful for it. You're a smart, perceptive, and talented scientist and individual, and I wish you only the best in your next steps, which will no doubt be stellar.

For her unconditional love and support since we've met, I thank my girlfriend, Laura. You have made me a better person in countless ways, and I am so fortunate and grateful to have you in my life. You understand me better than I do myself, and it's equal parts frightening and reassuring. Thank you for being there for me, throughout.

I'd like to thank my family, as well as my relatives around the world, for their unwavering support these five years. My uncle, Sasha, grandparents, Klaudziya and Mikhail, my sister Maria, and my parents, Sergey and Oksana, have been an inexhaustible well of moral support, and I dedicate the full body of my achievements to them. I'm especially thankful for the unconstrained, trusting, and supportive environment that my parents provided me, and for their many sacrifices that enabled my academic journey thus far.

Я хочу поблагодарить всю мою семью: моего дядю Сашу, бабушку Клаву, дедушку Мишу, сестрёнку Марию, отца Сергея и маму Оксану. Я очень вам благодарен за вашу любовь, заботу, и поддержку, и всех вас люблю!

Curriculum Vitae

Pavel Shapturenka

EDUCATION

University of California – Santa Barbara, Santa Barbara, CA — June 2021
Ph. D., Chemical Engineering

Macaulay Honors at The City College of New York, New York, NY — June 2016
B. Eng., Chemical Engineering, *Summa cum laude*; Mathematics minor

PUBLICATIONS

Shapturenka, P., Gaillard, P., Chan, L., and Gordon, M. J. "Hierarchical colloid-based lithography for wettability tuning of semiconductor surfaces." Under review, *JVST A*.

Shapturenka, P., Zakaria, N. I., and Gordon, M. J. "Extending the diatom's color palette: engineering non-iridescent coloration in wafer-scale TiO_2 nanomembranes." *In Preparation.*

Shapturenka, P., Pynn, C.D., Chan, L., DenBaars, S.P., and Gordon, M. J. "Hybrid plastic-elastic strain relaxation of $(11\bar{2}2)$ semipolar InGaN buffer layers via area-scalable colloidal structuring." *In Preparation.*

Shapturenka, P., Pynn, C.D., Chan, L., DenBaars, S.P., and Gordon, M. J. "Enhanced defect-free indium incorporation and red-shifted emission in $(11\bar{2}2)$ semipolar InGaN quantum wells templated by patterned InGaN buffers." *In Preparation.*

Shapturenka, P., Stute, H., Zakaria, N. I., Denbaars, S. P. & Gordon, M. J. "Color-changing refractive index sensor based on Fano-resonant filtering of optical modes in a porous dielectric Fabry-Pérot microcavity." *Opt. Express* **28**(19), 28226–28233 (2020).

Shapturenka, P., Birkholz, F., Zakaria, N. I., DenBaars, S. P., and Gordon, M. J. "Quasi-ordered, sub-wavelength TiO_2 hole arrays with tunable, omnidirectional color response." *J. Vac. Sci. Technol. A* **38**(5), 053403 (2020). *Featured in*: Patrick, C. "Method fabricates nanostructures with angle-independent structural color." *Scilight* **2020**, 321102 (2020).

Chan, L., Karmstrand, T., Chan, A., **Shapturenka, P.**, Hwang, D., Margalith, T., DenBaars, S.P., and Gordon, M. J. "Fabrication and chemical lift-off of sub-micron scale III-nitride LED structures." *Opt. Express.* **28**(23), 35038-35046 (2020).

Chan, L., **Shapturenka, P.**, Pynn, C. D., Margalith, T., DenBaars, S.P., and Gordon, M. J. "Lift-Off of Semipolar Blue and Green III-Nitride NanoLEDs Grown on Free-Standing GaN." *Appl. Phys. Lett.* **117**(2), 021104 (2020).

Ley, R., Chan, L., **Shapturenka P.**, Wong M. S., DenBaars, S. P., and Gordon, M. J. "Strain relaxation of InGaN/GaN multi-quantum well light emitters via nanopatterning." *Opt. Express* **27**(21), 30081 (2019).

Carlson, A., **Shapturenka, P.**, Eriksson, B., Lindbergh, G., Lagergren, C., & Lindstrom, R. W. (2018). "Electrode parameters and operating conditions influencing the performance of anion exchange membrane fuel cells." *Electrochimica Acta* **277**, 151-160 (2018).

Cui, J., Long, D., **Shapturenka, P.**, Kretzschmar, I., Chen, X., & Wang, T. "Janus particle-based microprobes: Determination of object orientation." *Colloids and Surfaces A: Physicochemical and Engineering Aspects* **513**, 452-462 (2017).

PATENTS

Chan, L., Karmstrand, T., Hwang, D., Shapturenka, P., Gordon, M. J., DenBaars, S. P., and Margalith, T. "Control of photoelectrochemical etch parameters for minimization of interfacial roughness of III-ntirde LEDs and other light-emitting device structures." US Provisional Patent, UC Case No. 2019-392.

Chan, L., Pynn, C. D., Hwang, D., Shapturenka, P., Gordon, M. J., DenBaars, S. P., and Margalith, T. "Method to create and release nanoscale light emitting diodes from their growth substrates." US Provisional Patent, UC Case No. 2019-391.

Shapturenka, P., DenBaars, S.P., and Gordon, M.J. "Colloidal lithography-enabled creation of metasurface-integrated micro-LEDs and devices." US Provisional Patent, UC Case No. 2019-180.

CONFERENCES

UCSB-Chalmers Colloquium (Oral, remotely via Zoom). "Colloid-based design of bio-inspired structural color and optical sensing." 28 April 2021, Santa Barbara, CA.

UCSB-Chalmers Colloquium (Oral). "Scalable nanopatterning for light extraction and strain engineering in III-nitride LEDs and displays." 27 August 2018, UCSB, CA.

AVS 65th International Symposium (Oral). "Scalable, tunable, and polarization-independent high contrast grating reflectors for integration into resonant-cavity micro-LEDs." 21 October 2018, Long Beach, CA.

Solid State Lighting and Energy Electronics Center Annual Review (Oral). "Scalable and tunable fabrication of grating reflectors for resonant-cavity micro-LEDs." 8 November 2018, UCSB, CA.

SERVICE & LEADERSHIP

Co-instructor and TA: ChE 166, Mechatronics & Instrumentation	**01/20 – 03/21**
2020 ChE Graduate Student Symposium – Organizing Co-chair	**06/20 – 09/20**
ChE GSA - Professional Development Committee, Member	**09/17 – present**
Teaching Assistant: Separation Ops., Theory/Practice (ChE 128/180B)	**09/17 – 03/19**
ESTEEM Tutor, UCSB Chemical Engineering	**11/18 – 01/19**

HONORS & DISTINCTIONS

CSP Technologies Teacher-Scholar Fellow	**2020/2021**
Szilagyi Energy Breakthrough Fellow, Institute for Energy Efficiency	**2018/2019**
Outstanding Graduate Research Achievement, SSLEEC Annual Review	**2018**
Honorable Mention Recipient, NSF GRFP	**2016/2017, 2017/2018**

Abstract

Photonic & Epitaxial Design of Bio-inspired, Structured Surfaces
for Optoelectronic Materials and Devices

by

Pavel Shapturenka

In recent decades, technological developments in optics, optoelectronics, and wetting phenomena have benefited from the principles behind some of nature's periodically structured and multifunctional surfaces. Particularly inspiring are the wavelength selectivity of vivid butterfly and bird wings, the light-coupling efficiency of the moth's eye, and the self-cleaning properties of the lotus leaf. Bridging the technological gaps in structure, function, and design of such functional surfaces requires a simple, geometrically tunable, and high-resolution patterning method to probe the emergent phenomena that arise when materials are heterogeneously arranged at these critical nanoscale dimensions. One compromise between bottom-up scalability and top-down pattern precision comes in the form of close-packed colloidal monolayers, which can be coupled with plasma-based pattern transfer to form highly correlated micron and sub-micron patterns in a variety of substrate materials.

This dissertation work focuses on extending this paradigm to hole-array and pillar structures in high-refractive index dielectrics and optoelectronic semiconductors, namely visible-wavelength optical TiO_2 nanostructures, micron-scale InGaN-based visible light emitters, and hierarchically structured GaN/Si surfaces for tunable wetting.

These were interrogated through a combination of microscopic and spectroscopic experimental methods (SEM, X-ray diffraction, photo/cathodo/electroluminescence, reflectometry, contact angle goniometry) to quantify and elucidate the mechanistic nature of various physical phenomena, which were corroborated and further illuminated by computational work (transfer-matrix and finite-difference time domain [FDTD] methods).

First, we computationally investigate the optical response of the micro-periodic, honeycombed glass exoskeleton of the centric diatom microalgae species in its natural aqueous environment. By drying the structure and replacing the top silica slab layer with TiO_2 (increasing refractive index contrast), a dramatic increase in electromagnetic field confinement was observed, yielding intense, wavelength-selective reflection at normal incidence owing to strong modal coupling between thin-film and hole-induced interference. The effect of structure geometry (i.e., hole spacing & layer thickness) on optical response was explored and a dimensionless design space was isolated, allowing wavelength-independent design of highly reflective and transmissive surfaces at visible wavelengths. Furthermore, translational pore disorder inherent to the diatom structure transformed this intense, broadband behavior into wavelength-selective, omnidirectional scattering. As a proof of concept, partially suspended TiO_2 hole arrays (pitch = 404, 507, and 690 nm) were fabricated with silica colloid deposition, metal masking, and sacrificial Si layer removal. The resulting angle-independent colors spanned the visible spectrum and were in excellent modal agreement with FDTD computations. These optical elements were integrated as hybrid color filters and

reflectors in a compact, color-responsive, and quickly recoverable interference-based (Fabry-Pérot microcavity) refractive index sensor.

Micron- and nanoscale structuring was also implemented for mitigating problematic defects introduced through lattice mismatch and device processing in long-wavelength III-nitride LED materials. To reduce lattice mismatch between the GaN substrate and InGaN quantum wells (QW), elastic relaxation was encouraged in lattice-expanded crystal growth templates ("buffers") for subsequent light-emitting layer deposition by etching free boundaries into the material. Accordingly, a $In_{0.06}Ga_{0.94}N$ buffer layer grown with metalorganic chemical vapor deposition (MOCVD) on free-standing $(11\bar{2}2)$ GaN substrates was patterned with colloidal lithography, forming micro- and nanopillars with aspect ratios of 1:4 and 1:2 (height:diameter), respectively. These patterned buffers showed extensive biaxial relaxation as verified by X-ray diffraction and cathodoluminescence measurements. A suite of microscopic and spectroscopic (SEM, photo/cathodoluminescence) methods were then used to probe the emission quality from subsequently grown QW layers; a longer-wavelength emission profile with orders-of-magnitude defect reduction was observed on patterned buffer structures relative to planar layers.

To circumvent non-radiative sidewall defects formed through ion bombardment and implantation during processing of micron-scale LEDs for display and augmented-reality applications, selective-area MOCVD growth of GaN and InGaN layers was conducted on the commercially tractable (0001) c-plane and scientifically interesting $(11\bar{2}2)$ semipolar orientations. A versatile set of processes was developed for producing

colloid-defined SiO_2 and Si_3N_4 growth masks with tunable geometry and fill fraction. After conducting GaN and multi-QW growth out of growth masks with 200 and 2000 nm apertures, the resulting structures were characterized with spatially mapped cathodoluminescence, and emerging crystal facets were assigned based on emission wavelength, facet morphology, and substrate orientation.

Finally, drawing inspiration from the waxy, textured surface of the lotus leaf, the dynamic range of wetting states afforded through simple, two-step patterning of GaN and Si surfaces was explored. A critical wetting transition from the impregnated Wenzel state to the hydrophobic Cassie-Baxter state was observed at a 1-μm feature spacing of Si pillars; further sample etching at this transition yielded a unique hydrophobic, all-adhering rose-petal wetting state at an aspect ratio of 4:1, and superhydrophobic lotus-leaf behavior at 10:1 (height:diameter) aspect ratio. Modification of the two plasma etching steps in the patterning process achieved superhydrophobic surfaces with a maximum contact angle of 157°, in line with the limitations set by the Cassie-Baxter model for wetting of chemically heterogeneous surfaces. Finally, Si pillars were patterned with dual (6 μm and then 310 nm) length scales, transforming a nominally Wenzel-wetting hydrophilic surface into a hydrophobic surface robust to atmospheric aging. Similar reversion to higher contact angles were observed when introducing dual length scales in GaN surfaces.

Table of contents

Acknowledgements v
Curriculum Vitae x
Abstract xiii
1 Introduction 1
Leveraging nature's nano-engineering for novel materials and functionalities 1
References 6
2 Background 7
2.1 Overview 7
2.2 Optical physics of light and computational tools for probing its interactions with planar and structured materials 8
2.2.1 Light as electromagnetic radiation 8
2.2.2 Analyzing Fresnel reflection at planar interfaces, thin-film interference, and multi-layered coatings 11
2.2.3 Interactions of light with structured surfaces 16
2.2.4 Finite-difference time-domain optical simulations 19
2.2.5 Color perception by mapping to the CIE 1931 color space 20
2.3 Fundamentals and challenges of achieving efficient GaN/InGaN-based light-emitting devices 21
2.3.1 The GaN LED revolution 21
2.3.2 III-nitride metalorganic chemical vapor deposition (MOCVD) 23
2.3.3 Relative merits and challenges of MOCVD growth on various crystal planes 26
2.3.4 Optoelectronic implications of polarization fields in the ternary InGaN alloy system 28
2.3.5 State-of-the-art in long-wavelength III-nitride devices 30
2.4 Surface wetting models for uniform and structured solid surfaces 33
2.5 Langmuir-Blodgett deposition 35
References 38
3 Optical physics of diatom-inspired dielectric nanostructures 40
3.1 Introduction 40
3.2 Re-thinking the humble diatom's geometry 43
3.2.1 Computationally elucidating diatom frustule optical response 43
3.2.2 Rational design of optical responses in "bionic" frustules 51

3.3 Fabrication, characterization, and computational validation of diatom-inspired TiO_2 frustule surfaces 56
3.3.1 TiO_2 hole array fabrication 56
3.3.2 Optical measurements 58
3.3.3 Optical simulations 59
3.4 Results and discussion 60
3.4.1 Fabrication results 60
3.4.2 Optical characterization of TiO_2 hole arrays 62
3.5 Conclusion 66
References 68
4 Diatom-inspired TiO_2 nanomembranes for optical refractive index sensing 70
4.1 Introduction 70
4.2 Experimental and simulation methods 72
4.2.1 Structure fabrication 72
4.2.2 Optical measurements 73
4.2.3 Optical simulations 73
4.3 Experimental results and discussion 75
4.3.1 Structure fabrication 75
4.3.2 Sensor performance 77
4.3.3 Discussion of operating principles 78
4.3.4 Effect of short-range order on FPMC color response 81
4.3.5 Enhancing sensor performance and sensitivity: permeable distributed Bragg reflectors 82
4.3.6 Diffuse optical behavior of the FPMC 84
4.4 Conclusion 86
References 88
5 Stress engineering of III-nitride emitters via patterned, relaxed 1122 semipolar InGaN buffers 90
5.1 Introduction 90
5.2 Semipolar InGaN buffers 93
5.2.1 Strategies for controllable relaxation 93
5.2.2 Characterization of 1D-relaxed InGaN buffers 99
5.2.3 Realizing micro- & nanopatterned InGaN buffers 104
5.2.4 Quantum-well re-growth on patterned, relaxed InGaN buffers 114
5.2.5 Buffer relaxation and consolidation after MOCVD re-growth 126

5.3 Conclusions 128
References 129
6 Scalable, selective-area MOCVD growth of micro- and nano-structured InGaN emitters 131
6.1 Introduction 131
6.2 Old SAG, new tricks 134
6.2.1 Interplay of reaction and mass transport in selective-area MOCVD growth 135
6.2.2 Preparing geometry-tunable, large-area micro- and nano-SAG substrates via colloidal lithography 137
6.3 Nanoscale, selective-area growth and characterization of GaN/InGaN materials 140
6.4 Conclusions 151
References 152
7 Topographic control of semiconductor surface wettability 153
7.1 Introduction 153
7.2 Experimental methods 155
7.2.1 Substrate preparation and processing 155
7.2.2 Characterization and analysis 157
7.3 Results and discussion 158
7.3.1 Wetting transition via colloid mask size 158
7.3.2 Obtaining superhydrophobicity within the Cassie-Baxter state by tuning plasma processing 161
7.3.3 Hierarchical patterning for dramatic changes in wetting 163
7.3.4 Wetting properties of GaN surfaces patterned at single & dual length scales 164
7.3.5 Study limitations 165
7.4 Summary 166
References 167
8 Outlook and future directions 169
8.1 Deep-ultraviolet reflecting diatom surfaces 169
8.2 Long-wavelength microLEDs via semipolar RIBs 171
8.3 Light-emitting diatoms for efficiency benefits 172
References 177

1
Introduction

Leveraging nature's nano-engineering for novel materials and functionalities

We are at an exciting scientific and technological inflection point in human history; we are learning more than ever before about our place in the universe, the environment around us, and the ways in which we can improve the quality and sustainability of life. The recent, rapid development of electronic materials such as silicon (Si) and gallium nitride (GaN) has supported multiple efforts in these venues, with Si-based integrated circuits advancing electronics, Si photovoltaics providing alternative energy sources, and GaN-based light-emitting diodes efficiently illuminating the world. However, challenges exist in achieving the theoretically predicted wall-plug efficiencies for the latter optoelectronic devices, as material and optical losses prevent the full utilization and generation of usable photons. More specifically, III-nitride materials suffer from defects generated by nontrivial crystallographic strain and device processing, and it is equally nontrivial to couple light into and out of such optically dense materials owing to significant reflections from planar interfaces, light-absorbing device layers, and losses from accumulated surface dust/debris.

Solutions to the above challenges can be inspired by naturally occurring structured interfaces, which bestow a staggering variety of competitive advantages to living organisms. For instance, the micron-scale protuberances on the surface of the moth's eye improve in-coupling of light and remove glint that alerts potential prey [1,2]. The near-wavelength periodic structures within some beetle, butterfly, and bird wings afford diverse coloration for camouflaging, warning, and mate attraction; this translates well to the development of wavelength-selective optics and pigment-free, fade-resistant color [1,3–5]. Finally, the lotus plant rids its leaves of sunlight-robbing dust and debris by rolling water around its repellent, hierarchically structured surface, and can inform the chemical and geometric design space for anti-fouling coatings on land and sea [6,7]. Figure 1.1 shows these organisms and the corresponding phenomena they leverage.

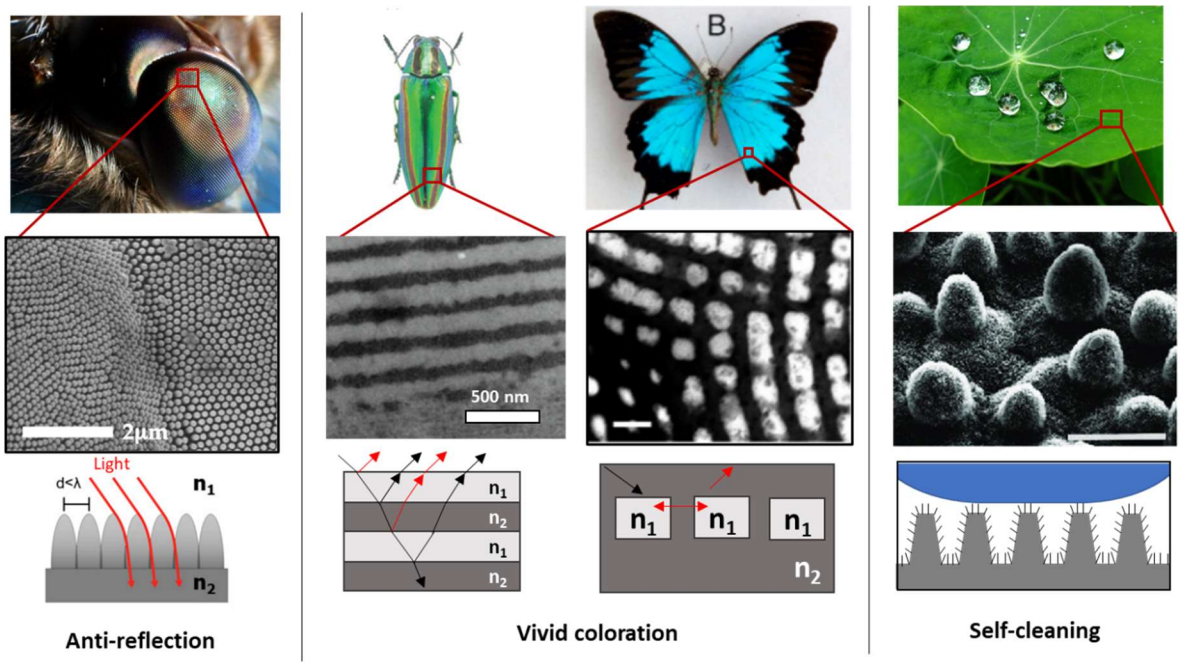

FIG. 1.1. Optical and scanning electron microscope images of various naturally occurring surfaces on moth eyes, beetle/butterfly wings, and lotus leaves, along with a schematic representation of the microscopic phenomena enabling their impressive functionality. Reprinted and adapted with permission. © 2006 & 2018, IOP Publishing Ltd.

The functional surfaces developed by living organisms tend to possess short-range correlated order. To emulate this important characteristic and harness relevant pattern length scales, we employ Langmuir-Blodgett dip-coating, which forms close-packed nanosphere monolayers on a wide variety of planar and curved material surfaces [8]. Coupled with plasma-based pattern transfer with the particles acting as etch masks, this affords rapid, area-scalable, and locally correlated patterns at micron and sub-micron length scales. By combining the governing principles behind nature's work with an ever-expanding base of accessible materials and patterns, we can explore a richer bed of physical phenomena and engineer surfaces with improved or novel functionality relative to natural counterparts. The work presented herein explores several manifestations of this paradigm, namely:

- Leveraging colloid-based, large-area nanopatterning towards developing:
    - Compact, bio-inspired optical elements for engineering light-matter interactions, enabling wavelength-selective reflection and propagation control in the visible-wavelength regime (350-750 nm)
    - Methods for strain relaxation, defect mitigation, and light extraction to afford efficiency improvements in long-wavelength (>500 nm) and micron-scale III-nitride light-emitters grown via metalorganic chemical vapor deposition (MOCVD)
    - Tunable semiconductor surface wetting via single- and multi-scale patterning

These objectives were achieved by:

- Probing and understanding relevant optical, compositional, and morphological trends affecting structure and surface behavior using a suite of characterization tools, including reflectometry, X-ray diffraction (XRD), cathodo-/electro-/photoluminescence, electron microscopy, and contact angle goniometry
- Modeling, generalizing, and designing optical/electronic behavior through theory and computation based on transfer-matrix (TMM), finite-difference time-domain (FDTD), and electronic band-structure/carrier transport simulation methods.

In addressing these goals, this dissertation will first discuss the fundamental underpinnings of optical and surface interactions in planar and structured materials, generally review the opportunities and current challenges of the III-nitride material system, and describe the ubiquitous Langmuir-Blodgett dip-coating methodology (Chapter 2). Next, a joint computational and experimental platform is presented to simulate, design, and fabricate diffusely colored TiO_2 nanomembranes inspired by the microperiodic exoskeleton of the centric marine diatom (Chapter 3). Leveraging this platform, a TiO_2 diatom nanostructure is integrated into a compact, interference-based refractive index sensor as a partial mirror and diffuse filter, which shows color-changing, cyclable, and sensitive performance which is on par with standard refractometers (Chapter 4). Chapter 5 elaborates on the nuance of managing strain in the III-nitride system, and colloidal patterning is employed to create fully relaxed, $(11\bar{2}2)$ semipolar InGaN buffer templates for subsequent light-emitter deposition. The deposited emitting layers showed reduced defect density and red-shifted emission relative to a planar reference, demonstrating great promise for efficient long-wavelength device

development. To circumvent emission-robbing point defects introduced through standard device processing, Chapter 6 explores the synthesis and characterization of micron and submicron light-emitters created with colloid-defined selective-area MOCVD growth. Chapter 7 explores a wealth of wetting behaviors by tuning simple plasma processing parameters and achieving hydrophobic hierarchical surfaces by transferring colloidal patterns into Si and GaN substrates. Finally, Chapter 8 describes future directions for this work, including the extension of diatom-inspired hole array structures to UV wavelengths, expanding the relaxed InGaN buffer design space toward longer wavelengths and larger mesas, and engineering III-nitride diatom nanostructures for improved light-extraction and material performance.

References

1. L. W. Chan, D. E. Morse, and M. J. Gordon, "Moth eye-inspired anti-reflective surfaces for improved IR optical systems & visible LEDs fabricated with colloidal lithography and etching," Bioinspiration and Biomimetics **13**(4), (2018).

2. F. L. Gonzalez and M. J. Gordon, "Bio-inspired, sub-wavelength surface structures for ultra-broadband, omni-directional anti-reflection in the mid and far IR," Opt. Express **22**(11), 12808 (2014).

3. S. Magkiriadou, J. G. Park, Y. S. Kim, and V. N. Manoharan, "Absence of red structural color in photonic glasses, bird feathers, and certain beetles," Phys. Rev. E - Stat. Nonlinear, Soft Matter Phys. **90**(6), 1–9 (2014).

4. V. Hwang, A. B. Stephenson, S. Barkley, S. Brandt, M. Xiao, J. Aizenberg, and V. N. Manoharan, "Designing angle-independent structural colors using Monte Carlo simulations of multiple scattering," Proc. Natl. Acad. Sci. U. S. A. **118**(4), (2021).

5. S. Yoshioka and S. Kinoshita, "Effect of macroscopic structure in iridescent color of the peacock feathers," Forma **17**(2), 169–181 (2002).

6. B. Bhushan, Y. C. Jung, and K. Koch, "Micro-, nano-, and hierarchical structures for superhydrophobicity, self-cleaning and low adhesion," Philos. Trans. R. Soc. A Math. Phys. Eng. Sci. **367**(1894), 1631–1672 (2009).

7. T. Darmanin and F. Guittard, "Superhydrophobic and superoleophobic properties in nature," Mater. Today **18**(5), 273–285 (2015).

8. F. L. Gonzalez, L. Chan, A. Berry, D. E. Morse, and M. J. Gordon, "Simple colloidal lithography method to fabricate large-area moth-eye antireflective structures on Si , Ge , and GaAs for IR applications," J. Vac. Sci. Technol. B **32**(5), 051213 (2014).

2
Background

2.1 Overview

As detailed above, the phenomena leveraged by nature and artificial technologies arise from the arrangement of microscopic, multi-component materials in a particular geometry, and the effect rendered by these assemblies can often exceed the performance of each individual component. Below, we cursorily review the fundamental physics governing this emergent behavior. First, we introduce the interactions of light with planar interfaces (Fresnel reflection) and periodic structures (gratings and metasurfaces), as well as material property approximations (effective-medium theory) and computational tools (e.g., transfer-matrix and finite-difference time-domain simulations) that appropriately capture experimentally occurring resonances. CIE/XYZ color mapping is introduced as a method to accurately capture perceived colors from spectral data. Further, we introduce the III-nitride material system, and briefly review the basics and challenges of realizing efficient InGaN-based light emitters across the entire visible spectrum. Finally, the interfacial science governing the adhesion of fluids to planar and patterned solid surfaces is introduced, and extended to the principles and procedures for Langmuir-Blodgett colloidal dip-coating.

2.2 Optical physics of light and computational tools for probing its interactions with planar and structured materials

2.2.1 Light as electromagnetic radiation

In classical physics, electromagnetic radiation (EMR) is described as a synchronized oscillation of electric (**E**) and magnetic (**B**) fields, which is represented in Fig. 2.1(a). EMR is generally created by accelerating charges but can also arise from the chemical and physical mechanisms by which charges carry and transduce energy within materials. The oscillation frequency (and energy) of radiation relates inversely to its characteristic wavelength. The time-varying azimuthal orientation of the electric field vector with respect to the propagation axis vector (**v**) is referred to as the polarization, and can either oscillate in a single plane (linear polarization) or exhibit some form of precession around the axis (elliptical polarization), depending on its interaction the surroundings. Electromagnetic radiation that is detectable by the human eye is what we usually refer to as "light"; this is only a small portion of the entire EMR frequency range, which spans over 16 orders of magnitude (Fig. 2.1(b)).

The propagation of electromagnetic waves through any media is described by Maxwell's equations, a coupled set of partial differential equations that were first reported by James Clerk Maxwell in 1861. The integral form of Maxwell's equations is as follows:

$$\oint \mathbf{E} \cdot d\mathbf{A} = \frac{Q}{\varepsilon_0} \tag{2.1}$$

$$\oint \mathbf{B} \cdot d\mathbf{A} = 0 \tag{2.2}$$

$$\oint \mathbf{E} \cdot d\mathbf{s} = -\frac{d\Phi_m}{dt} \tag{2.3}$$

$$\oint \mathbf{B} \cdot d\mathbf{s} = \mu_0 I + \varepsilon_0 \mu_0 \frac{d\Phi_e}{dt} \tag{2.4}$$

where Q is the net charge contained by the system under consideration, ε_0 is the free-space permittivity, μ_0 is the free-space permeability, I is the electric current within the medium, and Φ_e/Φ_m are the electric/magnetic field fluxes, respectively.

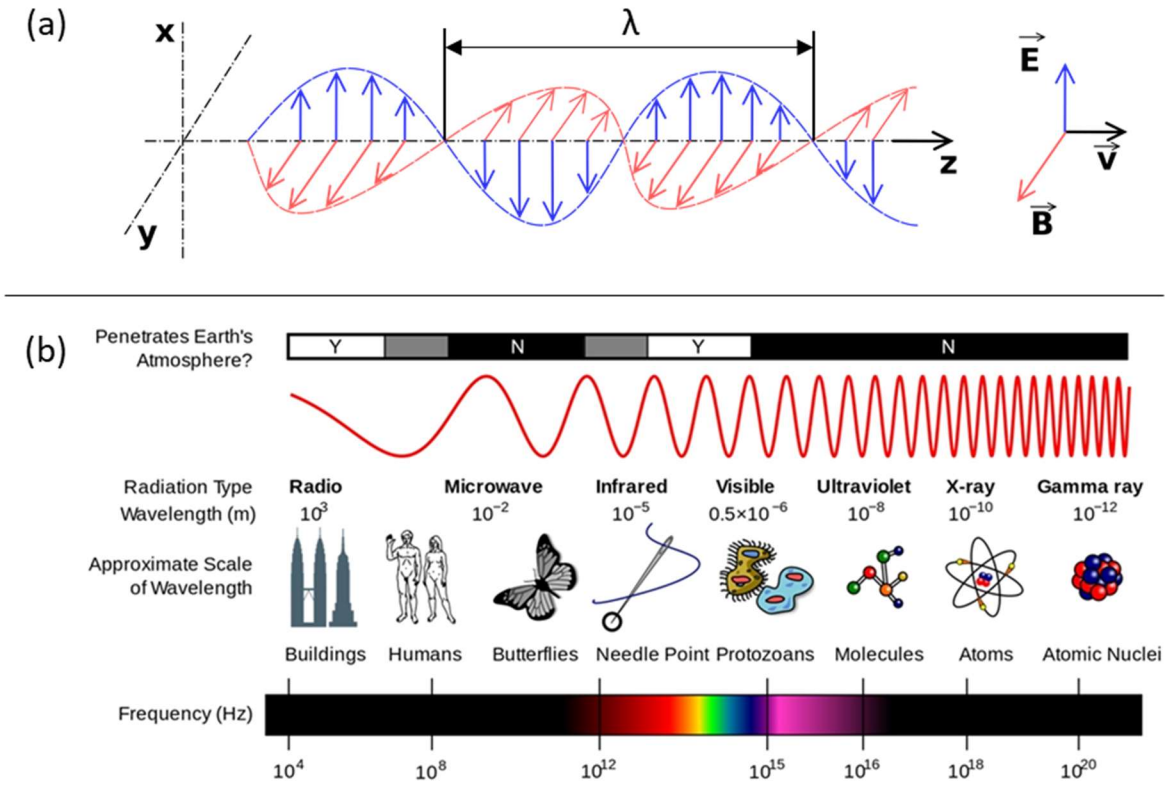

FIG. 2.1. (a) Schematic of linearly polarized electromagnetic radiation (EMR) of wavelength λ propagating in the z-direction [1]. (b) The EMR spectrum, with order-of-magnitude wavelength scale references, atmospheric interaction, and corresponding EMR frequencies [2].

If the medium is not an electrical conductor (no mobile charges), I → 0, and Eq. 2.4 gives rise to the wave equation in free space, which is given by:

$$\nabla^2 \mathbf{E} = \varepsilon_0 \mu_0 \frac{\partial^2 \mathbf{E}}{dt^2} \tag{2.5}$$

The plane-wave solution to Eq. 2.5 is of the form $E_0 e^{i(\mathbf{k}\cdot\mathbf{v}-\omega t)}$, where ω is frequency, **k** is the wavevector, and **v** is the direction of propagation as introduced in Fig. 2.1(a). It follows that the propagation velocity of an electromagnetic wave in free space is $\frac{1}{\sqrt{\varepsilon_0 \mu_0}}$, which is defined as the speed of light in vacuum (c = 3×10^8 m/s). Accordingly, in a non-conducting medium, light propagates with a velocity (v_m) whose square is inversely proportional to the product of the permittivity and permeability, ε and μ. For the sake of equal parts convenience and convention, these values are normalized by the vacuum values, yielding their relative counterparts, ε_r and μ_r. Accordingly:

$$v_m = c \cdot \frac{1}{\sqrt{\varepsilon_r \mu_r}} = \frac{c}{n} \tag{2.6}$$

where n is known as the refractive index of the material; it is notable that n is strongly wavelength-dependent. For a material that contains moving charges or nonzero dipole moments, the current term from Eq. 2.4 is re-introduced, and the resulting refractive index must be complex to reconcile the resulting plane-wave solution to Maxwell's equations. Accordingly, the wavelength-dependent complex refractive index, $\tilde{n}(\lambda)$, is given by:

$$\tilde{n}^2 = \mu_r \varepsilon_r + \frac{\mu_r \sigma}{\varepsilon_0 \omega} i \rightarrow \tilde{n}(\lambda) = n(\lambda) + i\kappa(\lambda) \tag{2.7}$$

where σ is the electrical conductivity, and κ is the complex refractive index, which is also known as the extinction coefficient. κ is a lumped term for all mechanisms by which light is absorbed inside a particular medium. As we will see, the wavelength-dependent n and κ is the only material data necessary to accurately capture reflection, transmission, and absorption in a wide variety of materials. Further, $\mu_r \approx 1$ and $\kappa \approx 0$ are generally reasonable approximations for dielectrics at visible wavelengths, which comprise most of the materials discussed herein.

2.2.2 Analyzing Fresnel reflection at planar interfaces, thin-film interference, and multi-layered coatings

It is not trivial to solve for the interactions of light with an abrupt, planar interface between two media with refractive indices n_1 and n_2. For simplicity, we take the case of normal-incidence, linearly polarized light. Ensuring continuity of parallel E/B-field components and conservation of both fields at the interface ("i" → incident, "r" → reflected, "t" → transmitted), as well as representing the electric fields as plane-wave solutions once again, we can represent the field balance across the boundary as:

$$\frac{\tilde{n}_1}{\mu_1}(E_i - E_r) = \frac{\tilde{n}_2}{\mu_2}E_t \tag{2.8}$$

Since reflected light intensity is the square of the electric field amplitude ($|E_r|^2$), the reflectance (R) and transmittance (T) is given by the normal-incidence Fresnel equations:

$$R = |r|^2 = \left|\frac{E_r}{E_i}\right|^2 = \left|\frac{\tilde{n}_2 - \tilde{n}_1}{\tilde{n}_1 + \tilde{n}_2}\right|^2 \tag{2.9}$$

$$T = |t|^2 = \left|\frac{E_t}{E_i}\right|^2 = \frac{\tilde{n}_2}{\tilde{n}_1}\left|\frac{2\tilde{n}_1}{\tilde{n}_1 + \tilde{n}_2}\right|^2 \tag{2.10}$$

where r and t are the complex Fresnel coefficients.

Figure 2.2 below shows the more general version of the above case, with light incident at an arbitrary angle Θ_i relative to the surface normal, with the peaks of the plane wave highlighted normal to the propagation vector. The group velocity decreases in the higher-index material, which causes the wavefronts to compress slightly within medium 2. The off-normal Fresnel treatment becomes polarization-sensitive as the electric and magnetic field components are oriented differently relative to the interface; thus, the polarization states are dubbed transverse-electric (TE) or transverse-magnetic (TM). The resulting surface-parallel components to be conserved vary accordingly, and the equations are as follows:

$$R_{TE} = \left|\frac{\tilde{n}_1 \cos\theta_i - \tilde{n}_2 \cos\theta_t}{\tilde{n}_1 \cos\theta_i + \tilde{n}_2 \cos\theta_t}\right|^2 \tag{2.11}$$

$$R_{TM} = \left|\frac{\tilde{n}_1 \cos\theta_t - \tilde{n}_2 \cos\theta_i}{\tilde{n}_1 \cos\theta_t + \tilde{n}_2 \cos\theta_i}\right|^2 \tag{2.12}$$

$$T_{TE} = \frac{\tilde{n}_2 \cos\theta_t}{\tilde{n}_1 \cos\theta_i}\left|\frac{2\tilde{n}_1 \cos\theta_i}{\tilde{n}_1 \cos\theta_i + \tilde{n}_2 \cos\theta_t}\right|^2 \tag{2.13}$$

$$T_{TM} = \frac{\tilde{n}_2 \cos\theta_t}{\tilde{n}_1 \cos\theta_i}\left|\frac{2\tilde{n}_1 \cos\theta_i}{\tilde{n}_1 \cos\theta_t + \tilde{n}_2 \cos\theta_i}\right|^2 \tag{2.14}$$

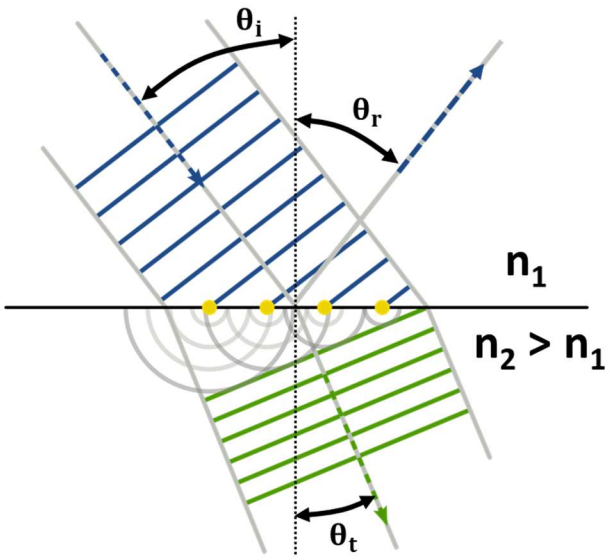

FIG. 2.2. Schematic representation of a plane wave of linearly polarized light incident on a planar interface with angle Θ_i between two media with refractive indices of n_1 and n_2. The Huygens-Fresnel principle is also depicted, which assumes that each point along the interface emits its own spherical wavelet upon illumination, and the superposition of all wavelets form the refracted beam. Periodic wavefronts are highlighted with lines perpendicular to the propagation vector (adapted from [3]).

Introducing an additional interface a small (near-wavelength) distance away from the original interface (i.e., deposition of a thin dielectric layer on a surface) complicates the electromagnetic behavior slightly, as the resulting phase shifts from consecutive reflection and transmission effects at the two interfaces will cause the propagating waves to interfere. This phenomenon is referred to as "thin-film interference", and is schematically represented in Fig. 2.3(a), with three media present (labeled n_1, n_2, and n_3) and with medium 2 having the highest index. A common example of this system is the vivid color profile on soap bubble surfaces, where surfactants stabilize an extremely thin layer of water "suspended" in the surrounding air. Similar behavior emerges with oil deposited on a water surface.

When considering a beam of light incident on a series of thin-film layers, the problem becomes even more complicated, as waves propagating in opposite directions can have different path lengths and phase shifts, resulting in complicated wave interference. We can track the reflection and transmission events of the original beam at each interface, accounting for the accumulated phase shifts and intensities. By adding consecutive transmission and reflection events within the three-medium structure in Fig. 2.3(a), we can calculate the total transmission and reflection amplitude at each wavelength. This approach is formalized with the transfer matrix method (TMM), which involves two types of matrices: a *propagation* matrix ($\mathbf{T_i}$) within layer *i*, and a transfer matrix ($\mathbf{T_{ij}}$) between layers i and j in the multi-layer stack. The transfer matrix initializes the Fresnel coefficients described earlier as follows:

$$\mathbf{T}_{ij} = \frac{1}{t_{ij}}\begin{bmatrix} 1 & r_{ij} \\ r_{ij} & 1 \end{bmatrix} \tag{2.15}$$

The propagation matrix $\mathbf{T}_i$ describes the forward- and backward-propagating waves (E_F & E_B in Fig. 2.3(b)) within each film:

$$\mathbf{T}_i = \begin{bmatrix} e^{i\delta_i} & 0 \\ 0 & e^{-i\delta_i} \end{bmatrix} \tag{2.16}$$

where the phase difference (δ_i) between interfering waves inside a layer of thickness d_i is $\delta_i = \frac{2\pi d_i}{\lambda} n_i \cos\theta_i$. The full transfer matrix calculation is then a product of all transfer matrices for N+1 interfaces and N layers within the structure:

$$\mathbf{T}_N = \prod_{i=1}^{N} \mathbf{T}_{(i-1)i}\mathbf{T}_i \tag{2.17}$$

Provided one has tabulated data for the material's optical dispersion, transmission and reflection amplitudes at each desired wavelength can be calculated with the above formalism.

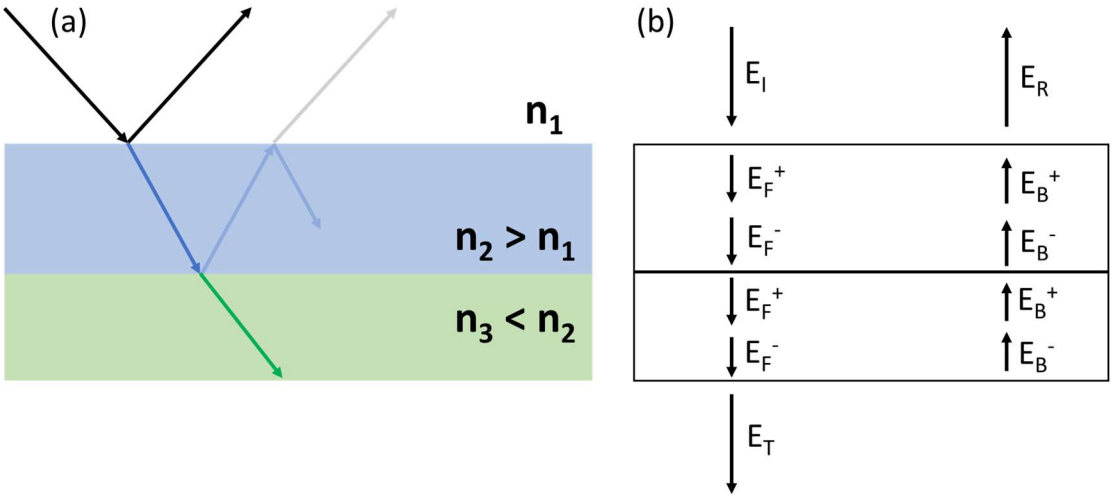

FIG. 2.3. (a) The "soap-bubble" case of thin-film interference, where light is incident on a higher-index surface, with another lower-index medium underneath. (b) Schematic representation of the electric fields (F ≡ forward, B ≡ backward) propagating in both directions inside a multi-layer structure, forming a conceptual basis for the transfer-matrix method (TMM).

Multi-layer dielectric stacks are present in both natural and technological settings. For example, the wings of certain beetles contain a laminar arrangement of distinct tissues, which contribute to the iridescent behavior they exhibit. In strikingly similar fashion, our ever-improving ability to deposit and modify chemically distinct dielectric and semiconductor layers has allowed us to realize high, wavelength-selective reflection, owing to a periodic bilayer structure called a distributed Bragg reflector (DBR). Both are shown for reference in Fig. 2.4 below, along with a standard DBR reflectance spectrum.

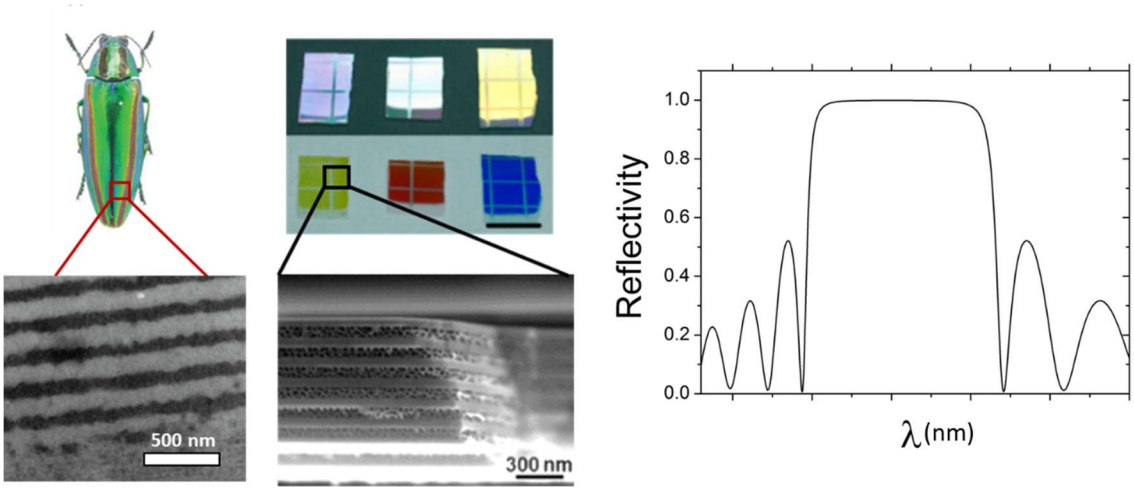

FIG. 2.4. Optical and cross-sectional scanning electron microscope images of the Japanese jewel beetle and selectively porosified III-nitride material comprising a distributed Bragg reflector (DBR), with both surfaces leveraging constructive thin-film interference to afford intense, wavelength-selective reflection. A reflectance spectrum of a typical DBR is shown at right. Adapted and reprinted with permission. ©2011, American Physical Society and © 2015, American Chemical Society.

2.2.3 Interactions of light with structured surfaces

In the previous section, we discussed how out-of-plane interference between thin layers of varying media gives rise to various optical phenomena, which can be easily calculated with TMM. Nature also contains many structures with in-plane variation in media; the characteristic size of this variation relative to the wavelength of incident light determines the governing interaction regime and the optical phenomena that occur (Fig. 2.5). For example, if the wavelength of incident light (λ) is much greater than the characteristic structural length scale (d), the structured portion of the surface can be approximated as a homogeneous material layer. If d is of the same order as λ, then the nature of the structuring determines the optical behavior and can be generally categorized as scattering (continuous, incoherent distribution of incident intensity) or diffraction (coherent, discrete partitioning of light into various interference orders). In

recent years, the rapid development and investigation of optical metasurfaces has allowed a greater set of coherent scattering behavior to emerge, such as beam deflection, focusing, and holography. Finally, if λ is much shorter than d, the optical behavior within the structure reverts to standard Fresnel reflection, and is commonly referred to as geometric ray optics to generalize the multiple reflections rendered from nonplanar geometries. Below, we elaborate on the effective-medium and scattering regimes.

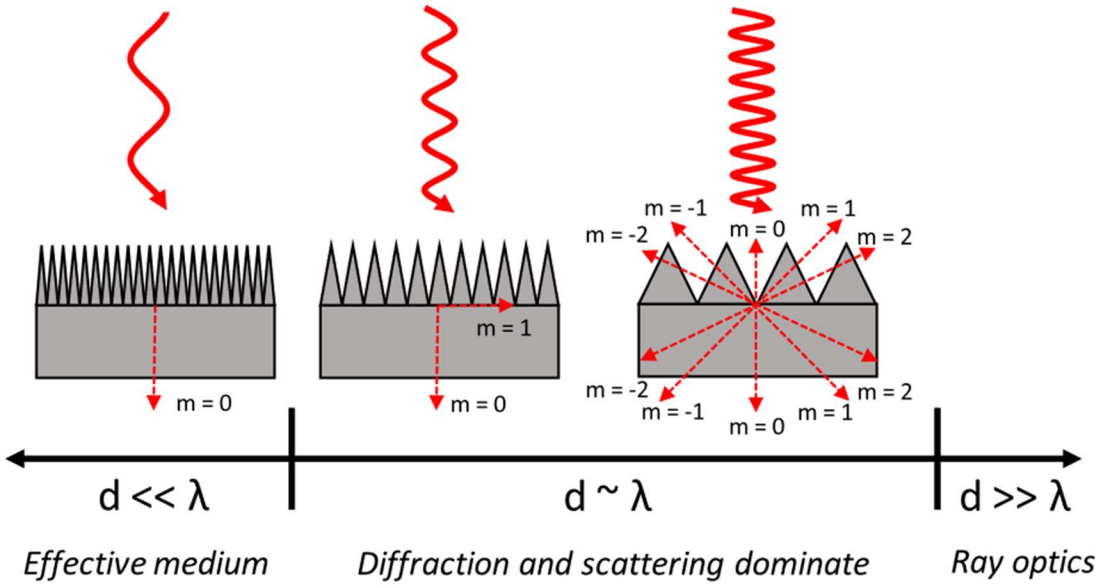

FIG. 2.5. Regimes of light-matter interactions in structured surfaces with characteristic feature spacing d, and incident wavelength λ.

Effective-medium theory (EMT) was developed to capture the propagation of electromagnetic waves in heterogeneous (e.g., porous or periodic) media. Generally, EMT is valid if no plane-wave diffraction is supported, given the wavelength (λ) and period (d) considered. The diffraction condition for transmitted propagating grating orders (m) of a plane wave with incident angle θ_i from index n_1 onto a grating comprised of index n_2 is given by:

$$n_1 \sin\theta_i + n_2 \sin\theta_m = -\frac{\mathrm{m}\lambda}{d} \tag{2.18}$$

If no orders are real besides the zeroth order (transmission and reflection), EMT is valid, and an effective index approximation n_{eff} can be expanded with respect to (d/λ):

$$n_{eff} = \mathrm{n}^{(0)} + n^{(2)}\left(\frac{d}{\lambda}\right)^2 + n^{(4)}\left(\frac{d}{\lambda}\right)^4 + \cdots \tag{2.19}$$

Higher-order terms, while useful for more complex geometries, can be neglected for a reasonable approximation of planar layers that are sufficiently thin relative to the incident wavelength. If this is the case, a versatile effective-medium approximation developed by Bruggeman can be used, which implicitly treats a mixture of k materials with volume fractions f_i:

$$\sum_{i=1}^{k} f_i \frac{n_i^2 - n_{eff}^2}{n_i^2 + 2n_{eff}^2} = 0 \tag{2.20}$$

If, however, Eq. 2.18 yields one or more non-zeroth propagating grating orders, we must tread lightly in using EMAs, especially if the volume fraction of periodic inclusions is non-negligible. In this case, an alternative formalism (e.g. Bloch-wave, coupled mode theory) is needed to properly capture the electrodynamics of the structure [4,5] . One recurring thematic in this work is the emergence of Fano resonances, which arise from a coupling of slowly varying thin-film interference modes and localized waveguided modes induced by air inclusions. These can be modeled by coupled oscillators driven by the incident

light, with the phase difference between the two individual resonances determining the degree of symmetry in the resonance lineshape [4,6].

2.2.4 Finite-difference time-domain optical simulations

While certain geometries have analytical solutions to Maxwell's equations (including multilayer planar interfaces, spheres, and infinite cylindrical rods [7]), most complex geometries require a rigorous numerical solution. Drawing inspiration from fluid dynamics, a discrete finite-difference approach for electromagnetism was formulated by Kane S. Yee in 1966 and is called the finite-difference time-domain (FDTD) method. Briefly, the method involves discretizing (also known as "meshing") the geometry of interest, and spatially staggering the coordinates of the electric and magnetic field components to be calculated (forming a unit cell known as the "Yee cell"). As the name suggests, the calculation proceeds sequentially in the time domain, solving the electric and magnetic field vector equations in a leapfrog manner as the system evolves to a steady state or relaxes all transient processes (depicted in Fig. 2.6). Time-domain methods are advantageous for their natural handling of non-linear materials and the ability to simultaneously treat a wide range of frequencies.

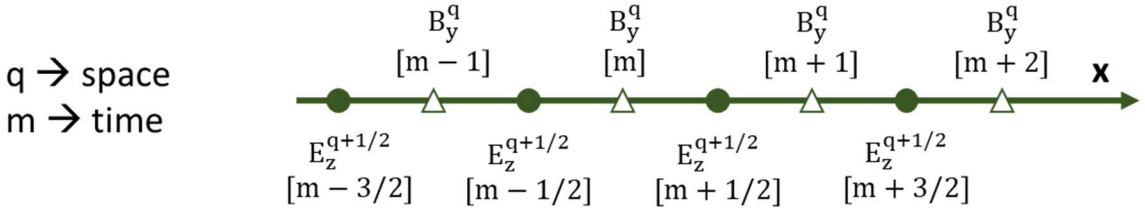

FIG. 2.6. Schematic representation of the 1D finite-difference time-domain method, simplified to light propagating in the x-direction. Electric (E) and magnetic (B) field values are computed on a discrete, spatially (indexed by "q") and temporally (indexed by "m") staggered grid, and each half-step in time is solved sequentially based on the field value in the previous time and space point.

Despite its power and accuracy in predicting optical behavior in virtually any geometry, the computational cost for FDTD scales poorly with simulation volume relative to the wavelengths of interest. As a result, simulating structures that exhibit mesoscale order or hierarchical structuring can prove too computationally expensive. Hybrid, multi-level approaches can be taken to circumvent this, e.g., combining FDTD-generated empirical scattering functions and implementing them as boundary conditions in Monte-Carlo ray-tracing simulations.

2.2.5 Color perception by mapping to the CIE 1931 color space

Color is a construct of human perception and relies on the sensitivity of three different types of "cone" receptor cells in the human retina. These are known as S (short), M (medium), and L (long) cones, named for the cursory range of visible wavelengths that are sensed by their photopsin proteins (Fig. 2.7(a)). Since three distinct receptors can be used for color perception, the full locus of possible perceived colors is a three-dimensional space. However, this can be distilled into two main "axes": apparent brightness (luminance) and color quality (chromaticity), where chromaticity is further subdivided into hue (distinguishable color) and saturation (depth). Conversion of spectral data to an accurate perceived color is achieved by the tristimulus values, which are a new set of functions (color-matching functions) responsible for a subset of the "axes" described above. One common color-matching variant is represented by $\{X(\lambda), Y(\lambda), Z(\lambda)\}$ and is shown in Fig. 2.7(b) below. Y represents luminance and nearly fully captures information about M-cone response, while X and Z split most of the duties

in defining chromaticity. Given this definition, we can further reduce the variable space by defining x, y, and z as follows:

$$x = \frac{X}{X+Y+Z}, \qquad y = \frac{Y}{X+Y+Z}, \qquad z = \frac{Z}{X+Y+Z} = 1 - x - y \tag{2.21}$$

This allows most of the chromaticity information to be displayed in two dimensions and comprises the commonly known CIE 1931 chromaticity diagram (Fig. 2.7(c)). If the white point on the CIE color space below is treated as a polar coordinate origin, the angular coordinate relates to hue, and the radial coordinate roughly represents saturation.

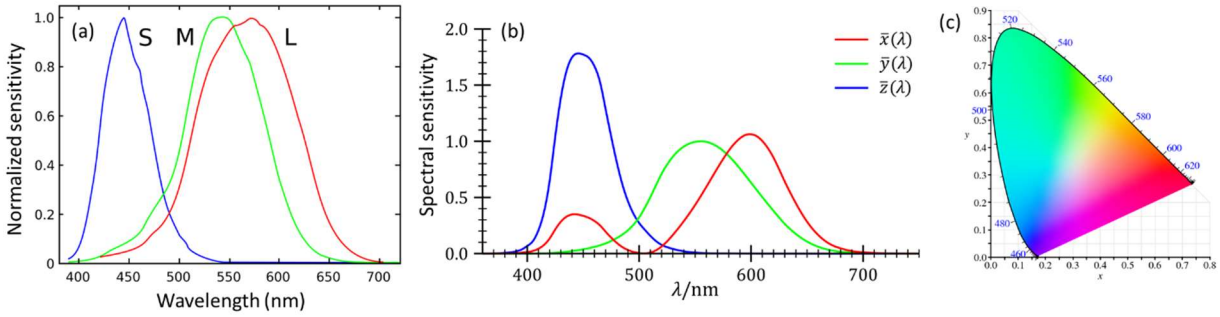

FIG. 2.7. (a) Normalized spectral sensitivity of the three types of cone photoreceptors (Small, Medium, Long wavelegnths) in the human retina. (b) Color-matching functions used in the CIE 1931 RGB color space, which are referenced to wavelengths that are more evenly spaced across the entire visible spectrum. Negative $\bar{r}$ values are introduced to account for this adjusted spacing and the significant overlap of the M and L cone cell sensitivities. (c) The CIE 1931 chromaticity diagram; if the white point is treated as the origin of a polar coordinate system, the angular coordinate corresponds to hue, and the radial component corresponds to purity/saturation.

2.3 Fundamentals and challenges of achieving efficient GaN/InGaN-based light-emitting devices

2.3.1 The GaN LED revolution

The III-nitride alloy family (namely, Al-, Ga-, and In-nitride) has shown exceptional promise for solid-state lighting technologies given its high carrier mobility

and thermal conductivity, as well as tunable band-gap across the entire visible range (i.e., red-shifting with increasing indium content, as seen in Fig. 2.8). The advent of efficient nitride-based solid-state lighting came in the 1990s, when Shuji Nakamura and collaborators developed the 2-flow reactor geometry and a straightforward thermal anneal to eliminate magnesium-hydrogen complexation during MOCVD growth, which prevented high hole concentrations and mobilities in Mg-doped, p-type GaN. Thereafter, the use of III-nitride InGaN/GaN heterostructures and down-converting yellow-emitting phosphors in place of incandescent/fluorescent lighting brought a dramatic increase in power conversion efficiency (from <5% to >40%). Now, it is poised to transform emissive pixel display technologies in the same manner [8].

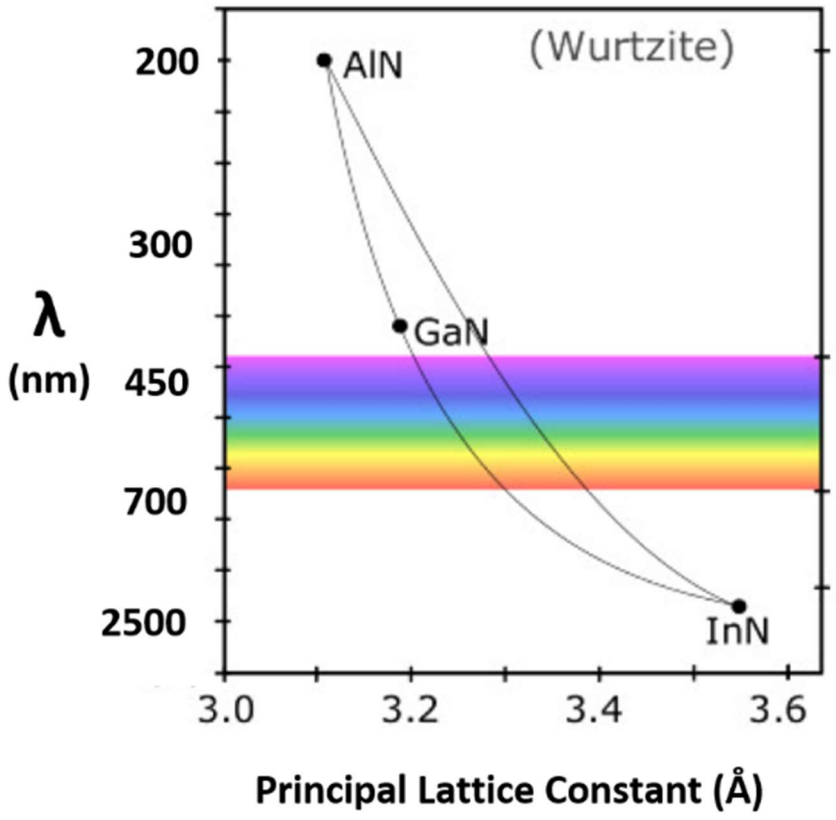

FIG. 2.8. Parameter space of lattice constants and band-gap energies (corresponding to emission wavelength) for the III-nitride alloy family.

2.3.2 III-nitride metalorganic chemical vapor deposition (MOCVD)

In the past several decades, III-nitride optoelectronic devices have been viably produced through metalorganic chemical vapor deposition (MOCVD). MOCVD forms highly crystalline semiconductor thin films by reacting metalorganic precursors with various anion-delivering gases such as ammonia, phosphine, arsine, and ozone [9,10]. Reactants are delivered to the growth surface by laminar flow and through a diffusion boundary layer. The optimal temperature range for III-nitride growth is between 500 and 1200^{o}C, high enough to ensure maximum MO precursor utilization and low enough to prevent premature adatom desorption. This provides excellent control over growth rate and stoichiometry, which translates to effective control over device structures (Fig. 2.9), where nanometer deviations in layer thicknesses can drastically affect performance [11,12].

The standard metalorganic precursors used for MOCVD growth of GaN and InGaN are trimethylgallium (TMGa), triethyl gallium (TEGa), and trimethylindium (TMIn), with cracked ammonia delivering the nitrogen. The dominant reaction mechanism is sequential homolytic cleavage, where each methyl group leaves one after another as the metalorganic adsorbs to the growth surface. The corresponding reactions for GaN and InGaN, respectively, are as follows:

$$Ga(CH_3)_3 + NH_3 \rightleftarrows GaN + 3CH_4 \tag{2.22}$$

$$In(CH_3)_3 + NH_3 \rightleftarrows InN + 3CH_4 \tag{2.23}$$

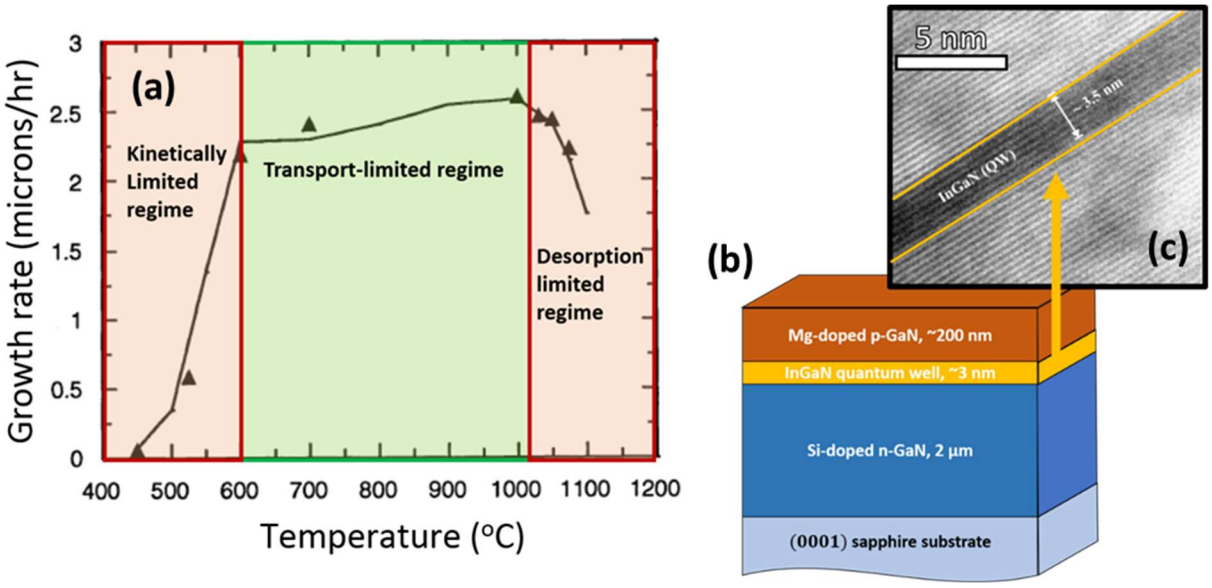

FIG. 2.9. (a) Temperature-dependent MOCVD growth rate regimes, with undesirable growth-limiting extremes highlighted in red. (b) Typical III-nitride p-i-n LED device structure that can be achieved with MOCVD. (c) Transmission electron microscopy (TEM) image of a thin InGaN active region layer, surrounded by GaN. The layered fringes are projections of individual crystal planes (adapted from [11,12] with permission).

Due to its low cracking efficiency (4-5% even above 600°C), a high molar flow of ammonia is always present in the chamber. By Le Chatelier's principle, this pushes the equilibrium to the right of Eq. 1 and prevents decomposition of already-grown GaN. By the same principle, low-pressure MOCVD can push the reaction equilibrium further to the right, and it has been successfully performed [13]; however, atmospheric pressures growth is often chosen for safety and lowered maintenance costs. Nitrogen and hydrogen, the carrier gases of choice Metal-organic (MO) precursors are carried by nitrogen and hydrogen, which are bubbled through the liquid MO sources at carefully regulated temperatures, delivering them to the reactor chamber through heated lines (below 100°C to minimize pre-reactions).

Film quality and uniformity are target deliverables, and the type of reactor one uses can drastically affect both. A schematic of one such reactor chamber is shown in Fig. 2.10. The earliest MOCVD reactors were horizontal chambers with a stationary susceptor; this led to uniformity issues along the direction of precursor flow, as it proved difficult to equalize the diffusive flux of precursor downstream and down through a boundary layer that varies with position. In later years, tilted and rotating susceptors, as well as vertical reactor configurations, helped with uniformity to varying degrees. The two-flow reactor setup, which improved growth uniformity by flattening the boundary layer with a vertical sub-flow gas column, was developed by Nakamura *et al.* in the 1990's and yielded a significant improvement in quality of MOCVD-grown GaN. Popular industrial designs mostly fall between showerhead reactors and planetary reactors, which involve rotation of both individual susceptors and the entire assembly.

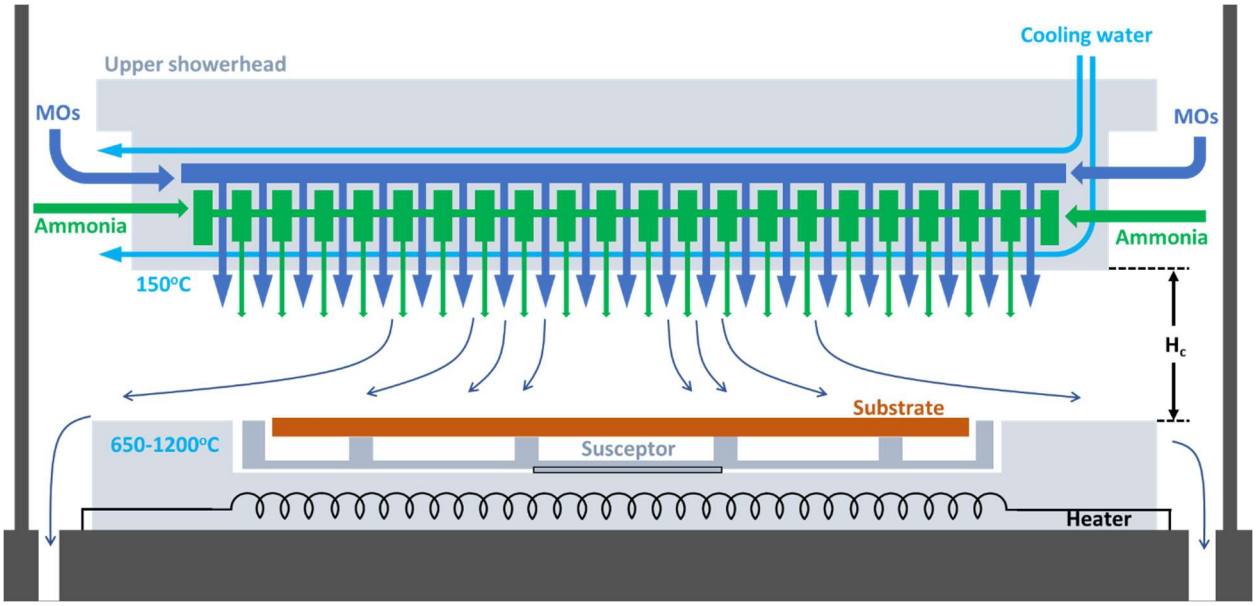

FIG. 2.10. Schematic of an MOCVD reactor with a close-coupled showerhead configuration.

For a close-coupled showerhead reactor with ceiling height H_C, gas kinematic viscosity ν, and inlet velocity v_{in}, the boundary layer thickness, δ, can be approximated by:

$$\delta \approx 3\sqrt{\frac{\nu H_C}{v_{in}}} \tag{2.24}$$

It is assumed that the thermal and chemical boundary layers for the different species, although different due to density and viscosity variations, are of the same order.

2.3.3 Relative merits and challenges of MOCVD growth on various crystal planes

The highest-quality epitaxial GaN/InGaN films are achieved through homoepitaxy on free-standing gallium nitride substrates, cut from larger boules that are grown by seed-initiated hydride vapor-phase epitaxy [14]. However, this technique is costly and produces relatively small-area substrates (~1 cm^2). In order to allay free-standing substrate cost, growth on alternative substrates, such as sapphire and silicon, has been and continues to be intensively studied [15-18]. Sapphire, especially patterned sapphire, has shown most promise for commercially interesting (0001)-plane InGaN devices, reducing threading dislocation density (TDD) to 10^8/sq. cm [19]. Although still relatively high, this TDD is sufficiently suppressed for efficient optoelectronic operation in the GaN system due to its low minority carrier diffusion length. Equivalent defect densities in GaAs, for example, are catastrophic; a functioning GaAs-based device would require at least a hundredfold defect reduction.

Despite their nontrivial cost, less defective (TDD ~ 10^6 cm^{-2}) free-standing substrates offer a wide variety of crystallographic planes, which is useful for investigations into crystal growth and optoelectronic phenomena that strongly depend on facet orientation. These are prepared by slicing c-plane oriented GaN boules grown by hydride vapor phase epitaxy (HVPE) at different angles, followed by chemical-mechanical polishing. If we consider the wurtzite hexagonal crystal structure of GaN, it is possible to classify all crystal faces into three categories (i.e., *polar*, *semipolar*, and *nonpolar*) by their inclination angle from the principal *c* axis. As shown in Fig. 2.11, the polar *c*-plane is 90 degrees to the corresponding c-axis, 0 degrees is nonpolar, and any faces between 0 and 180 (excluding 90) are considered semipolar.

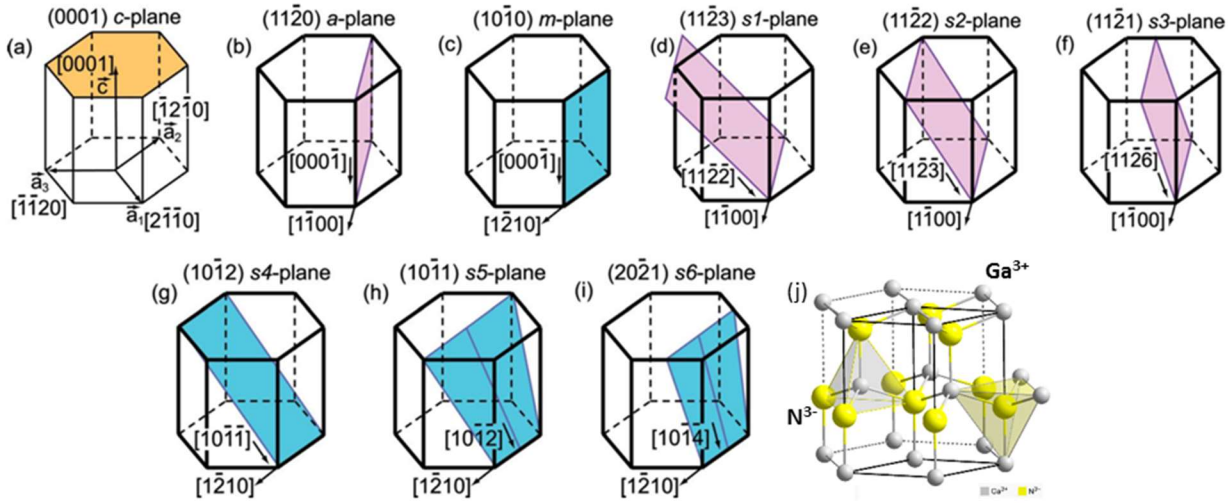

FIG. 2.11. (a-i) Various crystallographic planes of the GaN hexagonal lattice that are indexed by the hexagonal Miller-Bravais indices and their corresponding letter-plane names. (j) The GaN wurtzite structure for reference (Ga in gray, N in yellow). Reprinted with permission from [22]. © 2011, AIP Publishing.

2.3.4 Optoelectronic implications of polarization fields in the ternary InGaN alloy system

GaN is pyroelectric, meaning that it exhibits a nonzero natural electric polarization. This is caused by the polarity of the III-nitrogen bond, as well as a lack of inversion symmetry in the wurtzite lattice. On crystal orientations where the growth surface contains more gallium than nitrogen atoms (or vice versa), the polarity results in positive (or negative) surface charges. These charges build up a spontaneous electric field ($\mathbf{P_{sp}}$) parallel to the polar *c*-axis[20] (Figure 2.12(a)). As the growth direction moves away in inclination angle from the *c*-axis, this field is diminished, and is completely removed in the case of the non-polar *a*- and *m*-planes, where $\mathbf{P_{sp}}$ is then perpendicular to the growth direction [17].

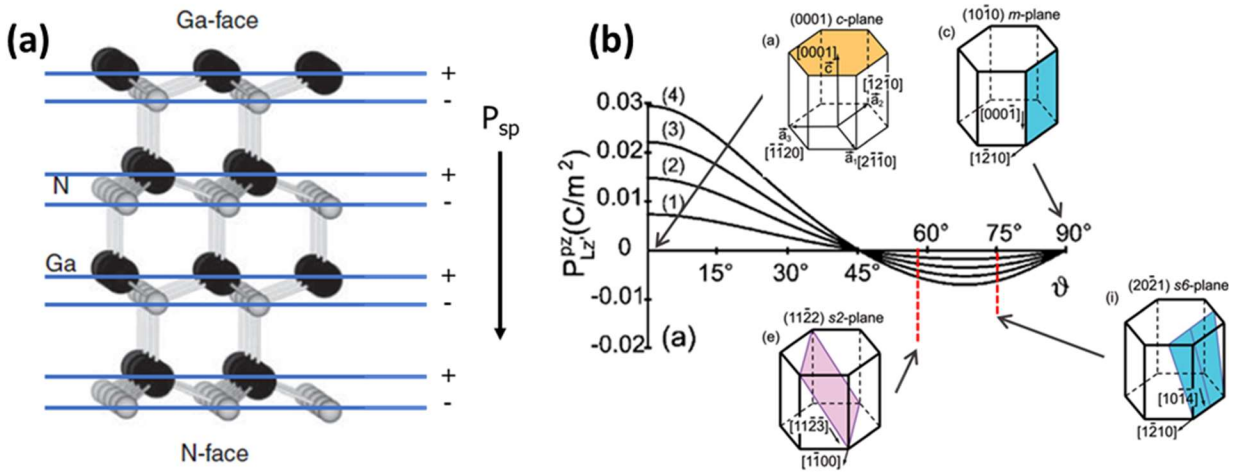

FIG. 2.12. (a) c-plane-oriented GaN lattice, highlighting the ion-formed sheet charges and resulting spontaneous polarization field, $\mathbf{P_{sp}}$. Right: the piezoelectric polarization field $\mathbf{P_{pz}}$ as a function of inclination angle, as well as several key planes and their locations along the curve (adapted from [21,22] with permission). Semipolar planes have a diminished piezoelectric field relative to the c-plane. © 2005 & 2011, AIP Publishing.

We must now consider a full LED device, which contains InGaN layers surrounded by the spontaneously polarized GaN. The main determinant of emission wavelength in an LED is the band energy of the quantum well, which is tuned by the layer's indium molar fraction. Since the InN bond is longer than that of GaN, the lattice constant of the ternary InGaN alloy is correspondingly higher. This leads to in-plane compressive stress in the InGaN layer as it seeks to accommodate the lattice mismatch (Fig. 2.13). This in-plane compressive stress is countered by an out-of-plane tensile strain, which induces an out-of-plane piezoelectric polarization, $\mathbf{P_{pz}}$, in addition to the spontaneous polarization field of the GaN lattice (Fig. 2.12(b)).

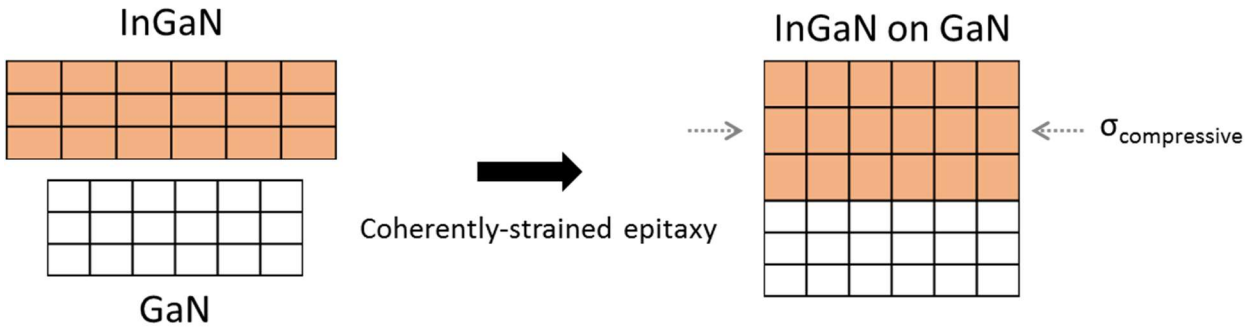

FIG. 2.13. Schematic showing the lattice mismatch of InGaN epitaxially grown on GaN, and the resulting out-of-plane tensile strain that increases the normal lattice plane spacing (the c lattice constant).

The combined effect of $\mathbf{P_{sp}}$ and $\mathbf{P_{pz}}$ plays out differently depending on the heterostructure's growth direction – that is, the crystal plane on which the structure is grown. Since charge carriers within the semiconductor (i.e., electrons and holes) are oppositely charged, they move in opposite directions in an electric field, and they become energetically and spatially separated in the vicinity of the quantum well. This effect, called the quantum-confined Stark effect (QCSE) [23-26], reduces the probability of a

radiative transition, and therefore the quantum efficiency in the context of a light-emitting diode (Fig. 2.14). In the GaN/InGaN system, the effect of piezoelectric polarization is generally more significant than spontaneous polarization. Therefore, the more polar the orientation, the more catastrophic the decline in wavefunction overlap with increasing indium content [21], and the more drastic the decline in IQE.

2.3.5 State-of-the-art in long-wavelength III-nitride devices

In a world where crystal morphology is devoid of defects, we would certainly use nonpolar orientations to maintain high wavefunction overlap out to arbitrarily long wavelengths (high In%), given our discussion of polarization fields in the previous section. However, not all planes are created equal; while coherently strained heteroepitaxy breaks down at some In% threshold regardless of orientation, certain facets are more tolerant to breakdown, owing to a combination of thermodynamic and kinetic factors. Unfortunately, nonpolar growth planes are prone to stacking faults at rather tame indium contents, dramatically limiting their usefulness in long-wavelength applications.

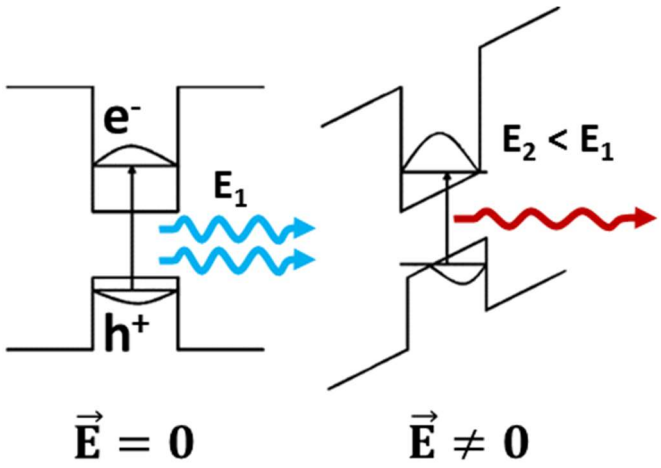

FIG. 2.14. The piezoelectric field-induced quantum-confined Stark effect results in a reduction of carrier wavefunction overlap and a redshift in band-gap energy.

It has been shown computationally and experimentally that semipolar planes appear to incorporate more indium than other facets, in addition to a reduced piezoelectric field and correspondingly lower QCSE. Computational studies of readily available substrate orientations conducted by Wernicke et al. found the longest emission wavelengths (loosely tied here to In incorporation efficiency) to be on the $(11\bar{2}2)$ and $(10\bar{1}1)$ semipolar growth surfaces, as well as the polar c-plane [27] (Fig. 2.15). Northrup also found that the range of optimal growth conditions for indium incorporation is wider for $(11\bar{2}2)$ than for $(10\bar{1}0)$ due to lower transition energies associated with semipolar binding sites [28]. In ammonia-rich molecular beam epitaxial growth studies, Browne et al. found the highest indium incorporation and lowest surface roughness at constant growth conditions to be on the $(20\bar{2}1)$ plane [29].

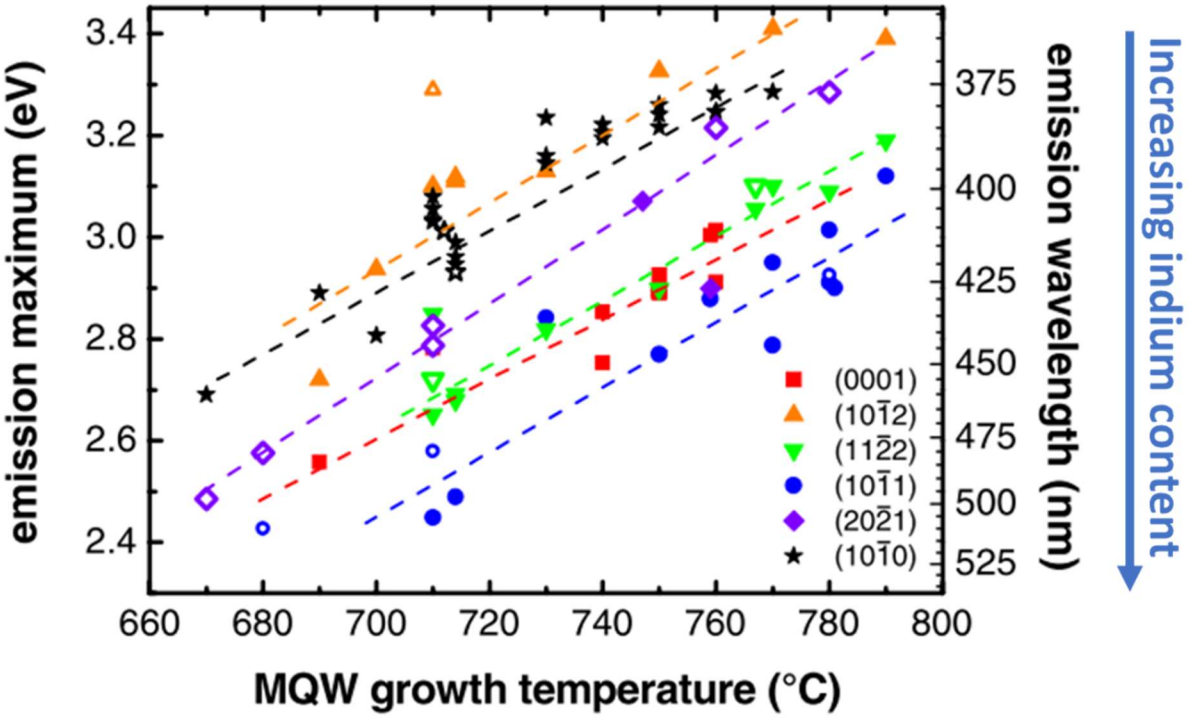

FIG. 2.15. Emission wavelengths of InGaN quantum wells grown on various crystal facets [20], indicating the variation in indium uptake with the growth surface. Adapted from [27],© 2012, IOP Publishing Ltd.

Of the crystal facets considered in the above computational studies, all of the nonpolar and several semipolar planes have experimentally been shown to suffer morphological breakdown through catastrophic defects such as stacking faults and misfit dislocations with indium contents above 15-20% [30,31]. The (11$\bar{2}$2), (20$\bar{2}$1), and (0001) planes have shown most promise in long-wavelength device operation, and over the last half-decade, the latter two have led to demonstrations of green, yellow, and red-emitting diodes [27–29]. However, at external quantum efficiencies of 30, 20, and <2%, respectively, with no evident theoretical limit to internal efficiency (and with light extraction efficiencies in the 40-60% range), the current state of material quality and strain-related issues warrants further investigation and improvement.

2.4 Surface wetting models for uniform and structured solid surfaces

Solid-liquid interactions provide a wealth of information on the adhesive and cohesive forces present in the system. For instance, water beading up on the surface of a lotus leaf tells us that the surface energy of the system is high, and that any additional contact between the water and leaf surface would be unfavorable, owing both to the high cohesion of water and the lack of adhesion between water and the surface. Put another way: the water would rather interact with the surrounding air than the surface underneath. Starting with the simple case of a droplet of liquid L in a surrounding atmosphere of gas G, incident on a smooth, planar, chemically homogeneous surface comprised of solid S, the solid-gas surface tension (γ_{SG}) is given by the Young equation:

$$\gamma_{SG} = \gamma_{SL} + \gamma_{LG} \cos \theta_C \tag{2.25}$$

where γ_{SL} and γ_{LG} are the solid-liquid and liquid-gas surface tension, respectively, and Θ_C is the angle formed by the solid surface and a tangent plane to the droplet surface at the three-phase contact line. Figure 2.16 depicts this system below. Θ_C is known as the Young angle or contact angle and is often experimentally measured to probe the surface energy of various materials. The Young equation is obtained by considering an equilibrium force balance that ensures the net force along each interface is zero.

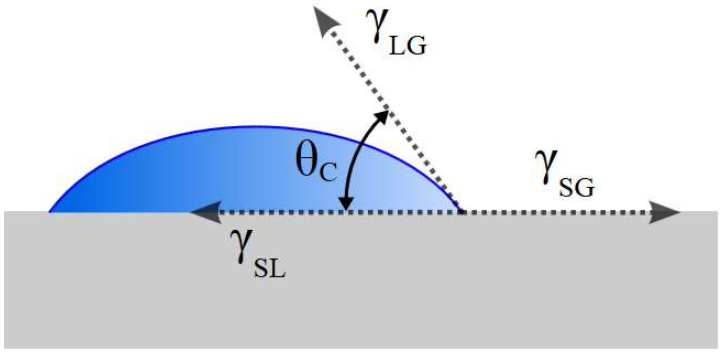

FIG. 2.16. Schematic of a water droplet forming an interfacial contact angle of Θ_C with a planar, perfectly smooth, and chemically homogeneous solid surface in a gas environment.

If solid surface topography is introduced, the Young equation above breaks down, as the apparent contact angle could be affected by the inclination angle of the microscopic surface on which three-phase contact line rests, and the droplet is exposed to a greater solid surface area per additional unit of spreading distance. If the surface topography is shallow and its features are much smaller than the droplet size, the surface area enhancement can be represented by a ratio r (true area normalized by apparent area), and the resulting relationship between apparent contact angle Θ^* and the inherent contact angle Θ_C is given by the Wenzel model:

$$\cos\theta^* = r\cos\theta_C \tag{2.26}$$

While the Wenzel model accounts for surface area enhancements, it does not account for chemical heterogeneity or topography with high aspect ratios. This can be achieved with the Cassie-Baxter wetting model, which accounts for the interactions of the liquid with each of the chemically distinct media on the surface (contact angles θ_i), weighted by their respective area fraction, f_i:

$$\cos\theta^* = f_1\cos\theta_1 + f_2\cos\theta_2 \tag{2.27}$$

In the case of the two media being solid and air (cos(π) = -1), the model simplifies to:

$$\cos\theta^* = f_1\cos\theta_1 - f_2 = f_1\cos\theta_1 - (1 - f_1) = \boldsymbol{f_1(\cos\theta_1 + 1) - 1} \quad (2.28)$$

The Cassie-Baxter model is the simplest relation that successfully describes superhydrophobic behavior (θ* > 150°) as an interplay of chemical and topographic factors. For instance, it can effectively capture how the waxy and sparsely structured surface of the lotus leaf provides an efficient highway for dirt-scavenging dew and raindrops.

2.5 Langmuir-Blodgett deposition

Having reviewed some of the basics of macroscopic wetting physics, we are well poised to describe the Langmuir-Blodgett (LB) dip-coating approach to forming colloidal monolayers on substrates. The LB method was developed by Irving Langmuir and Katharine B. Blodgett while at General Electric in 1926-27, where it was found that highly uniform monolayers of organic molecules could be transferred onto glass substrates by immersing them in a water subphase, depositing and closely packing molecules at the air-water interface, and withdrawing the substrates. LB dip-coating has since been used for depositing a variety of chemical moieties and particles for electronic, optical, and biological applications. Herein, LB-coating is adapted for producing highly close-packed monolayers of silica spheres (diameters 0.31-4 μm) to be used as pattern-defining plasma etch masks for nanoscale light emitters, selective-area MOCVD growth masks, and wavelength-selective, diffusely colored nanomembranes. Details of LB deposition are shown below in Fig. 2.17.

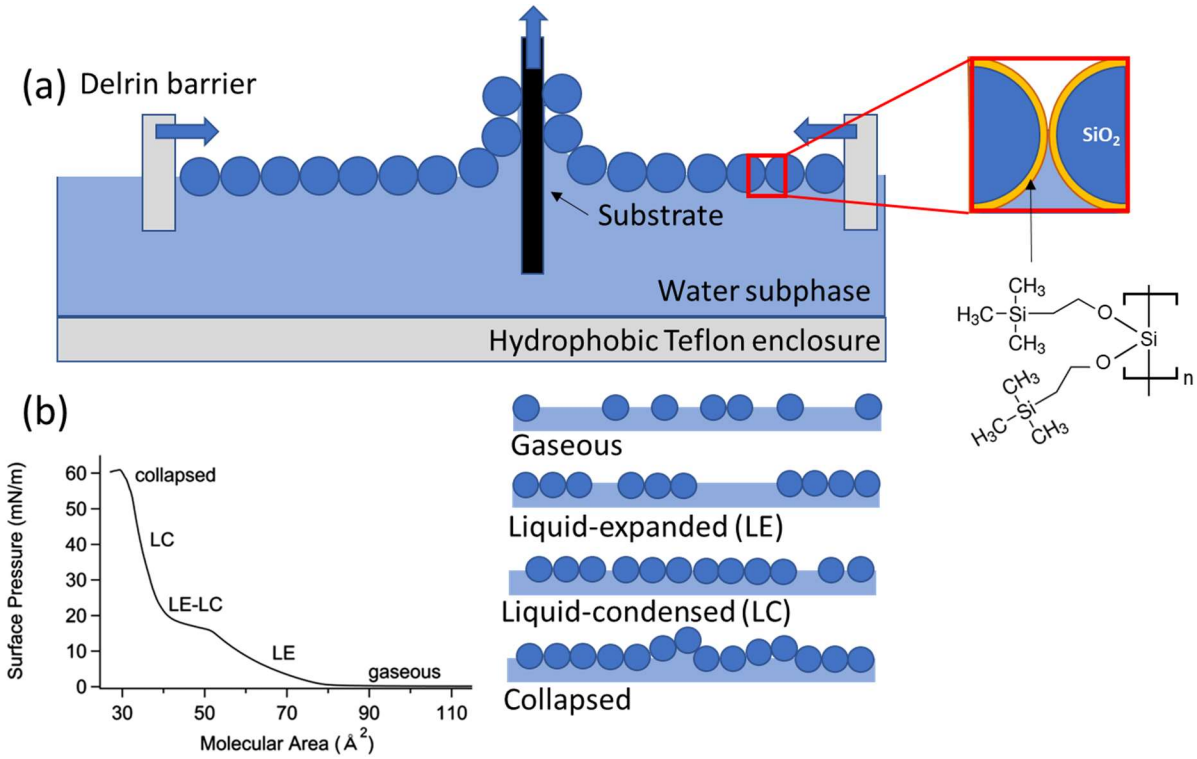

FIG. 2.17. (a) Conceptual schematic of Langmuir-Blodgett deposition, where a close-packed array of allyltrimethylsilane-functionalized SiO_2 spheres are transferred to a substrate of interest. (b) Typical LB isotherm, showing the various of colloid packing behavior present at the air-water interface, mediated by with increasing surface pressure with reduced system area as defined by barrier-induced compression.

Silica colloids (Bangs Laboratories) were functionalized with allyltrimethylsilane (ATMS) in acidic ethanol (pH ~ 5.5, acetic acid, 10% H_2O, and ~15 mM ATMS), giving their surface a hydrophobic character. These were dried under low vacuum (70°C, 12 h) and dispersed in a 1:3 ethanol/chloroform solution prior to deposition. Chloroform is volatile and has low surface tension, making it an optimal solvent for delivering colloidal particles to the air-water interface. Ethanol is added to help with colloidal dispersion while maintaining improved colloidal droplet adhesion to the water subphase. Once the chloroform evaporates, the hydrophobic surface of the silica colloids prevents sedimentation and dispersion into the subphase, pinning the particles at the interface.

LB deposition proceeded in a KSV Nima Langmuir trough (Biolin Scientific), which was comprised of a Teflon (polytetrafluoroethylene) enclosure to reduce edge deposition, Delrin (polyoxymethylene) barriers to ensure low-friction glide along the trough surface, a dipping mechanism, and a surface pressure sensor fitted with a platinum Wilhelmy plate. The sensor detects small changes in surface pressure (Π) by tracking deflections of a laser beam off a cantilever on which the Wilhelmy plate is suspended; by defining the dimensions and contact angle of water on the plate, one can estimate the changes in Π at the interface. After submerging the substrate of interest, colloids are pipetted dropwise onto the de-ionized water subphase and given time to distribute on the surface. A pressure-area (Π-A) isotherm (Fig. 2.17(b)) is then recorded to track the phase behavior of colloids at the interface as they evolve from a gas-like to fully close packed state with slow, continuous barrier compression. The final approach to close packing is signaled by an acceleration in Π increase followed by a sudden plateau, indicating the start of film collapse and buckling. The midpoint of the sharply sloped linear increase regime is chosen as a Π regulation target during deposition.

Pressure regulation during substrate withdrawal, afforded by adjusting barrier positions, ensures a consistent surface-thermodynamic state and a 1-to-1 monolayer transfer. However, given that the deposition behavior and quality is mediated by the moving three-phase contact line as the substrate is withdrawn, the surface should ideally be as hydrophilic as possible. Alternatively, wetting contrasts may be employed to direct colloid deposition exclusively to selected areas. Once withdrawal is complete and the sample dries, a quasi-ordered hexagonal colloid monolayer remains on the sample surface through attractive van der Waals forces and may be processed further.

References

1. "Electromagnetic wave," https://en.wikipedia.org/wiki/Electromagnetic_radiation#/media/File:Onde_electromagnetique.svg%0A.
2. "Electromagnetic spectrum properties," https://commons.wikimedia.org/wiki/File:EM_Spectrum_Properties_edit.svg.
3. "Huygens' refraction principle," https://commons.wikimedia.org/wiki/File:Refraction_-_Huygens-Fresnel_principle.svg.
4. S. Fan and W. Suh, "Temporal coupled-mode theory for the Fano resonance in optical resonators," J. Opt. Soc. Am. A **20**(3), 569–572 (2003).
5. B. C. P. Sturmberg, K. B. Dossou, L. C. Botten, R. C. McPhedran, and C. M. de Sterke, "Fano resonances of dielectric gratings: symmetries and broadband filtering," Opt. Express **23**(24), 1672–1686 (2015).
6. M. F. Limonov, M. V. Rybin, A. N. Poddubny, and Y. S. Kivshar, "Fano resonances in photonics," Nat. Photonics **11**(9), 543–554 (2017).
7. F. Frezza, F. Mangini, and N. Tedeschi, "Introduction to electromagnetic scattering: tutorial," J. Opt. Soc. Am. A **35**(1), 163–173 (2018).
8. Z. Y. Fan, J. Y. Lin, and H. X. Jiang, "III-nitride micro-emitter arrays: Development and applications," J. Phys. D. Appl. Phys. **41**(9), (2008).
9. P. J. Wright, M. J. Crosbie, P. A. Lane, D. J. Williams, A. C. Jones, T. J. Leedham, and H. O. Davies, "Metal organic chemical vapor deposition (MOCVD) of oxides and ferroelectric materials," J. Mater. Sci. Mater. Electron. **13**(11), 671–678 (2002).
10. G. B. Stringfellow, "Organometallic Vapor-Phase Epitaxy," (1999).
11. T. Mihopoulos, "Reaction and Transport Processes in OMCVD : Selective and Group III-Nitride Growth," (1999). PhD Dissertation, MIT.
12. C. Skierbiszewski, P. Perlin, I. Grzegory, Z. R. Wasilewski, M. Siekacz, A. Feduniewicz, P. Wisniewski, J. Borysiuk, P. Prystawko, G. Kamler, T. Suski, and S. Porowski, "High power blue–violet InGaN laser diodes grown on bulk GaN substrates by plasma-assisted molecular beam epitaxy," Semicond. Sci. Technol. **20**(8), 809–813 (2005).
13. D. G. Chtchekine, L. P. Fu, G. D. Gilliland, Y. Chen, S. E. Ralph, K. K. Bajaj, Y. Bu, M. C. Lin, F. T. Bacalzo, and S. R. Stock, "Properties of low-pressure chemical vapor epitaxial GaN films grown using hydrazoic acid (HN3)," J. Appl. Phys. **81**(5), 2197–2207 (1997).
14. L. Solymar and D. Walsh, "Electrical properties of materials," (2010).
15. F. Tendille, P. De Mierry, P. Vennéguès, S. Chenot, and M. Teisseire, "Defect reduction method in (11-22) semipolar GaN grown on patterned sapphire substrate by MOCVD: Toward heteroepitaxial semipolar GaN free of basal stacking faults," J. Cryst. Growth **404**(October 2014), 177–183 (2014).
16. N. Kriouche, P. Venénguès, M. Nemoz, G. Nataf, and P. De Mierry, "Stacking faults blocking process in (1 1 -2 2) semipolar GaN growth on sapphire using asymmetric lateral epitaxy," J. Cryst. Growth **312**(19), 2625–2630 (2010).
17. J. Ma, X. Zhu, K. M. Wong, X. Zou, and K. M. Lau, "Improved GaN-based LED grown on silicon (111) substrates using stress/dislocation-engineered interlayers," J. Cryst. Growth **370**, 265–268 (2013).
18. S. Pal and C. Jacob, "Silicon—a new substrate for GaN growth," Bull. Mater. Sci. **27**(6), 501–504 (2004).

19. Y. C. Shen, G. O. Mueller, S. Watanabe, N. F. Gardner, A. Munkholm, and M. R. Krames, "Auger recombination in InGaN measured by photoluminescence," Appl. Phys. Lett. **91**(14), (2007).

20. F. Bernardini, V. Fiorentini, and D. Vanderbilt, "Spontaneous polarization and piezoelectric constants of III-V nitrides," Phys. Rev. B - Condens. Matter Mater. Phys. **56**(16), R10024–R10027 (1997).

21. A. E. Romanov, T. J. Baker, S. Nakamura, and J. S. Speck, "Strain-induced polarization in wurtzite III-nitride semipolar layers," J. Appl. Phys. **100**(2), (2006).

22. A. E. Romanov, E. C. Young, F. Wu, A. Tyagi, C. S. Gallinat, S. Nakamura, S. P. Denbaars, and J. S. Speck, "Basal plane misfit dislocations and stress relaxation in III-nitride semipolar heteroepitaxy," J. Appl. Phys. **109**(10), (2011).23. S. Chichibu, T. Azuhata, T. Sota, and S. Nakamura, "Recombination of Localized Excitons in InGaN Single- and Multiquantum Well Structures," MRS Proc. **449**(May), 3–4 (1996).

24. T. Takeuchi, S. Sota, M. Katsuragawa, M. Komori, H. Takeuchi, H. Amano, and I. Akasaki, "Quantum-Confined Stark Effect due to Piezoelectric Fields in GaInN Strained Quantum Wells," Jpn. J. Appl. Phys. **36**(Part 2, No. 4A), L382–L385 (1997).

25. J.-H. Ryou, P. Douglas Yoder, J. Liu, Z. Lochner, H. Kim, H. Jin Kim, and R. D. Dupuis, "Control of Quantum-Confinement Stark Effect in InGaN-Based Quantum Wells," IEEE J. Sel. Top. Quantum Electron. Vol. 15, No. 4 **15**(4), 1080–1091 (2009).

26. S. Mokkapati and C. Jagadish, "III-V compound semiconductors for optoelectronic devices," Mater. Today **12**(4), 22–32 (2009).

27. T. Wernicke, L. Schade, C. Netzel, J. Rass, V. Hoffmann, S. Ploch, A. Knauer, M. Weyers, U. Schwarz, and M. Kneissl, "Indium incorporation and emission properties of nonpolar and semipolar InGaN quantum wells," Semicond. Sci. Technol. **100**(27), (2012).

28. J. E. Northrup, "GaN and InGaN (1122) surfaces: Group-III adlayers and indium incorporation," Appl. Phys. Lett. **95**(13), 3–5 (2009).

29. D. A. Browne, E. C. Young, J. R. Lang, C. A. Hurni, and J. S. Speck, "Indium and impurity incorporation in InGaN films on polar, nonpolar, and semipolar GaN orientations grown by ammonia molecular beam epitaxy," J. Vac. Sci. Technol. A Vacuum, Surfaces, Film. **30**(4), 041513 (2012).

30. Y. Kawaguchi, C. Y. Huang, Y. R. Wu, Q. Yan, C. C. Pan, Y. Zhao, S. Tanaka, K. Fujito, D. Feezell, C. G. Van De Walle, S. P. Denbaars, and S. Nakamura, "Influence of polarity on carrier transport in semipolar (20$\bar{2}$1) and (20$\bar{2}$1) multiple-quantum-well light-emitting diodes," Appl. Phys. Lett. **100**(23), 1–5 (2012).

31. M. T. Hardy, E. C. Young, P. S. Hsu, D. A. Haeger, I. L. Koslow, S. Nakamura, S. P. Denbaars, and J. S. Speck, "Suppression of m-plane and c-plane slip through Si and Mg doping in partially relaxed (20$\bar{2}$1) InGaN/GaN heterostructures," Appl. Phys. Lett. **101**(13), (2012).

32. S. Yamamoto, Y. Zhao, C. C. Pan, R. B. Chung, K. Fujito, J. Sonoda, S. P. DenBaars, and S. Nakamura, "High-efficiency single-quantum-well green and yellow-green light-emitting diodes on semipolar (20$\bar{2}$1) GaN substrates," Appl. Phys. Express **3**(12), 1–4 (2010).

33. Y. Kawaguchi, C. Y. Huang, Y. R. Wu, Y. Zhao, S. P. DenBaars, and S. Nakamura, "Semipolar (20-21) single-quantum-well red light-emitting diodes with a low forward voltage," Jpn. J. Appl. Phys. **52**(8 PART 2), 1–4 (2013).

34. J. Il Hwang, R. Hashimoto, S. Saito, and S. Nunoue, "Development of InGaN-based red LED grown on (0001) polar surface," Appl. Phys. Express **7**(7), (2014).

3

Optical physics of diatom-inspired dielectric nanostructures

(Adapted from the JVST A article: Shapturenka, P., Birkholz, F., Zakaria, N. I., DenBaars, S. P., and Gordon, M. J. "Quasiordered,, subwavelength TiO_2 hole arrays with tunable, omnidirectional color response." *JVST A*, **38**(5), 2020.)

3.1 Introduction

As discussed in the previous section, composite materials with near-wavelength spatial variations in dielectric constant give rise to interesting and useful optical behaviors in nature. These micro- and nanoscopic morphologies manifest in interference-based phenomena such as diffraction and etaloning, as well as focusing and graded-index (GRIN) waveguiding, at visible and infrared wavelengths. In natural environments, this yields useful evolutionary advantages such as vivid coloration (beetles, birds, butterflies), camouflaging (chameleons, squid), and sensitive night vision (moths) [1–3].

In addition to the creatures mentioned above, nature has also proliferated organisms that possess remarkably ordered microstructures but lack the remarkable optical properties one might expect. One such family is the centric marine diatoms, which boast honeycombed, micro-periodic siliceous frustules as their exoskeleton, often

referred to as the “glass menagerie” given their diversity (Fig 3.1). It has been posited that this biosilica cage affords the marine diatom UV-scattering and visible-wavelength focusing abilities that reduce harmful irradiation and improve photosynthetic efficiency, respectively [4–6]. Moreover, owing to their high surface area and hierarchical structure, diatom frustules have garnered decades-long academic interest as potential components in molecular sieves, chemical sensors, and heterogeneous catalysts[7–9]. Scale-up of these types of surfaces is desirable for commercial feasibility, and this has been attempted in the form of acid-promoted wafer bonding and fluidic assembly [10–12]. Despite sparse reports of bright coloration and a potential photonic bandgap when the diatom is coated or comprised of higher refractive index materials [13,14], there has yet to be a systematic study of structural color emergence in diatom-based nano- and microstructures.

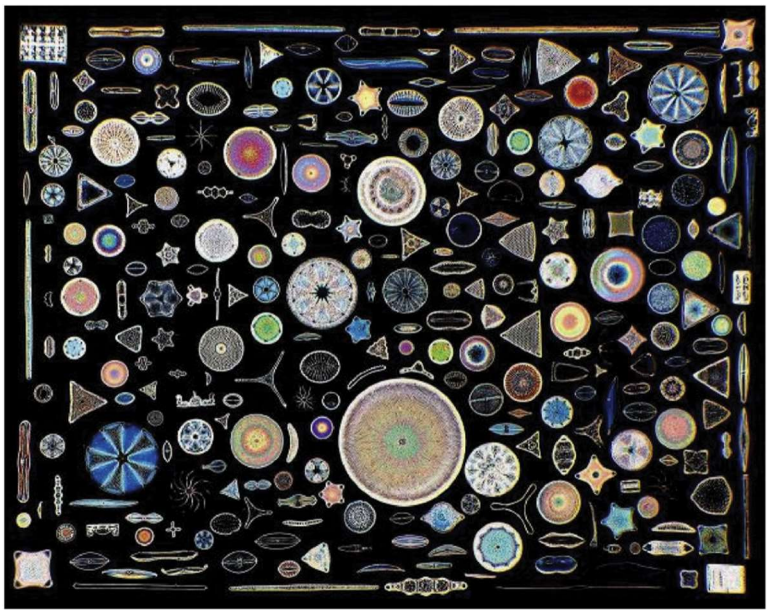

FIG 3.1. Three hundred diatom species, sourced from a variety of places on Earth, mounted by hand on a display board, showing the mind-boggling variety of different morphologies of phytoplankton in Earth’s aqueous environments. Reprinted with permission from [15]. © 2008, Elsevier Ltd.

Herein, we consider a simplified structural model for the diatom frustule, assign the resulting optical contributions to the various components of the frustule, and extend the material design space beyond biosilica to high-index, low-absorption materials such as TiO_2. We first find a set of high-intensity Fano modes supported by a perfectly ordered thin-film silica nanomembrane in air, which was attributed to coupling between the lattice-supported guided modes and internal Fabry-Pérot etaloning sustained by the top and bottom membrane interfaces. This coupling was found to intensify in TiO_2 structures, with near-100% reflectance in place of nearly full transmission in the analogous silica case. The emergent modal behavior was re-cast in terms of a dimensionless optical path length and a wavelength-normalized lattice period, allowing us to extend the behavior to all wavelengths where the dielectric material is reasonably lossless. Moreover, higher-index nanomembranes are found to support broadband reflection and transmission properties, in line with recent investigations in optoelectronics and photonics literature, where analogous structures are known as high-contrast gratings [16–18]. This broadband behavior stems from the coupling of adjacent, opposite-polarity Fano resonances and was found to be hindered by the thin silica framework supporting the top nanomembrane layer by introducing a lower index contrast relative to an idealized floating film.

The biochemical processes by which the diatom's intricate structures are created remain at the whim of thermal, mechanical, and hydrodynamic forces, which makes them prone to various types of morphological disorder. Accordingly, we explored the effects of hole diameter polydispersity and translational hole displacement on the optical behavior of the supported TiO_2 structures. Translational disorder is found to decouple the Fano

resonance pair, resulting in a dramatic decay in normal-incident transmission and reflection. A corresponding increase in angle-independent diffuse scattering is observed at the same Fano mode wavelengths, paving the way to rational modal design of non-iridescent structural color.

Having explored the relevant optical design space, we target a set of wavelengths spanning the visible spectrum and develop a fabrication platform to realize TiO_2 hole arrays designed to operate at three visible wavelengths. Optical characterization showed a consistent, angle-independent color response and Fourier transforms of plan-view SEM micrographs indicated local, isotropic correlated order in the resulting hole arrays. Moreover, the modal locations at which backscattering was strongest were in excellent agreement with computationally predicted diffuse resonances. Finally, we show the importance of using absorbing materials (like silicon) to suppress higher-order Fano modes present in the TiO_2 slabs for improved color saturation.

3.2 Re-thinking the humble diatom's geometry

3.2.1 Computationally elucidating diatom frustule optical response

In this section, we investigate the structure-derived optical behaviors of several centric diatom exoskeletons (frustules), namely those of *Thalassiosira eccentrica* and *Coscinodiscus sp*. Scanning electron micrographs of these structures are shown in Figure 3.2(a) below. Briefly, frustules are comprised of an array of semi-permeable pores (areolae) embedded in two continuous biosilica films. The top valve surface contains microscopic openings (foramina, diameters of roughly 1 μm) arranged in an ordered

hexagonal array that also determine the spacing of the underlying wall support. The lower valve layers (cribra) within each areola contain an ensemble of fine, nanometer-sized pores arranged in a similar hexagonal arrangement as the much larger foramina above them (cribellum, <100 nm pore spacing).

To clearly identify fundamental optical resonances and pragmatically assign any interactions with visible light, we start with several idealized simplifications to the natural morphology of the *T. eccentrica* frustule. First, we assume the areolar arrangement is perfectly ordered with a characteristic period, p, and foramina are modeled as air cylinders of radius r_1 with height t. Second, given that the cribellum feature periodicity (<100 nm) is significantly smaller than visible wavelengths (350-750 nm) and localized to a small fraction of the layer, we assume that a thin, solid biosilica slab. The interior supporting walls in the intermediate layer (of height h, areolar radius r_2) are also air cylinders, made distinguishably wider than the foramina-containing top layer, as illustrated in the SEM image. We also neglect the natural curvature of the structure and additional scattering events by other diatom components as light passes through the diatom. This idealized structure and accompanying FDTD simulation configuration are depicted in Fig. 3.2(b).

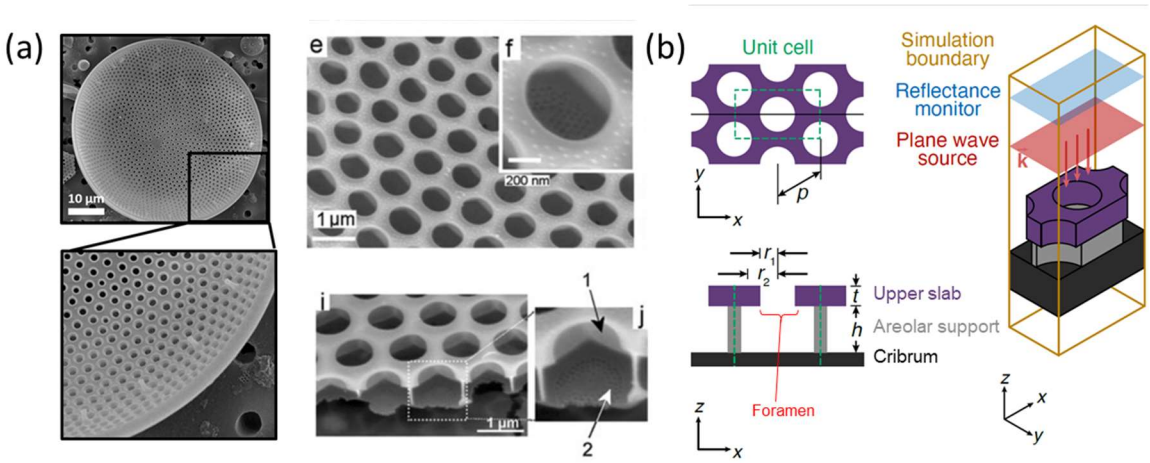

FIG 3.2. (a) Optical micrographs of *Coscinodiscus sp.* and *Thalassiosira eccentrica* diatom frustules. (b) Schematic depiction of a supported, perfectly periodic slab approximating the structure in (a). Reprinted and adapted with permission. © 2006, Royal Society of Chemistry and Centre National de la Recherche Scientifique.

Finite-difference time domain optical simulations were conducted (Lumerical FDTD) on the full idealized diatom frustules, as well as selected portions of the structure, to elucidate their modal contributions by comparing normal-incidence reflectance spectra. The specific geometry used in calculating optical responses was chosen to match naturally occurring frustules, and is as follows: p = 950 nm, r_1 = 310 nm, r_2 = 380 nm, t = 400 nm, h = 500 nm. The cribrum slab was set to a 50-nm thickness. Results of these simulations are shown in Figure 3.3. Starting with the spectrum of an isolated foramen-containing silica slab in air (panel (a), dashed blue), additional auxiliary components are sequentially replaced, which modifies the initial response. The original spectrum is quite simple, displaying a single prominent mode at ~920 nm. First, it is evident that the upper and lower slabs do not appreciably interact (orange curve, fine dashes), with reflectance curve overlays highlighting the negligible modification of the original spectrum. This is also sensible when considering the thinness of the lower cribrum slab relative to the wavelength range considered. Introducing the areolar supports instead of the cribrum

(panel (b), dashed green curve) modifies the prominent 920 nm mode, shifting the central mode location to ~850 nm and lowering the reflectance slightly, presumably by enhancing transmission (silica absorption is minimal). Two sharp, low-intensity modes remain at a higher wavelength closer to the original mode observed in the isolated slab. The fully assembled frustule structure (panel (c), solid red) appears to be a hybrid of the previous two cases, intensifying the two modal side lobes, but also recovering and red-shifting the original prominent mode sustained by the top frustule layer, settling at 880 nm.

Having surveyed the optical contributions of its structural elements, it is also instructive to track the evolution of the frustule's response with different environments and materials comprising the diatom frustule. Following guidance from prior reports to elicit a photonic bandgap by increasing refractive index contrast, three cursory combinations of surrounding environment and top layer material were simulated, in order of decreasing natural occurrence: water-silica (live diatom frustule), air-silica (dried frustule), and air-TiO_2 (biomimetic construct). The complete frustule geometry was simulated, yielding reflectance spectra and cross-sectional electric field maps which are shown in Figs. 3.3(d,e). Owing to the relatively low refractive index contrast between the exoskeleton and cytoplasm/surrounding water ($\Delta n \leq 0.1$), the live-diatom case shows little to no reflectance across the wavelength range considered. This is also evidenced by the weak coupling and confinement of the incident electric field within the structure, and significant down-welling of the electric field is observed at 550 nm. Moving to the dried frustule case ($\Delta n \approx 0.38$), several more intense, narrow-band resonances prominently emerge from a low-intensity, slowly varying spectral background, which

were identified in the above discussion. Finally, in the case of the silica-supported TiO_2 membrane surrounded by air ($\Delta n \approx 1.3$), a rich modal resonance profile emerges, surpassing the silica-air configuration in intensity and breadth. Most remarkably, a broader, high-intensity (>98% R) asymmetric mode emerges at 1140 nm (compared to near-zero % R in the analogous air-silica case). The corresponding electric field map suggests the mode originates from intense E-field confinement within the frustule foramina. Further, the E-field distribution inside the TiO_2 layer at 550 nm indicates confinement of secondary, higher-order thin-film resonant modes.

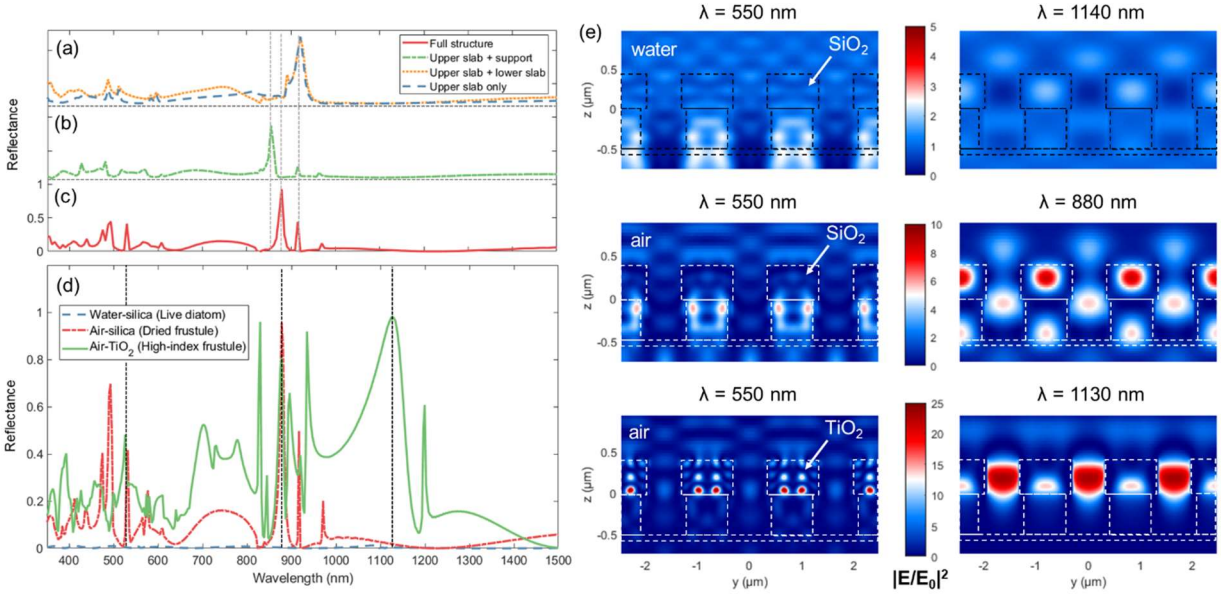

FIG 3.3. (a) Normal-incidence reflectance curves of a deconstructed diatom frustule in air, starting with an isolated top frustule slab (lowest curve) and sequentially added auxiliary frustule components. (b) Approximate T. eccentrica frustule geometry (p = 950 nm, r_1 = 310 nm, r_2 = 380 nm , t = 400 nm, h = 500 nm) modeled with three scenarios: in water, dried, and dried with top layer replaced by TiO_2. (c) Electric field maps for the three configurations in (b), sampled at λ = 550 nm and a secondary, highly resonant wavelength for each configuration.

Sharp, well-defined optical resonances are highly sensitive to the geometry that sustains them; given that the structure under study has well-defined, layered interfaces (foramen layer, support, and thin cribrum layer), it is instructive to look at the evolution

of the optical response with film thickness. Figure 3.4 shows the evolution of spectrally resolved normal-incidence reflectance with the thickness of the top foramina-containing layer (p = 550 and 950 nm, constant r_1/p ratio) for the same three configurations as depicted in Fig. 3.3. A set of broad, low-intensity resonances that vary linearly with top layer thickness can be discerned (dashed yellow lines), which comprise the thin-film interference background sustained by the top and bottom interface of the foramen-containing layer. For a given slab thickness (t) and effective index (n_{eff}), the peak locations, λ_{FP}, of thin-film Fabry-Pérot reflected orders b at normal incidence (i.e., with incident k-vector $k_{z,m}$ at grating order m = 0) can be obtained with the following resonance condition:

$$2k_{z,m}t \rightarrow 2k_{z,0}t = 2n_{eff}\left(\frac{2\pi}{\lambda_{FP}}\right)t = 2\pi b \tag{3.1}$$

The Fabry-Pérot background is barely discernible in the live diatom case; however, as the refractive index contrast increases, the thin-film interference intensifies and is increasingly modified by a set of sharply delineated high- and low- reflectance contours. This is particularly evident in the TiO_2-air configuration, which shows a warped "checkerboard" pattern; moreover, the wavelengths around which these dramatic reflectance oscillations occur seem to scale roughly with the characteristic areolar pitch p. This type of resonant behavior has been noted in optoelectronic and photonics literature with *photonic-crystal membranes* or *high-contrast gratings*, which exhibit a near-wavelength, periodic, and unusually high refractive index profile [16–18]. Strong thin-film interference couples to the resonant waveguide modes, laterally confining the

electric field to the high-index (TiO_2) and low-index (air) regions of the structure. Strategic choice of material thickness tunes the phase difference of light propagating in the two media to yield coherent, perfectly reflection (or transmission) at normal incidence for a set of design wavelengths [18,19].

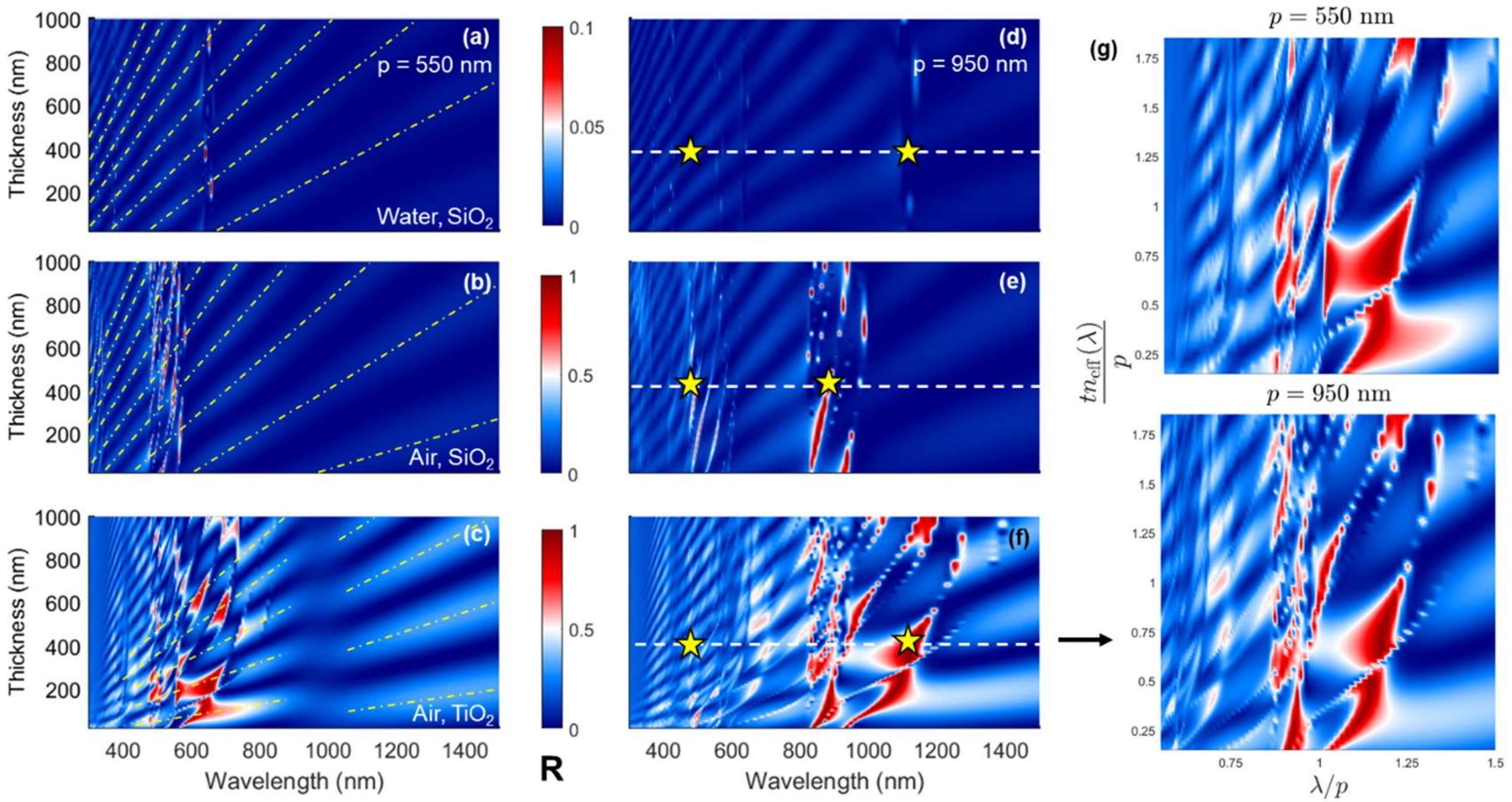

FIG 3.4. (a-f) Normal-incidence reflectance contour maps for naturally occurring frustule structures (period = 550 nm (a-c) and 950 nm (d-f)) in (a,d) water and (b,e) air, as well as (c,f) a silica-supported TiO_2 slab layer in air. Yellow dashed lines represent Fabry-Pérot resonance orders. White dashed lines and stars represent the top slab thicknesses (400nm) and mode locations sampled for the electric field maps shown in Fig. 3.3, respectively. (g) Rescaled versions of (c) and (f) are recapitulated in dimensionless form, showing the similarity of the two reflectance landscapes despite different areolar spacings.

3.2.2 Rational design of optical responses in "bionic" frustules

Given the fundamental role of structure geometry in eliciting the optical behaviors detailed in the previous section, we look to rational scaling parameters to generalize this behavior and inform wavelength-independent design by tuning geometric parameters. To generalize any phenomena involving thin-film interference, a reasonable first step is to define optical path length, given by the product of *t* and the wavelength-dependent refractive index of a homogenized thin film (cf. Ch. 2). Given that the structure's pitch is closely tied to the design wavelength and informs the wavelength-dependent phase behavior during thin film interference, we normalize the optical path length by p. Accordingly, the wavelength axis is also divided by p to yield a completely dimensionless high-contrast grating design space. The resulting dimensionless versions of the p = 550 and 950 nm TiO_2-air reflectance contour maps are shown in Fig. 3.4. While exact modal locations and intensity profiles are evidently different between the two maps, the locations of sharp Fano-like delineations align quite well on the non-dimensional reflectance landscape. Assuming a relatively lossless wavelength-regime for the high-index material used, these quantities can aid in informing and engineering tailored optical responses in perfectly ordered frustule-like structures for specific desirable wavelengths.

The pores embedded in the diatom frustule are created from a silicic acid feedstock; nanoscopic vesicles of siliceous material are delivered to the frustule site, where it is mineralized in the interstitial area between pore-forming, structure-directing proteins [15,20]. This delicate biochemical process can easily stray from (or indeed,

never arrive at) perfect hexagonal order the likes of which we have studied so far. Several foreseeable perturbations are diameter polydispersity (distributed r_1, r_2) and unequal areolar spacings (broad distribution of *p*), both of which can be observed in the SEMs shown in Fig. 3.1. To probe the effect of this type of disorder on the optical behavior of our set of simplified models, we expand the simulation to 72 unit cells and allow these two geometric disorder parameters to vary independently. Figure 3.5 below shows reflectance contour maps for the silica-air and TiO_2-air configurations from above with p = 550 nm, for three different cases: (1) top slab only, (2) full structure, and (3) full structure with translational areolar disorder.

The floating slab exhibits the simplest Fano-resonant behavior, as the changing thin-film interference background (only the first two FP orders are shown) couples to the guided modes set by the pore spacing (single-mode in the case of SiO_2, multi-mode in the TiO_2 case). By outlining several low- and high-order Fano resonance contours (dashed yellow lines), we track their evolution with additional simulation complexity. By introducing the silica support structure under the original silica slab, a more prominent Fabry-Pérot background emerges, and the low-order Fano resonance at ~550 nm is repartitioned into finer modal structure by the underlayer support. A similar repartitioning also occurs with the TiO_2 slab in the 500-600 nm range, where both regions of broad-high-reflectance behavior are slightly modified and de-tuned; this is most evident at a top slab thickness of 200 nm. However, a significant portion of the broadband behavior is still retained.

By far the most striking change to the spectral features occurs when random translational pore displacement is introduced (random, up to 10% of the lattice pitch),

which yields a dramatic reduction in normal-incidence reflectance across the board. In contrast to the perfect grating, a significant diffuse backscattering is observed, which is overlaid on the normal-incident reflectance contours in Figure 5 (shaded white, binarized with arbitrary threshold value to best depict spectral profile). In the silica case, the backscattering occurs in the UV and blue wavelength ranges and is relatively weak, comprising only 10% of the total incident source power at these wavelengths. In the TiO_2 case, the backscattering intensity is more than three times stronger, and originates from the crossing of Fano-resonant contours at 475-525 nm and 640 nm. We conclude that the two sets of adjacent Fano resonances giving rise to broadband reflectance within the perfectly ordered TiO_2 slab decouple due to hole disorder, and diffuse scattering at the centroids of these two modes arises from a distribution of local resonant phase differences between neighboring quasi-ordered unit cells, interfering with each other in the near-field and radiating out to a wide angle range in the far field.

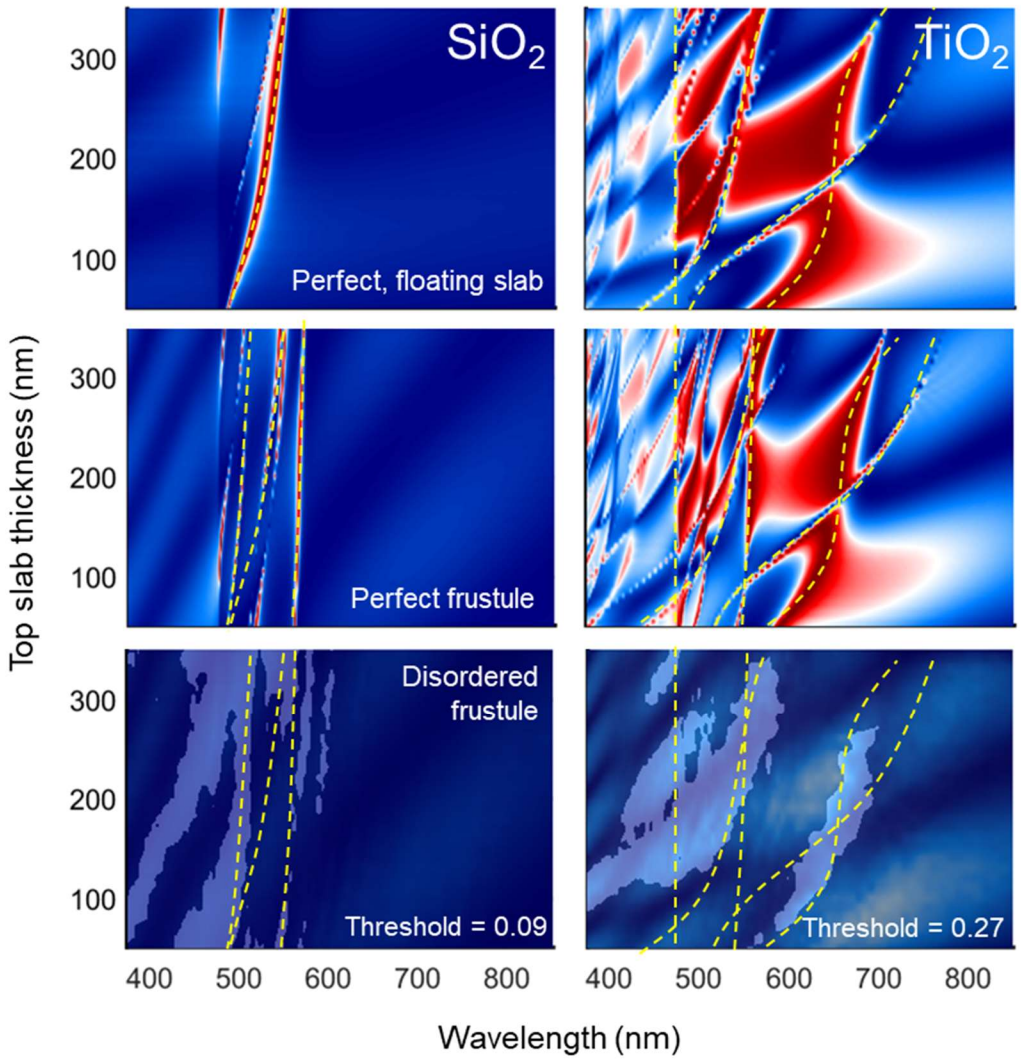

FIG 3.5. Reflectance contour maps of a diatom frustule with the top slab comprised of SiO_2 (left) and TiO_2 (right), with top slab thickness varied for a perfectly ordered floating slab, perfectly ordered full frustule, and disordered full frustule (translational pore displacement, up to 10% of the lattice pitch). For TiO_2, the lowest-order Fano contours are represented by the right-most pair of crossing yellow outlines. Shaded white contours in the disordered frustule plots depict total diffuse backscattering, binarized with scattering intensity thresholds (0.09 and 0.27 of incident source power) to best depict spectral profile.

Given this emergent diffuse scattering behavior, our above efforts to non-dimensionalize ideal frustule optics may also aid in selecting design specifications for wavelength-selective diffuse scattering of any color. Consulting the dimensionless plots in Figure 4, we can identify coordinates corresponding to highest-intensity structural

color near the design wavelength (i.e. crossing of low-order Fano contours) at $\left\{\frac{\lambda}{p}, \frac{tn_{eff}(\lambda)}{p}\right\} = \{1.2, 0.65\}$. As an example, for a TiO_2 slab layer to non-iridescently display a green color (530 nm), we select a pitch of $p = \frac{\lambda}{1.2} = \frac{530\ nm}{1.2} = 442$ nm. The optimal thickness of the structure is then given by $t = \frac{0.65 \cdot p}{n_{eff}(\lambda = 530\ nm)} \approx \frac{0.65(442\ nm)}{1.8} \approx 160\ nm$. It is to be noted that our investigations were conducted assuming a single constant ratio of hole diameter to lattice spacing (or duty cycle, with DC = 0.65). Additional tunability and/or optimization of the optical response may be attained by varying this parameter, which tunes the effective refractive index within the top frustule slab. In perfect hole arrays, increasing air fraction has been observed to narrow the broad reflectance behavior featured here, but these are also much more difficult to fabricate, and the resulting resonances are no doubt even more prone to imperfections.

Non-iridescent, long-wavelength structural color (e.g., yellow, orange, and red) is unique and not easily attainable with simple geometric systems, owing to high-order resonant modes which overwhelm the lowest-order target mode [21,22]. This is also true for the system we have considered herein, since the slabs are designed to sustain two or more Fabry-Pérot cavity modes, which are necessary for broadband reflection. One potential solution is to suppress the high-order mode, e.g. by placing absorbing materials within the structure. Another approach is to waveguide the high-order mode and prevent it from leaking out omnidirectionally, but this is a nontrivial (if impossible) feat. In the next section, we use the former approach, namely using silicon as a sacrificial, partially removable material, to demonstrate saturated, non-iridescent color across the entire visible spectrum.

3.3 Fabrication, characterization, and computational validation of diatom-inspired TiO_2 frustule surfaces

3.3.1 TiO_2 hole array fabrication

Partially-suspended TiO_2 hole arrays were fabricated using colloidal lithography, shadow deposition of a metal mask, and reactive ion and XeF_2 vapor etching, as depicted in Figure 3.6. The device stack before optical lithography and colloidal mask deposition consisted of the following from top layer to substrate: 10 nm Al_2O_3 protection layer (ALD); 50 nm sacrificial Si protection layer (e-beam PVD); (130, 180, or 235 nm thick) TiO_2 (RF sputter), depending on colloid size; 650 nm sacrificial Si "Fabry-Pérot (FP) cavity layer" (e-beam PVD); 10 nm Al_2O_3 chemical etch stop (ALD), and Si (100) substrate. The Al_2O_3 protection layer was used to prevent colloidal mask undercutting, and the 50 nm Si layer above the TiO_2 was used to protect the TiO_2 from the mask particle isotropic etch step (see below) and provide more anisotropic pattern transfer. Arrays of open square areas of various size (0.2-0.6 mm^2) were defined via photolithography (AZ nLOF 2020) on the aforementioned device stack, developed, and used as templates for colloidal mask (hydrophobic SiO_2, d = 404, 507, and 690 nm; Bangs Lab) deposition using a Langmuir-Blodgett (LB) dip-coating process that has been detailed elsewhere[23]. After colloid deposition, the photoresist mask was lifted off in n-methylpyrrolidone (80^oC), leaving behind square areas of hexagonally close-packed (HCP) colloidal sphere monolayers on the wafer surface. The mask particles were then size reduced to d = 250, 350, and 425 nm in an isotropic ICP-RIE (Panasonic E640) with 30/20 sccm of CHF_3/O_2 at 30 mTorr, 900 W ICP power, and no substrate bias. Nickel (60 nm) was then deposited

via e-beam using the size-reduced colloids as a shadow mask, and the particles were lifted off via ultrasonication, leaving behind an Ni hole array mask. The Ni hole pattern was transferred into the underlying device stack with a capacitively-coupled RIE with 20/2 sccm of SF_6/O_2 at 10 mTorr and 300 V substrate bias (Material Research E-51 etcher). The RIE was specifically stopped within the lower sacrificial Si layer, as stopping on the Al_2O_3 substrate protection layer proved difficult; the presence of this Al_2O_3 layer provided a robust chemical etch stop to clear the FP cavity using XeF2 (see below). The Ni mask was subsequently stripped, and the residual Al_2O_3 was then removed with TMAH-based developer. Finally, the sacrificial Si was removed from both sides of the TiO_2 layer using a 1:2 XeF_2/N_2 vapor etch (Xetch System, Xactix, Inc). The inset in Figure 3.6 shows the wafer surface immediately before and after XeF_2 exposure. Note that it was desired to leave some SiO_2/Si behind in the FP cavity layer to prevent collapse of the TiO_2 hole array membrane (cf. Fig. 3.8(d,e)).

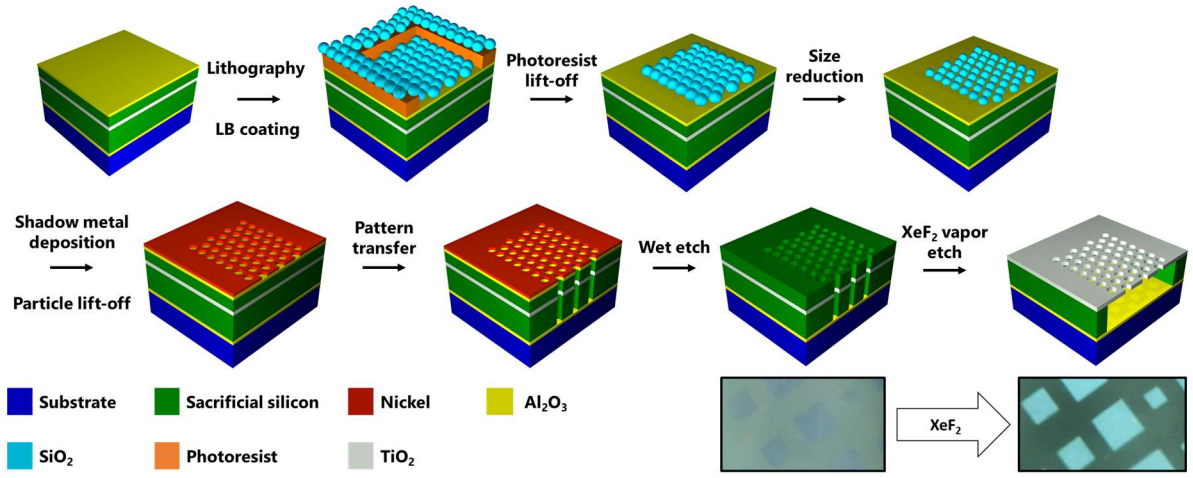

FIG 3.6. Fabrication process for partially-suspended TiO_2 hole arrays, based on colloidal lithography, metal mask deposition, and plasma RIE and XeF_2 vapor etching. Optical microscope images of the sample before and after exposure to XeF_2 vapor are shown in the insets at the lower right. © 2020, AIP Publishing.

3.3.2 Optical measurements

Optical measurements were performed in a specular and off-axis configuration (Fig. 3.7(a)) in a custom-built goniometer with a broadband D_2-halogen illumination source and fiber-coupled UV-Vis spectrometer (OceanOptics USB2000+). Specular and diffuse reflectance measurements were normalized to a UV-reinforced aluminum mirror (Thor Labs, PF10-03-F01) and a white Lambertian reference surface (roughened $BaSO_4$, LabSphere), respectively. Angle-resolved measurements were performed with focused optical fiber illumination (spot diameter ~300 μm); the reflection signal was collected at normal-incidence via a free-spaced optic fiber located 1 cm away from the sample surface.

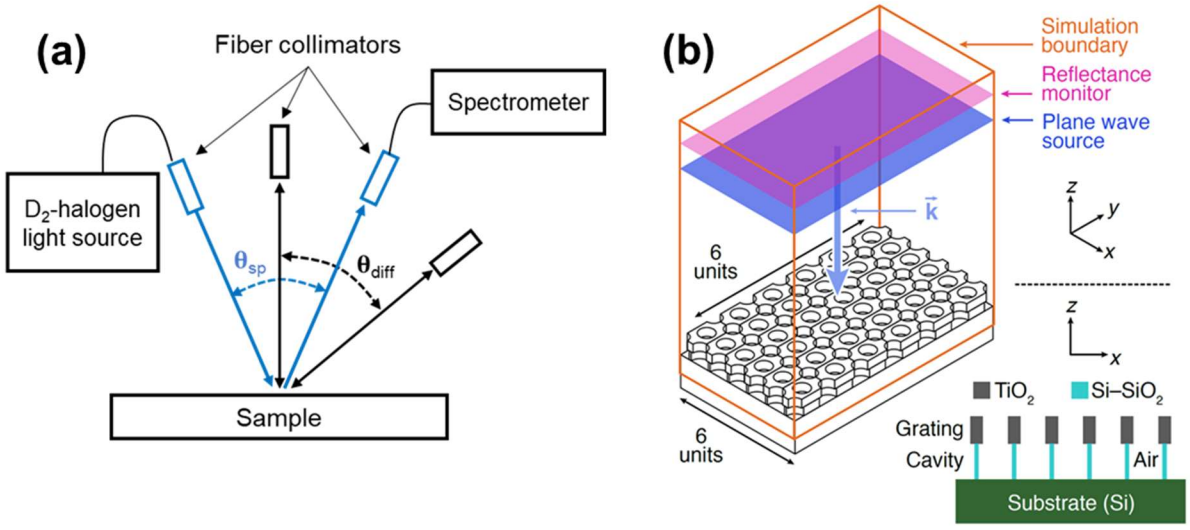

FIG 3.7. (a) Experimental setup for specular and diffuse measurements, with θ_{sp} = 40°, θ_{diff} = 45° for normal-incidence illumination, and θ_{diff} = 45-75° for normal-incidence collection. (b) Schematic of the FDTD simulation domain, featuring a 6-by-6 array of centered rectangular cells representing a disordered, pseudo-HCP pattern of 72 total holes for the TiO_2 array with perfectly matched top/bottom and periodic XY boundary conditions. © 2020, AIP Publishing.

3.3.3 Optical simulations

The optical behavior of fabricated hole arrays was calculated via finite difference time domain (FDTD) calculations with Lumerical. The simulation domain consisted of a TiO_2 slab with 72 HCP cylindrical air inclusions (holes with pitch = 507 nm and diameter = 365 nm), a 400-nm thick Si slab underlayer with coaxial air inclusions (diameter, d = 240-600 nm), and a semi-infinite Si substrate, as represented in Fig. 3.7(b). Simulation features were chosen to match SEM images of the fabricated structures. A broadband plane wave source (λ = 425-850 nm, blue) was injected near the top simulation boundary. The top/bottom z-boundaries of the simulation region were modeled as perfectly matched (absorbing) layers, with periodic boundary conditions applied in the x- and y-directions. A reflection field monitor (purple) was positioned between the top surface of the structure and the plane wave source. Disorder in the air hole location was introduced as a uniformly distributed random offset (maximum 10% of the pitch) for the (x,y) coordinates of each lattice position, scaled by the lattice pitch. Wavelength- and angle-dependent scattering data were extracted with Lumerical's grating analysis module, which provided the fraction of total source power delivered to each diffracted order present within the simulation domain. Three distinct hole configurations were sampled and averaged for all disordered structure simulations.

3.4 Results and discussion

3.4.1 Fabrication results

In line with the design principles described in the previous section, three partially-suspended TiO_2 hole arrays were fabricated with average hole-to-hole spacing (pitch) of 404, 507, and 690 nm, as depicted in Fig. 3.8. The thicknesses of these hole arrays were scaled with the pitch to maintain a near-constant optical path length, by consulting the dimensionless plots generated above (cf. Fig. 3.4(g)). The patterned areas appeared highly colored to the naked eye, and varied from blue to yellow to red in diffuse ambient light as the pitch increased. Holes in the TiO_2 layer were reasonably vertical with sharp features (Fig. 3.8(a-d)), which was aided by high etch selectivity against the Ni mask and 300V substrate bias. In general, hole arrays had a small amount of positional disorder due to non close packing of the mask particles, and defects associated with particle dimers/trimers and 5- and 7-fold packing faults that are commonly encountered in LB deposition. Lattice disorder also occurred due to under-etching of the particle-substrate contact point and from local electrostatic forces attracting neighboring nanospheres during the isotropic CHF_3/O_2 plasma etch for mask size reduction. Perfect long-range order from the LB method is also hampered by rapid and irreversible formation of small colloidal crystal domains or mosaics at the air-water interface during deposition, associated with colloid size dispersion (PDI $\sim$15% in our case) and surface chemistry [24].

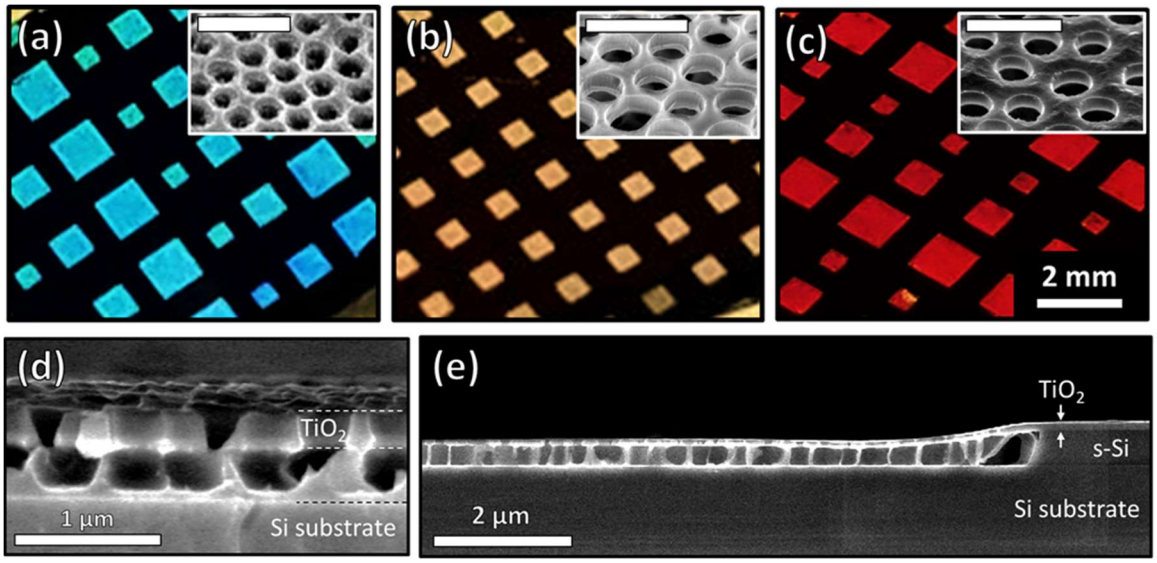

FIG. 3.8. (a-c) Optical images of TiO_2 hole arrays: (a) 404 x 130, (b) 507 x 180, and (c) 690 x 235 (hole pitch x TiO_2 layer thickness [nm]), with electron micrograph insets showing a bird's eye view; scale bars are 2 mm and 1 µm, respectively. (d) Cross-sectional view of the sample in (b). (e) Wide field-of-view cross-sectional image of a supported hole array structure, showing the top TiO_2 layer, sacrificial Si (labeled "s-Si") and highly porous underlayer, as well as the silicon substrate beneath.

The cross-section images in Figs. 3.8(d,e) reveal that the TiO_2 top layer is suspended on a porous underlayer (~400 nm thick) having a void fraction that is higher than the TiO_2 layer. The latter occurs because the SF_6/O_2 etch is more selective for the sacrificial Si underlayer compared to TiO_2. The suspending "wall" material is largely SiO_2 (or SiO_2 covered Si), created during Ni mask pattern transfer, that cannot be removed during clearance of the sacrificial Si with XeF_2 vapor. The presence of these walls, obtained by stopping the sacrificial Si (cavity layer) etch within the layer (forming SiO_2 in the process, followed by XeF_2 clearance of the remaining Si through the TiO_2 openings down to the Al_2O_3 chemical etch stop on the substrate), was deemed necessary to prevent collapse and preserve the modal behavior of the TiO_2 membrane, as well as create a well-defined interface for the cavity high reflector (Si substrate). The final thickness(es) of these "walls" was determined by variations in the vertical extent of SiO_2 formation during

the hole pattern RIE step with the SF_6/O_2 etch gas mixture. If an underlayer is not desired, this may be accomplished by reducing or eliminating O_2 from the etch chemistry. As discussed later, this underlayer Si can modify the refractive index profile at the underlayer-TiO_2 interface, which would attenuate and redshift the diffuse Fano mode supported by the TiO_2.

The generic processing steps employed above to fabricate hole arrays can be applied to virtually any material system. Deposition of sacrificial silicon is relatively substrate-agnostic, as is colloidal lithography and subsequent metal mask deposition. Proper selection of etch chemistry and conditions (e.g., pressure and substrate bias) is necessary to achieve a proper vertical etch profile, and XeF_2 etching is highly selective to silicon over oxides, metals, and photoresists. If a suspended Si hole array is desired, SiO_2 may be used as the sacrificial layer with HF vapor used as the selective etchant.

3.4.2 Optical characterization of TiO_2 hole arrays

To further probe and understand how array geometry and disorder affect optical behavior, the specular and diffuse reflectance properties of the 507 nm pitch (yellow) sample were measured and compared with simulation, as summarized in Fig. 3.9. In a specular arrangement (panel (a)), the reflectance spectrum (R, maximum ~10%) has a broad, overlapping doublet-like feature around 600 nm and a single FP-like etalon mode centered at 775 nm. The sample surface shows a slight distribution of colors from green to yellow-orange in different square patterns when viewed in direct light (Fig. 3.9(a) inset). The "air pore" diameters in the porous underlayer also vary (cf. Fig. 3.8(d,e)), so it is probable that the Si fraction of the (SiO_2) underlayer may be slightly different across

the 300 μm diameter illumination spot. FP resonances are highly sensitive to differences in underlayer thickness and Si fraction (i.e., refractive index), suggesting that at least one of the peaks comprising the 600-nm feature is a FP etalon that mediates the observed color profile in the Fig. 3.9(a) inset.

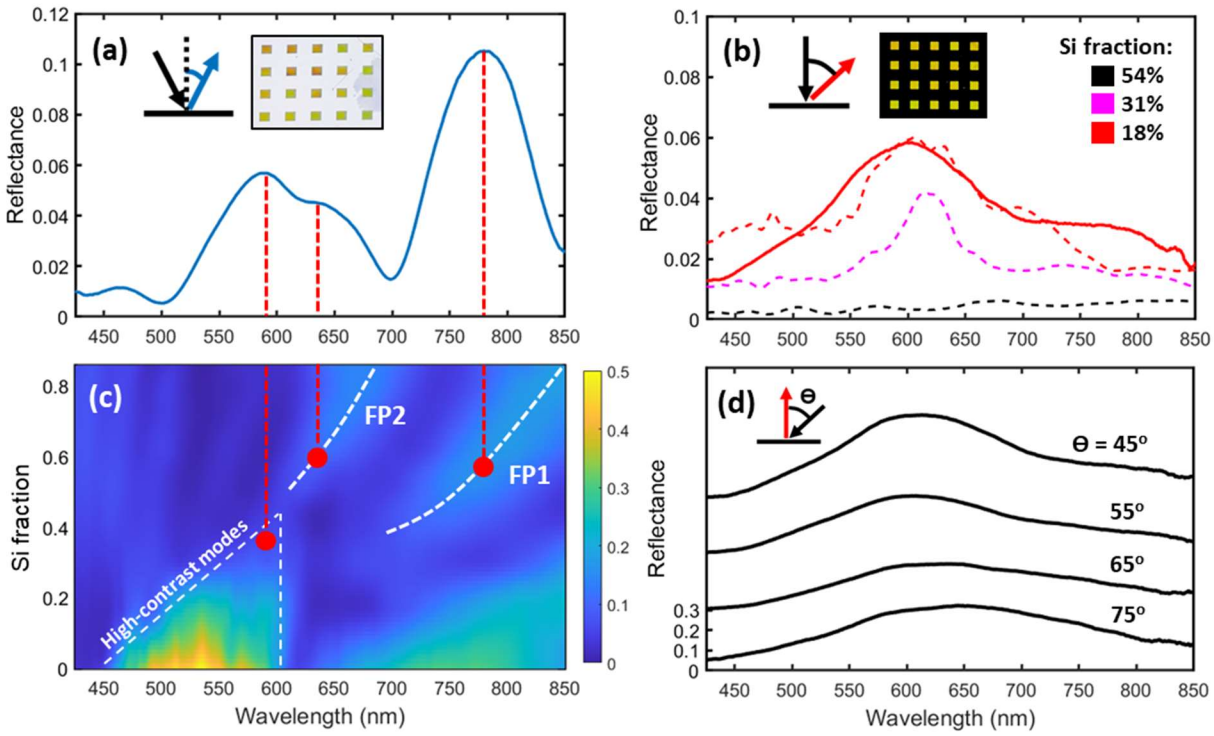

FIG. 3.9. Optical characterization and simulation of the 507 nm pitch TiO_2 hole array. (a) Specular reflectance spectrum with insets showing measurement configuration and optical image of the surface in direct light. (b) Diffuse reflectance spectrum (solid red), with overlaid reflectance curves for various underlayer Si fractions simulated with FDTD calculations. The inset shows the surface of the sample in diffuse light. (c) Simulated specular hole array reflectance contour map (10% disorder) as a function of underlayer Si fraction, showing long-wavelength FP etalon modes (FP1 and FP2, caused by the external cavity formed by the TiO_2 layer and substrate) transitioning to a broadband, high-contrast grating (HCG) mode. Dashed lines are only intended to guide the eye. (d) Diffuse reflectance spectra with variable-angle illumination (45-75° off-normal) and normal-incidence collection. Curves are offset for clarity. © 2020, AIP Publishing.

FDTD simulations were carried out to understand the origin of the optical behavior described above; these calculations were conducted to evaluate the extent of Si removal from the underlayer by varying the diameter of air pores embedded in the

(remaining) sacrificial Si between the TiO_2 and substrate. Figure 3.9(c) shows a contour map of specular reflectance as a function of the underlayer Si fraction (calculated from air pore diameters). At high Si fraction (>50%), two Fabry-Pérot etalon modes ("FP1" and "FP2", panel (c), caused by the external cavity formed by the TiO_2 layer and substrate) can be discerned that correspond well with the experimentally observed peaks at ~640 and 780 nm, as shown in panel (a). Moving further down in Si fraction, the FP modes disappear and a set of broad, high-reflectance features emerge between 500 and 600 nm that correspond to high-contrast grating (Fano-like[18]) modes expected for an air-suspended TiO_2 layer. A broad FP (external cavity) mode also emerges above 700 nm from the air cavity formed between the TiO_2 layer and the substrate. Careful examination of cross-sectional SEM images shows that the distribution of local Si fractions in the FP cavity lies between ~40-60%, the range where the three principal optical modes (high-contrast, FP1, and FP2) occur in experiment (Fig 3.9(a)) and simulation (Fig. 3.9(c)).

The diffuse reflectance spectrum in Fig. 3.9(b) is more simple and rather broad (max R occurs at 600 nm), and the patterned areas appeared yellow to the eye (see inset). The spatial color profile across the wafer was remarkably uniform, which suggests that the diffuse color behavior depends mostly on optical interactions within the TiO_2 film, rather than external FP air-cavity effects, as in the specular case. Simulated diffuse reflectance curves at various Si underlayer fraction (dashed lines) show significant sensitivity, with >50% Si content (dashed, black) removing all structural color. Lower Si content allows a symmetric mode to emerge around 600 nm (31% and 18% Si, dashed magenta and red, respectively), corroborating the experimentally observed feature and is likely the lower-order Fano resonant pair from our simulations above. With even lower

Si content (< 20%), the higher-order mode of the Fano resonance pair emerges (~475 nm for the yellow hole array), which would reduce the saturation of the apparent yellow color. The 600-nm symmetric mode is suspected to emerge from the perturbed hexagonal pore arrangement in the TiO_2 film that repartitions any normal-incident light captured by the TiO_2 slab (through its effective-index, internal FP resonances), into guided modes that preferentially and omni-directionally leak yellow light out into free space [18].

Omni-directionality of the diffuse yellow color was probed by variable-angle illumination and normal-incidence spectral collection, as shown in Fig. 3.9(d), as well as the converse of this configuration (Fig. 3.10) for all structures. The measured spectral features closely resemble those seen in Fig. 3.9(b), which would suggest similar optical mode origin. A slight red-shift is observed with increasing incidence angle, which can be attributed to the change in path length for light being coupled into the top TiO_2 layer via internal FP resonance. However, the color remains reasonably constant to the eye, and is a promising feature for implementation in wide-angle color applications such as passive display elements.

The above computational workflow was repeated for the remaining two samples, with SEM imaging informing top and underlayer geometry, which informed the subsequent Si content parameter sweep to account for modal suppression by the sacrificial underlayer material. All samples were found to be in excellent agreement with measured spectra, and well within physically reasonable parameters. The 404-nm pitch sample was especially devoid of sacrificial Si remnants, which allowed the higher-order Fano mode to feature prominently in the diffuse reflectance spectrum at ~400 nm.

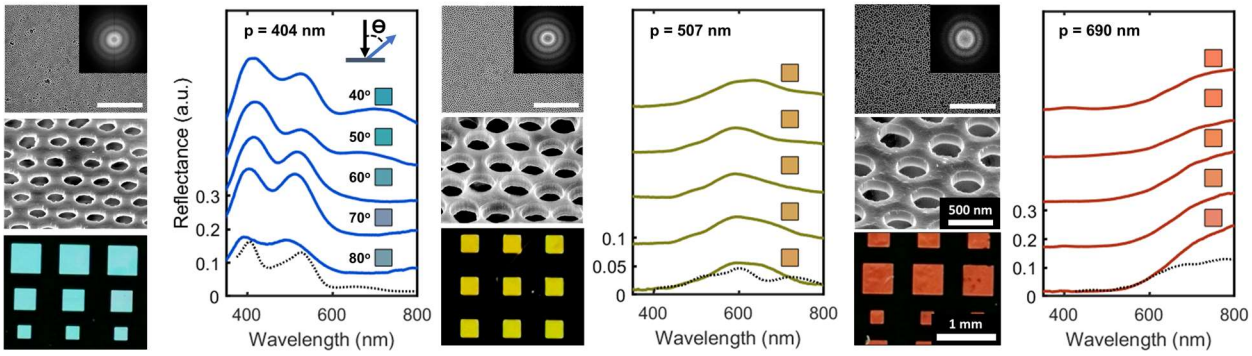

FIG. 3.10. Characterization and simulation of the designed and fabricated TiO_2 diatoms. Scanning electron micrographs and corresponding 2D Fourier transforms of the images (inset). Diffuse reflectance spectra with normal-incidence illumination and variable-angle collection (40-80° off-normal) and normal-incidence collection, along with computationally predicted scattering spectra for 45° collection in dashed black. Curves are offset for clarity.

3.5 Conclusion

In this chapter, we explored the optical behavior of diatom frustules, and showed how an increasing index contrast brings a rich optical modality and provides a wavelength-tunable platform for broadband reflection, transmission, and (if inevitable geometric disorder is present) non-iridescent color. As a proof-of-concept, scalable fabrication of diatom-inspired TiO_2 hole arrays (gratings) was developed via Langmuir-Blodgett deposition, vertical pattern transfer, and XeF_2 etching of a sacrificial Si layer. These structures showed angle-independent, saturated color, aided by the remaining Si underlayer material to suppress high-order Fano modes.

FDTD simulations indicated that the specular reflectance behavior of the 507 nm pitch TiO_2 hole array was attributed to superposition of external FP etalon and high-contrast grating reflectance (Fano-like) modes created by the inhomogeneous, Si-containing underlayer supporting the hole array. The diffuse, angle-independent

(yellow) color of the structure was attributed to lowest-order, de-tuned Fano modes originating from the disordered hexagonal lattice perforations (holes) in the TiO_2 layer itself. Thus, through simple changes in colloid size and processing, it is possible to easily create TiO_2 hole array structures with well-defined color response across the visible spectrum. Also, given the high etch selectivity of XeF_2 to Si over a variety of oxides and metals, the fabrication methodology presented herein can be used to create ultrathin, suspended hole arrays of virtually any material for applications in photonics, photovoltaics, optical displays, photocatalysis, and sensing.

References

1. L. W. Chan, D. E. Morse, and M. J. Gordon, "Moth eye-inspired anti-reflective surfaces for improved IR optical systems & visible LEDs fabricated with colloidal lithography and etching," Bioinspiration and Biomimetics **13**(4), (2018).
2. S. Kinoshita and S. Yoshioka, "Structural colors in nature: The role of regularity and irregularity in the structure," ChemPhysChem **6**(8), 1442–1459 (2005).
3. H. Ghiradella, "Light and color on the wing: structural colors in butterflies and moths," Appl. Opt. **30**(24), 3492 (1991).
4. L. De Stefano, I. Rea, I. Rendina, M. De Stefano, and L. Moretti, "Lensless light focusing with the centric marine diatom Coscinodiscus walesii," Opt. Express **15**(26), 18082 (2007).
5. E. De Tommasi, R. Congestri, P. Dardano, A. C. De Luca, S. Managò, I. Rea, and M. De Stefano, "UV-shielding and wavelength conversion by centric diatom nanopatterned frustules," Sci. Rep. **8**(1), 1–14 (2018).
6. L. E. Aguirre, L. Ouyang, A. Elfwing, M. Hedblom, A. Wulff, and O. Inganäs, "Diatom frustules protect DNA from ultraviolet light," Sci. Rep. **8**(1), 1–6 (2018).
7. D. Losic, J. G. Mitchell, and N. H. Voelcker, "Fabrication of gold nanostructures by templating from porous diatom frustules," New J. Chem. **30**(6), 908–914 (2006).
8. D. Losic, J. G. Mitchell, R. Lal, and N. H. Voelcker, "Rapid fabrication of micro- and nanoscale patterns by replica molding from diatom biosilica," Adv. Funct. Mater. **17**(14), 2439–2446 (2007).
9. C. Jeffryes, T. Gutu, J. Jiao, and G. L. Rorrer, "Metabolic insertion of nanostructured TiO2 into the patterned biosilica of the diatom Pinnularia sp. by a two-stage bioreactor cultivation process," ACS Nano **2**(10), 2103–2112 (2008).
10. A. Li, M. Moges, J. Morales, A. Saccoccio, S. Anderson, and X. Zhang, "FACILE ASSEMBLING METHOD FOR COSCINODISCUS SP . DIATOM FRUSTULE MONOLAYERS TOWARDS CONTROLLED ORIENTATIONS," Transducers 1742–1745 (2017).
11. J. Pan, Y. Wang, J. Cai, A. Li, H. Zhang, Y. Jiang, and D. Zhang, "Bonding of diatom frustules and Si substrates assisted by hydrofluoric acid," New J. Chem. **38**(1), 206–212 (2014).
12. A. Li, W. Zhang, R. Ghaffarivardavagh, X. Wang, S. W. Anderson, and X. Zhang, "Towards uniformly oriented diatom frustule monolayers: Experimental and theoretical analyses," Microsystems Nanoeng. **2**(December 2015), (2016).
13. D. Losic, G. Triani, P. J. Evans, A. Atanacio, J. G. Mitchell, and N. H. Voelcker, "Controlled pore structure modification of diatoms by atomic layer deposition of TiO2," J. Mater. Chem. **16**(41), 4029–4034 (2006).
14. E. De Tommasi, "Light Manipulation by Single Cells: The Case of Diatoms," J. Spectrosc. **2016**, (2016).
15. R. Gordon, D. Losic, M. A. Tiffany, S. S. Nagy, and F. A. S. Sterrenburg, "The Glass Menagerie: diatoms for novel applications in nanotechnology," Trends Biotechnol. **27**(2), 116–127 (2009).
16. C. Chang-Hasnain and W. Yang, "High-contrast gratings for integrated optoelectronics," Adv. Opt. Photon. **4**(3), 379–440 (2012).
17. E. Hashemi, J. Bengtsson, J. S. Gustavsson, S. Carlsson, G. Rossbach, and Å. Haglund, "TiO2 membrane high-contrast grating reflectors for vertical-cavity light-emitters in the visible wavelength regime," J. Vac. Sci. Technol. B **33**(5), 050603 (2015).
18. B. C. P. Sturmberg, K. B. Dossou, L. C. Botten, R. C. McPhedran, and C. M. de Sterke, "Fano resonances of dielectric gratings: symmetries and broadband filtering," Opt. Express **23**(24), 1672–1686 (2015).

19. P. Lalanne, J. P. Hugonin, and P. Chavel, "Optical properties of deep lamellar gratings: A coupled Bloch-mode insight," J. Light. Technol. **24**(6), 2442–2449 (2006).

20. M. Hildebrand, S. J. L. Lerch, and R. P. Shrestha, "Understanding diatom cell wall silicification-moving forward," Front. Mar. Sci. **5**(APR), 1–19 (2018).

21. S. Magkiriadou, J. G. Park, Y. S. Kim, and V. N. Manoharan, "Absence of red structural color in photonic glasses, bird feathers, and certain beetles," Phys. Rev. E - Stat. Nonlinear, Soft Matter Phys. **90**(6), 1–9 (2014).

22. T. Darmanin and F. Guittard, "Superhydrophobic and superoleophobic properties in nature," Mater. Today **18**(5), 273–285 (2015).

23. F. L. Gonzalez, L. Chan, A. Berry, D. E. Morse, and M. J. Gordon, "Simple colloidal lithography method to fabricate large-area moth-eye antireflective structures on Si , Ge , and GaAs for IR applications," J. Vac. Sci. Technol. B **32**(5), 051213 (2014).

24. E. Sirotkin, J. D. Apweiler, and F. Y. Ogrin, "Macroscopic ordering of polystyrene carboxylate-modified nanospheres self-assembled at the water-air interface," Langmuir **26**(13), 10677–10683 (2010).

4

Diatom-inspired TiO_2 nanomembranes for optical refractive index sensing

(Adapted from the Optics Express article: Shapturenka, P., Stute, H., Zakaria, N. I., DenBaars, S. P., and Gordon, M. J. "Color-changing refractive index sensor based on Fano-resonant filtering of optical modes in a porous dielectric Fabry-Pérot microcavity." *Optics Express*, **28**(19), 2020.)

4.1 Introduction

In the previous chapter, we explored the design space for subwavelength-thickness, diatom-inspired 2-D hole arrays and developed a robust fabrication scheme for manufacturing them at wafer scales. The fabricated structures exhibited planar, abrupt interfaces out-of-plane that support strong thin-film interference phenomena. The short-range correlated order within the nanomembrane de-tuned, but did not extinguish, the guided mode resonances supported by the hole array, which coupled to the thin-film interference to provide the observed diffuse color.

In line with our earlier discussion of high-contrast gratings, this modal behavior is highly sensitive to the refractive index of the surrounding environment. Naturally, this would prove useful in refractive index (RI) sensing, or refractometry, which is employed in a variety of fields for process control, substance identification, and diagnostics [1–3].

RI sensing is generally performed with hand-held or bench-top instruments incorporating prisms, optical fibers, and/or attenuated total reflection (ATR) optics that rely on reflections from multiple interfaces; many of these approaches have impressive optical sensitivity and resolution [4–9]. Development of multi-point, in-line process control and lab-on-a-chip diagnostics requires increasingly smaller sensors [10], and the need for a compact form factor often precludes straightforward integration of the aforementioned incumbent technologies.

Recent advances in optofluidics and nanophotonics have enabled the deployment of miniature refractometers [11]. These devices often incorporate microfluidic channels [12–17] and/or resonators that rely on waveguided or whispering-gallery optical modes [18–22] to minimize analyte volumes and deliver sensitive and high-quality spectral response, respectively. However, ultra-high resolution and defect-intolerant patterns are often necessary, leading to a costly tradeoff between production throughput and device sensitivity. To enable mass deployment of technologies fully leveraging these advances, there remains a need for scalable, defect-tolerant, and low-cost device schemes.

Toward this goal, the fabrication, characterization, and optical simulation of a Fabry-Pérot microcavity (FPMC)-based refractive index sensing device that is mechanically and optically robust, sensitive, and can be feasibly scaled up to mass-producible wafer areas, is presented. A silicon high reflector (the substrate), porous SiO_2 underlayer, and sub-λ thick TiO_2 nanohole array membrane make up the FPMC. The high-index, quasi-ordered nanohole array filters high-order Fabry-Pérot (FP) cavity modes via Fano-like resonances, while also allowing facile access of condensable vapors and

nanoliter liquid analyte volumes to the FPMC. This provides an easy-to-assess color change, quick response and recovery, and spectral sensitivity of up to 680 nm/RIU.

4.2 Experimental and simulation methods

4.2.1 Structure fabrication

The FPMC device stack (Fig. 4.1) was fabricated by depositing 10 nm of Al_2O_3 (ALD), 600 nm of sacrificial Si (e-beam PVD), 132 nm of TiO_2 (RF sputter), and an additional 100 nm sacrificial Si (e-beam PVD) in succession on a (100) Si wafer. Open square areas for each sensor, with edge lengths of 300, 500, and 800 μm, were defined via photolithography using AZ nLOF 2020 resist. A monolayer of 404 nm diameter SiO_2 colloids (Bangs Lab) was then deposited using a Langmuir-Blodgett (LB) interfacial assembly method that has been detailed elsewhere [23]. The overall substrate coating area is only limited by LB trough dimensions. The square arrays of SiO_2 particles remaining after photoresist lift-off (heated n-methyl pyrrolidone) were size-reduced in a CHF_3/O_2 ICP plasma (30 mTorr, 900 W, no bias), and subsequently used as a shadow mask to create an Ni hole array (60nm thick, e-beam) with ultrasonication to remove the particles. The Ni hole array pattern was transferred into the device stack using an SF_6/O_2 RIE (10 mTorr, 300 V bias) with etch stop on the substrate; the metal was then lifted off and the sacrificial Si in the FPMC cavity was partially removed with a XeF_2 vapor etch (Xetch System, Xactix). The TiO_2 nanohole array membrane was thus suspended above the substrate with a partial SiO_2 support (etch residue created by the SF_6/O_2 step, and

not removed by XeF_2), as illustrated in Fig. 4.1(a). Further details of the processing can be found elsewhere [24].

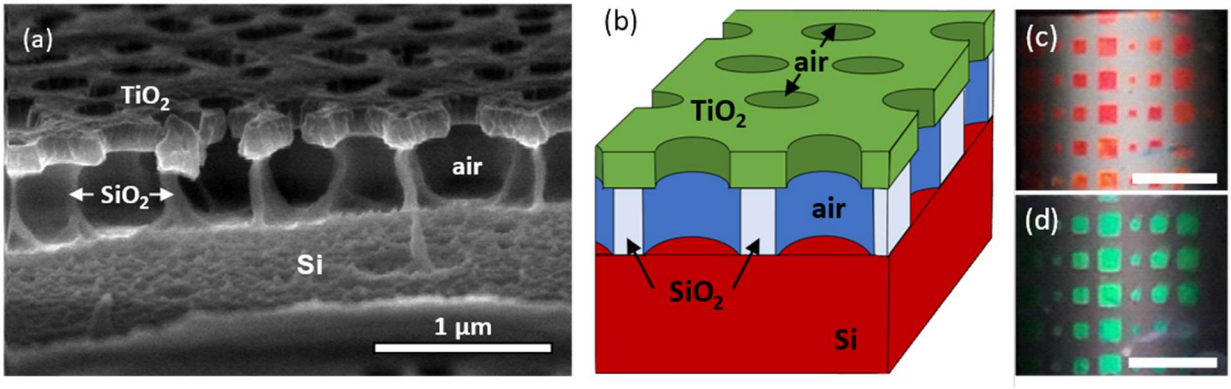

Fig. 4.1. (a) Scanning electron microscope (SEM) image of the on-wafer Fabry-Pérot microcavity (FPMC) sensor. (b) Schematic representation of the structure in (a). Optical images of multiple FPMC sensors in the (c) as-fabricated (in air) and (d) water vapor-infiltrated (i.e., detection of water in human breath) states. Scale bars in (c) and (d) are 3 mm. © 2020, OSA..

4.2.2 Optical measurements

Reflectance (R) spectra of the FPMC sensor were measured at normal-incidence (±5°) using a six-around-one fiber bundle (solarized UV-vis with a 60 mm focal length lens, giving a ~300 µm spot diameter); the bifurcated ends of the bundle were connected to a D_2-halogen broadband white light source (center fiber) and OceanOptics USB2000+ spectrometer (outer six fibers). Reflectance was referenced to a UV-protected aluminum mirror (Thor labs PF10-03-F01).

4.2.3 Optical simulations

The optical behavior of the FPMC sensor was simulated using transfer-matrix (TMM) [25] and finite-difference time-domain (FDTD) methods (Lumerical). Cross-

sectional schematics of the simulated structures are shown in Fig. 4.2. The TMM simulation domain (Fig. 4.2(a)) was set up with three homogeneous layers, the effective refractive indices of which were obtained via the Bruggeman effective medium model [26]: top (partial reflector) layer (75 vol% TiO_2, 25 vol% analyte fluid), intermediate (cavity) layer (40 vol% SiO_2, 60 vol% analyte fluid), and Si substrate (high reflector). The relative fraction of FPMC material vs. air (and where the analyte fluid would be present in sensing mode) was first assessed with SEM imaging, and subsequently optimized to match the simulated reflectance (R) with experiment.

The FDTD simulation setup for the sensor is shown in Figs. 4.2(b,c), which correspond to a TiO_2 nanohole array supported by an effective-index, semi-infinite underlayer, and the full FPMC structure (as measured from SEM images), respectively. The TiO_2 layer was 132 nm thick with 214 nm diameter holes on a hexagonal lattice with hole-to-hole pitch of 404 nm. The SiO_2 underlayer for the full FPMC structure was 380 nm thick, contained coaxial holes with a diameter of 328 nm, and placed on a 200 nm thick Si (substrate) layer modeled with a perfectly matched boundary condition (i.e., no reflection of light that was transmitted into the Si layer). The cylindrical inclusions in both the TiO_2 and SiO_2 were filled with analyte with a variable refractive index of n_{fill}. The simulation domain encompassed a rectangular area equivalent to two hexagonal unit cells, with perfectly matched (absorbing) out-of-plane boundaries and periodic in-plane boundaries. A broadband plane wave source (λ = [300, 1000] nm, 1 μm above the FPMC structure) was injected downward at normal incidence onto the FPMC structure, and a reflection monitor was placed near the top simulation boundary.

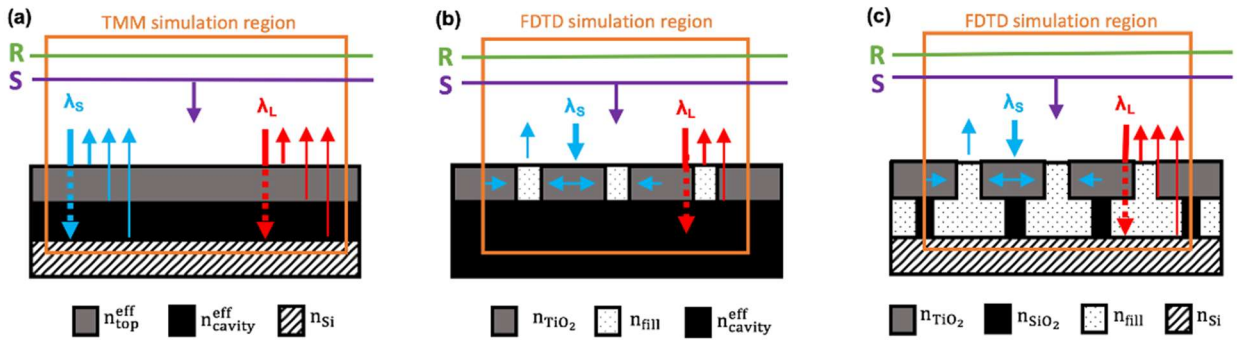

FIG. 4.2. Optical simulation domain configurations for the FPMC. (a) FPMC structure generated via effective-medium approximation, calculated via TMM. (b) Patterned TiO_2 slab supported by a semi-infinite, effective-index underlayer, calculated via FDTD. (c) Patterned TiO_2 and SiO_2 slab on an Si substrate, calculated via FDTD. The resonances observed for all three configurations are schematically represented by blue and red arrows for short (λ_S < 600 nm) and long (λ_L > 600 nm) wavelengths, respectively. Simulation boundaries (orange), reflected field monitors (green, denoted "R") and downward-injected broadband plane wave source (purple, denoted "S") are positioned relative to the simulated geometries as shown. © 2020, OSA.

4.3 Experimental results and discussion

4.3.1 Structure fabrication

The optical response of the sensor was investigated via liquid infiltration with isopropanol (IPA, Fig. 4.3(a)) and ethanol (EtOH, see Fig. 4.4), as well as with vapor infiltration (humid air, Fig. 4.3(b)) by breathing on it. For Fig. 4.3, reflectance spectra were collected from two different sensor areas (0.8 x 0.8 mm^2) on the wafer surface, labeled sensor I and II, respectively. Infiltrating the structure with isopropanol (n_{IPA} = 1.38, sensor I) resulted in a redshift of the reflectance spectrum above 600 nm by ~100 nm, and reweighting of peaks below 600 nm. Visually, the sensor switched from deep red (as-fabricated) to bright green (infiltrated), as indicated by the optical image swatches (solid borders) in Fig. 4.3. Correspondence of spectra with the observed colors was evaluated by convolving spectra with the human photopic response according to the

CIE 1931 XYZ color space via the open-source *colorpy* package [27] (dashed borders), and agreement was excellent. Due to a measured dependence of reflectance spectra on the collection angle (~2 nm/degree, due to slightly longer path length in the FPMC) and a slight off-angle camera set-up, the simulated color swatches were obtained by red-shifting all spectra by 5 nm.

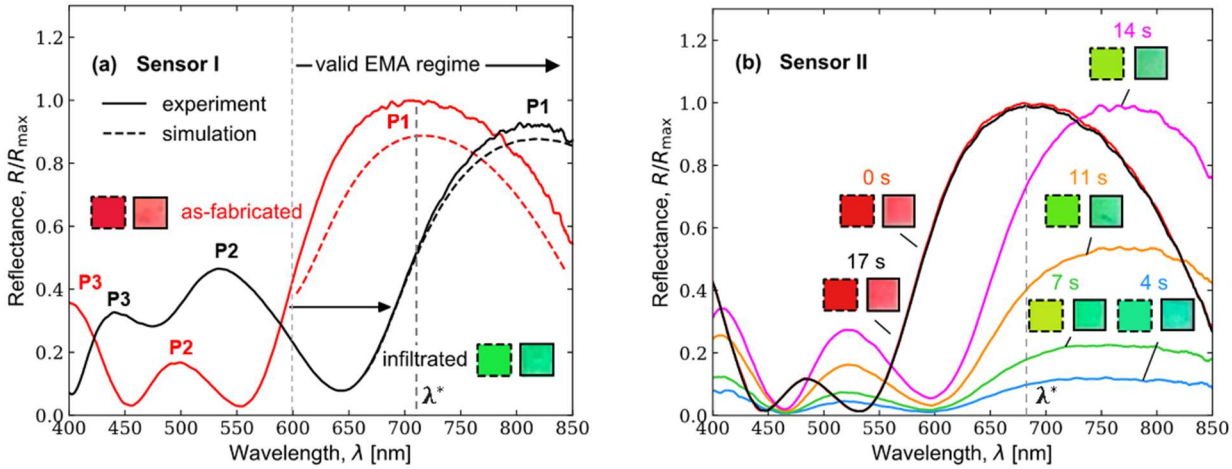

FIG. 4.3. (a) Normalized reflectance at normal-incidence (±5°) of the porous FPMC sensor in the as-fabricated (solid red, in open air) and infiltrated with isopropanol (solid black) states. Reflectance curves simulated with the effective-medium approximation (EMA) via the TMM are also shown (dashed). Key spectral features are labeled (P1-3). (b) Normalized time-dependent reflectance collected during water vapor infiltration (0 s, by breathing on it) and sensor recovery (17 s). Swatches containing optical images (solid border) and human photopic function-weighted simulation (dashed border) of the sensor color are featured for each spectrum. Sensor I and Sensor II denote two distinct square sensor areas on the wafer surface. λ* represents the maximum-reflectance wavelength for each un-infiltrated sensor. © 2020, OSA.

Figure 4.3(b) shows time-resolved, normalized reflectance spectra collected during breath-based water vapor infiltration; observed and calculated colors were in good agreement, as in Fig. 4.3(a). The sensor rapidly responded to water vapor infiltration (< 1 s response, not shown) as water condensed onto the walls of the porous underlayer and the reflected intensity sharply decreased. Spectral shape and mode

location remained unchanged as the infiltrated sensor recovered, before returning to its exact initial state upon complete analyte evaporation at 17 s.

4.3.2 Sensor performance

The refractive index sensitivity of the FPMC was obtained by tracking spectral shifts of the P1 peak and the valley between P1 and P2 in sensor I and II spectra (un-infiltrated features were used as reference), for all three tested analytes (IPA, EtOH, and water from human breath). This yielded a linear response to analyte refractive index (n_{fill}), with sensitivities of 680 and 635 nm/RIU, respectively (Fig. 4.3(a)). Notably, these sensitivities are comparable to other reported photonic crystal and interference-based schemes [21,22,28–31]. The refractive index detection range is at least n_{fill} = 1.3-1.4 as validated herein, which captures a variety of aqueous and organic solutions. Given the generic fabrication protocol, changes in structure and material composition may further extend this range of applicability. Additionally, a dramatic change in normalized reflectance at the un-infiltrated P1 peak wavelength (700 nm) was recorded, resulting in a negative change of up to 50%, equivalent to ~600 % change in normalized R per RIU (Fig. 4.3(b)). The latter suggests that the FPMC sensor may be used effectively in spectral or single-wavelength (laser-based) detection configurations. Moreover, each FPMC sensor cell (0.8 x 0.8 mm^2) can hold up to 120 nL of analyte for full infiltration, calculated from the lateral dimensions, total thickness, and void fraction of the device. Temperature sensitivity of the sensor, i.e., due to thermal expansion of the cavity (SiO_2 support and TiO_2), was also considered via FDTD simulations, and found to result in less than a 1-nm redshift of the P1 mode peak for 100 K change.

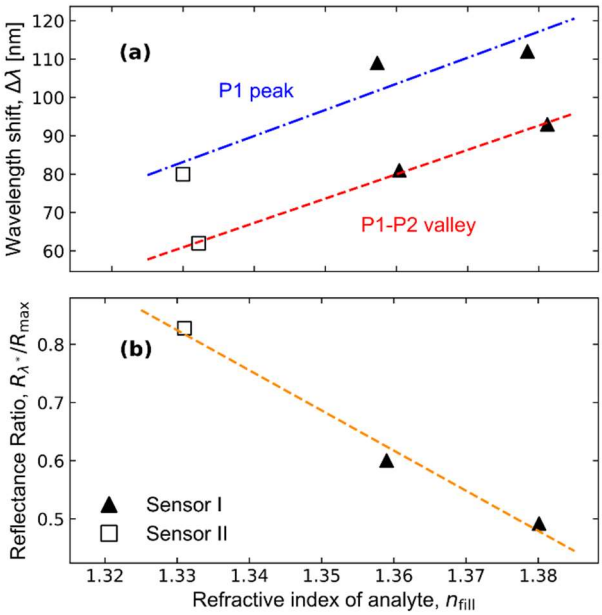

FIG. 4.4. Refractive index sensitivity of the FPMC obtained by (a) spectral shifts of the P1 peak and the valley between P1 and P2 (680 and 635 nm/RIU, respectively), and (b) the ratio of reflected and maximum intensity at the un-infiltrated P1 mode wavelength, λ^* (see Fig. 4.3). © 2020, OSA.

4.3.3 Discussion of operating principles

The operating principle of the sensor was deduced by assigning experimentally observed spectral features to optical modes. In order to discern modal origins, simulations were performed with an effective-medium approximated structure, an isolated TiO_2 hole-array, and the full-device configuration. Figure 4.5 shows reflectance contours generated as a function of n_{fill} (1 to 1.5) for each configuration. The effective-medium dielectric stack simulated in Fig. 4.5(a) shows three main Fabry-Pérot etalon modes (FP1-3). The most prominent and experimentally relevant mode is FP1, which redshifts significantly with n_{fill}, and appears nearly identical to the FP1 mode seen in the full-scale simulation in Fig. 4.5(c), and experimentally observed feature P1 in Fig. 4.3. FP1 is the only mode with appreciable intensity in the 600-650 nm range, resulting in the

bright red color observed for the un-infiltrated sensor. The remaining higher-order FP modes, FP2 and FP3, also redshift upon analyte infiltration, in line with expected thin-film interference. It is of note that the reflected intensities of these simulated modes are significantly greater than those of the measured P2 and P3 peaks; however, the model does not consider any scattering effects induced by nanostructuring in the TiO_2 layer and therefore does not accurately represent optical behavior at shorter wavelengths.

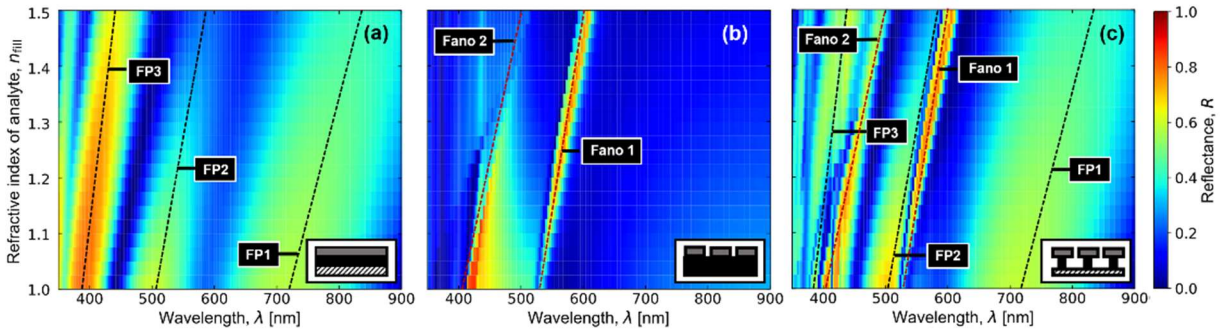

FIG. 4.5. Simulated normal-incidence reflectance contour maps of the FPMC sensor with analyte refractive index n_{fill} = 1 to1.5, configured as shown in the simplified schematics in each panel corner (cf. Fig. 4.2). (a) Effective-medium approximated layers via TMM, (b) patterned TiO_2 layer supported by an effective-index underlayer via FDTD, and (c) patterned TiO_2 and SiO_2 slab on an Si substrate via FDTD. FP1-3 denote Fabry-Pérot resonances. © 2020, OSA.

Guided modes supported by high-index-contrast nanostructures are known to interact strongly with slowly-varying broadband continua, and this coupling can be modeled by Fano resonances [32–34]. In order to isolate these modal contributions within the sensor, a nanopatterned TiO_2 slab was simulated with a semi-infinite, effective-medium approximated underlayer beneath it. Two sets of Fano resonances (denoted "Fano 1" and "Fano 2") featuring the characteristic asymmetric and narrow-linewidth shape can be discerned in Fig. 4.5(b). The Fano lineshape varies based on the phase difference between the internal TiO_2 Fabry-Pérot continuum state (out-of-plane

FP modes) and localized states (guided in-plane modes), resulting in either enhanced (Fano 1) or attenuated (Fano 2) reflectance relative to the FP continuum. Although P2 and P3 track the central mode positions of Fano 1 and 2, respectively, they are neither as sharp nor as intense. We attribute the observed modal breadth to (i) the imperfect normal-incidence measurement (±5° solid angle) and (ii) high translational disorder in hole positions, given the high sensitivity of sharp optical Fano modes to angle and ordering [24,35]. Regardless of ordering, the TiO_2 layer essentially acts as a highly wavelength-selective filtering element below 600 nm within the n_{fill} range of interest.

The simulation results in Fig. 4.5(c) depict reflectance contours for the full sensor structure calculated with analyte-infiltrated TiO_2 hole array and SiO_2 underlayer features, as well as a silicon substrate beneath. FP1 fully retains the behavior observed in Fig. 4.5(a), while FP2 and FP3 are modified by the Fano resonances observed in Fig. 4.5(b), induced by the nanostructured TiO_2 layer. The convolution of FP2/3 modes and Fano 1/2 resonances, respectively, more accurately represent the mode locations and intensities of P2 and P3 than the pure FP2/FP3 modes in Fig. 4.5(a). Notably, Fano 2 retains high reflectivity despite a considerable redshift, which explains sustained increases in P2 intensity as the cavity is infiltrated (Fig. 4.3(a)). As discussed above, these distributed Fano modes tend to diffusely scatter light off-axis at or near the locations of FP2 and FP3, which favors a vivid red appearance in specular view. P2 is particularly prominent while the sensor is infiltrated and contributes most directly to the apparent green sensor color. We conclude that P1 is a pure Fabry-Pérot etalon mode, while P2 and P3 are comprised of convolved Fabry-Pérot and nanohole-induced, broadly distributed

Fano resonances that suppress specular blue light and yield a striking red-to-green color transition.

When comparing experimental sensor performance in Figure 4a to the simulated result in Fig. 4.5(c), it becomes evident that the approximately linear sensitivity in the simulated FP1 peak (~250 nm/RIU) is less than demonstrated experimentally for n_{fill} = 1.3-1.4 (~650 nm/RIU). While we have no definitive justification for this, several plausible contributing factors may be (1) under-estimation of underlayer porosity due to presence of hollow/nanoporous SiO_2 supports, and/or (2) inaccessible pockets of air inside the sensor, which can yield significant local differences in infiltration as dictated by the surface tension of the analyte. As such, further iterations of the sensor could feature surface treatments to help or control the degree of analyte infiltration.

4.3.4 Effect of short-range order on FPMC color response

As detailed above, the specular-view sensor color is highly sensitive to the interplay of two distinct and sensitive optical resonances (microcavity Fabry-Pérot and hole-array Fano), which in turn span the entire visible spectrum. The optical simulations conducted (both TMM and FDTD), while proving useful in assigning modal locations, did not fully account for the short-range correlated order of the TiO_2 nanomembrane. The resulting inaccuracy in relative modal intensities lead to unrealistic colors obtained by CIE tristimulus weighting. In the case of TMM, layer homogenization precludes any Fano-resonant behavior, and the intense high-order Fabry-Pérot peaks observed in the 400-500 nm range for the dry sensor (Fig. 4.6(a,b)) therefore overwhelm the prominent red color observed in experiment, yielding a turquoise-to-purple transition (Fig. 4.6(c)). The

FDTD simulations improve color accuracy (Fig. 4.6(d)) showing the expected red color for the dry sensor. However, the blue-violet modes supported by the perfectly ordered high-contrast grating give a purplish hue instead of the experimentally observed green color.

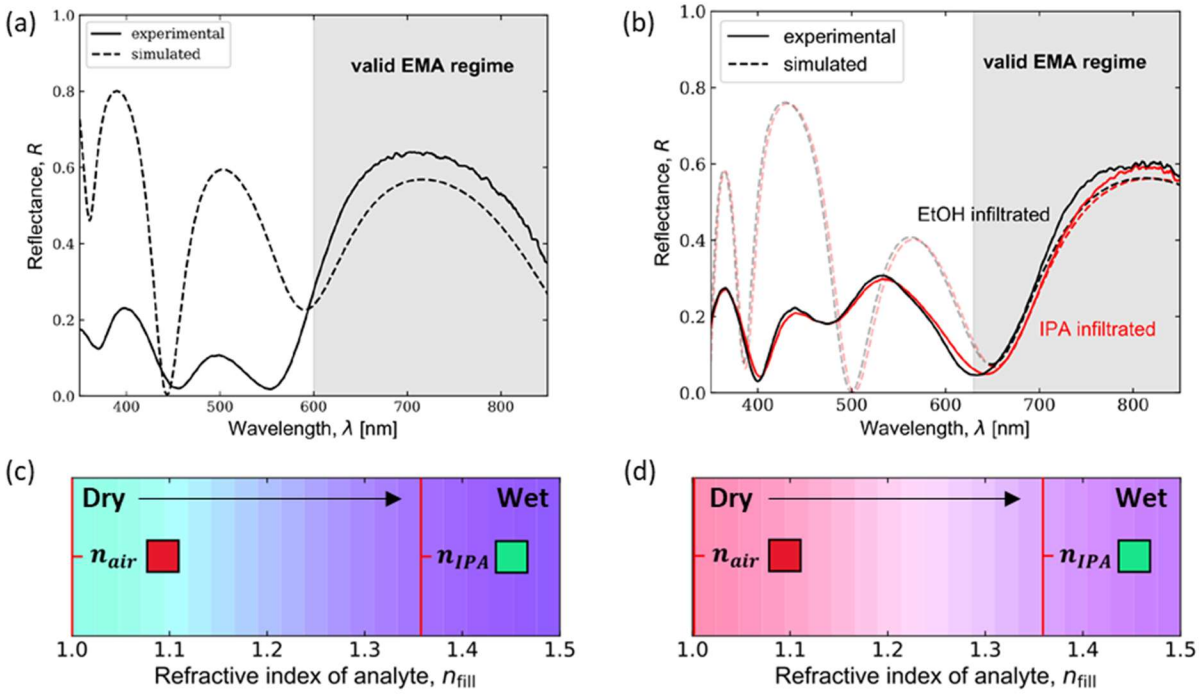

FIG. 4.6. TMM-simulated and experimental specular reflectance curves of the (a) dry and (b) infiltrated sensor, as well as apparent color profiles of the FPMC sensor with analyte refractive index, n_{fill} ,varied from 1 to 1.5, calculated with tristimulus values mapped onto the CIE color space simulated with (c) transfer-matrix and (d) FDTD methods. Figures courtesy of Helen Stute and reprinted from [36].

4.3.5 Enhancing sensor performance and sensitivity: permeable distributed Bragg reflectors

The sensors discussed herein comprised the first iteration of such interferometric devices, and as such, may warrant further investigation into improving future iterations. As with any sensor, the signal transduction range must match the application desired; in the case of refractometric sensing of liquids, we must be able to detect n_{fill} from ~1.3 to

1.5. If we choose to retain a clearly visible readout, then we must target a modal transition that moves in and out of the visible-wavelength range. If the exact same structural geometry is desired, we may consider improving the inherent finesse of the cavity (i.e., the sharpness of its resonances) by making the bottom reflector a non-absorbing metallic layer (e.g., Ag or Al) for higher reflectivity at this interface, both owing to the reduced absorption and increased overall reflectance relative to silicon. If the sensor is used in a single-wavelength (laser-reflectance) configuration, care must be taken to harness the corresponding increase in sensitivity and choose the proper wavelength to probe. If, however, geometric constraints are lifted, we may tune a variety of parameters in the existing structure such as underlayer thickness (cavity length) and hole pitch/radius to design mode-selective filtering.

Given that our sensor leverages a constructive thin-film interference effect with a two-layered dielectric structure, a natural extension of this structure is a periodic, repeated lattice of this two-layer unit cell, which is expected to amplify the optical response and extend the total analyte capacity and adsorption area. Technically, this sort of structure falls under the category of a DBR, which was introduced in Chapters 1 and 2. The unique features of our particular structure lie in its porosity and permeability, yielding a highly reflecting element with relatively few periods, and the ability to fully infiltrate the reflecting element itself with various media of interest. Figure 4.7 shows the FDTD simulation configuration, as well as the effect of introducing up to three additional bilayer periods to the FPMC stack. As expected, the absolute reflectance increases dramatically, affording >95% reflectance over a ~100-nm stop-band with only 4 DBR periods, while retaining all of the desirable qualities of the original design.

Accordingly, with some tuning of the FP1 band-edge position, it is possible to leverage a much sharper and dynamic reflectance change than in the original design, improving sensitivity and signal-to-noise ratio.

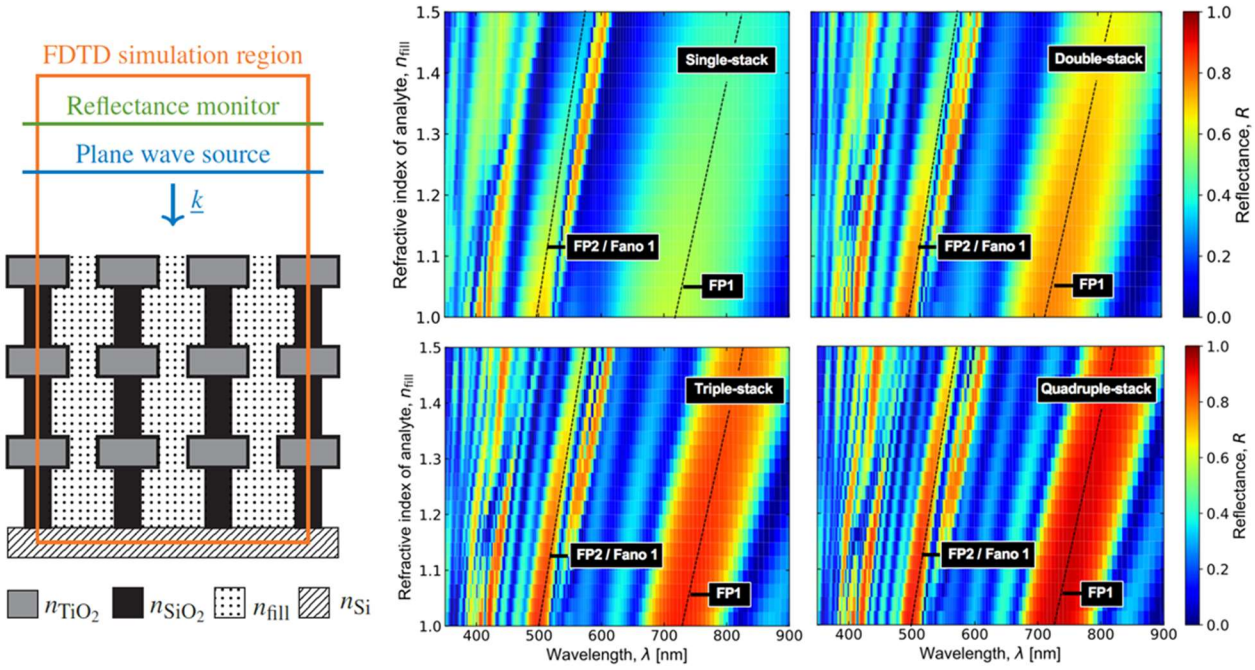

FIG. 4.7. Semi-permeable FPMC-DBR simulations. At left: FDTD simulation configuration. At right: contour maps of the specular reflectance response with increasing n_{fill} for FPMC sensors with an increasing number of top/underlayer bilayer stacks (1-4). Previously established modal assignments are highlighted with dashed lines and text labels.

4.3.6 Diffuse optical behavior of the FPMC

Having looked extensively at the specular response of the sensor we discuss the off-axis optical behavior of the structure to assess any discernible modal changes. Figure 4.8 shows the measured, spectrally-resolved diffuse scattering from the FPMC with normal-incidence illumination and off-axis spectral collection via solarized fiber (Ocean Optics). The diffuse spectrum of the dry sensor is, as expected, consistent with that of the blue-colored TiO_2 nanomembrane sample featured in Chapters 3 and 4, featuring the two

prominent Fano modes which carry out the filtering required for the vivid red appearance of the dry sensor. There is also a broad, low-intensity feature around 700 nm, which appears to be diffuse scattering of the low-order Fabry-Perot mode (FP1), presumably by the TiO_2 membrane, after any photons transmitted through it have made at least a single round-trip within the porous layer beneath it.

When the sensor is infiltrated (water vapor delivered by human breath), the lowest-order diffuse Fano mode (Fano 1) vanishes and Fano 2 appears to undergo a slight blueshift. Given that we see corresponding increases in the intensity of Fano 1 in the specular reflectance during analyte infiltration, there may in fact be a re-partitioning of incident light back into specular reflectance. Given that our analytes approach the index of the underlayer silica material, analyte infiltration will in fact reduce the refractive index variation in the highly disordered underlayer, rendering the curved and highly irregular surfaces of the etched silica invisible to in-coupled light. The TiO_2 slab itself may also be effectively "planarized", further reducing diffuse reflectance. The diffuse FP1 remnant experiences a redshift, which is consistent with specular reflectance measurements and simulations.

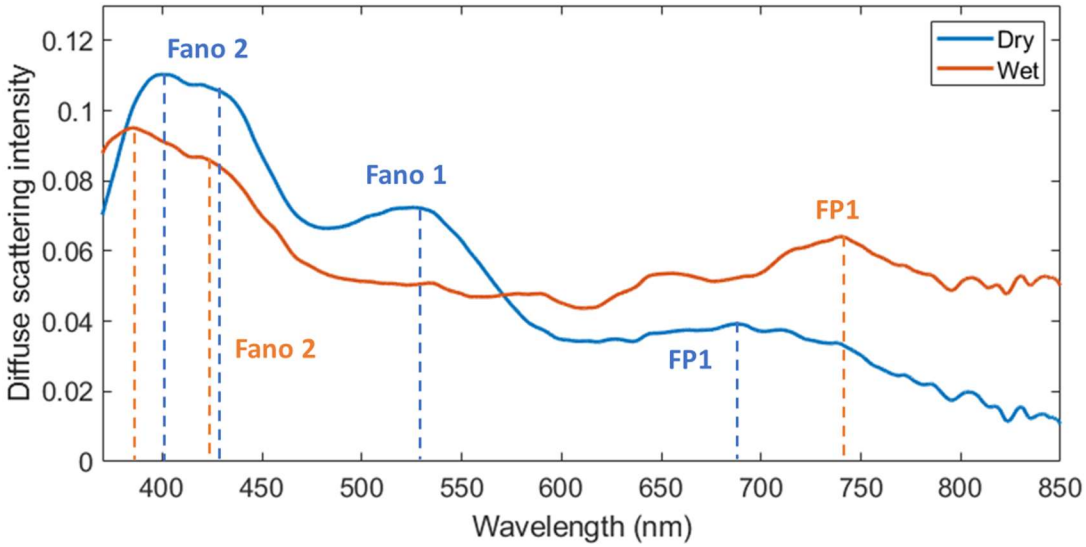

FIG. 4.8. Diffuse reflectance of the FPMC sensor in the dry (blue curve) and infiltrated (orange) states. Previously established and further postulated modal assignments are highlighted with dashed lines and text labels, with the dry sensor exhibiting a prominent Fano 1 mode, which vanished upon sensor infiltration.

4.4 Conclusion

In this chapter, we have demonstrated an all-dielectric Fabry-Pérot microcavity resonator, comprised of a high-index TiO_2 output coupler and microporous SiO_2 cavity, for refractive index sensing. Analyte infiltration increases the effective refractive index of the structure, red-shifting the primary Fabry-Pérot resonance wavelength. The TiO_2 outcoupling membrane function is twofold, enabling facile analyte transport to the microcavity and acting as a diffusely scattering photonic slab that filters higher-order Fabry-Pérot cavity modes and affords an easily detectable color transition during operation. The sensor is made via wafer-scalable techniques, shows sensitivities on par with incumbent refractometers, and can be used in spectral and single-wavelength

sensing modes, making it a versatile candidate for commercial deployment in applications ranging from in-line process control to respiratory measurements.

References

1. L. G. Lindberg, H. Ugnell, and P. Å. Öberg, "Monitoring of respiratory and heart rates using a fibre-optic sensor," Med. Biol. Eng. Comput. **30**(5), 533–537 (1992).
2. J. G. Groetsch, "Theory and Use of In-Line Refractive Index Analyzers for Improved Process Control," Sensors Ind. Conf. (November), 219–223 (2001).
3. I. Noiseux, W. Long, A. Cournoyer, and M. Vernon, "Simple fiber-optic-based sensors for process monitoring: An application in wine quality control monitoring," Appl. Spectrosc. **58**(8), 1010–1019 (2004).
4. J. Rheims, J. Köser, and T. Wriedt, "Refractive-index measurements in the near-IR using an Abbe refractometer," Meas. Sci. Technol. **8**(6), 601–605 (1997).
5. P. P. Herrmann, "Determination of thickness, refractive index, and dispersion of waveguiding thin films with an Abbe refractometer," Appl. Opt. **19**(19), 3261–3262 (1980).
6. M. Shao, X. Qiao, Z. Jia, H. Fu, Y. Liu, H. Li, and X. Zhao, "Refractive index measurement based on fiber Bragg grating connected with a multimode fiber core," Opt. Commun. **351**, 70–74 (2015).
7. S. W. James and R. P. Tatam, "Optical fibre long-period grating sensors: characteristics and application," Meas. Sci. Technol. **14**(5), R49–R61 (2003).
8. V. Bhatia, "Applications of long-period gratings to single and multi-parameter sensing," Opt. Express **4**(11), 457–466 (1999).
9. L. Coelho, D. Viegas, J. L. Santos, and J. M. M. M. de Almeida, "Enhanced refractive index sensing characteristics of optical fibre long period grating coated with titanium dioxide thin films," Sensors Actuators B **202**, 929–934 (2014).
10. A. A. P. Trichet, J. Foster, N. E. Omori, D. James, P. R. Dolan, G. M. Hughes, C. Vallance, and J. M. Smith, "Open-access optical microcavities for lab-on-a-chip refractive index sensing," Lab Chip **14**(21), 4244–4249 (2014).
11. C. Monat, P. Domachuk, and B. J. Eggleton, "Integrated optofluidics: A new river of light," Nat. Photonics **1**(2), 106–114 (2007).
12. D. Brennan, P. Lambkin, and P. Galvin, "Refractive index measurements in a shallow multichannel microfluidic system," Meas. Sci. Technol. **19**(8), 085403 (2008).
13. G. A. C. Tellez, S. Hassan, R. N. Tait, P. Berini, and R. Gordon, "Atomically flat symmetric elliptical nanohole arrays in a gold film for ultrasensitive refractive index sensing," Lab Chip **13**(13), 2541–2546 (2013).
14. W. Z. Song, X. M. Zhang, A. Q. Liu, C. S. Lim, P. H. Yap, and H. M. M. Hosseini, "Refractive index measurement of single living cells using on-chip Fabry-Ṕrot cavity," Appl. Phys. Lett. **89**(20), 203901 (2006).
15. P. Domachuk, I. C. M. Littler, M. Cronin-Golomb, and B. J. Eggleton, "Compact resonant integrated microfluidic refractometer," Appl. Phys. Lett. **88**(9), 093513 (2006).
16. R. St-Gelais, J. Masson, and Y. A. Peter, "All-silicon integrated Fabry-Ṕrot cavity for volume refractive index measurement in microfluidic systems," Appl. Phys. Lett. **94**(24), 243905 (2009).
17. V. Lien, K. Zhao, and Y. H. Lo, "Fluidic photonic integrated circuit for in-line detection," Appl. Phys. Lett. **87**(19), 194106 (2005).
18. Y. Xu, P. Bai, X. Zhou, Y. Akimov, C. E. Png, L. K. Ang, W. Knoll, and L. Wu, "Optical Refractive Index Sensors with Plasmonic and Photonic Structures: Promising and Inconvenient Truth," Adv. Opt. Mater. **7**(9), 1801433 (2019).
19. S. M. Harazim, V. A. Bolaños Quiñones, S. Kiravittaya, S. Sanchez, and O. G. Schmidt, "Lab-in-a-tube:

On-chip integration of glass optofluidic ring resonators for label-free sensing applications," Lab Chip **12**(15), 2649–2655 (2012).

20. C. Li, G. Bai, Y. Zhang, M. Zhang, and A. Jian, "Optofluidics refractometers," Micromachines **9**(136), (2018).

21. S. Wang, Y. Liu, D. Zhao, H. Yang, W. Zhou, and Y. Sun, "Optofluidic Fano resonance photonic crystal refractometric sensors," Appl. Phys. Lett. **110**(9), 091105 (2017).

22. W. Zhou, D. Zhao, Y. C. Shuai, H. Yang, S. Chuwongin, A. Chadha, J. H. Seo, K. X. Wang, V. Liu, Z. Ma, and S. Fan, "Progress in 2D photonic crystal Fano resonance photonics," Prog. Quantum Electron. **38**(1), 1–74 (2014).

23. F. L. Gonzalez, L. Chan, A. Berry, D. E. Morse, and M. J. Gordon, "Simple colloidal lithography method to fabricate large-area moth-eye antireflective structures on Si , Ge , and GaAs for IR applications," J. Vac. Sci. Technol. B **32**(5), 051213 (2014).

24. P. Shapturenka, F. Birkholz, N. I. Zakaria, S. P. S. P. DenBaars, and M. J. M. J. Gordon, "Quasiordered, subwavelength TiO2 hole arrays with tunable, omnidirectional color response," J. Vac. Sci. Technol. A **38**(5), 053403 (2020).

25. S. J. Byrnes, "Multilayer optical calculations," arXiv e-prints (2016).

26. D. A. G. Bruggeman, "Berechnung verschiedener physikalischer Konstanten von heterogenen Substanzen," Ann. Phys. **5**(24), 636–664 (1935).

27. M. Kness, "ColorPy - A Python package for handling physical descriptions of color and light spectra," (2012).

28. W. Knoll, O. Azzaroni, H. Duran, J. Kunze-Liebhäuser, K. H. A. Lau, E. Reimhult, and B. Yameen, "Nanoporous thin films in optical waveguide spectroscopy for chemical analytics," Anal. Bioanal. Chem. **412**(6), 3299–3315 (2020).

29. W. Liu, J. Yan, and Y. Shi, "High sensitivity visible light refractive index sensor based on high order mode Si3N4 photonic crystal nanobeam cavity," Opt. Express **25**(25), 31739 (2017).

30. F. B. Barho, F. Gonzalez-Posada, M.-J. Milla-Rodrigo, M. Bomers, L. Cerutti, and T. Taliercio, "All-semiconductor plasmonic gratings for biosensing applications in the mid-infrared spectral range," Opt. Express **24**(14), 16175 (2016).

31. T. Wei, Y. Han, Y. Li, H.-L. Tsai, and H. Xiao, "Temperature-insensitive miniaturized fiber inline Fabry-Perot interferometer for highly sensitive refractive index measurement," Opt. Express **16**(8), 5764–5769 (2008).

32. W. Zhou, Z. Ma, H. Yang, Z. Qiang, G. Qin, H. Pang, L. Chen, W. Yang, S. Chuwongin, and D. Zhao, "Flexible photonic-crystal Fano filters based on transferred semiconductor nanomembranes," J. Phys. D. Appl. Phys. **42**(23), 234007 (2009).

33. B. C. P. Sturmberg, K. B. Dossou, L. C. Botten, R. C. McPhedran, and C. M. de Sterke, "Fano resonances of dielectric gratings: symmetries and broadband filtering," Opt. Express **23**(24), 1672–1686 (2015).

34. O. Kilic, S. Kim, W. Suh, Y.-A. Peter, A. S. Sudbø, M. F. Yanik, S. Fan, and O. Solgaard, "Photonic crystal slabs demonstrating strong broadband suppression of transmission in the presence of disorders," Opt. Lett. **29**(23), 2782–2784 (2004).

35. V. N. Astratov, I. S. Culshaw, R. M. Stevenson, D. M. Whittaker, M. S. Skolnick, T. F. Krauss, and R. M. De La Rue, "Resonant coupling of near-infrared radiation to photonic band structure waveguides," J. Light. Technol. **17**(11), 2050–2057 (1999).

36. Stute, H. “Invetigating a color-changing refractometric sensor, based on an on-wafer porous dielectric Fabry-Pérot microcavity.” Masters thesis, TU München (2020).

5

Stress engineering of III-nitride emitters via patterned, relaxed $(11\bar{2}2)$ semipolar InGaN buffers

5.1 Introduction

Despite significant progress and multiple creative approaches taken toward the realization of long-wavelength III-nitride based devices over the past decade, high double-digit external quantum efficiencies remain elusive for GaN/InGaN based devices for wavelengths longer than 525 nm (green, yellow, orange, and red). As detailed in the introductory chapters, the reasons for this stem from the large lattice mismatch between GaN and InGaN, which manifests in local and macroscopic crystal strain gradients that degrade surface growth morphology, introduce diverse and potent nonradiative defects, and amplify the deleterious effects of both spontaneous and piezoelectric polarization fields inherent to the material system.

Efforts to realize efficient long-wavelength nitride-based devices can be roughly classified into four main groups: (1) strain management, (2) strain templating, (3) quantum dot and ion-assisted frequency down-conversion (e.g., phosphors and GaN:Eu^{3+} doping), and (4) growth of quaternary alloys, also known as total and non-negotiable

capitulation. Here, (1) and (2) will be given the privilege of a more extended overview, leaving the review for (3) and (4) as an exercise for the reader to enjoy at their leisure, given the many limitations of (3) and currently insurmountable difficulty of (4).

A strain-management approach looks to mitigate existing or unavoidable crystallographic strain. Possible strategies include micro- and nanopatterning device layers and growing coherent and semi-coherent layers on alternative GaN substrate orientations (for piezoelectric and/or %In uptake benefits) [1–3]. Another approach to manage strain is polarization screening, which uses heavily doped or tensile adjacent layers to counteract the large electric fields within the active region, leading to reduced carrier densities and increased carrier wavefunction overlap [4].

Strain templating refers to the preparation of a growth surface that reduces the lattice mismatch between compositionally distinct layers during heteroepitaxy and relaxes the overall strain state of the system, removing the need for post-growth mitigation. For the InGaN/GaN system, this is achieved with either bulk or thin buffer layers that offer a lattice-expanded growth substrate relative to GaN. By growing on a nominally In-containing surface, epitaxially grown emitting layers experience less additional lattice mismatch, are more tolerant to In-rich layers, and expand the attainable long-wavelength emitter design space. Strain-templating approaches include epitaxially grown buffer layers (both uniform and compositionally graded), coalescence of re-growth on masked or well-defined topographic features, and growth on mechanically compliant layers prepared by thin-film transfer or underlayer porosification [5–7].

Recently, the latter methods have been touted as highly promising; devices on compliant and lattice-expanded InGaN buffer layers have been demonstrated, though

there is plenty of room for improvement in material quality, with estimated external LED efficiencies of less than 1% [7,8]. In-rich InGaN growth on c-plane orientations quickly nucleates V-pit formation from existing threads, and the resulting morphological breakdown is difficult to manage [9]. Moreover, buffer quality can be quite irreproducible, stemming from the mechanism by which basal-plane oriented layers seek to relax strain, and accordingly the sensitivity of growth morphology to the epilayer composition and growth conditions (e.g., temperature, pressure, III/V precursor ratio). Once strain precludes step-flow crystal growth, clustering-prone modes and spinodal InGaN alloy decomposition dominate the landscape, severely limiting the material's usefulness for device epitaxy [10,11].

Owing to the hexagonal wurtzite crystal structure of GaN, built-up compressive stress in GaN/InGaN systems manifests quite differently on inclined crystallographic planes relative to the basal plane (also known as *semipolar* planes). Heteroepitaxy of moderately indium-rich layers on semipolar GaN faces elicits a resolved shear stress on the closest-packed (0001) basal plane (also the most energetically favorable slip plane), and is mediated by anisotropic glide and bend of threading dislocations (TDs) at the heterointerface, forming misfit edge dislocations (MDs) (Fig. 5.1) [12,13]. This effect was actively investigated in past decades for realizing semi-coherently strained waveguides and cladding for laser diodes [2,3]; here, we instead look to semipolar InGaN layers as an alternative frontier for fully stress-relaxed buffers for long-wavelength InGaN emitter growth. Recent progress toward controllable, thick buffer templates is outlined, and possible pathways for further template relaxation are proposed featuring both elastic and plastic relaxation of thick InGaN buffer layers via micro- and nano-patterning.

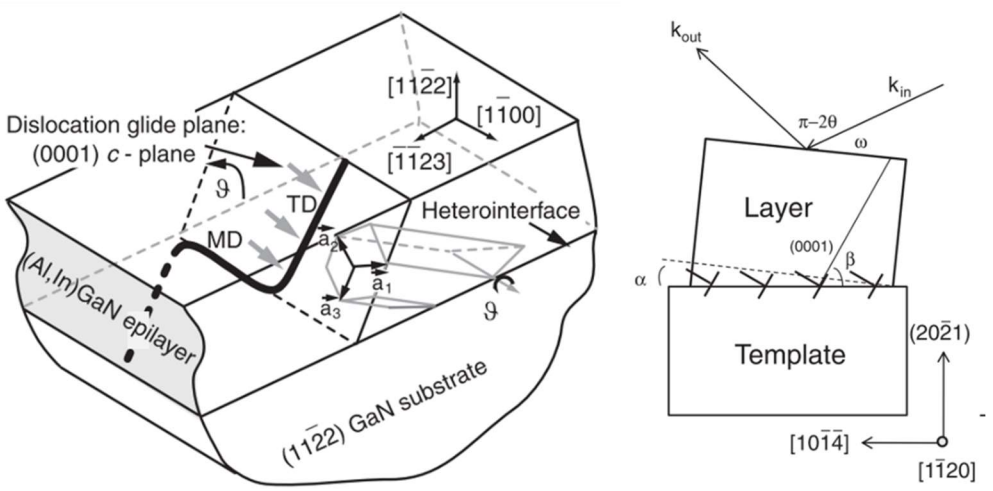

FIG 5.1. (a) Bird's-eye view of an epilayer grown on a (11-22) GaN surface, showing the bend and glide of a threading dislocation along the basal glide plane, forming a misfit dislocation at the heterointerface. (b) Cross-sectional schematic of epilayer tilt induced by the perpendicular component of the basal-plane misfit dislocations formed at the InGaN/GaN heterointerface, depicted here on the (20-21) crystal plane [13,14].

5.2 Semipolar InGaN buffers

5.2.1 Strategies for controllable relaxation

Two distinct strategies exist for leveraging semipolar InGaN buffers for long-wavelength devices. The first approach seeks to limit dislocation glide and maintain a coherent, if metastable, heterostructure for subsequent epitaxial growth; this has been demonstrated in the past with techniques such as limited-area epitaxy and growth on 1D-relaxed buffers [15,16]. The second approach embraces the eventual demise of fully and partially coherent InGaN layers, and seeks to intentionally and fully relax the buffer material into a pseudo-substrate. The second approach is of particular interest; as we will see, the route proposed here combines the plastic relaxation mechanisms inherent to semipolar stress relaxation with elastic Poisson relaxation, obtained by introducing

free boundaries in the material through patterning, in the hopes of achieving full bi-axial strain relaxation.

A fully coherent InGaN epilayer on GaN experiences an increasing compressive stress with increasing thickness due to lattice mismatch between the two materials. On semipolar orientations, the most energetically favored strain-releasing defect is a basal-plane (BP) misfit dislocation (MD). At a certain thickness, the misfit strain released (ϵ_m) by forming such a dislocation (with Burgers vector $\boldsymbol{b}$, and parallel/perpendicular/screw components $b_\parallel/b_\perp/b_s$, respectively) exceeds the energetic cost to create it, at which point MD formation proceeds spontaneously. This threshold is known as the Matthews-Blakeslee (MB) critical thickness, h_c, given by:

$$h_c = \frac{b_\parallel^2 + b_\perp^2 + (1-\nu)b_s^2}{\epsilon_m(1+\nu)8\pi b_\parallel} \ln\left(\frac{2h_c}{r_0}\right) \tag{5.1}$$

where ν is the material's Poisson ratio and r_0 is the dislocation core radius.

As mentioned above, misfits are initiated by the motion of glissile TDs along slip planes, the most favorable of which is the basal (0001) plane for most orientations and conditions (followed by $(10\bar{1}1)$ prismatic and $(11\bar{2}2)$ pyramidal planes). This is shown for the $(11\bar{2}2)$ growth plane below, in Fig. 5.1(a). The basal plane only intersects the semipolar growth face on a single trace vector, which dictates that all basal-plane misfits run parallel to one another; this is not the case for all other slip systems mentioned, which propagate MDs along at least two symmetric traces and encourage TD multiplication via MD intersection (seen as cross-hatching under cathodoluminescent imaging). Generic slip vector traces are shown in Fig. 5.2 below for semipolar growth planes, as well as

specifically for the {11$\bar{2}$2} growth plane [17]. Given the 1D nature of basal plane slip, strain is released in only one direction. Furthermore, only the parallel component of the misfit contributes to strain relaxation; the perpendicular component contributes to the formation of a dislocation wall, leading to macroscopic epilayer tilt.

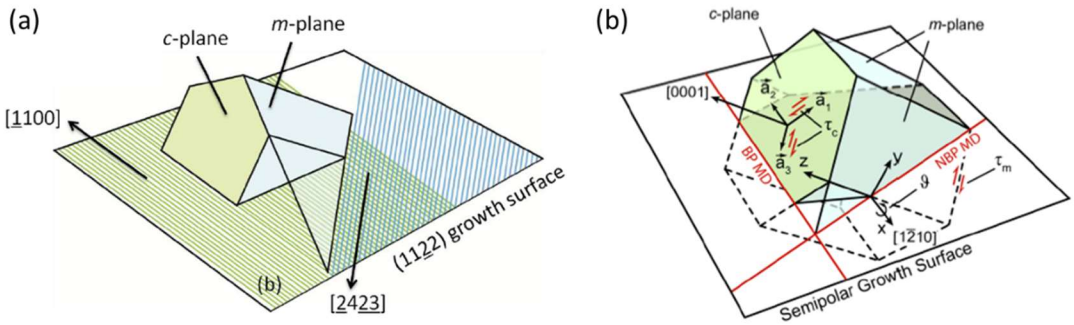

FIG 5.2. (a) Schematic of the hexagonal wurtzite crystal intersecting a semipolar growth plane, resulting in delineated basal and non-basal plane misfit dislocation propagation vectors. (b) Schematic of slip planes associated with misfit dislocation formation specifically on the (11-22) crystal plane [17].

The MB thickness criterion, while instructive and theoretically robust, remains quite conservative in its estimations of usefully implementable epilayers in devices. Studies exploring the epilayer composition and thickness design space on InGaN epilayers achieved nearly double-digit InGaN compositions and thicknesses of over 100 nm, expanding the thickness design space by more than twofold over MB-delineated limits [18,19]. It is to be noted, however, that these layers were partially relaxed, with at least one active slip system. Unfortunately, growth of emitting layers atop these buffers proved to be another nontrivial effort, as the elevated temperatures of subsequent re-growth steps can provide enough energy to surmount barriers to further dislocation generation and glide, exacerbated by the additional compressive stress generated by depositing additional In-rich (>20%) layers. The introduction of tensile AlGaN layers and

InGaN-based barriers/contact layers provided a reasonably successful strategy to maintain a uniform, metamorphic strain state throughout the device stack.

Hardy *et al.* further extended the limits of thick, semi-coherent layers by suppressing non-basal plane slip with heavy p- and n-type doping, yielding high-single digit In% buffers over 200 nm in thickness with nearly full 1D relaxation [20,21]. Koslow et al. experimentally probed the onset of various slip systems on the $(11\bar{2}2)$ orientation and showed the benefits of additional relaxation by patterning nanostripes in the direction orthogonal to BP MD propagation [21]. Building on this work, Koslow *et al*. also showed slight improvements in long-wavelength single-quantum well LEDs by growing on 1D-relaxed buffers relative to planar GaN reference substrates, as well as improved EQEs of devices grown on nanostripe-patterned, 1D-relaxed buffers relative to planar GaN references [15,21].

Having thoroughly surveyed the benefits of uniaxial relaxation, a rather natural conclusion can be made about the additional benefits that may arise from biaxial relaxation. Unfortunately, owing to the unfavorable non-basal slip that can easily activate upon emitter re-growth, alternative approaches may be required that do not push the thickness and composition design space to its very limits. One such approach is to spur elastic buffer relaxation via micro and nanopatterning, which has been used effectively to pattern quantum wells for relaxation of compressive strain in InGaN multiple quantum well layers [1,22]. Below, this method is introduced, where a simple theoretical system helps establish the potential impact of the technique.

The creation of a free boundary next to compressively strained material reduces the volume-averaged stress components in the direction perpendicular to the boundary.

Considering the simple case of uniform patterned stripes of width w of a strained epilayer of thickness h and material Poisson ratio ν_f, the approximate volume-averaged stress components orthogonal ($\langle\sigma_{xx}\rangle$) and along ($\langle\sigma_{yy}\rangle$) the pattern direction are given by:

$$\langle\sigma_{xx}\rangle \approx \sigma_{\mathrm{m}}\left\{1 - \frac{l}{w}\tanh\frac{w}{l}\right\} \tag{5.2}$$

$$\langle\sigma_{yy}\rangle \approx \sigma_{\mathrm{m}}\left\{1 - \nu_f\frac{l}{w}\tanh\frac{w}{l}\right\} \tag{5.3}$$

where l is proportional to h [23]. Assuming that the material elastic constants are similar for substrate and epilayer, one can reasonably approximate the hyperbolic tangent as a summation [23]. The approximate misfit strain relaxed as a function of aspect ratio h/w for an $In_{0.25}GaN$ layer is shown below in Fig. 5.3. Evidently, an aspect ratio of only 0.4 is sufficient to relax the majority of the misfit strain in the x-direction. A typical partially relaxed InGaN epilayer relaxes misfit strain by approximately 50% owing to BP-MD's; an additional >80% reduction in the other axis through patterning would be a significant step toward full biaxial relaxation. Even more promising is the extension of stripes to pillars, such that both axes experience the full benefits of elastic release. While promising, this is non-trivial to implement in practice; for a microLED with a 2-micron mesa width (w = 2 μm), an aspect ratio of 0.4 would require a buffer thickness of 800 nm, which heavily limits the buffer's indium content if catastrophic relaxation is to be avoided. Evidently, dilute indium compositions, thick layers and small structures are optimal to best leverage this effect.

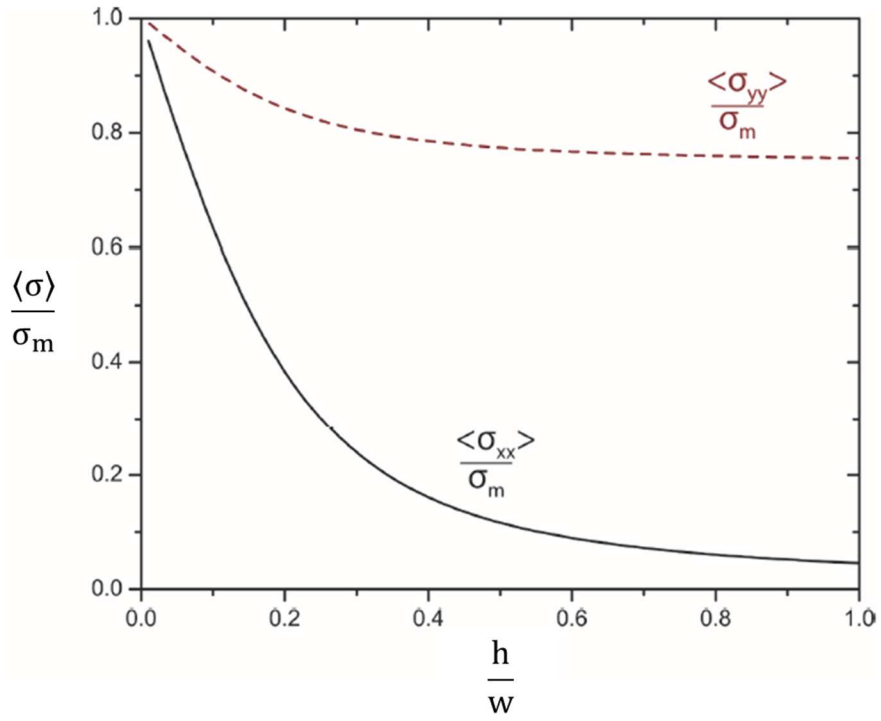

FIG 5.3. Normalized volume-averaged shear stress components along (y) and orthogonal (x) to parallel stripes (width, *w*) etched into a $In_{0.25}GaN$ epilayer (thickness, *h*).

Several nanofabrication routes are possible for creating submicron patterns. Nanoimprint, electron-beam, and holographic lithography are all possible and can be straightforward with commensurate development efforts; however, if we seek to merely understand the strain and emission state of the buffer materials, we only need exert a degree of control over the average feature size to control *w*. Device layouts often make mesas sparse, small, and therefore difficult to probe spectroscopically. Colloidal lithography (introduced in Chapters 2 and 3) proves to be sufficient (and in fact ideal) for this application, providing a reasonable degree of feature monodispersity, radial uniformity (circular pillars), and a large material area to probe for X-ray diffraction and luminescence measurements.

5.2.2 Characterization of 1D-relaxed InGaN buffers

A prerequisite for properly studying relaxed buffers is to grow a proper planar buffer layer; it is nontrivial to navigate the composition and thickness design space to render extensive 1D relaxation without crossing the critical thickness for activating non-basal plane slip. If unsuccessful, intersection of various misfit dislocations initiates and propagates TDs through any subsequently deposited layers. To this end, 250 nm of heavily Si-doped ($\sim 1\times10^{19}$ cm^{-3}) $In_{0.06}GaN$ (henceforth called a relaxed InGaN buffer or 'RIB') was grown on a 5 mm x 16 mm, free-standing, single side polished $(11\bar{2}2)$ GaN substrate (Mitsubishi Chemical Corp.). This substrate was sectioned into 4 pieces (each ~4 mm wide) for process splits. Cathodoluminescence (CL) imaging (ThermoFisher Apreo C with Gatan MonoCL4 retrofit) and high-resolution x-ray diffraction was conducted on the RIBs (SmartLab Hypix 2000, Rigaku Corp.) to qualitatively confirm 1D epilayer relaxation and quantify composition/strain state, respectively. Fig. 5.3 shows a suite of CL and x-ray diffraction data collected on RIB samples.

As shown in panel (a), CL imaging confirmed the exclusive formation of parallel basal-plane misfit dislocations; no cross-hatching was observed (Fig 5.4a), suggesting that one-dimensional MD formation was the single (or at least heavily predominant) relaxation mechanism. This was further corroborated by reciprocal space maps taken with the incident X-ray beam aligned along (projected m-axis) and orthogonal (projected c-axis) to the TD glide direction, showing a significant Q_x displacement due to a tilt boundary only in one of the two directions. An m-parallel ω-2θ scan of one of the four sectioned InGaN samples shows a cross section of the RSM in (d) along the Q_x origin.

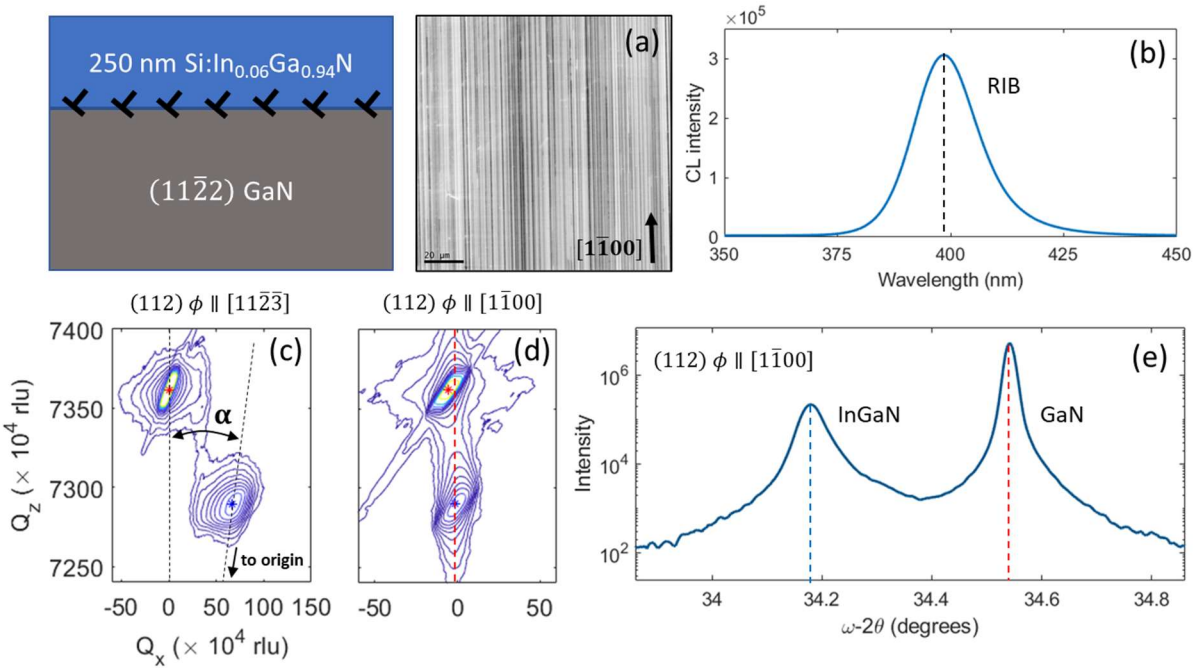

FIG 5.4. Characterization of the partially relaxed $In_{0.06}GaN$ epilayer grown on a free-standing (11$\bar{2}$2) GaN substrate. (a) Spatially resolved panchromatic cathodoluminescence from the RIB; parallel dark-line defects originate from the basal-plane MDs. (b) CL emission from the image in (a); substrate emission at 365 nm is likely suppressed due to re-absorption by the RIB. (c) On-axis c-parallel RSM, with substrate-layer (red-blue) tilt magnitude (α) denoted. (d) On-axis RSM with beam parallel to [1$\bar{1}$00], showing the InGaN layer fully coherent with the substrate in this direction. (e) High-resolution x-ray diffraction omega-2-theta scan down the Q_x origin of (d), showing a projection of the substrate and layer peaks.

Epilayer tilt and composition was determined with the method developed by Young *et al*., wherein a simple relation between basal-plane misfit dislocation spacing and epilayer tilt allows direct determination of composition and 1-D relaxation via a single c-parallel on-axis reciprocal space map [14]. Briefly, the plastic strain released by an ensemble of parallel basal-plane misfit dislocations with average spacing L is given by $\varepsilon_p = b/L$, where b is the magnitude of the MD Burgers vector. As mentioned previously, the perpendicular component, $b_\perp$, contributes to epilayer tilt; accordingly, the macroscopic epilayer tilt α supported by the formation of a low-angle misfit dislocation wall can be approximated as $L \approx b_\perp/\alpha$, which is a function of θ, the inclination angle from

the basal plane (~58° for $(11\bar{2}2)$). Finally, the plastic strain released can be represented as $\varepsilon_p = \alpha \cot\theta$. Epilayer tilt can be extracted from an on-axis reciprocal space map, with beam optics aligned perpendicular to the MD glide direction (see Fig. 5.3(c)). The angle subtended by the two lines connecting the substrate and layer peaks to the origin in reciprocal space is the exact magnitude of epilayer tilt.

To fully account for the transformations that the RIB may undergo throughout its entire processing history, it is important to precisely determine the epilayer composition and relaxation state prior to buffer patterning and regrowth. Composition was verified in two separate ways: x-ray diffraction and band-edge photoluminescence (PL). Once again, we turn to Young et al., who extend their analysis of semipolar epilayer heteroepitaxy to determining composition. By assuming that no relaxation mechanisms besides basal-plane slip are active at the time of epilayer growth, the total misfit strain in the epilayer is only a function of composition, minus the plastic strain relieved by the MD array leading to epilayer tilt. By relating the residual elastic strain to the peak splitting observed in the c-projected on-axis RSM we measured above, it is possible to arrive at a single, unique solution for indium molar fraction in the epilayer.

As introduce above, the misfit strain profile on semipolar layers is anisotropic, with ε_{m1} and ε_{m2} designating the projected m- and c-components. 1D relaxation acts to relieve the misfit strain in the projected c-direction, yielding a new resultant strain, $\varepsilon_{m2}^{*} = \varepsilon_{m2} - \varepsilon_p$. In parallel, the substrate-layer peak splitting can be considered with the differential form of Bragg's law:

$$\Delta\theta = \theta_L - \theta_S = -\frac{\Delta d}{d_S}\tan\theta_S \tag{5.4}$$

where θ_S and θ_L are the substrate and epilayer Bragg angles, and the corresponding d-values are interplanar spacings. By rearranging Eq. 5.4 and modifying the experimentally obtained interplanar spacing to account for the composition-dependent normal component of the strain tensor, ε_{zz}, (i.e., transforming $d_L \rightarrow d_L(1+\varepsilon_{zz})$), we obtain:

$$-d_S(\theta_L - \theta_S)\cot\theta_S = d_L(1+\varepsilon_{zz}) - d_S \tag{5.5}$$

ε_{zz} depends on the misfit strains ε_{m1} and ε^*_{m2}, which in turn change with InGaN alloy composition. This system is fully specified; with the measured epilayer tilt specifying one variable, the only remaining unknown becomes the alloy composition, which is then obtained by implicitly solving Eq. 5.5. The four RIB sections were all independently measured with high-resolution c-parallel on-axis RSMs; the resulting epilayer tilt, layer composition, and degree of relaxation (given by $\varepsilon_p/\varepsilon_{m2}$) calculated with the method described above are shown in Table 5.1 below. The average indium mole fraction of the epilayers was approximately 0.061. There appeared to be a slight gradient in both composition and relaxation with increasing sample number (left to right across the full substrate), very plausibly due to the slight radial non-uniformity across the growth surface.

Sample	$2\theta_{GaN}$	$2\theta_{InGaN}$	Tilt α (^{o})	In%	% 1D-relaxation
1	69.1015	68.3455	0.4854	6.13	82.21%
2	69.0968	68.3243	0.5329	6.35	87.15%
3	69.0955	68.3515	0.5205	6.13	88.10%
4	69.113	68.39	0.4924	5.93	86.20%

TABLE 5.1. Bragg angles for the GaN substrate and InGaN epilayer, extracted tilt magnitudes, and calculated composition and relaxation values for each of the RIB sample sections.

Epilayer alloy composition was further confirmed by correlating band-edge photoluminescence to Vegard's Law. InGaN layers were resonantly pumped at five locations on each sample section (corners and center) with a continuous-wave 375 nm diode laser (MKS Spectra-Physics Excelsior) in order to avoid absorption by the GaN substrate. Emission was collected with an OceanOptics USB2000 spectrometer. Figure 5.5 below shows the PL centroid distributions for each sample (s1-s4); the centroids appear to be rather tightly distributed and significantly different between samples, with standard deviations less than or equal to 1 nm for all samples. Most strikingly, the XRD and PL emission data correlated extremely well (Table 5.2); to verify this, Vegard's law was used to predict PL emission wavelengths for relaxed InGaN bulk layers from XRD-derived composition values, with energy gaps and bowing parameter obtained from the work of Orsal *et al* [24]. Conversely, bandgap energies were estimated from PL centroid wavelengths, which were used to calculate alloy mole fractions. For the ternary InGaN alloy system with molar In fraction x_{In} and band-gap energies E_i, Vegard's law gives:

$$E_{InGaN} = x_{In}E_{InN} + (1 - x_{In})E_{GaN} - bx_{In}(1 - x_{In}) \tag{5.6}$$

where b is the bowing parameter, which empirically accounts for nonlinear deviations in bandgap with alloy fraction.

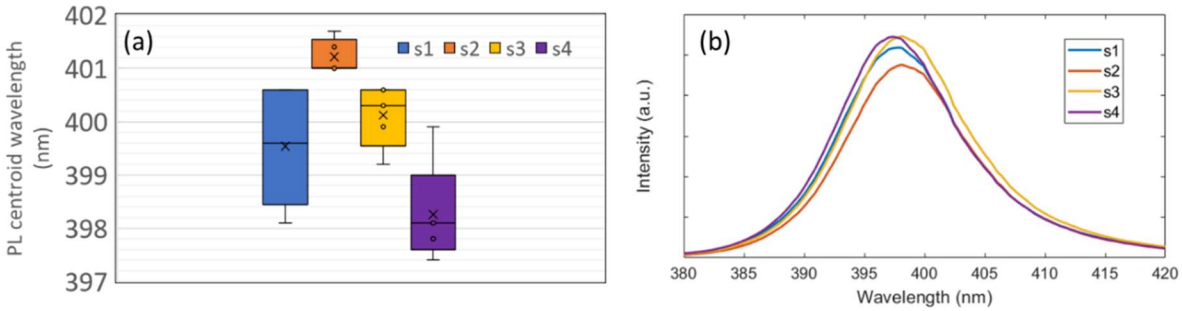

FIG 5.5. (a) Box-and-whisker plot showing distributions of planar RIB photoluminescence (PL) centroid wavelengths; samples (s1-s4) were pumped with a CW 375 nm laser at five locations. (b) Location-averaged PL spectra for each RIB sample at band-edge emission wavelengths.

Sample	In% (XRD)	$\frac{\varepsilon_p}{\varepsilon_{m2}}$	In% from λ_{PL} (factoring in exp. 1D relaxation)	E_g/λ_{PL} from XRD (fully relaxed layer)	Mean PL centroid (nm)
1	6.13	82.21%	6.34%	3.10 eV / 399.7 nm	399.5 ± 1.1
2	6.35	87.15%	6.58%	3.09 / 401.0	401.2 ± 0.3
3	6.13	88.10%	6.38%	3.10 / 399.7	400.12 ± 0.6
4	5.93	86.20%	6.08%	3.10 / 398.4	398.26 ± 0.96

TABLE 5.2. Corroborated XRD and PL measurements for InGaN composition determination. Both sets of measurements were cross-referenced by using Vegard's law parameters to predict band energies for XRD-derived compositions and predict compositions from PL-derived bandgap energies, assuming partial relaxation as per XRD measurements. Excellent agreement was found.

5.2.3 Realizing micro- & nanopatterned InGaN buffers

Having fully and reproducibly verified the composition and strain state of the RIBs under study, we are well prepared to track the evolution of this initial crystallographic state with subsequent processing. As introduced theoretically in Section 5.2.1, patterning stripes at an aspect ratio of close to unity is expected to relieve a significant portion of strain in the direction orthogonal to the stripes. Although this would require rigorous verification, it can be entertained that a Cartesian-to-cylindrical coordinate transformation of the shear stress analysis above would yield comparable results for

biaxial strain relaxation in cylinders of diameter *w*. Considering the point at which relaxation tapers in Fig. 5.3, $\frac{h}{w} \in \{0.25, 0.5\}$ would make for instructive aspect ratios to experimentally evaluate; for a RIB 250 nm in nominal thickness, this corresponds to cylinder diameters of 500 and 1000 nm. Both feature dimensions are in the proverbial "wheelhouse" of colloidal lithography, which we identified as a suitable and simple method for our suite of spectroscopic measurements. Furthermore, silica exhibits a reasonable etch selectivity to nitrides in chlorine plasma (~5:1), allowing the nanosphere itself to be viably used as an etch mask. Having patterned the buffers, we may proceed to re-growth on the top face of these etched structures and re-apply the characterization suite featured in Fig. 5.4. Figure 5.6 below shows a simplified, idealized schematic of the fabrication process.

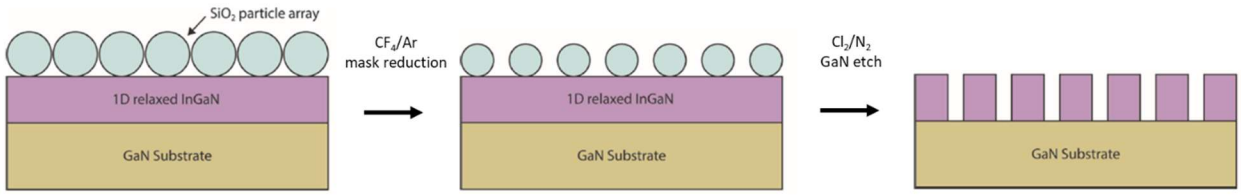

FIG 5.6. Idealized process flow for fabricating patterned InGaN buffer features with colloid deposition, followed by plasma-based mask reduction and pattern transfer. Adapted from [23].

Aside from the set of patterned RIB samples, it is instructive to introduce a set of reference samples to deconvolve the many effects of topography on subsequent buffer performance metrics, once emitting layers are deposited on top of it. As such, all patterned RIBs were accompanied with an analogously processed GaN substrate, with nearly identical etch geometry to the InGaN buffers. A summary of samples thar were processed, along with pattern sizes, is featured below in Table 5.3.

Sample	**Material**	**Pillar size/original mask diameter (nm)**	**Re-grown material (co-loaded)**
1	RIB	Planar reference	3 multi-quantum wells (MQWs, nominally 3/14 nm well/barrier thickness) with thin GaN buffer and cap (total: ~110 nm)
2		1000/1800	
3		500/690	
4	GaN	Planar reference	
5		1000/1800	
6		500/690	

TABLE 5.3. Summary of all samples involved in the RIB study.

Micro- and nanopillars were fabricated as follows: three RIB samples and three free-standing GaN substrate sections were cleaned by submerging them sequentially in each of acetone, isopropanol, and DI water for three minutes under high-intensity ultrasonication, and then dried with N_2 gas. 15 nm of Al_2O_3 was deposited on the nitride surface at 300°C via atomic layer deposition (FlexAL, Oxford Instruments) to protect the surface from subsequent processing steps. A 200-nm amorphous SiO_2 hard mask was then deposited via PECVD (PlasmaTherm 790), with two sequential depositions of 100 nm separated by a 30-second DI water dip to interrupt the formation and propagation of random pinhole defects. Deposited Al_2O_3 and SiO_2 thickness was measured on a silicon witness sample with ellipsometry (J. A. Woollam M2000-DI); thickness was extracted from the data by fitting with a model assuming a Cauchy-dispersive layer on silicon (CompleteEASE software). A thin photoresist (PR) layer (THMR-IP3600 HP) was spin-coated and baked at 90°C for 90 seconds, to serve as an etch mask and protection layer for the underlying SiO_2 hard mask layer. The PR was treated with 5 minutes of UV/O_3 (M-144AX, Jelight Company Inc.), rendering it hydrophilic in preparation for LB dip-coating.

Close-packed colloid monolayers (d = 690 nm and 1800 nm) were deposited on a total of four of the six samples (Table 5.3) via LB deposition (see Ch. 2 for details). To define the diameter of the eventual pillar structures, colloids were reduced in size to d =

475 and 1100 nm with CF_4/Ar plasma (40/10 sccm) in an isotropic ICP (Panasonic E640) at 30 mTorr, 900/0 W forward/bias power (avg etch rate: ~20 nm/min, increases with etch time); several cycles of SEM imaging and etching were necessary to arrive at the final diameter. Subsequently, the resulting mask pattern was transferred into the PR via O_2 plasma (40 sccm) at 4 mTorr, 75/75 W forward/bias power (etch rate ~80 nm/min). The PR pillars were used as an etch mask for the underlying conformal SiO_2 hard-mask; samples were subjected to an anisotropic, capacitively coupled reactive ion etch containing a $CHF_3/CF_4/O_2$ gas mixture (5/15/2 sccm) at 4 mTorr and 350 V bias voltage (E-51 RIE system, Materials Research Corp., etch rate: ~15 nm/min). PR and any remaining particle residue were removed by ultrasonicating in n-methyl pyrrolidone (NMP) at 80°C for 10 minutes. The result was an array of roughly cylindrical SiO_2 pillars on a pristine nitride surface. Finally, the SiO_2 pillars served as an etch mask for a Cl_2/N_2 (12.5/7.5 sccm) vertical ICP etch at 500/200 W forward/bias power and 9 mTorr (Panasonic E640) to transfer the circular pattern down, leaving an array of cylindrical nitride posts with tapered sidewalls. Care was taken to etch through the entirety of the InGaN layer, which established a free boundary along the entire RIB and fully removed the InGaN/GaN heterointerface. SiO_2 and Al_2O_3 residue was removed with a 5-minute 25% aqueous HF acid treatment. A process schematic and accompanying set of SEMs are shown in Fig. 5.7.

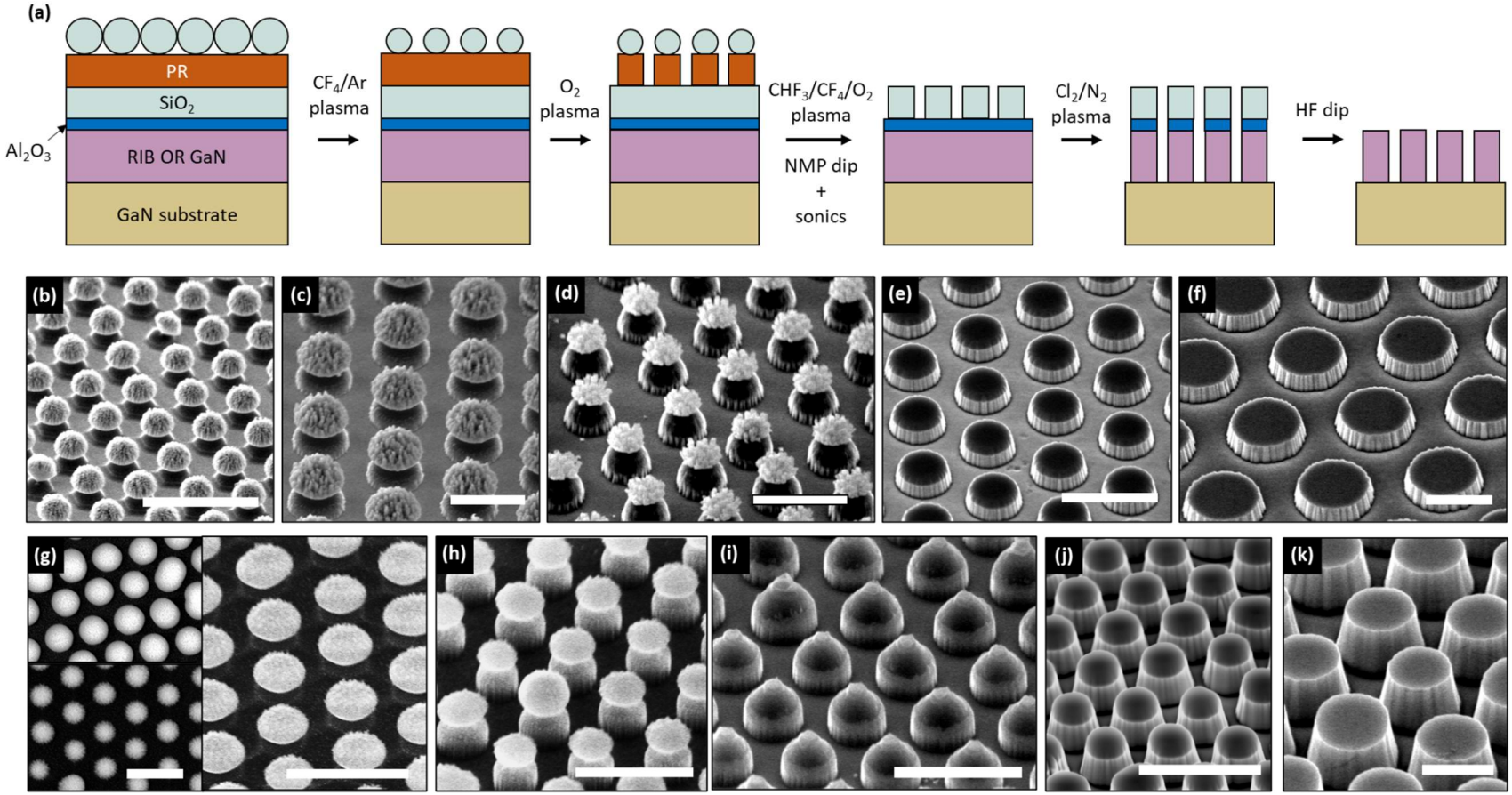

FIG 5.7. (a) Schematic and (b-k) bird's eye view electron micrographs of micro- and nanopatterned RIB processing. SEM images show the results of each of the latter five processing steps in (a) for (b-f) micron-scale and (g-k) sub-micron features. The insets in (g) show a plan view of varying extents of particle mask size reduction. Scale bars are (b) 5 μm, (c-e) 2 μm, (f-j) 1 μm, and (k) 500 nm, respectively.

Patterned RIB samples were characterized with PL, CL, and reciprocal space mapping to assess changes in buffer material emission and strain state. Figure 5.8 shows the results of PL measurements performed on the patterned and planar samples (SpectraPhysics, CW 375 nm laser diode pumping). A very slight blueshift (401 → ~399 nm) is observed in the nanopillar RIB emission peak, which may suggest a reduction of the piezoelectric polarization field within the bulk InGaN layer [1]. The increased PL intensity with reduced feature size is attributed to enhanced light extraction. CL imaging confirmed the PL emission trend and is shown below in Fig. 5.9(a); the blueshift observed here was greater in magnitude (399 → 397 → 393 nm). As 365-nm peak appears after patterning, attributed to the now-exposed GaN substrate which can be observed in panel (b). While blueshifts can also arise from carrier-induced band saturation and subsequent electric field screening at the high carrier densities achieved by a focused electron beam spot, all samples experienced the same beam conditions (5 kV, 1.6 nA injection), making this contribution unlikely.

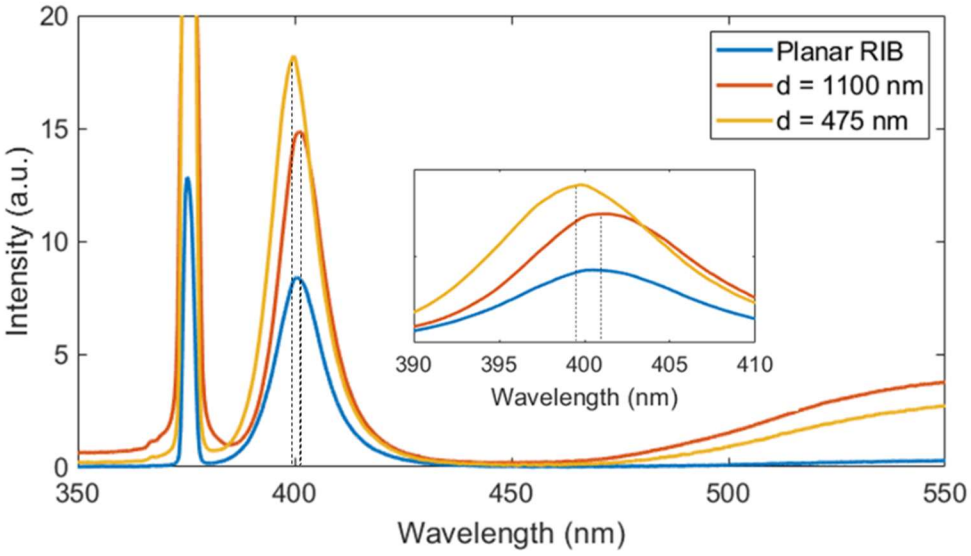

FIG 5.8. Photoluminescence (PL) of patterned relaxed InGaN buffers. The inset zooms in on RIB emission near 400 nm, showing the nanopillar blueshift relative to micropillar and planar samples.

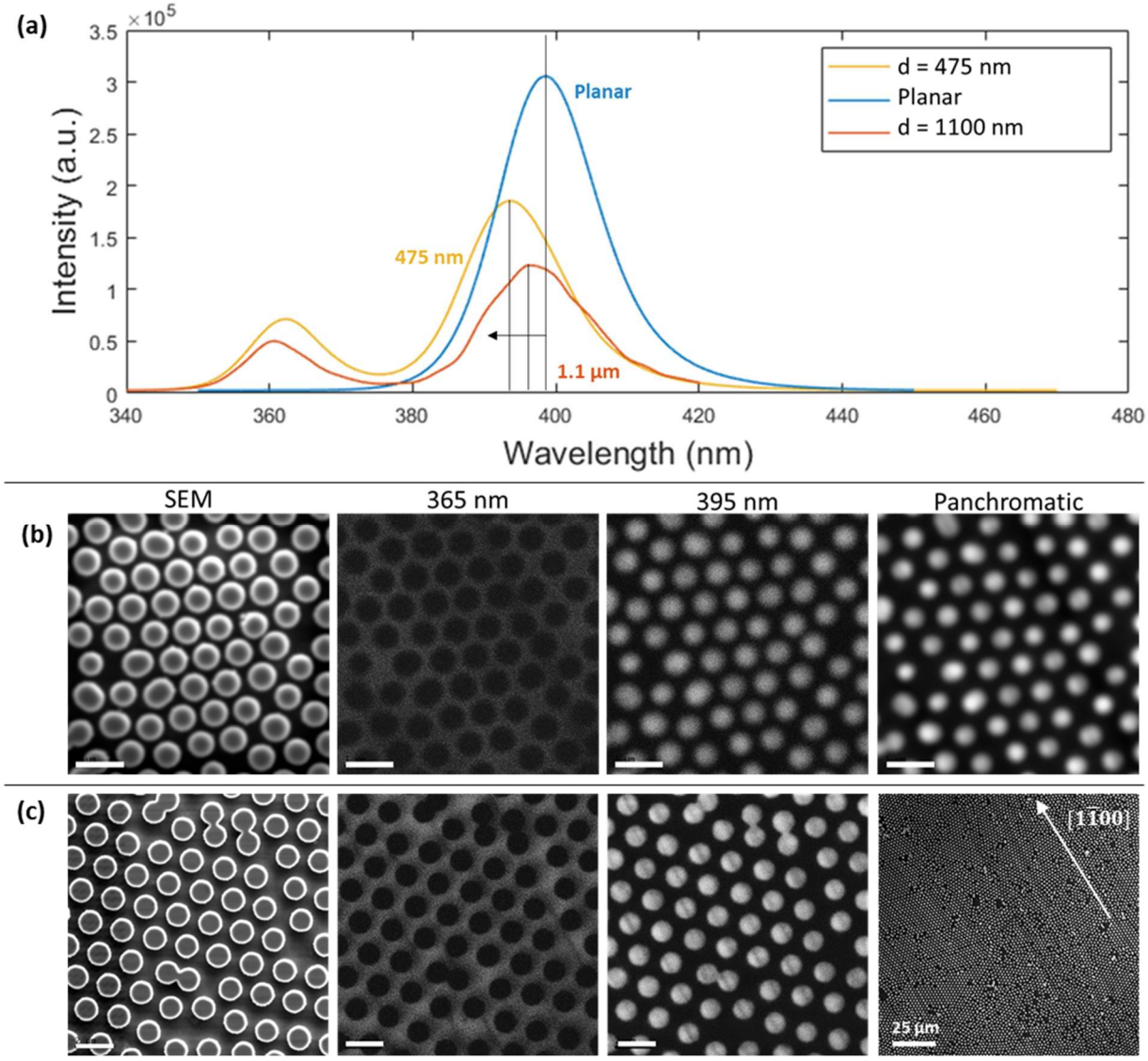

FIG 5.9. Cathodoluminescence (CL) characterization of (b) 1.1-micron and (b) 475-nm patterned RIB pillars. CL spectra are shown in (a), plotted against the planar RIB emission spectrum as reference. A monotonic emission blueshift is observed with reduced feature size. Plan-view scanning electron micrographs, monochromatic CL micrographs for λ = 365 nm (GaN substrate) and 395 nm ($In_{0.06}GaN$ buffer), and panchromatic CL micrographs are shown for each sample. The basal-plane misfit dislocation propagation vector, [1$\bar{1}$00], is highlighted in the panchromatic image in (c). Scale bars are 1 µm in (b), and 2 µm in (c) unless otherwise noted.

Plan-view SEMs in panels (b) and (c) show pillars arranged in a quasi-ordered hexagonal configuration and helped identify the sources of emission in the CL spectrum. Monochromatic CL imaging at 365 nm and 395 nm confirmed the two emission peaks in Fig. 5.8(a) to be the GaN substrate and RIB layer, respectively. The RIB pillars absorbed the GaN substrate emission at 365 nm, creating a silhouette that was expectedly filled by the RIB emission profile at 395 nm. Some pillars contained dark-line defect fragments, which are the remnants of the basal-plane misfit dislocations generated at the substrate/layer interface during epilayer growth. Although present in both patterned samples (discernible in the panchromatic image in (b)), they are particularly visible in the micron-sized pillars at all magnifications, as evidenced by the panchromatic CL image in panel (c). No further defect formation or rearrangement was expected; clearing the energetic barriers required to initiate plastic relaxation and defect propagation requires MOCVD-like temperatures (>600°C), which were not approached at any point in cleanroom processing.

While CL provided a promising trend in emission wavelength with feature size, X-ray diffraction, in particular reciprocal space mapping, more quantifiably revealed the change in RIB strain state. The epilayer peak shape and its separation from the substrate significantly changed after patterning; RSMs of the (112) on-axis symmetric reflection along the projected m- and c-axes, as well as the (213) m-parallel asymmetric reflection, are shown before and after patterning for both pillar sizes in Fig. 5.10. As found earlier in this section, a significant portion (80-90%) of the c-projected (parallel to $[11\bar{2}3]$) misfit strain was relaxed via basal-plane MDs, meaning no significant change (i.e., less than 10% additional relaxation) is expected in that direction. This was indeed the case; the $[11\bar{2}\bar{3}]$-aligned scan showed a slight decrease in peak separation, but the peak topography was mostly unchanged.

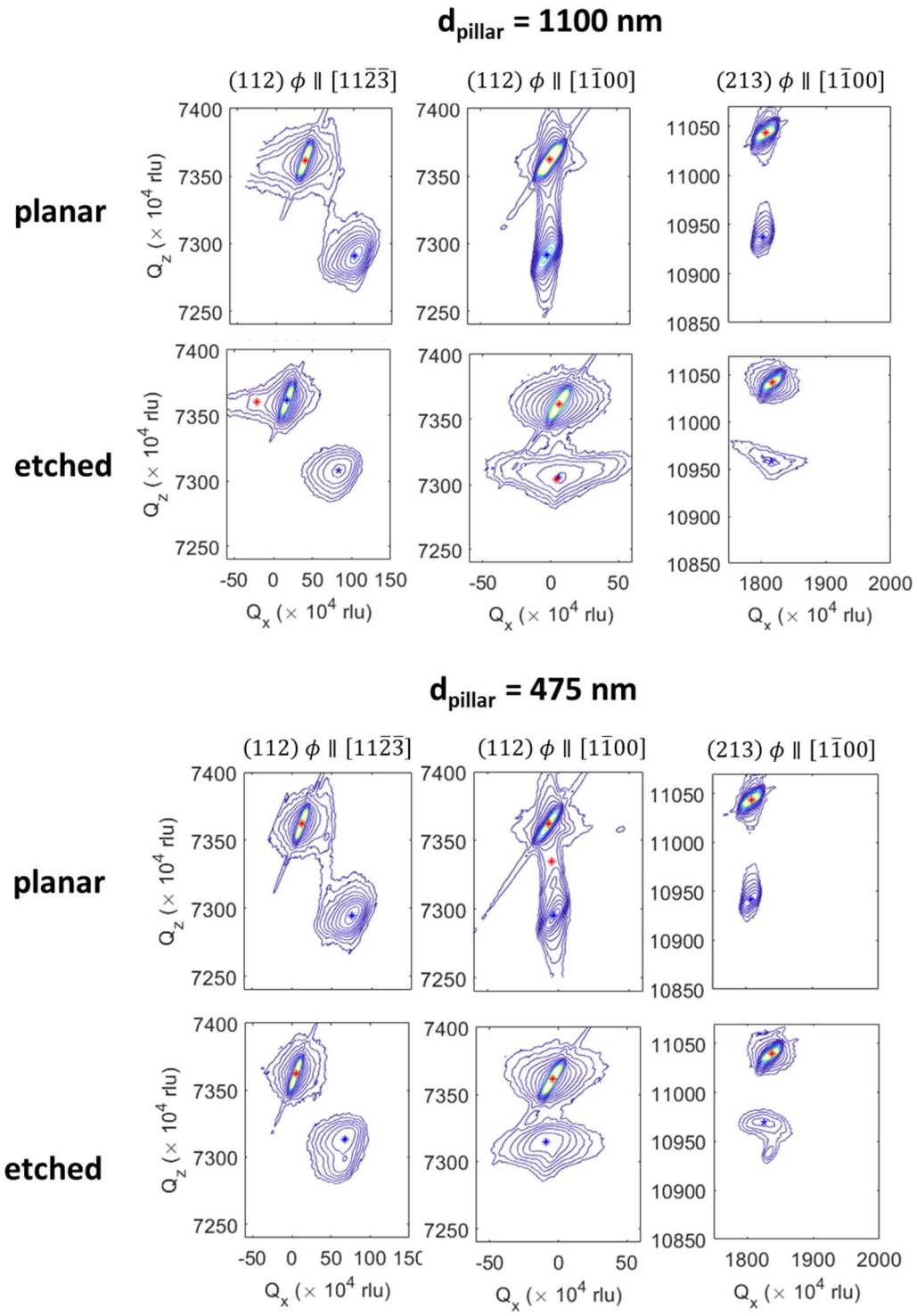

FIG 5.10. On-axis a/symmetric reciprocal space maps of patterned RIBs with feature diameters d ~ 475 and 1100 nm, pre- and post-processing. Secondary small peaks in the nanopillar RSMs originate from the planar, un-patterned area at the edges of the nanopillar sample. Long, diffuse streaks in the GaN substrate peak arise from monochromator divergence along the 2Θ scan axis.

The m-parallel on- and off-axis reflections change much more dramatically with patterning. Significant peak broadening is observed in the ω scan axis for the 1100 nm RIB, indicating limited lateral correlation lengths, often through mosaic spread [25]; however, given the single-crystal nature of the sample, this may instead correspond to a broad distribution of strain-induced lattice states radially from the center of the InGaN pillar along this direction. The d-spacing (Q_z) distribution appeared to be relatively unchanged, while the overall peak splitting was greatly reduced after patterning. The 475-nm RIB sample showed a similarly distributed, but sharper set of InGaN peaks; substrate-layer peak splitting was even more reduced than the micropillar sample. Secondary, smaller peaks that appear to have a higher peak splitting in fact originate from a planar, unpatterned edge area on the nanopillar sample. Interplanar spacing differences for the full suite of accessed reflections are tabulated in Table 5.4. A monotonic decrease in all peak splitting magnitudes was observed with decreasing diameter.

Reflection (sample phi-orientation)	Δd_{planar}	$\Delta d_{1100\ nm}$	$\Delta d_{475\ nm}$
112 (c)	0.01360	0.01060	0.008727
112 (m)	0.01355	0.01009	0.009101
114 (c)	0.01374	0.01111	0.010228
202 (m)	0.00924	0.00679	0.005813
213 (m)	0.01341	0.01145	0.007532

TABLE 5.4. Set of all samples in the RIB study.

While this is the subject of current work, several approaches can be taken to determine the exact RIB lattice constants. If we assume total c-projected strain relaxation, the relations from Young et al. can be modified to yield an m-projected degree of relaxation exclusively through on-axis layer peak shifts. Alternatively, direct interrogation of the in-

plane lattice constant is possible with off-axis, asymmetric reflections, and/or specialized sample mounting for access to nominally inaccessible reflections that yield lattice constants directly through Bragg's law.

5.2.4 Quantum-well re-growth on patterned, relaxed InGaN buffers

The previous section showed that dramatic, non-destructive biaxial relaxation was achievable in relatively thick, moderately indium-rich InGaN buffers through a unique combination of built-in plastic relaxation during epitaxial growth and patterning at micro- and nanometer length scales. Having confirmed these relaxation trends with multiple spectroscopic techniques, we deposit emitting layers on top of these buffers to assess their efficacy in managing strain and non-destructively increasing indium uptake.

Discerning the effects of strain on active regions is challenging on planar samples, not to mention on micro- and nanoscale topography. Indium-rich ($x_{In} > 0.2$) quantum well emission wavelengths are particularly sensitive to indium mole fraction and thickness; when strain-induced piezoelectric fields are introduced, it becomes difficult to deconvolve various contributions. Moreover, micro- and nanopatterning introduces several additional considerations that should be carefully taken into account; in order of decreasing dynamic wavelength range, they are as follows: (1) faceting and subsequent emission from a variety of emerging, stable crystallographic planes with differing growth rates, QW thicknesses, and indium uptake (>100 nm spread); (2) substantially increasing surface area per nominal substrate area with decreasing feature size, reducing the growth rate and corresponding QW thickness (leading to considerable emission blueshift, up to 40 nm/nm); (3) increased indium incorporation, owing to varying extents of relaxation and resulting lattice constants,

undoubtedly red-shifting emission; and (4) greater strain relaxation reducing active-region piezoelectric fields, which blue-shifts emission. Evidently, a tug-of-war of epic proportions can arise between these competing effects.

To manage and distinguish between the contributions of each effect detailed above, growth substrates should have minimal variation in growth rate and minimal crystal faceting. Identical surface area with varying feature size would demand selective and exclusive masking of the etched sidewalls, which is difficult with a self-aligned process; however, a reasonably vertical etch profile will help parse growth rate reduction using the simple geometry of a field of cylinders (to be explored later in this section). Limiting faceting is difficult; finding the growth conditions (e.g., pressure, temperature, III/V precursor ratio) that preferentially conserve the top semipolar growth facet is nontrivial, if impossible; a more pragmatic way to limit the effect of faceting is to minimize the total thickness of the re-grown active region while ensuring sufficient signal for further spectroscopic studies. Thus, three regrown quantum wells (~3/14 nm nominal well/barrier thickness) were chosen for a proper thickness-signal tradeoff; factoring in a small amount of GaN spacer material under the QWs and a protecting GaN cap on top, total deposited thickness comes out to no more than ~110 nm (on a nominally flat surface).

Quantum well regrowth was performed by co-loading all GaN reference and RIB samples into one growth run to eliminate run-to-run reproducibility as a confounding factor. The following layers were grown via MOCVD (growth ID: 210325ER): 30 nm of high-temperature GaN (TMGa, 1000°C), another 20 nm of GaN at QW conditions (TEGa, 795°C), 3 periods of InGaN QWs/GaN barriers (~3/12 nm wells/barriers, 785°C), and 10 nm of capping GaN material (TEGa, 862°C). Samples were corralled with c-plane GaN grown on

sapphire and were arranged approximately a half-radius away from the center of the susceptor to minimize the effect of radial growth rate nonuniformity. The approximate x_{In} of the quantum wells was estimated to be 0.2-0.25 with XRD calibrations. Using GaN corrals (vs. the usual plain sapphire) also serves a built-in gauge for these non-uniformities and introduces another back-up to help characterize the emission of deposited material.

Samples were characterized with a suite of microscopic and spectroscopic measurements to extract layer morphologies, compositions, thicknesses, and emission properties. SEM imaging surveyed the microscopic regrowth morphology, and patterned sample micrographs are shown below in Figure 5.11(a). Multiple crystal facets asymmetrically protrude beyond the originally defined cylinders, especially on the smaller pillars. The top $(11\bar{2}2)$ plane area is reduced and partially replaced by prominent wings on two sides, which are presumably a family of m-plane nonpolar facets. Moreover, easily discernible V-pit defects are present on one facet, which can be unequivocally assigned as the (0001) basal plane. Surprisingly, the c-plane facet appears to be larger on the RIB pillars, while V-pit density seems lower; it is unclear whether the buffer's reduced lattice mismatch helps template higher-quality c-plane material, but this is a positive unintended result.

Cathodoluminescence was conducted after re-growth to probe RIB-templated emission. The resulting images are shown in Fig. 5.11(b), with the planar sample being the most visibly defective by far. Line and point nonradiative defects taint the landscape; the line defects are the misfit dislocations (MDs) introduced earlier. Given their prominence in the 400-nm monochromatic image (RIB layer emission), all MDs likely reside at the substrate-buffer interface. Lighter, vertical lines are the previously formed basal-plane misfits, while the darker lines that intersect them are non-basal plan (NBP) MDs. Evidently, the deposition

of emitting material atop the planar buffer introduced enough additional strain to activate a secondary, prismatic slip system across the sample, as evidenced by the high prevalence of NBP MDs across a large portion of the sample, as seen in the low-magnification panchromatic image. As mentioned previously, intersecting MDs form TDs, which are accordingly present in both pan- and mono-CL, and in the locations where the MDs intersect. In summary, by growing emitting layers on top of a thick, partially relaxed planar buffer, we have failed to avoid undesirable slip; this is fully consistent with observations in prior work [17,18].

In stark contrast to the planar buffer, both patterned samples were surprisingly devoid of defects. BP-MD fragments identified in the pre-growth RIB micropillars were still visible in both pan- and mono-CL, but they appeared to be much less prominent. Furthermore, they seemed to be almost completely undetectable in the nanopillar case, with only faint traces of the MDs observed in the low-magnification pan-CL images. The mono-CL at MQW emission is extremely uniform, and the basal-plane MDs do not appear to play any role, as they are pinned to the lower substrate-epilayer interface. Finally, it appears that the absolute basal-plane MD line density at the substrate/layer interface was reduced relative to the pre-growth MD count. This is remarkable and, to this author's knowledge, has not been observed in prior work. Nonetheless, careful TEM analysis is required to make any concrete claims about changes in MD distribution and density. For now, we shift the focus of our discussion to the spatially resolved mono-CL profile to assign emission contributions from various emerging facets.

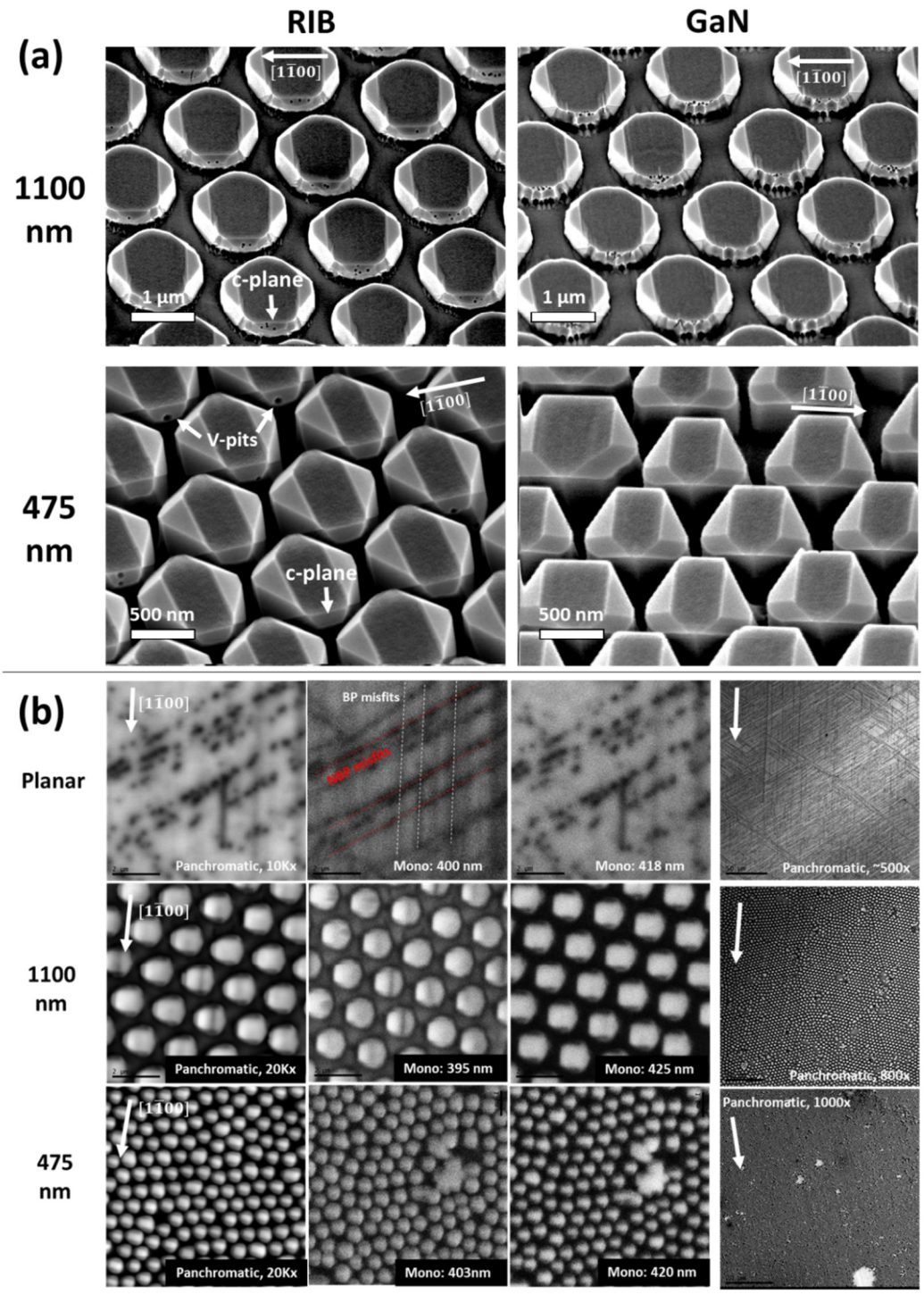

FIG 5.11. (a) SEM images of multi-quantum wells (MQWs) re-grown on patterned relaxed InGaN buffers (RIBs) and GaN pillars. The basal-plane misfit dislocation (MD) propagation vector, [1$\bar{1}$00], is highlighted in each image. The basal c-plane is highlighted, as well as the signature V-pit defects that form exclusively on it. (b) Pan- and mono-chromatic (RIB and MQW emission peak wavelengths) cathodoluminescence (CL) imaging of RIBs. Basal-plane (BP) and non-basal (NBP) MDs are labeled.

As previously mentioned, the effects caused by regrowth on a nonplanar surface are crystal faceting, as well as changes in QW thickness, indium content, and strain relaxation relative to a planar surface. The broadly distributed emission due to crystal faceting can be deconvolved by considering a finer wavelength sweep of spatially resolved mono-CL and assigning emission to discernible facets. Figure 5.12 shows mono-CL wavelength mapping (365-540 nm) and emission spectra (340-480 nm) of re-grown MQWs on RIB and GaN micropillars. The presence of a RIB layer is highlighted by the silhouette in the 365 nm image, which does not appear in the GaN pillar sample since the GaN substrate is present directly under the re-grown MQWs. After locating the top $(11\bar{2}2)$ face in SEM imaging in Fig. 5.11(a), top-area MQW emission peaks are 405/425 nm for GaN/RIB samples, respectively, which comprises a 20-nm redshift at the same nominal QW thickness (same feature size). Further, owing to the low symmetry of the $(11\bar{2}2)$ facet, the crescent-shaped areas emitting at long wavelengths are easily assigned to the previously identified basal c-plane. The mono-CL images for longer wavelengths appear more intense for the RIB sample than the GaN reference; 540-nm emission was detected in the RIBs (vs. 520 nm for GaN).

Comparing CL emission spectra within the RIB sample group (Fig. 5.13(a)) did not show a clear trend in emission wavelength, with micropillar-templated MQWs redshifted (423 nm) and nanopillars blue-shifted (415 nm) relative to the planar RIB case (419 nm). There may be several factors at play; in the previous section, we established a stark decrease in buffer strain with decreasing feature size, which, all else being equal, should red-shift the emission from increased MQW indium uptake and blue-shift the emission due to piezoelectric field reduction. However, a growth-rate reduction owing to increased sidewall surface area can reduce QW thickness and drastically impact emission.

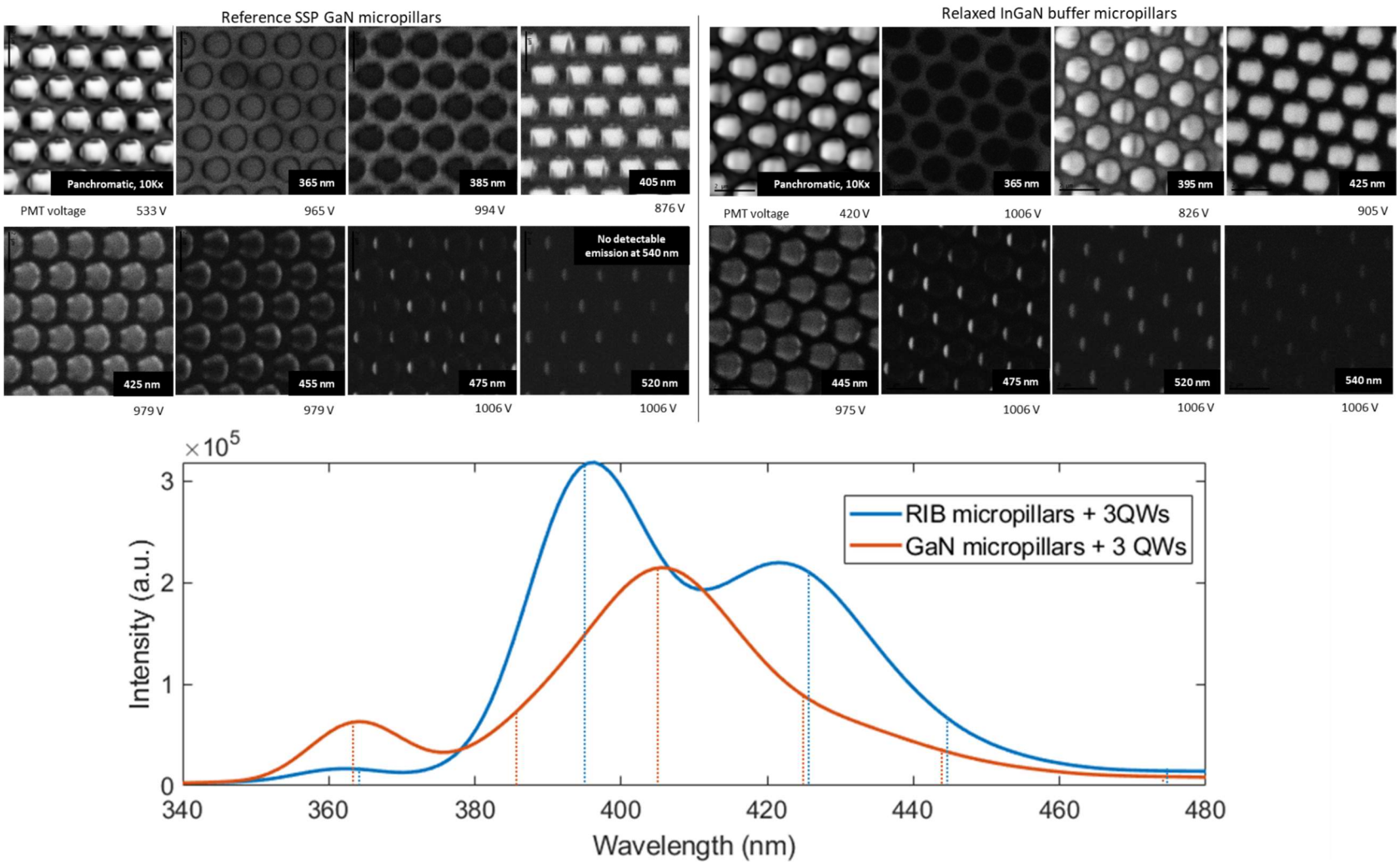

FIG. 5.12. Panchromatic and monochromatic cathodoluminescence (CL) characterization of GaN and RIB micropillars with a 3xMQW regrowth. CL spectra are plotted, with the mono-CL wavelengths demarcated with color-coded dashed lines. Photomultiplier tube (PMT) voltages featured below each image provide a rough guide for the necessary gain to detect sufficient light emission (lower PMT voltage → more intense material emission).

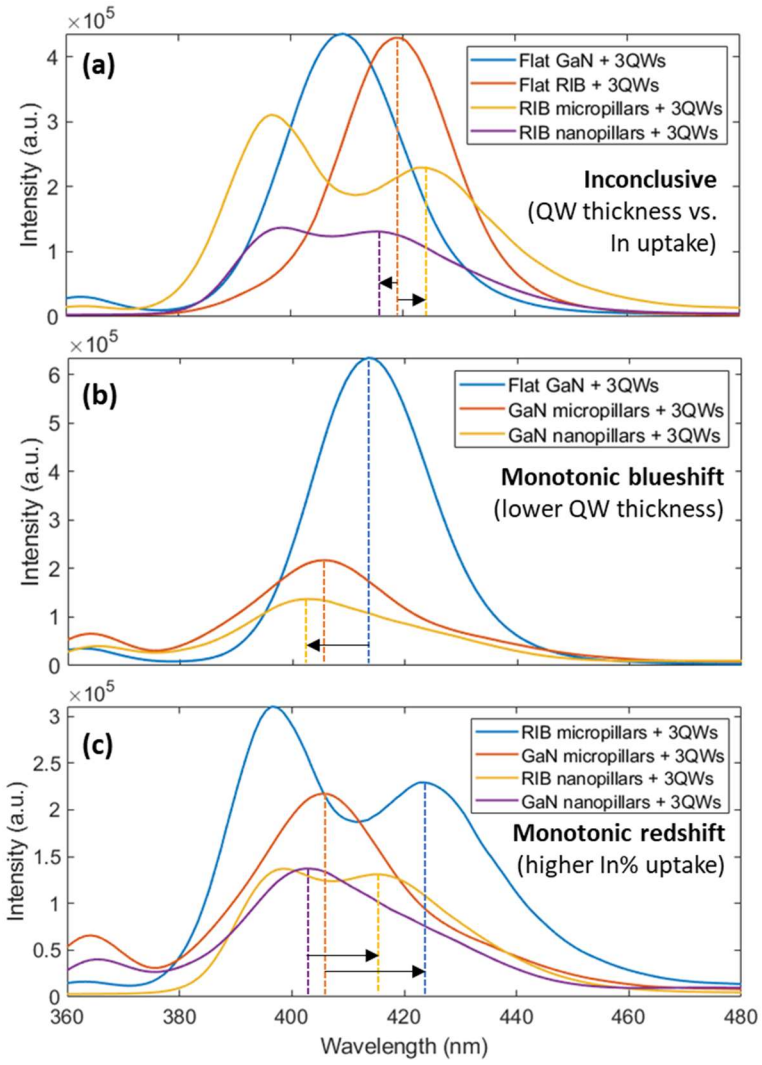

FIG 5.13. Cathodoluminescence (CL) spectra comparing various sample sub-groups to deconvolve the effects of QW thickness and In uptake on emission wavelength. (a) Comparison of MQW re-growths on flat GaN and all RIB samples, showing a reasonable redshift of planar RIB relative to GaN but inconclusive size-dependent trends. (b) Comparison of emission on all GaN samples, showing a blueshifted emission trend with smaller feature size, presumably due to QW thickness reduction. (c) Comparison of GaN and RIB pillars of different sizes, where a significant (> 10 nm), consistent redshift is observed in RIB vs. GaN samples of equal feature size.

Stepping back and comparing the planar re-growth cases (GaN and RIB), we observe a red-shift in the MQW emission, with comparable emission intensity from the RIB-templated sample despite significantly more NBP-MD/TD prevalence. This is sensible; assuming the QW thickness (i.e., growth rate) is comparable on the two planar surfaces, a

redshift can only suggest an elevated x_{In} in the RIB-templated MQW layer, which is our desired result (piezoelectric relaxation could only cause blueshift on this Ga-polar orientation). Unfortunately, the planar RIB template is not fully relaxed and has become defective, reducing its utility in devices. As mentioned and shown in prior work, AlGaN layers may help maintain a stable, metamorphic strain state that persists after active region growth, and can also act as carrier blocking layers to suppress nonradiative recombination (usually at the expense of voltage) [17,21]; however, this is difficult to achieve and optimize.

To isolate the effect of growth rate on emission wavelength, it is instructive to consider systems where the MQW strain state is consistent with different feature sizes. This can be straightforwardly probed by considering the full GaN sample set; the thin re-grown layers should be pseudomorphic to the free-standing GaN substrate surface, which in turn should be completely relaxed, and therefore unchanged by patterning. Fig. 5.13 (b) shows the CL emission of the GaN samples; as expected, the only two emission peaks present are the GaN substrate and MQW emission, and a monotonic blueshift in the MQW emission is observed with reduced pillar diameter. While probing the active region more directly to confirm QW thickness would help bolster our argument, this lends further credibility to a growth-rate decrease. Patterned GaN and RIB samples are shown in Fig. 5.13(c) to assess the role of the buffer with equal feature sizes; we see a consistent red-shift trend building on our CL-mapping observations in Fig. 5.12. Combining the above observations, we conclude that the RIBs successfully incorporated higher x_{In} *despite* thinner quantum wells, which detract from the redshift we would otherwise see on the smaller, more relaxed pillars.

Previously, we discussed our tradeoff of regrowth thickness and spectroscopic signal. Three QW periods form a repeating bilayer structure with two compositionally distinct

materials (also known as a superlattice); if the signal-to-noise ratio permits, we can resolve the fine structure of the resulting interference between each layer's Bragg diffraction. The separation of interference fringes thus formed can be converted into a real-space length, which is the sum of the QW and barrier thickness. Combining this with growth rate calibrations and the ratio of growth time for QWs and barriers, a reasonable estimate for QW thickness can be obtained. If successful, this yields unequivocal evidence of thinner quantum wells, and can be leveraged as indirect proof of increased indium uptake in RIB-templated emitters. Accordingly, coupled, symmetric ω-2Θ triple-axis scans along the m-projected crystal direction of our re-grown GaN reference samples were analyzed (GaN references were chosen to avoid fringe convolution from RIB layers). Figure 5.14 shows the planar GaN reference ω-2Θ scan, with discernible fringes labeled.

The characteristic spacing d_{SL} of a superlattice displaying n fringes in a coupled ω-2Θ scan, with initial and final fringe locations ω_i and ω_f, and X-ray wavelength λ, is given by:

$$d_{SL} = \frac{\lambda n}{2 \cdot \left(\sin \omega_f - \sin \omega_i\right)} \tag{5.7}$$

MQW periods were extracted from the three GaN samples; the RIB sample scans were less intense and more difficult to resolve; nonetheless, all six MQW sample spacings are given in Table 5.5. Simulations in X'Pert Epitaxy software were conducted thereafter to corroborate all experimentally measured scans. Nominal/expected QW and barrier thicknesses from growth rate calibrations were used to initialize thicknesses, and thickness parameters were varied slightly to arrive at a reasonable fit.

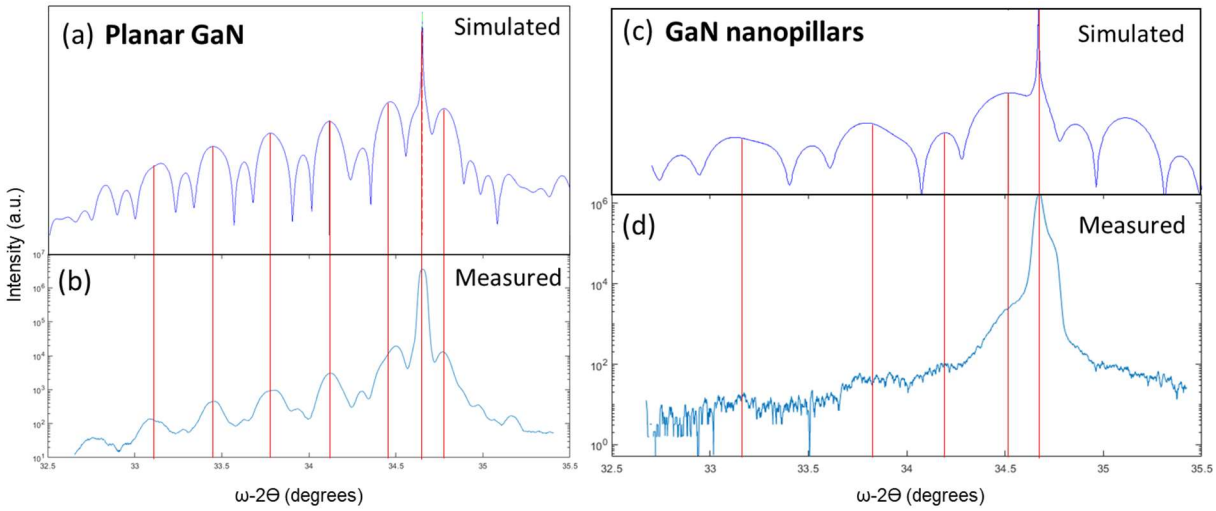

FIG 5.14. (a,c) Simulated and (b,d) measured triple-axis, symmetric, coupled ω-2θ scans for (a,b) planar and (c,d) nanopatterned GaN samples, with superlattice fringes labeled. Simulated QW/barrier thicknesses were (a) 4/11.7 nm and (c) 2/6 nm, respectively.

Feature size		RIB	GaN reference
Planar	$\Delta\omega_{avg}$ (deg)	0.3344 +/- 0.0094	0.3462 +/- 0.0087
	Period (nm)	15.77	15.29
Micropillars (d ~ 1100 nm)	$\Delta\omega_{avg}$	0.5248 +/- 0.046	0.5630 +/- 0.057
	Period	10.06	9.39
Nanopillars (d ~ 475 nm)	$\Delta\omega_{avg}$	0.6560 +/- 0.126	0.6376 +/- 0.050
	Period	8.08	8.33

TABLE 5.5. Measured average fringe spacings and corresponding extracted MQW periods from symmetric, coupled ω-2Θ scans.

The agreement between RIB and GaN MQW periods, as well as the results already shown prior, rather conclusively show that the quantum well period in patterned samples is significantly reduced; this makes a significant emission red-shift on the micropillar RIB sample even more impressive. Finally, in an attempt to get a sense of the topographic geometry and its effect on growth rate reduction, we consider a simplified system: pillars arranged on a flat GaN surface, in a perfect hexagonal lattice with average pillar spacing *a* (colloid size), diameter *d* (extent of mask reduction etching), and height *h* (vertical etch depth), as schematically represented in Fig. 5.15. Taking a basis of two hexagonal unit cells, we calculate the surface area increase as a function of the above described geometry. In

brief, the rectangular area spanned by a two-cell hexagonal basis is $a^2\sqrt{3}$, and the additional surface area generated by pillar sidewalls is $2\pi dh$. Summing these and normalizing by $a^2\sqrt{3}$, we obtain the patterned surface area, which is given by:

$$\frac{SA_{patterned}}{SA_{planar}} = 1 + \frac{2\pi dh}{a^2\sqrt{3}} \tag{5.8}$$

After careful SEM imaging of pre-growth patterned substrates, approximate geometries, calculated surface area enhancements, and corresponding calculated and measured MQW period reductions are shown in Table 5.6. Quite reasonable agreement (especially for micropillars) is found for both feature sizes, despite the highly idealized geometry assumed herein. Over-estimations of growth rate reduction can be attributed to the unaccounted-for decrease in sidewall and entrenched surface area as the conformal growth proceeds, which gradually planarizes the surface.

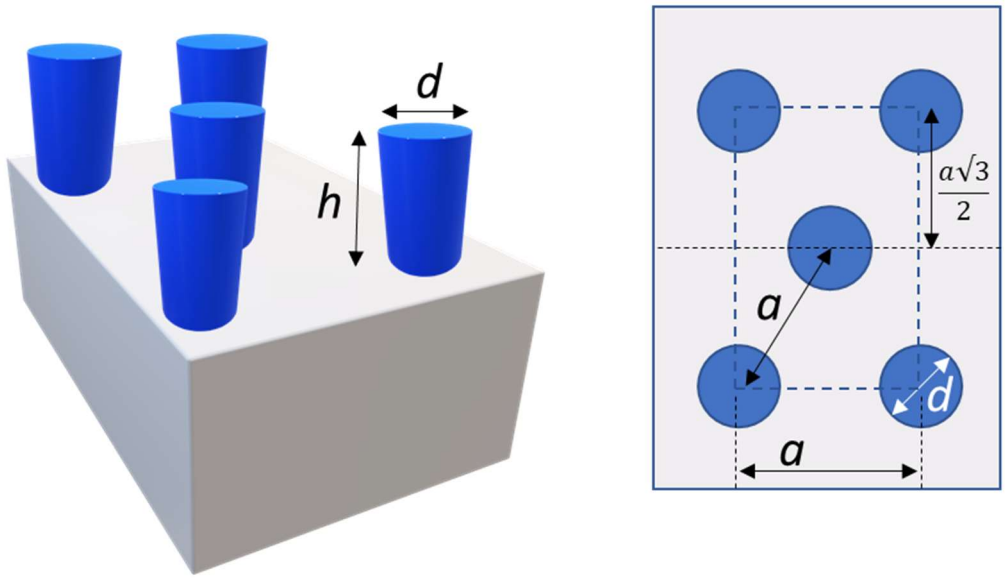

FIG 5.15. Schematic of the idealized geometry used to calculate surface area enhancements contributing to thin MQW layers on patterned substrates. Pillars are assumed to be smooth, perfect cylinders (vertical sidewalls), and uniformly arranged on a hexagonal lattice.

a (nm)	d (nm)	h (nm)	Surf. area relative to flat sample	Calculated growth rate reduction (predicted MQW period, nm)	Measured % growth rate reduction (MQW period, nm)
690	495	350	2.32x	56.9% (6.69)	47.1% (8.21)
1800	1150	370	1.68x	40.5% (9.24)	37.3% (9.73)
Unpatterned	N/A	N/A	1x	0% (15.53)	0% (15.53)

TABLE 5.6. Comparison of calculated and measured MQW period reduction on patterned re-grown samples, based on the surface area increase provided by the initial, experimentally measured pillar array geometries.

5.2.5 Buffer relaxation and consolidation after MOCVD re-growth

Reciprocal space mapping was conducted on the re-grown buffers to assess any visible changes in the buffer state after exposure to MOCVD temperatures, which are high enough to re-initiate dislocation propagation. RSMs are shown in Figure 5.16. Once again, as with the post-etch data, the c-projected peaks did not change appreciably, as full relaxation in that direction was already achieved prior. Remarkably, the broadly smeared peaks in the projected m-direction after etching re-consolidated and became much less broadly distributed in both patterned RIB samples, potentially signifying a reduced gradient in strain state throughout the pillar. Another possibility is the over-shadowing or modification of the original RIB peak by the main peak generated by the MQWs. Finally, given our previous observations of a potentially reduced misfit density (and certainly reduced TD density) on re-grown RIB pillars, a corresponding rearrangement of the heterointerface is not out of the question, and begs further investigation through high-resolution imaging techniques (e.g., with TEM).

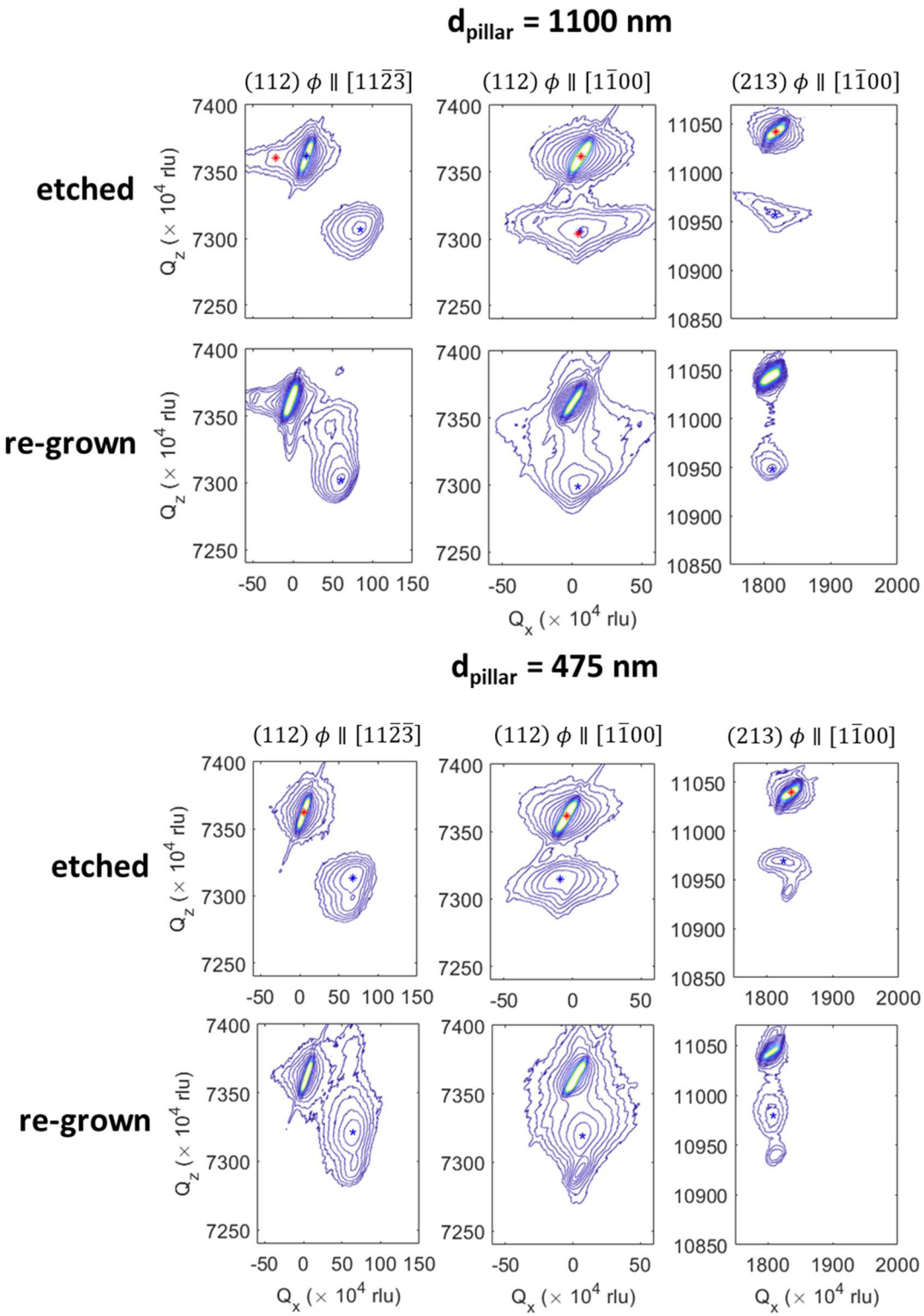

FIG 5.16. On-axis a/symmetric reciprocal space maps of patterned RIBs with etched pillars of d ~ 475 and 1100 nm, before and after MQW re-growth. As before, secondary, smaller peaks in the nanopillar RSMs originate from the planar, un-patterned area at the edges of the nanopillar sample.

5.3 Conclusions

In this chapter, we investigated the degree of controllable biaxial strain relaxation in thick semipolar buffer layers afforded by micro- and nanopatterning. XRD and CL imaging confirmed a significant degree of additional relaxation orthogonal to the projected c-direction, which was mostly relaxed owing to basal-plane MDs. Subsequent deposition of emitting layers triggered 2D relaxation and deleterious TD formation in planar buffer layers; remarkably, no secondary slip or TDs were observed on re-grown patterned RIBs. Further, a consistent emission redshift was observed on RIBs relative to GaN references, which suggested increased QW indium uptake. This effect was found to be robust despite being convolved with QW thickness reduction, which was accounted for by considering the surface area enhancement on patterned samples relative to a planar growth surface.

The work presented here, while promising, has not yet pushed the maximum mesa size and aspect ratio that could still experience significant relaxation, nor the wavelength range that would directly address current long-wavelength challenges. Work is underway to repeat this experimental series, expanding further in size and wavelength axes. Further efforts to investigate the distribution and propagation of defects in the patterned RIBs may prove fruitful, especially to understand if and how defect filtering occurs, and whether this effect can be applied to larger and alternative device geometries.

References

1. R. Ley, L. Chan, P. Shapturenka, M. Wong, S. DenBaars, and M. Gordon, "Strain relaxation of InGaN/GaN multi-quantum well light emitters via nanopatterning," Opt. Express **27**(21), 30081 (2019).
2. P. Shan Hsu, M. T. Hardy, F. Wu, I. Koslow, E. C. Young, A. E. Romanov, K. Fujito, D. F. Feezell, S. P. Denbaars, J. S. Speck, and S. Nakamura, "444.9 nm semipolar (11-22) laser diode grown on an intentionally stress relaxed InGaN waveguiding layer," Appl. Phys. Lett. **100**(2), 1–5 (2012).
3. Y.-D. Lin, M. T. Hardy, P. S. Hsu, K. M. Kelchner, C. Y. Huang, D. A. Haeger, R. M. Farrell, K. Fujito, A. Chakraborty, H. Ohta, J. S. Speck, S. P. DenBaars, and S. Nakamura, "Blue-green InGaN/GaN laser diodes on miscut m-plane GaN substrate," Appl. Phys. Express **2**(8), (2009).
4. N. G. Young, R. M. Farrell, S. Oh, M. Cantore, F. Wu, S. Nakamura, S. P. DenBaars, C. Weisbuch, and J. S. Speck, "Polarization field screening in thick (0001) InGaN/GaN single quantum well light-emitting diodes," Appl. Phys. Lett. **108**(6), 1–6 (2016).
5. S. Keller, B. P. Keller, D. Kapolnek, A. C. Abare, H. Masui, L. A. Coldren, U. K. Mishra, and S. P. Den Baars, "Growth and characterization of bulk InGaN films and quantum wells," Appl. Phys. Lett. **68**(22), 3147–3149 (1996).
6. K. Hestroffer, F. Wu, H. Li, C. Lund, S. Keller, J. S. Speck, and U. K. Mishra, "Relaxed c-plane InGaN layers for the growth of strain-reduced InGaN quantum wells," Semicond. Sci. Technol. **30**(10), (2015).
7. A. Even, G. Laval, O. Ledoux, P. Ferret, D. Sotta, E. Guiot, F. Levy, I. C. Robin, and A. Dussaigne, "Enhanced in incorporation in full InGaN heterostructure grown on relaxed InGaN pseudo-substrate," Appl. Phys. Lett. **110**(26), (2017).
8. S. S. Pasayat, R. Ley, C. Gupta, M. S. Wong, C. Lynsky, Y. Wang, M. J. Gordon, S. Nakamura, S. P. Denbaars, S. Keller, and U. K. Mishra, "Color-tunable < 10 μ m square InGaN micro-LEDs on compliant GaN-on-porous-GaN pseudo-substrates," Appl. Phys. Lett. **117**(6), (2020).
9. R. Liu, J. Mei, S. Srinivasan, F. A. Ponce, H. Omiya, Y. Narukawa, and T. Mukai, "Generation of misfit dislocations by basal-plane slip in InGaN/GaN heterostructures," Appl. Phys. Lett. **89**(20), 2004–2007 (2006).
10. R. C. White, M. Khoury, F. Wu, S. Keller, M. Rozhavskaia, D. Sotta, S. Nakamura, and S. P. Denbaars, "MOCVD growth of thick V-pit-free InGaN films on semi-relaxed InGaN substrates," Semicond. Sci. Technol. **36**(1), (2020).
11. J. Liu, H. Liang, X. Xia, Y. Liu, J. Liu, R. Shen, Y. Luo, Y. Zhang, and G. Du, "Indium-incorporation Induced Morphological Evolution and Strain Relaxation of High In- content InGaN Epilayers Grown by Metal-organic Chemical Vapor Deposition," Cryst. Growth Des. (2017).
12. A. E. Romanov, T. J. Baker, S. Nakamura, and J. S. Speck, "Strain-induced polarization in wurtzite III-nitride semipolar layers," J. Appl. Phys. **100**(2), (2006).
13. E. C. Young, F. Wu, A. E. Romanov, A. Tyagi, C. S. Gallinat, S. P. DenBaars, S. Nakamura, and J. S. Speck, "Lattice tilt and misfit dislocations in (11-22) semipolar GaN heteroepitaxy," Appl. Phys. Express **3**(1), 5–7 (2010).
14. E. C. Young, A. E. Romanov, and J. S. Speck, "Determination of composition and lattice relaxation in semipolar ternary (In,Al,Ga)n strained layers from symmetric x-ray diffraction measurements," Appl. Phys. Express **4**(6), (2011).
15. I. L. Koslow, C. McTaggart, F. Wu, S. Nakamura, J. S. Speck, and S. P. DenBaars, "Improved performance of (2021) long-wavelength light-emitting diodes grown with wide quantum wells on stress-relaxed $In_xGa_{1-x}N$ buffer layers," Appl. Phys. Express **7**(3), 1–5 (2014).
16. C. D. Pynn, S. J. Kowsz, S. H. Oh, H. Gardner, R. M. Farrell, S. Nakamura, J. S. Speck, S. P. Denbaars, C. D. Pynn, S. J. Kowsz, S. H. Oh, H. Gardner, R. M. Farrell, and S. Nakamura, "Green semipolar III-nitride light-emitting diodes grown by limited area epitaxy," **041107**, (2016).

17. P. Shan Hsu, "Stress-Relaxation in III-Nitride Based Semipolar Lasers," PhD Dissertation. UCSB (2013).

18. I. L. Koslow, M. T. Hardy, P. Shan Hsu, F. Wu, A. E. Romanov, E. C. Young, S. Nakamura, S. P. Denbaars, and J. S. Speck, "Onset of plastic relaxation in semipolar (11-22) InGaN/GaN heterostructures," J. Cryst. Growth **388**, 48–53 (2014).

19. M. T. Hardy, P. S. Hsu, F. Wu, I. L. Koslow, E. C. Young, S. Nakamura, A. E. Romanov, S. P. Denbaars, and J. S. Speck, "Trace analysis of non-basal plane misfit stress relaxation in 20-21 and 30-3-1 semipolar InGaN/GaN heterostructures," Appl. Phys. Lett. **100**, 202103 (2012).

20. M. T. Hardy, E. C. Young, P. S. Hsu, D. A. Haeger, I. L. Koslow, S. Nakamura, S. P. Denbaars, and J. S. Speck, "Suppression of m-plane and c-plane slip through Si and Mg doping in partially relaxed (20$\bar{2}$1) InGaN/GaN heterostructures," Appl. Phys. Lett. **101**(13), (2012).

21. I. L. Koslow, "Strain Relaxation in Semipolar III-V Nitrides for Light Emitting Diode Applications," PhD Dissertation, UCSB (2013).

22. S. Keller, N. A. Fichtenbaum, C. Schaake, C. J. Neufeld, A. David, E. Matioli, Y. Wu, S. P. DenBaars, J. S. Speck, C. Weisbuch, and U. K. Mishra, "Optical properties of GaN nanopillar and nanostripe arrays with embedded InGaN/GaN multi quantum wells," Phys. Status Solidi Basic Res. **244**(6), 1797–1801 (2007).

23. C. D. Pynn, "Strain Engineering and Epitaxial Design of Semipolar InGaN-based Light-Emitting Diodes," PhD Dissertation, UCSB (2018).

24. G. Orsal, Y. El Gmili, N. Fressengeas, J. Streque, R. Djerboub, T. Moudakir, S. Sundaram, A. Ougazzaden, and J. P. Salvestrini, "Bandgap energy bowing parameter of strained and relaxed InGaN layers," Opt. Mater. Express **4**(5), 1030 (2014).

25. M. A. Moram and M. E. Vickers, "X-ray diffraction of III-nitrides," Reports Prog. Phys. **72**(3), (2009).

6

Scalable, selective-area MOCVD growth of micro- and nano-structured InGaN emitters

6.1 Introduction

Recent commercial interest in efficient, self-emissive pixels for display applications has spurred development of efficient III-nitride LED materials at single- and sub-micron length scales. However, small devices made with standard foundry techniques suffer from non-radiative sidewall point defects (many of them interstitials and vacancies) formed through ion bombardment and implantation during plasma-based mesa definition. These defects introduce mid-gap trap-state energy levels which quickly relax excited charge carriers near the mesa sidewall and detract from full-gap emission. While mitigation methods such as cleaning, passivation, annealing, and material re-growth have been developed [1-3], it would be desirable to entirely circumvent sidewall damage. One approach to avoid plasma etching lies in selective-area MOCVD growth (SAG), which leverages the lack of adsorption and fixation of III-metal atoms on thin, amorphous SiO_2 and Si_3N_4 layers coating the nitride growth surface to define mesa geometry. SAG is schematically represented below in Fig. 6.1(b); by masking a portion of the substrate with growth-

inhibiting dielectric materials, epitaxial growth is preferentially directed to defined apertures on the substrate surface. With proper growth conditions (temperature, pressure, precursor flows, H_2 carry gas content), complete deposition selectivity to substrate-exposed regions can be achieved.

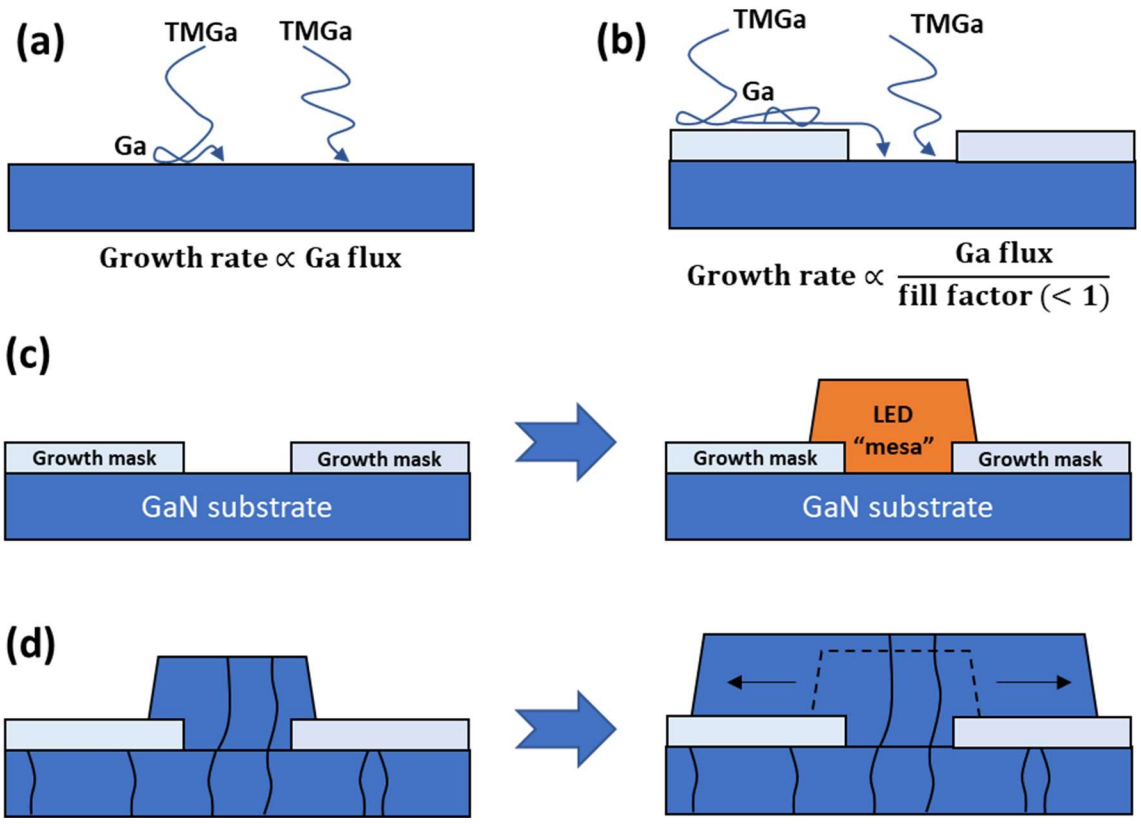

FIG 6.1. (a) Simplified schematic representation of MOCVD growth, highlighting the transport mechanisms by which trimethylgallium (TMGa) delivers Ga to a planar, unmasked growth surface, given standard MOCVD conditions and assuming an over-abundance of ammonia gas. TMGa adsorbs and deposits a Ga atom onto the surface by homolytic cleavage, where it diffuses and quickly incorporates at a crystal kink site by bonding with ammonia-supplied nitrogen. (b) On masked surfaces, Ga is deposited on the growth surface but does not readily covalently bond with the growth mask, instead diffusing further until it can interact with a III-nitride crystal surface within an open aperture. The growth rate is thus enhanced by the effective open area fraction (fill factor) of the mask. (c) Schematic representation of selective-area MOCVD growth of an LED "mesa" out of a dielectric growth-masking aperture defined on a GaN substrate in an attempt to realize micron-scale devices free of nonradiative recombination from sidewall defects. (d) Epitaxial lateral overgrowth (ELO), a defect-reduction technique in which material is grown vertically out of apertures, followed by lateral growth to reduce threading dislocations on the resulting "wings" which can be used for device epitaxy.

Achieving controllable selective-area growth on standard micro-LED device masks is nontrivial; layouts are often designed for packaging compatibility, leaving ample space around each mesa for contact pads and dicing. The large mesa spacing in such layouts is difficult to translate to SAG growth, where analogous area fractions would be prohibitively small, and dramatically increase the rate of material growth out of the mesa-defining apertures. To better limit and control this growth rate enhancement, it is important touse a mask with high mesa densities. If successful, this also generates a wealth of single devices and arrays to probe for electrical and optical studies. An envisioned short-loop process for fabricating such on-wafer diodes is shown below in Fig 6.2. Similar demonstrations have recently been reported from Bai *et al*. [1].

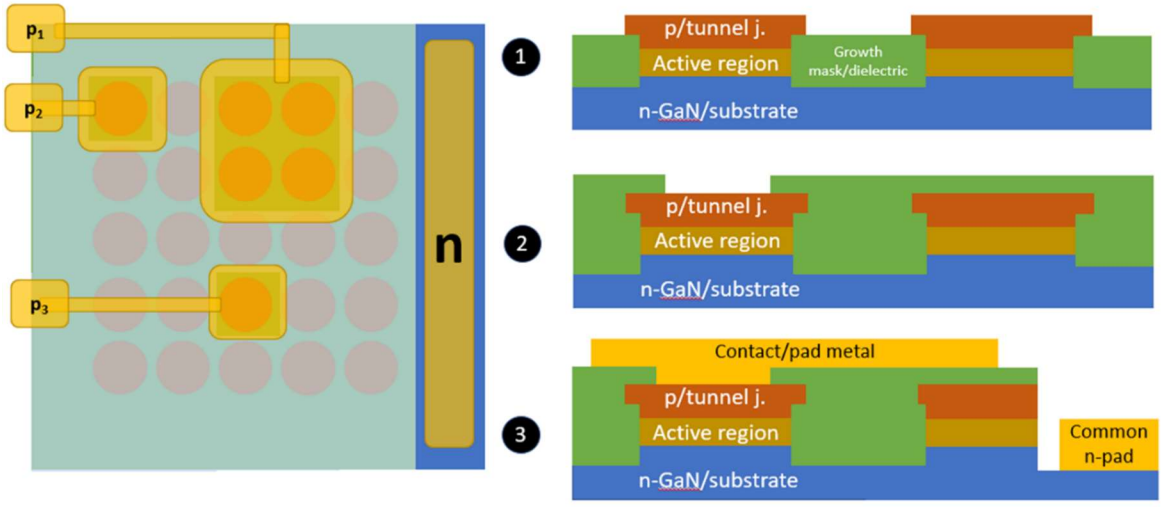

FIG 6.2. Envisioned top-view and cross-sectional schematics of a short-loop process flow for devices created with selective-area growth (SAG). (1) High-density mesa arrays are defined and LED material is grown, (2) secondary dielectric isolation is performed, and (3) etching and n-/p-metallization is performed, with a common n-contact. If a tunnel junction is grown after the p-layer, the same metallization can be used for both doped layers. Sacrificing certain device mesas may be necessary to probe devices, given the high-density configuration. P_1, P_2, and P_3 represent separate electrical p-side contacts addressing various devices in the SAG array.

In addition to growth of micron-scale emitters as display pixels, there is an active scientific interest in the realization of emitting nanostructures for the strain-relaxation and light-extraction benefits introduced previously. As we saw in Chapter 5, the high-density and geometrically tunable features afforded by colloidal patterning enabled a thorough interrogation of micro- and nanostructured light emitters in relaxed InGaN buffers. By using colloidal masks to obtain various mask fill factors and geometries, different size "mesas" can be fabricated simply and scalably, with sufficient emitting area to properly gauge the optical and crystallographic properties of the emitter ensemble. Accordingly, we develop a simple, reproducible process for making geometry-tunable colloidal growth masks, re-grow buffers and emitting quantum-well layers, and characterize the structures that result.

6.2 Old SAG, new tricks

Selective-area growth (SAG) is a well-established technique, first used in the late 80's and 90's to enable various innovations in III-V semiconductors (arsenides, phosphides) [4,5]. SAG was first implemented in the III-nitrides in a defect reduction technique called epitaxial lateral overgrowth (ELO), wherein GaN was first grown vertically out of patterned stripe apertures, and then laterally over the growth mask to create high-quality wings that reduced threading dislocation defect densities by orders of magnitude (Fig 6.1(d)). Subsequently deposited device layers showed improvements in efficiency; for example, the lifetime of ELO-grown InGaN lasers was dramatically expanded relative to the those grown on a planar GaN substrate [6]. Here, we briefly introduce the reaction-diffusion phenomena at the core of

SAG, discuss considerations for mask fabrication and growth, and introduce colloid-based growth mask fabrication.

6.2.1 Interplay of reaction and mass transport in selective-area MOCVD growth

Here, we briefly analyze the selective-area growth of GaN by delivering trimethylgallium (TMGa) to a GaN surface in the presence of an ammonia over-pressure (assuming a sufficient supply of ammonia, the limiting reactant is TMGa). Delivery of metalorganic (MO) precursors to the growth surface proceeds with laminar flow of MO-containing carry gas (usually N_2 and/or H_2, with MO molar concentration C_o) across the susceptor. By invoking a no-slip boundary condition at the growth surface, the gas velocity parallel to it diminishes as we approach the solid-gas interface, making diffusion the dominant transport mechanism for all species within the stagnant layer above the crystal surface. Above this diffusion layer, we assume the bulk MO concentration is C_o. We further assume an empirically first-order heterogeneous reaction mediated by the near-surface adatom concentration C_S, because a significant portion of surface atoms will quickly find available nitrogen species from cracking of over-abundant ammonia gas in the chamber environment.

Assuming diffusion-mediated delivery of MO down to an unmasked wafer surface, the lateral concentration profile $C_S(x)$ would be completely constant, with the steady-state value dictated by the tradeoff between reactant consumption and diffusion-mediated reactant delivery. When the surface is masked with patterns containing open areas of greater than 10 microns, $C_s(x)$ varies with distance away from the edge of the open aperture, since a greater

lateral adatom flux immediately near the edge would incorporate into the growth surface per unit time, as compared to the center of the aperture. As a result, we obtain a sharp increase in growth rate near the edge, which exponentially decays to the planar value in the middle of the exposed substrate surface. This is depicted in Figure 6.3 below.

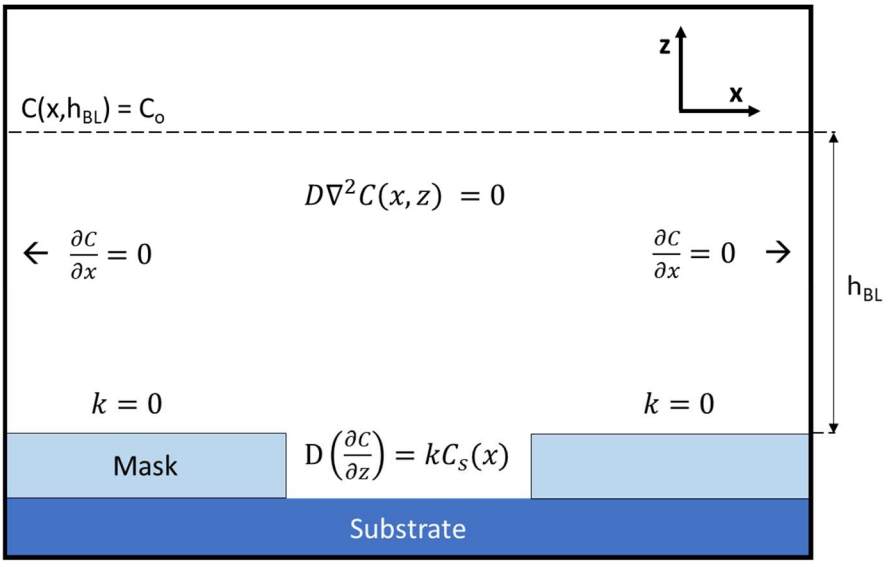

FIG 6.3. Schematic representation of the simplified reaction-diffusion system that encompasses selective-area MOCVD growth. A boundary layer (thickness h_{BL}) forms in the immediate vicinity of the growth surface, which is assumed to be periodic at the x-boundaries. Bulk metalorganic precursor concentration and diffusivity is C_o and D, respectively. C_S represents the local adatom surface concentration, which is a function of x and z, and the lumped effective first-order reaction rate constant in the open substrate area is represented by k.

The growth-rate enhancement effect at the mask edge described above is only observed if the mask pattern dimensions greatly exceed the lateral adatom diffusion length of the main III-element to be incorporated. Starting with aluminum and moving down the III-group column on the periodic table, we see that Al is the least mobile in MOCVD growth, with an effective diffusion length of approximately 1 μm. Gallium wanders greater distances (about 10 times greater) than Al on the growth surface; although this varies significantly based on the amount of V-element in the growth atmosphere (also pressure/temperature),

experimentally obtained adatom diffusion lengths for Ga can reach 10-15 μm [7,8]. Finally, indium is the most mobile element of the group, with a diffusion length of ~200 μm; it is often referred to as a "surfactant" for this reason, and encourages uniformly terraced incorporation of other III-atom species on the growth surface [9].

Our focus is exclusively on the ternary InGaN alloy system, and therefore our limiting adatom is gallium; in order to avoid mask loading, pattern periodicity should remain below 10 μm, which should reduce growth non-uniformity within and between mask apertures. This is compatible and inherently built in for our investigations with colloidal lithography, wherein sedimentation precludes deposition of colloids exceeding 6 μm diameter. As a result, adatom surface migration should predominate over mask loading as described above.

6.2.2 Preparing geometry-tunable, large-area micro- and nano-SAG substrates via colloidal lithography

Colloidal masks provide independent control over "mesa" size and mask fill fraction through two independent variables: original colloid diameter (D) and degree of sphere size reduction (leaving a final diameter, d). Figure 6.4 shows a hexagonal close-packed layer of colloids on a growth-masking SiN_x layer, demonstrating how the colloids change size during processing. The open area fraction, f, is given by

$$\mathrm{f} = \frac{\text{Area of aperture}}{\text{Total unit area}} = \frac{2\left(\frac{\pi d^2}{4}\right)}{D^2\sqrt{3}} = \boldsymbol{\frac{\pi}{2\sqrt{3}} \cdot \left(\frac{d}{D}\right)^2} \tag{6.1}$$

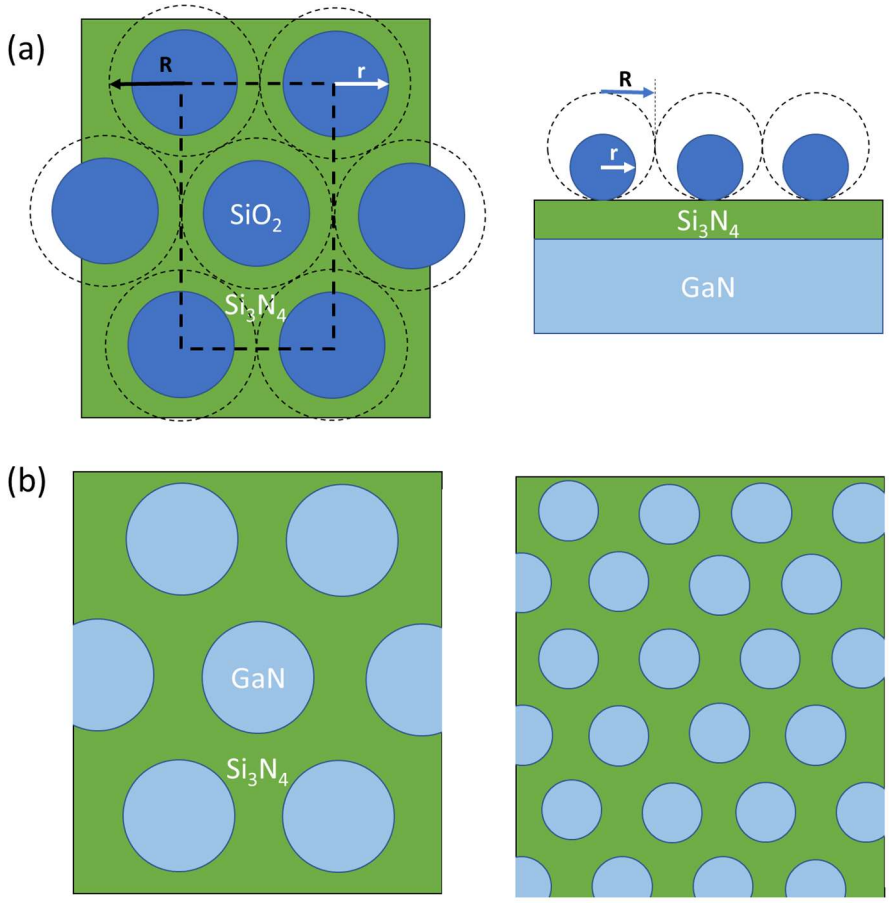

FIG 6.4. (a) Schematic of top (left) and cross-sectional side view (right) of a rectangular unit cell of HCP-arranged colloids, showing the original (R) and reduced (r) radii of the colloidal nanospheres used in defining mesa size and open area fraction of the surface. Growth mask processing will form apertures where the particles are currently positioned, and this is explored later in the chapter. (b) Top views of two processed SAG masks with different nominal mesa sizes, but identical fill fraction.

Two distinct processes were developed for colloidally patterned SAG masks; these are featured below in Fig. 6.5. The first approach works for a greater range of dielectric layer thicknesses and virtually any mask material. First, the growth-masking material is deposited over the entire substrate, followed by deposition of a protecting photoresist layer. After colloid deposition and mask reduction (which defines both fill fraction and final mesa size), ~50 nm of metal (Cr or Ni) was shadow-deposited with electron-beam evaporation, which formed the negative image of the deposited colloids in the underlying, planar masking layer.

The colloids were lifted off, and the remaining metal pattern was transferred into the PR and the growth mask with O_2 and then fluorine-based plasma, respectively. Finally, surfaces were cleaned of PR and metal residue with metal etchant and solvent/piranha cleans.

The second approach is simpler and quicker, though more limited in its scope; here, SiO_2 is physically evaporated through mask-reduced colloids directly on the GaN substrate, quickly yielding centimeter-scale nanostructured surfaces for extensive growth studies. In its current form, this approach leaves re-deposited SiO_2 within the growth apertures, which (as we will see shortly) affects the uniformity of grown structures. In future process lots, introducing a photoresist or ALD-deposited alumina interlayer between the substrate and deposited SiO_2 (and then selectively dissolving it later in AZ-300MiF developer) may be an effective approach to leave the growth surface as pristine as possible and reduce the possibility of mesa non-uniformity from small amounts of undesired redeposition interfering with crystal growth. Overall, masks were fabricated in SiO_2 and Si_3N_4 with a variety of aperture sizes and area fractions, as evidenced by the SEMs of processed SAG masks in the lower panel of Figure 6.5.

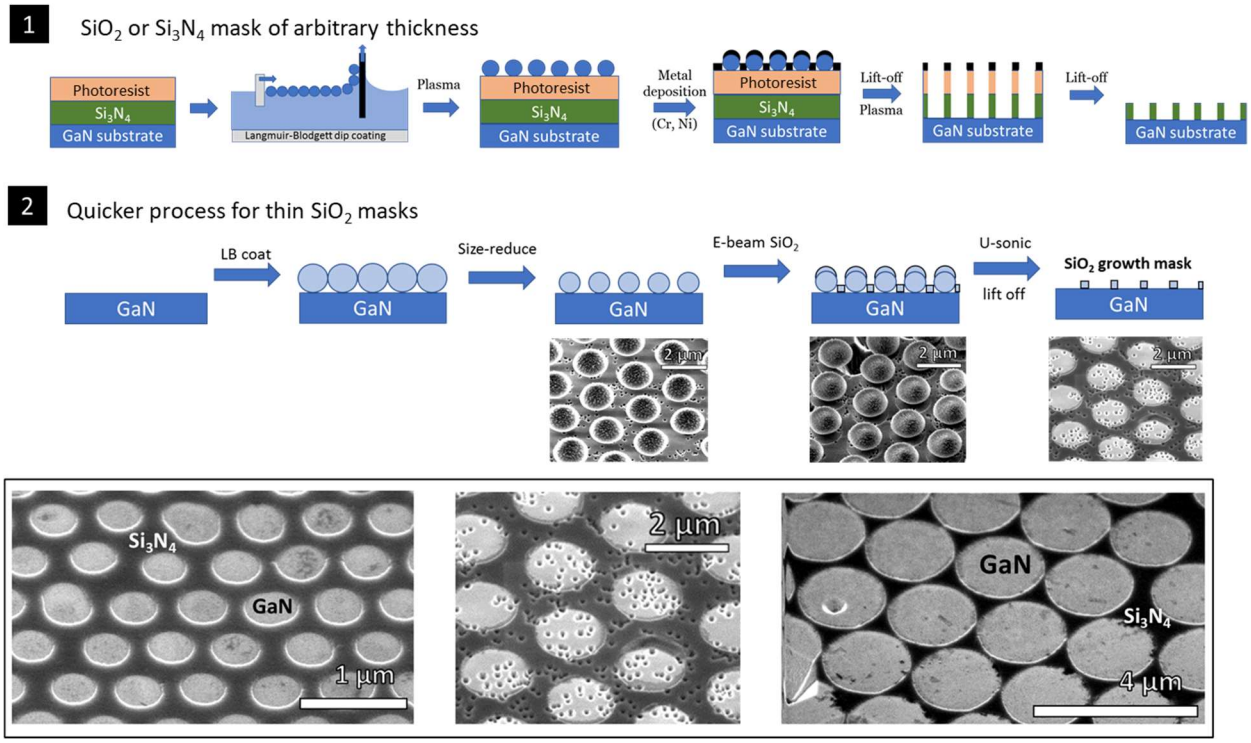

FIG 6.5. Two fabrication approaches for realizing large-area SAG substrates with colloidal lithography. Process 1 involves the deposition of a flat growth-masking film, photoresist, colloids, and a metal shadow-mask. Pattern transfer then opens apertures to the growth surface. Process 2 is quicker, simply requiring LB deposition, mask reduction, shadow-deposition of SiO_2, and ultrasonication to lift off residual colloids, though is limited in growth mask thickness and only to SiO_2. SEMs are shown below each process step schematic. The lower SEM images shows some of the growth masks achieved, displaying a variety of micron and sub-micron apertures, and tunable open area fractions.

6.3 Nanoscale, selective-area growth and characterization of GaN/InGaN materials

Selective-area growth studies were first conducted with high-temperature GaN (HT-GaN) growth, which helped confirm the degree of mask-induced growth rate enhancement and assign emerging crystal facets. Masked substrates (c-plane GaN on sapphire and free-standing $(11\bar{2}2)$ semipolar GaN) were cleaved into 5-mm sections and cleaned with the same procedure as described for RIBs in Ch. 5 (cf. Section 5.2.3). Growth substrates with average

aperture diameters (nm)/spacings (nm)/fill fractions of 200/310/58%, 450/690/59%, and 1500/2500/54% were used.

First, to make any useful conclusions about the selectively grown material, it is important to grow the proper amount of material to control and clearly identify facet formation. Calibration of the planar GaN growth rate was conducted by fitting normal-incidence reflectance curves with a thin-film interference model of a GaN buffer on sapphire (Filmetrics) before and after 15 minutes of growth (10 SCCM TMGa, 1050°C). TMGa flow rate was halved to 5 SCCM from the nominal planar flow rate for SAG; ammonia was also adjusted accordingly to keep the III/V molar ratio constant. As a first test case to observe SAG-induced growth rate enhancement, the 450/690 nm SAG samples (made with Process 2 in Fig. 6.5) were loaded for 60, 120, and 180 seconds of growth with corresponding expected deposition thicknesses of 36, 71, and 107 nm, respectively. Figure 6.6 shows close-up SEM images of the growth results, at the edge and in the middle of each sample.

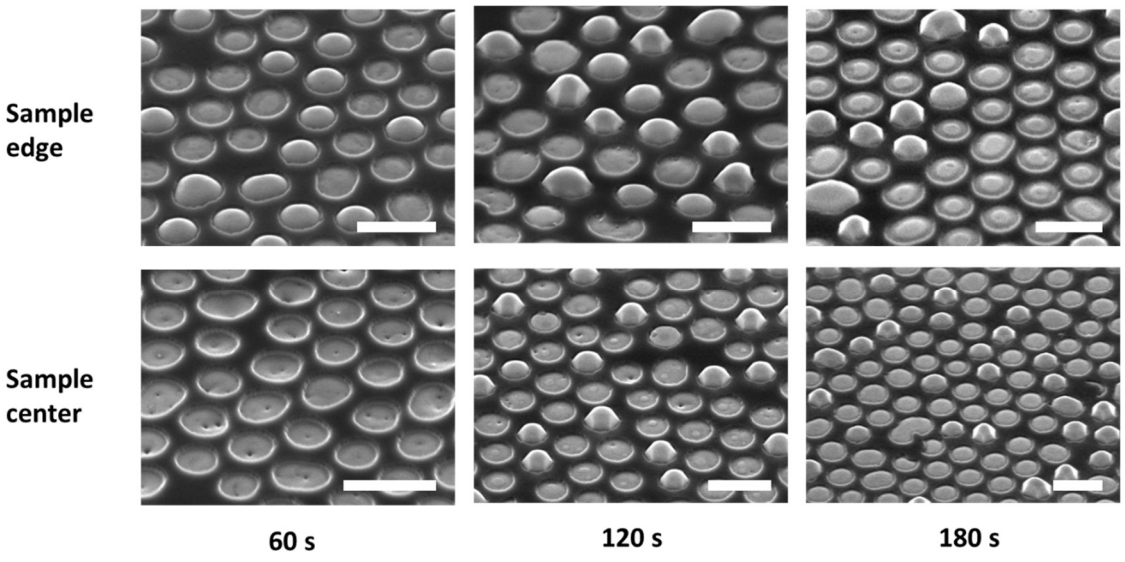

FIG 6.6. Scanning electron micrographs of selective-area GaN growth out of colloid-defined apertures (d = 450 nm) defined on a c-plane GaN substrate for various growth durations. All scale bars are 1 μm. Larger protrusions ("bumps") as well as flatter features can be discerned ("pancakes").

As hoped, deposition is visible on the initially planar growth surface, but not nearly enough for coalescence, which allows us to appreciate the growth morphology and hole-to-hole uniformity. Remarkably, the height profile in adjacent apertures appears bi-modally distributed with certain apertures showing little to no deposition while others protruding significantly out of the mask (cf. "bumps" vs. "pancakes"). Although our sampling area with these images is limited, it appears that the non-uniform size distribution is amplified in the images taken at the sample edge. More prominent features also show faint hexagonal faceting, presumably as the growth rate of the (0001) c-plane outpaces other stable semipolar planes.

While it is difficult to fully understand the origins of the observed non-uniformity by simply imaging the surface, several recurring features in the apertures that exhibit suppressed growth suggest residual surface SiO_2 residue as the cause. Many areas have a circular "hillock" exclusively near the center of each growth aperture; this marks the particle-surface contact point, where plasma-based size reduction of the mask likely re-deposited SiO_2 on the GaN surface. The resulting SiO_2 residue remains exposed to air after the SiO_2 e-beam deposition step, and therefore affects the growth rate and morphology at the start of material re-growth. Since SiO_2 residue is also growth-masking, adatom flux may be redirected to those neighboring apertures without residue, increasing the effective growth rate, and thereby forming the bimodal size distribution. In further support of this explanation, apertures supporting more growth do not have "hillocks". To conclude, it is wise to selectively remove residue prior to growth, or to protect the surface with another interlayer during mask reduction where selective removal is untenable, as in the present case. Processing details for introducing such a layer are found above in Section 6.2.2.

Another advantage of our first processing scheme is a lack of particle-substrate contact, preventing redeposition of masking particle material on the final growth surface. Moreover, the growth surface is etched uniformly by the pattern-transfer step. The 1500-nm mesa samples mentioned above were fabricated in this way, and continuous-flow, HT-GaN growth was performed at similar conditions to the previous samples. The resulting structures appear in Fig. 6.7 below; while partial V-pit defects nucleated by substrate threading dislocations are visible, the overall growth profile between different apertures is much more uniform, with the hexagonal facets that emerged in the previous sample now fully formed and prominent. Furthermore, no "hills" caused by particle-substrate contact were observed in the centers of any of the features.

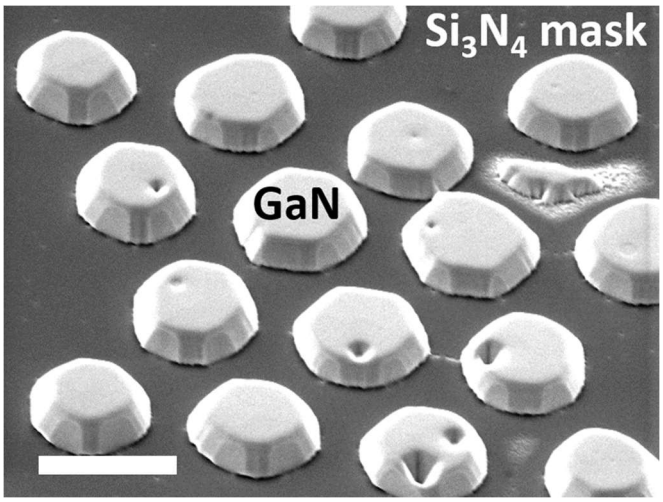

FIG 6.7. Scanning electron micrograph of selective-area GaN growth out of colloid-defined apertures (d ~ 1500 nm) on a c-plane GaN substrate. The scale bar is 2 μm.

Many studies in literature have focused on c-plane substrate SAG, demonstrating a variety of growth modes and resulting 3-dimensional crystal morphology [10,11]. Recently, electrically addressable SAG-based green microLED arrays were demonstrated with a claimed 9% external quantum efficiency [12]. While promising, higher efficiencies still are

necessary to compete effectively with OLED technologies. Growth on alternative planes that accommodate larger amounts of indium and reduce piezoelectric strain have not been fully investigated and deserve attention as an alternative way to increase long-wavelength emitter efficiency. As such, in line with the previous chapter, we explore $(11\bar{2}2)$ GaN substrates as a viable SAG growth surface for emitting materials.

Micro- and nanoscale Si_3N_4 growth masks were formed on a $(11\bar{2}2)$ free-standing GaN substrate with diameters of 200 and 2000 nm. As with the c-plane SAG studies, HT- GaN was first grown to gauge facet emergence and growth rate. GaN was grown with 2 SCCM of TMGa at 1050°C for 2 and 5 minutes, respectively. Figure 6.8 shows images of the resulting GaN buffers. The top facet area disappears completely for the nano-SAG sample, closed out by two slower-growing nonpolar facets that face the projected m-axis. This effect is also observed in the micro-SAG sample at the edges. The structure elongates and narrows in the orthogonal axis, owing to a high growth rate on c-projected crystal faces, but the remaining top area appears to be quite smooth, with only minor corrugations present on the wings that extend past the aperture confines.

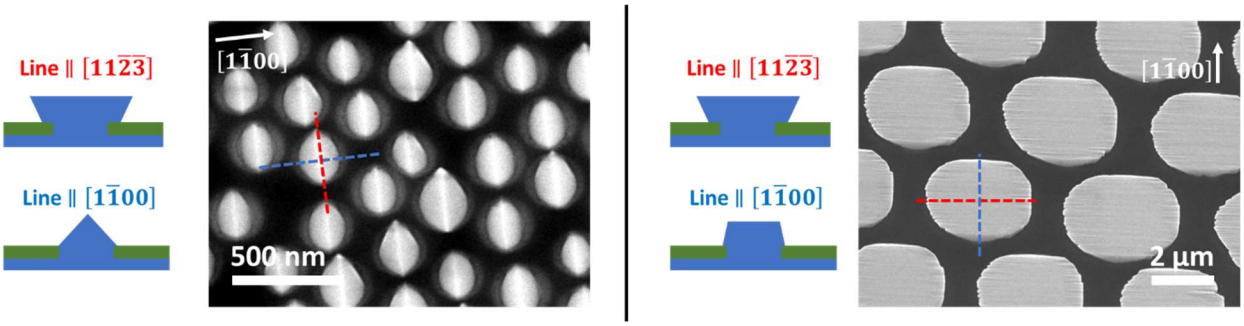

FIG 6.8. Scanning electron micrographs of selective-area GaN growth out of colloid-defined apertures (d = 200 and 2000 nm) on a free-standing $(11\bar{2}2)$ GaN substrate.

Evidently, at the current growth temperatures and precursor ratios, thickness budgets for the top $(11\bar{2}2)$ facet are severely limited, especially in nanostructures. This

introduces additional challenges in depositing quantum wells, where a smaller portion of each successive well remains on the top facet, therefore changing QW indium content, thickness, and degree of polarization-induced wavelength shift. To demonstrate the sensitivity of the resulting emission to faceting in different mesa sizes, light-emitting layers were deposited in apertures of both sizes; the amount of HT-GaN buffer was further varied in the nanoscale aperture case, where the thickness budget is particularly tight.

All quantum-well layers were deposited with 10 SCCM of TEGa at 815°C, with an additional 90 SCCM of TMIn flowed for InGaN layers. Nominal quantum well thickness was 2.5 nm, with 14-nm barriers. For 2-μm apertures, 6 QWs were deposited after 5 minutes of HT-GaN growth. 200-nm apertures were filled for 30 seconds and 3 minutes of GaN buffer growth, and subsequently 3 QWs were deposited at the same conditions as the 2-μm SAG. Figure 6.9 shows SEM images, a CL emission spectrum, and corresponding monochromatic CL maps of the 2-μm emitters. As seen in panels (a) and (b), the emitters are anisotropic, with mirror symmetry across the $[11\bar{2}\bar{3}]$ axis, but lack symmetry across the m-axis, with one edge rather flat/square while the other is more rounded, having an anvil-like shape. The surface is quite heavily corrugated parallel to the c-projected axis, except for a consistent, flat area on each individual emitter near the square anvil edge described earlier. Smooth, inclined facets protrude toward the projected m-direction from the mesa edge, very much like the wings on RIB re-growths in the previous chapter; these may very well be the same stable semi/nonpolar facets that form corrugations on the top surface of the pillar.

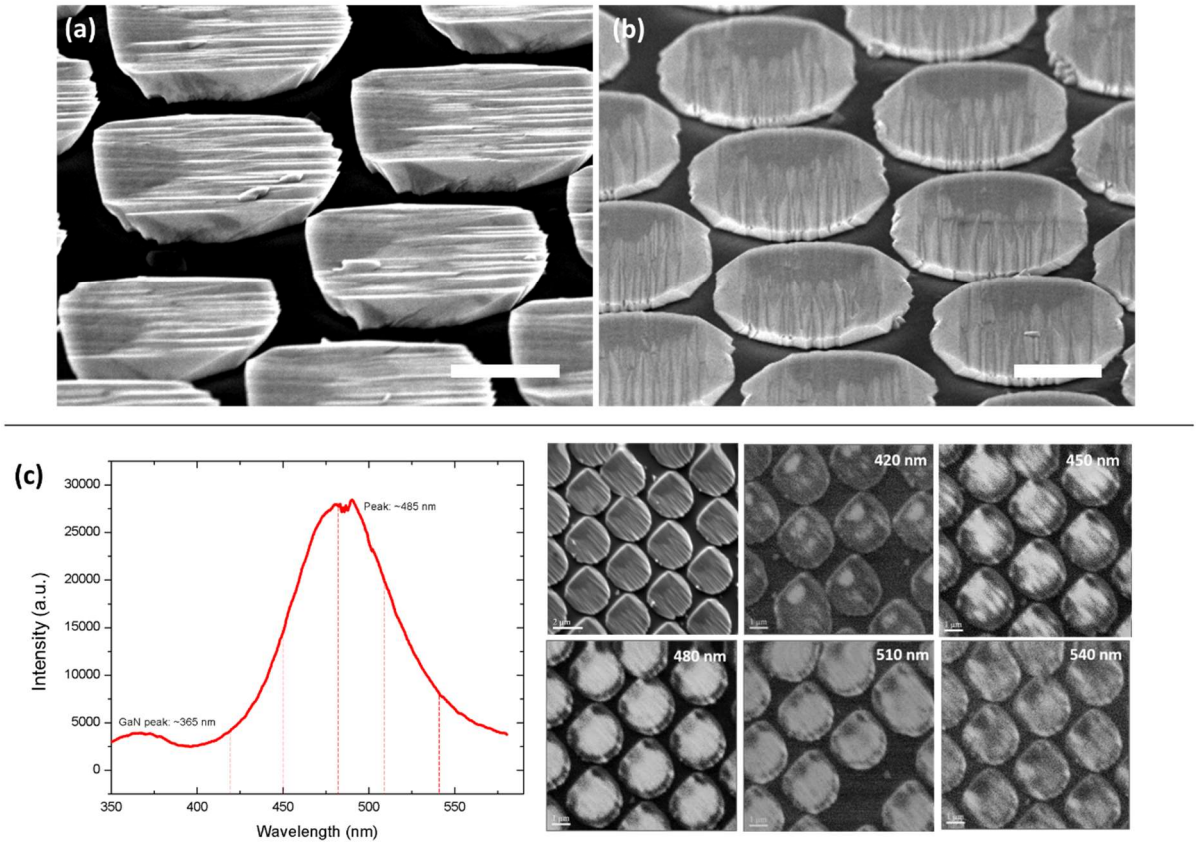

FIG 6.9. (a,b) Scanning electron micrographs and (c) SEM-overlaid CL imaging of 6 QW's deposited via selective-area growth. Colloid-defined apertures (d = 2000 nm) were defined on a $(11\bar{2}2)$ free-standing GaN substrate; micrographs in (a) and (b) are aligned parallel to the c- and m-projected substrate orientations. Unlabeled scale bars are 1 μm.

The emission originating from the various facets identified above span over 100 nm in wavelength, which all contribute to the single, broad peak centered around 485 nm in the CL spectrum. Probing at ~420 nm with monochromatic CL revealed emission from the smooth patch of material near the flat edge; both smoothness and relatively short-wavelength emission suggests a nonpolar facet. 450 nm emission was more distributed across the entire structure and appeared striped, which hints at the corrugation-inducing facets discussed earlier as a possible origin. 480 and 510 nm monochromatic imaging appeared quite uniform, emitting throughout the central area of the pillar. Finally, sparse 540 nm emission was distributed across each emitter, but also particularly favoring one of

the corners adjacent to the nonpolar facet. This may be the basal c-plane, but higher resolution imaging and more rigorous mapping is necessary to properly verify this. Overall, top facet area is still quite well maintained with 6 QWs on 2-μm apertures, allowing us to reap the potential benefits of the original growth orientation in a micron-scale form factor. Surface corrugations of an appropriate size may also bring about polarization selectivity, which is desirable for display optics integration.

Having looked extensively at the emission and morphology of micron-scale GaN/InGaN structures, we move to submicron apertures. As previously mentioned, 3 QWs were deposited on HT-GaN grown by SAG. The extent of HT-GaN growth was varied (0.5 and 3 minutes) before MQW deposition; SEMs and CL emission from the growth results are shown below in Fig. 6.10. Structures grown with longer buffer times (panel (a)) appear sharply terminated by two inclined, symmetric facets pointing outward to the m-projected direction. The same anvil shape is observed as with the micropillars, with one end completely flat, with its edge normal to the c-projected axis. The opposing anvil edge terminates at either a single or pair of sharp points. The short-buffer structures (panel (b)) have not completely closed out the top $(11\bar{2}2)$ facet, and similar corrugations are visible as in the micro-structured case. Overall, the structures extend well past their original aperture diameter in the projected c-direction and have conjoined with neighbors at several points, making for a very exotic landscape. Given that the margins for defect-free coalescence fronts are slim, the contact points between adjacent structures may be ridden with threading dislocations (to be determined by CL).

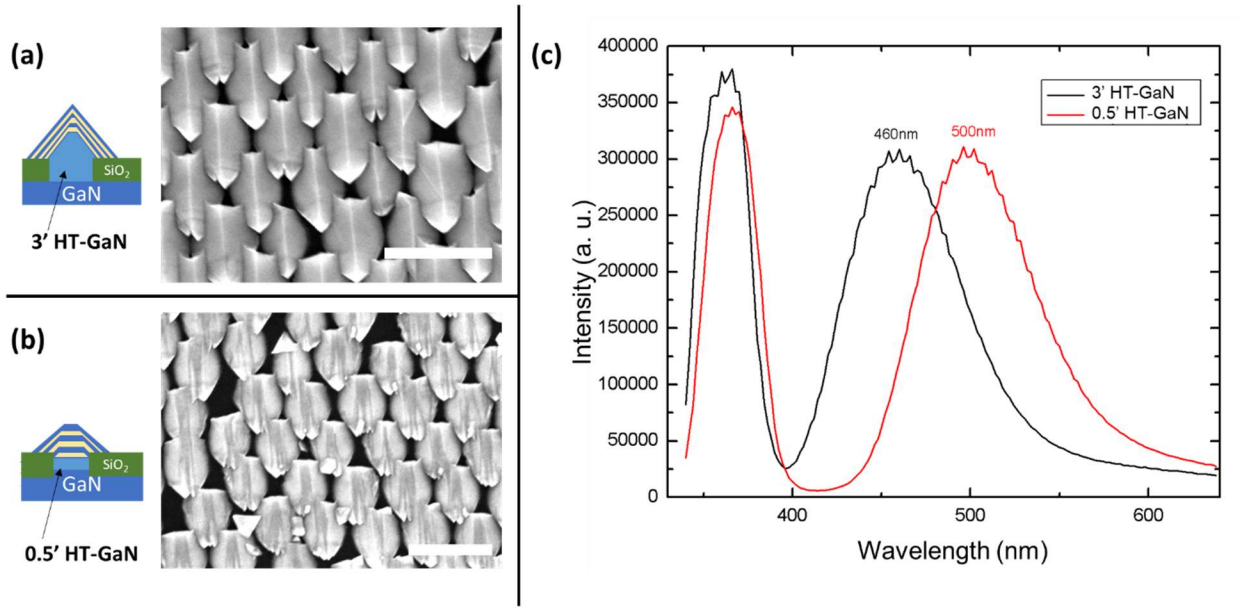

FIG 6.10. (a,b) Plan-view scanning electron micrographs and envisioned m-parallel cross-section profiles, as well as (c) CL emission spectra of selective-area GaN and 3x MQW growth out of hole-array SiO_2 masks (d = 200 nm) defined on a $(11\bar{2}2)$ free-standing GaN substrate, with (a) 3 minutes and (b) 30 seconds of GaN buffer growth prior to active region deposition. Approximate peak centroid wavelengths are shown above each QW emission peak. SEM scale bars are 500 nm.

CL spectra of the two nanostructured samples in panel (c) show a single, broad emission peak, in line with the emission profile of the micro-structured sample. Despite identical QW growth conditions for both surfaces, the 30"-buffer samples (Fig 6.10(b)) showed a 40-nm redshift relative to the sharply faceted structures (a). While more characterization is necessary (TEM, atom probe) to resolve the origin of emission contributions from various facets, the most plausible reasons for this redshift are high indium uptake on the more present native $(11\bar{2}2)$ facet, a thicker set of quantum wells (growth rate enhancement is highest at the start of SAG), and a lesser prevalence of stable semi-polar side facets that yield thinner and less indium-incorporating QWs (both blue-shifting).

Monochromatic CL was conducted on both nanostructured SAG samples to relate crystallographic facets with discrete spectral emission ranges; the CL maps obtained are shown in Fig. 6.11. Unfortunately, the resolution of the CL-fitted SEM (FEI Inspect) used for imaging was unable to resolve individual facets. As a result, separately conducted higher-resolution field-emission imaging was used to better spatially correlate wavelength with morphology. The emission location for the peak centroid in both samples (460 and 500 nm, respectively, top right panel) originates in the middle of each individual emitter. However, short- and long-wavelength emission tails appear to migrate to opposite ends of the structure along the c-projected vector for the 3'-buffer sample. The 30"-buffer sample likely has less fully formed facets and more of the emission is present on the original growth plane, which explains the more static and uniformly distributed emission profile.

By focusing on a selected group of nanostructures in each sample (panel (c)), the corresponding emission distribution and migration noted above can be discerned more clearly. It is notable that a similar type of emission distribution has been reported on the $(11\bar{2}2)$ growth plane with selective-area deposition via molecular-beam epitaxy [13], although the overall topography and relative size of emerging facets observed were quite different given the very different crystal growth dynamics that occur with incident elemental beams in a UHV environment. Evidently, small differences in MOCVD growth parameters can bring about considerable changes in emission, and understanding the contributions outlined in this and prior chapters can help guide the design of long-wavelength microLED devices.

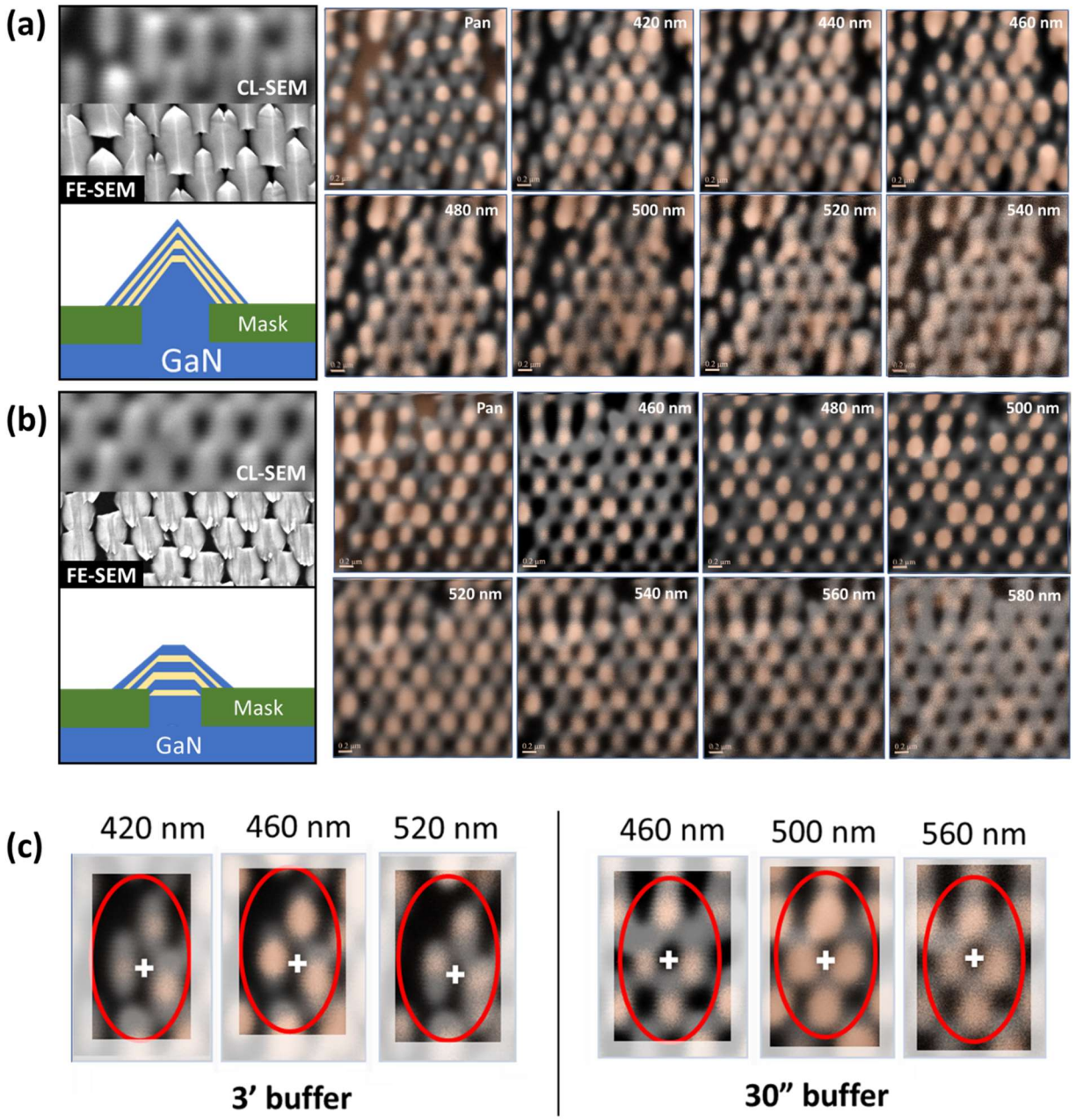

FIG 6.11. (a,b) Monochromatic CL maps of the 200-nm aperture SAG growths on $(11\bar{2}2)$ free-standing GaN substrates, with 3 quantum wells deposited on different nominal thicknesses of high-temperature GaN buffers. (c) Selected regions of the CL maps in (a) and (b), showing the emission coming from distinct locations on the emitter surface. "Pan" refers to panchromatic imaging; that is, light of all wavelengths is being collected simultaneously.

6.4 Conclusions

In this chapter, we developed and demonstrated a versatile set of methods to create geometry-tunable selective-area growth masks for structured InGaN/GaN light emitters at micron and sub-micron length scales. After performing III-nitride material deposition, the emergence of various crystal planes was explored, which informed the spectrally and spatially assigned emission arising from subsequent deposition of multiple quantum-well heterostructures. Blue-green emission (~500 nm) was achieved in 200-nm structures, which is promising for demonstrating submicron, electrically addressable emitters that can emit at long wavelengths, while circumventing plasma-based damage inherent to standard micro-LED processing. Future work includes realizing entire p-i-n junctions, and testing the optical and electronic performance of the resulting devices. Plenty of growth optimization can take place; GaN buffer temperature, III/V precursor ratio, and pulsed/intermittent reactant delivery would all help in reducing undesired crystal faceting by controlling the timing and energetics of gallium atoms finding their resting place on the growth surface. Finally, quantum-well growth temperature and thickness series would help assess attainable emission red-shift while maintaining reasonable device efficiencies.

References

1. J. R. T. Ley, J. M. Smith, M. S. Wong, T. Margalith, S. Nakamura, S. P. Denbaars, and M. J. Gordon, "Revealing the importance of light extraction efficiency in InGaN/GaN microLEDs via chemical treatment and dielectric passivation," Appl. Phys. Lett. **116**(25), (2020).
2. S. Keller, N. A. Fichtenbaum, C. Schaake, C. J. Neufeld, A. David, E. Matioli, Y. Wu, S. P. DenBaars, J. S. Speck, C. Weisbuch, and U. K. Mishra, "Optical properties of GaN nanopillar and nanostripe arrays with embedded InGaN/GaN multi quantum wells," Phys. Status Solidi Basic Res. **244**(6), 1797–1801 (2007).
3. M. S. Wong, D. Hwang, A. I. Alhassan, C. L. Lee, R. Ley, S. Nakamura, and S. P. DenBaars, "High efficiency of III-nitride micro-light- emitting diodes by sidewall passivation using atomic layer deposition," **26**(16), 21324–21331 (2018)
4. S. Naritsuka and T. Nishinaga, "Spatially resolved photoluminescence of laterally overgrown InP on InP-coated Si substrates," J. Cryst. Growth **174**(1–4), 622–629 (1997).
5. D. W. Shaw, "Selective Epitaxial Deposition of Gallium Arsenide in Holes," J. Electrochem. Soc. **113**, 904–908 (1966).
6. S. Nakamura, M. Senoh, S. Nagahama, N. Iwasa, T. Yamada, T. Matsushita, H. Kiyoku, Y. Sugimoto, T. Kozaki, H. Umemoto, M. Sano, and K. Chocho, "Present status of InGaN / GaN / AlGaN-based laser diodes," **190**, 820–825 (1998).
7. M. M. Rozhavskaya, W. V. Lundin, S. I. Troshkov, A. F. Tsatsulnikov, and V. G. Dubrovskii, "Determination of the diffusion lengths of Ga adatoms using GaN stripe profiling," Phys. Status Solidi Appl. Mater. Sci. **212**(4), 851–854 (2015).
8. X. Wang, J. Hartmann, M. Mandl, M. Sadat Mohajerani, H. H. Wehmann, M. Strassburg, and A. Waag, "Growth kinetics and mass transport mechanisms of GaN columns by selective area metal organic vapor phase epitaxy," J. Appl. Phys. **115**(16), (2014).
9. Y. Yin, H. Sun, L. Sang, P. Chen, Y. Zheng, B. Dierre, M. Sumiya, Y. Shi, and T. Sekiguchi, "Influence of dislocations on indium diffusion in semi-polar InGaN/GaN heterostructures," AIP Adv. **5**(5), (2015).
10. Y.-T. Lin, T.-W. Yeh, and P. Daniel Dapkus, "Mechanism of selective area growth of GaN nanorods by pulsed mode metalorganic chemical vapor deposition," Nanotechnology **23**(46), 465601 (2012).
11. S. Albert, P. De Mierry, and X. Kong, "Selective area growth of III-nitride nanorods on polar , semi-polar , and non-polar orientations : device applications .," **9370**, 1–24 (2015).
12. J. Bai, Y. Cai, P. Feng, P. Fletcher, X. Zhao, C. Zhu, and T. Wang, "A Direct Epitaxial Approach to Achieving Ultrasmall and Ultrabright InGaN Micro Light-Emitting Diodes (μLEDs)," ACS Photonics **7**, 411–415 (2020).
13. A. Bengoechea-Encabo, S. Albert, J. Zuñiga-Perez, P. de Mierry, A. Trampert, F. Barbagini, M. A. Sanchez-Garcia, and E. Calleja, "Selective area growth and characterization of GaN nanocolumns, with and without an InGaN insertion, on semi-polar (11–22) GaN templates," Appl. Phys. Lett. **103**(24), 241905 (2013).

7

Topographic control of semiconductor surface wettability

(Adapted from the manuscript: Shapturenka, P., Gaillard, P., Chan, L., and Gordon, M. J. "Hierarchical colloid-based lithography for wettability tuning of semiconductor surfaces." Under review, *JVST A*.)

7.1 Introduction

Textured surfaces have enjoyed centuries-long study, yielding fundamental insights into, and enabled engineering of, interfacial, chemical, and optical properties in various material systems [1,2]. In particular, anti-reflective (AR) nanostructures patterned into semiconductor surfaces have been shown to significantly reduce reflection losses, in turn improving the external efficiencies of photovoltaics, detectors, and light emitters [3–5]. In many such applications, control over the wetting properties of the surface is also vital for water-harvesting, self-cleaning, and/or anti-biofouling functionality, e.g., to reduce dust/dirt-induced scattering and absorption losses that hamper AR-based efficiency gains [6,7]. In both natural and technological settings, controlled wetting is often achieved with a combination of chemical and structural treatments [8,9]. While chemical modification of surfaces offers a rich suite of contact angles (wetting states) [10], and can encode the surface with specific electrostatic and reactive affinities, topographic patterning of surfaces provides a large dynamic range of achievable wetting states [11], does not rely on chemical

functionalization or non-native materials, can decouple wetting behavior from chemical functionality, and provides a versatile platform to precisely engineer the wetting characteristics laterally across a material surface.

Silicon (Si) surfaces comprise an effective vehicle for studying and engineering structure-induced surface wetting behaviors. Si is relatively inert, can be readily functionalized with a variety of chemical moieties, and is precisely patterned with standard microelectronics processes at the nanoscale. The material system can be further enabled by area-scalable, sub-micron nanopatterning methods. One such platform is colloidal lithography, which can be achieved by combining Langmuir-Blodgett (LB) dip-coating and plasma etching. This approach is simple, area-scalable, and has been robustly demonstrated in a variety of semiconducting materials (Si, Ge, GaAs, GaN, etc.) for antireflection and light-extraction applications [4,5,12,13]. GaN is a commercialized, bio-compatible III-V semiconductor platform for optical and power electronics that holds promise in a variety of fields, from efficient lighting to optogenetics [14-17]. GaN also exhibits robust etch selectivity to SiO_2, making it amenable to LB-based colloidal lithography.

Here, we demonstrate how colloidal lithography can be used to pattern Si and GaN surfaces at the micro- and nanoscales, and explore the range of wetting behaviors that can be achieved. Varying the diameter of the colloid mask and associated mask reduction steps, i.e., leading to variation in pillar size and spacing, the transition from Cassie-Baxter (CB) to Wenzel wetting behavior was identified at feature spacings of $\sim$1 μm. Looking further at this transition point, we highlight how varying degrees of vertical etch duration lead to two different topographies and wetting states, with a shallow etch yielding a hydrophobic surface resembling a rose petal in form and function [18], while a deeper etch results in

superhydrophobic behavior that is similar to a lotus leaf. At submicron pattern periods when the wetting state is firmly in the CB regime (with a feature spacing of 690 nm), we explore the processing parameter space to minimize the solid-liquid interfacial contact area and maximize aspect ratio; by varying the duration of various plasma process steps, superhydrophobic surfaces were achieved. Building on this understanding, we demonstrate hierarchical patterning by applying dual length scales to a Si surface on either side of the above-noted wetting transition. By patterning a CB-wetting surface (310 nm spacing) onto a nominal Wenzel-state topography with 6-μm spacing, we drastically modify the wetting properties and recover a highly hydrophobic surface that retains its wetting state after aging in ambient conditions. Finally, we reproduce this hierarchical patterning in GaN surfaces, where a micron-scale Wenzel-wetting surface also becomes less hydrophilic with the addition of nanoscale topography, albeit with a less pronounced absolute change due to an inherently lower GaN-liquid contact angle.

7.2 Experimental methods

7.2.1 Substrate preparation and processing

Semiconductor substrates ([100] Si wafer or 3 μm thick MOCVD-grown c-plane GaN on single-side polished sapphire) were cleaved into ~1x1-cm^2 sections and cleaned with 5-minute etches in piranha solution (to clean and repeatably oxidize the wafer surface) and 50% hydrofluoric acid (oxide stripping). Monolayers of functionalized colloidal spheres (hydrophobic SiO_2, Bangs Laboratories, d = 310, 690, 960, 2530, 4000, and 6000 nm) were deposited on the substrates via surface pressure-regulated Langmuir-Blodgett dip-coating

with a room-temperature deionized water subphase. The resulting samples were split into various lots and underwent various degrees of plasma processing to create nano- and micropillars. Isotropic nanosphere mask reduction was performed at 30 mTorr with a CHF_3/O_2 (30/20 sccm) plasma etch at 900 W and no forward bias (Panasonic E640 ICP etcher). Vertical pattern transfer was achieved via inductively coupled plasma etching; Si surfaces were etched with SF_6/C_4F_8/Ar chemistry (24/56/20 sccm) at 825 W RF power, 20 W forward bias, and 19 mTorr (PlasmaTherm 770 SLR ICP etcher). GaN surfaces were patterned with Cl_2/N_2 chemistry (12.5/7.5 sccm) at 500 W power, 300 W forward bias, and 1.5 mTorr (Panasonic E640 ICP etcher).

Table 7.1 features a comprehensive summary of the plasma-processed samples in this study. After processing, samples in Lot 1 underwent an HF acid clean and 5-minute CF_4/Ar plasma clean to remove silica material, 5-minute O_2 plasma clean to remove any organic contaminants present, and finally by a 5-minute aqueous HF acid etch to remove surface oxides. All other lots were simply immersed in 50% aqueous HF after plasma processing. Hierarchical patterning (Lot 6) was achieved using two successive, independent cycles of LB deposition, pattern transfer, and HF mask/oxide stripping with different size mask particles.

Lot no.	Material	Colloid mask sizes (nm)	Isotropic mask-reduction etch time (min)	Vertical etch time (min)
1	Si	690, 960, 2530, 4000, 6000	0	10, 20, 50, 65, 80 (respectively)
2	Si	960	0	15, 30
3	Si	690	0.5, 1, 2, 4, 6, 8, 10	10
4	Si	690	0	5, 10, 15, 20, 25, 30
5	GaN	2530, 4000	4, 5 (respectively)	20
6	GaN, Si	6000 + 310	20 + 1.3 (respectively)	80 + 5 (respectively)

TABLE 7.1. Summary of sample lots and corresponding processing steps for all samples featured herein.

7.2.2 Characterization and analysis

All samples were characterized via scanning electron microscopy (FEI Sirion XL30) and sessile water-drop contact angle goniometry (Ramé-Hart Instrument Co.). Samples were immersed in 50% aqueous HF acid prior to contact angle measurements, except in the case of intentionally measuring samples aged under ambient conditions. Sessile drop contact angle measurements, θ_A (apparent angle), were compared with the Cassie-Baxter model using a solid contact angle θ_s measured from an unmasked plasma-etched witness sample, and solid area fractions f_s calculated from SEM-imaged pillar top diameters, given by:

$$\cos\theta_A = f_S(\cos\theta_S + 1) - 1 \tag{6.1}$$

Unmasked, plasma-etched Si witness samples were further characterized with X-ray photoelectron spectroscopy (Kratos Axis Ultra) to assess the chemical composition of the surface after plasma etching and before/after HF treatment. As expected, the surfaces were

found to be highly fluorocarbon-containing, with similar distributions of CF_x-bonded moieties on the surface before and after HF treatment.

7.3 Results and discussion

7.3.1 Wetting transition via colloid mask size

To probe the effect of pattern periodicity on wetting state, a series of silicon surfaces coated with various colloid mask sizes were patterned with an anisotropic, pattern-transferring vertical etch, with no prior mask reduction. Vertical etch times were chosen to maintain approximately equal pillar aspect ratios for all colloid sizes. Figure 7.1 shows SEM images, average pillar spacings, aspect ratios, and sessile drop contact angles for samples with center-to-center pillar spacings from 690 to 4000 nm. Pillars of all sizes appear to have rather smooth and vertical sidewalls, with the larger pillars exhibiting a prominent top area. Perhaps most strikingly, we see a dramatic wetting transition over these length scales, with the crossover from hydrophobic to hydrophilic wetting occurring at ~1 mm.

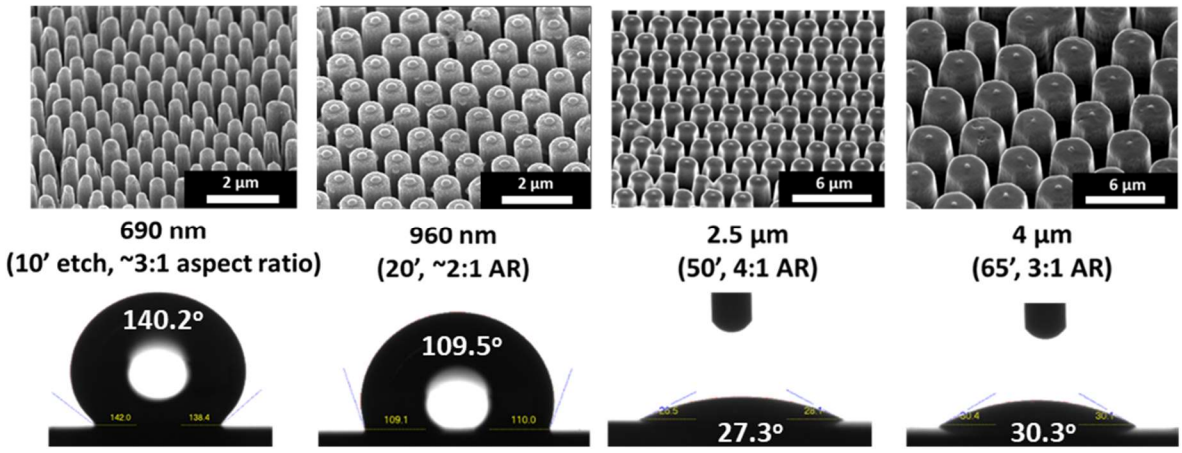

FIG. 7.1. Series of silicon surfaces patterned with colloids of various diameters (690 nm to 4 µm), showing the spectrum of wetting states achievable by changing pillar spacing. Scanning electron micrographs, reactive ion vertical etching times, and aspect ratios are shown in the top row, with sessile drop images underneath. All samples underwent an HF acid clean, 5-minute CF_4/Ar plasma clean, 5-minute O_2 plasma clean (to strip organic contaminants), and a 5-minute aqueous HF acid etch to remove surface oxides. Averaged contact angles are shown within each drop. Small dot/circle features at the center of each pillar are etch shadows from the stripped silica nanosphere mask.

Having identified a wetting transition, the vertical etching duration was varied at this critical pillar spacing to probe the effect of aspect ratio and pillar profile on the surface wetting state. Two samples masked with 960 nm colloids underwent vertical reactive ion etching for 15 and 30 minutes and were compared with SEM imaging and contact angle goniometry. Scanning electron micrographs, sessile drops, and details of processing and geometry are shown in Fig. 7.2. Both samples exhibited amplified hydrophobic behavior relative to the original 960 nm sample, with sessile contact angles of 134.5° and 150.7°, respectively. Water droplets deposited on the shallower sample (15' RIE) adhered to the substrate and maintained their shape regardless of substrate orientation, behaving similarly to the petal of a rose [18,19]. In contrast, facile drop roll-off was observed for the 30' RIE sample, mimicking the self-cleaning properties of a lotus leaf [1,9].

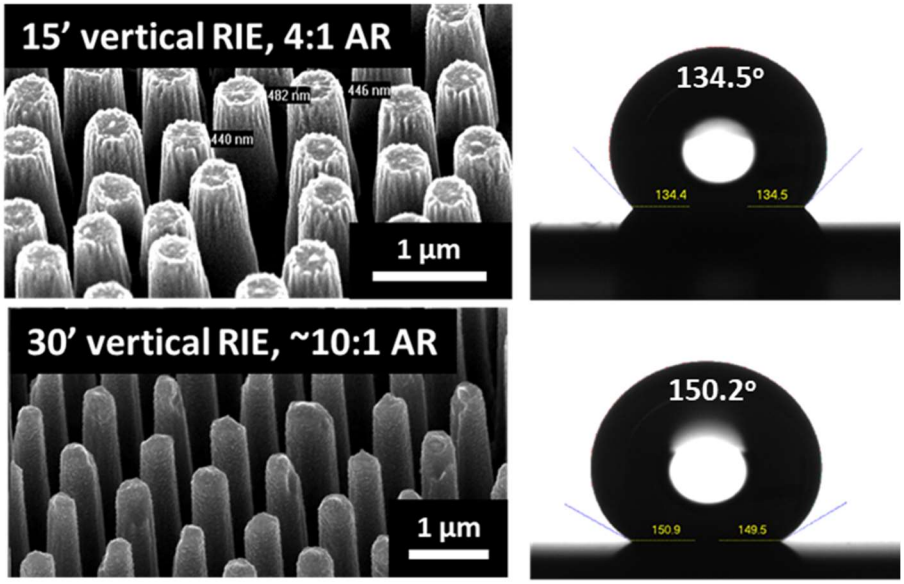

FIG. 7.2. SEM micrographs and sessile drop images of two Si samples fabricated with a 960 nm colloid mask, no mask reduction, and varying extents of reactive ion etching (15 and 30 minutes). Aspect ratios were calculated from image-derived pillar heights (images not shown). The trapezoidal silhouette below the contact line in the sessile drop images is a reflection from the substrate surface. The 15’ RIE sample exhibited the “rose petal” effect, with drops adhering to the sample at all orientations while maintaining large contact angle; facile roll-off was observed for drops deposited on the 30’ RIE sample.

There are several notable differences in topography between these two surfaces that help elucidate differences in wetting behavior. The shallow-etch sample resulted in pillars with a low aspect ratio (4:1), tapered sidewalls, and relatively higher solid fraction (~0.28), which enables a high degree of drop contact with the solid material and allows water impregnation between the pillars. A series of sharp, corrugated edges present on the pillar edges further extend their resemblance to the topography of a rose petal surface and are likely to facilitate pinning of the three-phase contact line. Conversely, the deeper-etched sample exhibits smoother and more blunt pillar features, a lower solid fraction (~0.16), and more than a twofold increase in pillar aspect ratio (10:1), which would reduce the likelihood of water entrapment and droplet pinning.

7.3.2 Obtaining superhydrophobicity within the Cassie-Baxter state by tuning plasma processing

As seen in Fig. 7.1, surfaces patterned with sub-micron features (namely, 690 nm pillar spacings) showed hydrophobic character and facile roll-off, indicating a classical Cassie-Baxter wetting state. To probe the full extent of obtainable hydrophobic behavior by only changing the surface topography, the CB model suggests decreasing the solid contact area. This is readily achieved with colloid mask reduction prior to vertical pattern transfer, or by vertical pattern transfer alone, as a spherical mask will also gradually reduce in size as it is eroded from the top. This has the added benefit of a high aspect ratio, preventing interactions of water with the entrenched surface. Accordingly, to elicit superhydrophobic character, increasing etch times for mask reduction (0.5-10 minutes) and vertical etching (5-30 minutes) were used to reduce solid contact area and increase aspect ratio, respectively. Ten minutes of vertical pattern transfer was applied to each sample in the mask-reduction time series. A Cassie-Baxter model referencing a planar etched witness sample was used as a theoretical benchmark for all samples, where solid fractions were calculated from SEM-imaged pillar top diameters.

Figure 7.3 summarizes the results of this study. As expected, the apparent sessile contact angle for all structured samples increased relative to the unstructured reference, and there was an overall upward trend in hydrophobicity that approached (but did not exceed) the theoretical CB limit. As seen in panel (a), superhydrophobicity (contact angles exceeding 150^{o}) was achieved with vertical etch times of 20', 25' (Fig. 7.4(b) and (d)), and 30', as well as the 8' mask-reduction (MR) etch (Fig. 7.4(c)). Both electron micrographs show sharply tapered features with a low solid fraction, which is expected to amplify the inherent

hydrophobicity of the etched silicon material. The samples undergoing the longest plasma etching steps (30' vertical and 10' MR) showed a lower contact angle relative to neighboring samples. It is likely that there was over-etching of the top pillar surface (observed in SEMs), leading to a highly nonuniform and shallow, tapered top surface, exposing a greater surface area (despite a decrease in the nominal pillar width) and ultimately preventing the formation of stable air pockets beneath the droplet.

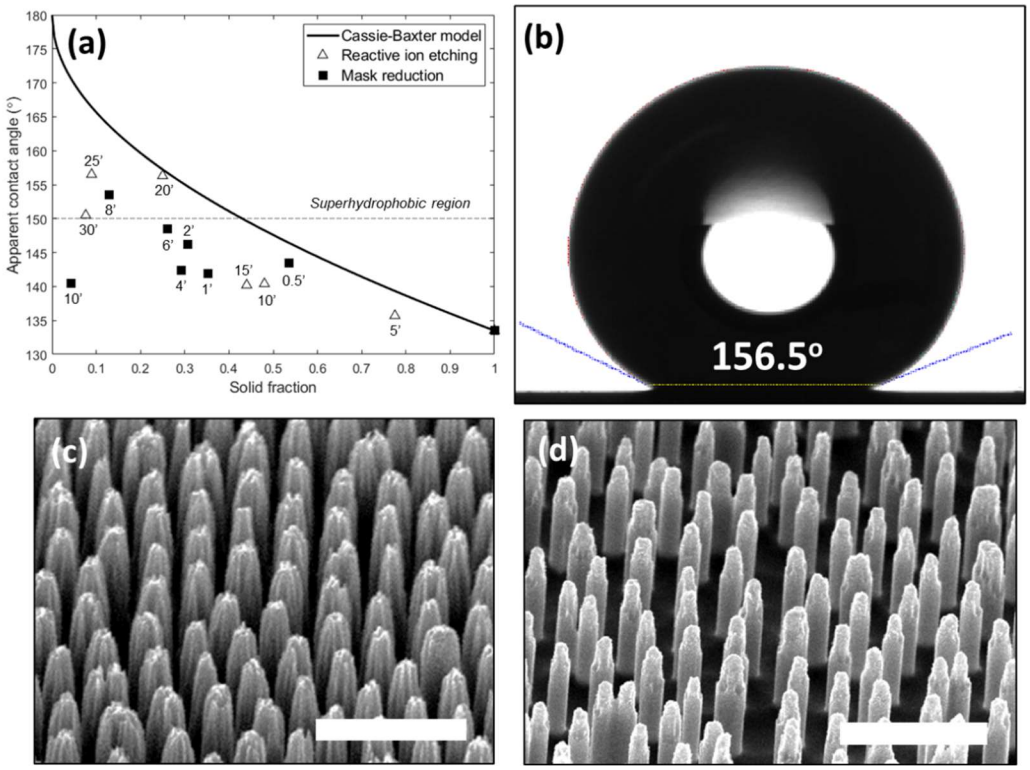

FIG. 7.3. (a) Measured sessile water drop contact angles of all Si surfaces patterned with 690 nm silica nanosphere masks, plotted against surface solid fraction (assessed by SEM imaging). Various extents of mask-reduction (square) or reactive ion etching (RIE, triangle) are shown above/below each point. All mask-reduced samples underwent RIE for 10 minutes. The Cassie-Baxter (CB) wetting model is also shown for reference (solid line), with the data points at a solid fraction of unity experimentally measured from a nominally unstructured, plasma-etched reference Si wafer. (b) Sessile drop on the surface featured in (c), with an averaged contact angle of 156.5°. (c,d) scanning electron micrographs of two superhydrophobic surfaces, undergoing: (c) 25' of vertical etching with no prior mask reduction, and (d) 8' of mask reduction and 10' of subsequent vertical etching. Scale bars are 2 μm.

7.3.3 Hierarchical patterning for dramatic changes in wetting

As shown above, patterning Si with fluorine chemistry and pillar spacings above 1 μm induced a capillary-driven Wenzel wetting state. Hierarchical patterning, i.e., surface topography at multiple length scales, is known to dramatically change or enhance the repellent properties of naturally occurring surfaces [1,9,20,21]; accordingly, we explored the effect of hierarchical patterning with two successive cycles of colloidal lithography (6 μm mask, followed by 310 nm) and compared the wetting behavior to the single-patterned case. Figure 7.4 shows scanning electron micrographs and sessile drops of the single- and hierarchically patterned Si wafers. The large pillar widths for both samples are nearly identical (~4.5 μm). In the single-step patterned case, the pillar tops and sidewalls are smooth, exposing a wealth of surface area for capillary action to dominate the wetting behavior. However, the hierarchically patterned sample has additional high aspect-ratio structuring at a pitch of 310 nm, which is expected to induce Cassie-Baxter wetting. Indeed, the wetting state changed from hydrophilic at a contact angle of 32^{o} to nearly superhydrophobic, at 146.4^{o}, with a localized change in topography. Not only is the contact area solid fraction reduced by at least another 50%, the wetting state crosses back over the CB-Wenzel transition. Furthermore, after aging the sample in ambient laboratory conditions for 20 days, oxide growth appears to have minimal impact, given the relatively small change in contact angle and similar wetting behavior (Fig. 7.4(f)).

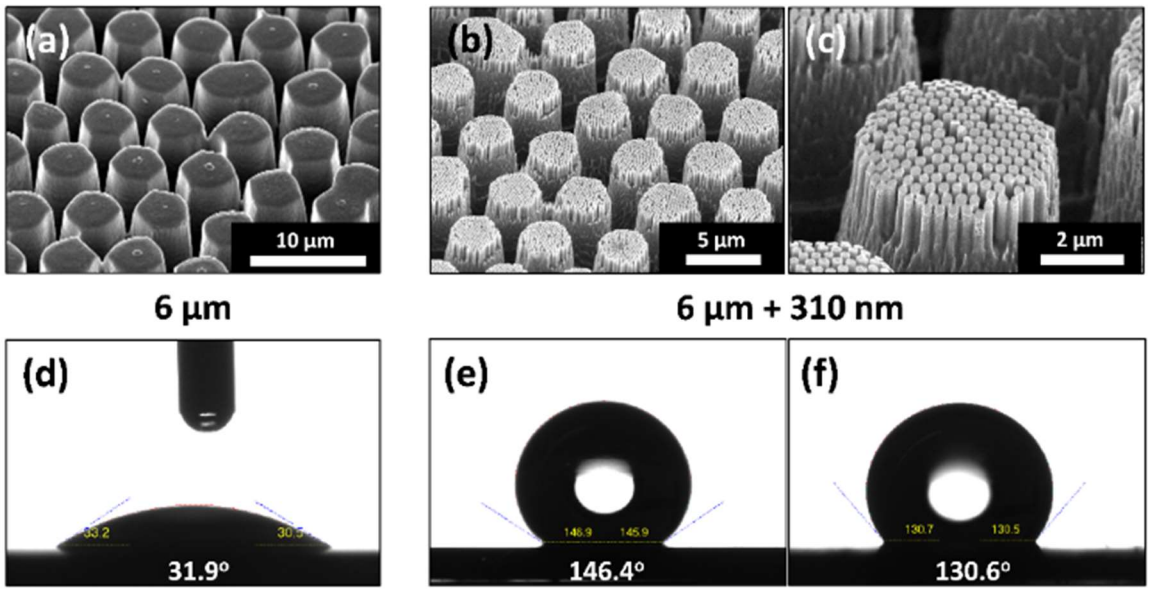

FIG. 7.4. Scanning electron micrographs, sessile drop images, and contact angles of (a,d) a single-step patterned Si wafer with 6-micron features and (b,c,e,f) hierarchically patterned (6 µm + 310 nm) Si wafer. Sessile drop images were taken (e) immediately after stripping surface oxides (HF acid), and (f) after aging the sample at ambient laboratory conditions for 20 days and no other surface treatment.

7.3.4 Wetting properties of GaN surfaces patterned at single & dual length scales

Having observed the effects of patterning on Si, we investigated the wetting behavior of patterned GaN substrates. Figure 7.5 shows the SEM-imaged surfaces and sessile contact angles obtained by patterning GaN at single-micron length scales as well as hierarchically with 6 µm and 310 nm features with chlorine-based plasma. The features obtained via single-step colloidal lithography are well-defined frusta, with smooth, sharply sloped sidewalls, which would tend to favor capillary-induced water adhesion. The tops of the frusta are planar and contain hexagonal V-pits seeded by threading dislocations that propagate upward during epitaxial growth. As with the case of patterned silicon, an apparent capillary-driven decrease in the contact angle was observed for large features (2.5 and 4 microns)

relative to a flat surface. Upon patterning with a secondary submicron colloid mask of 310 nm, the top planar surface was transformed into a quasi-ordered array of nanopillars that resemble rounded cones, further reducing at least 50% of the original frustum-droplet contact area. This patterning also gave rise to a significant increase in contact angle.

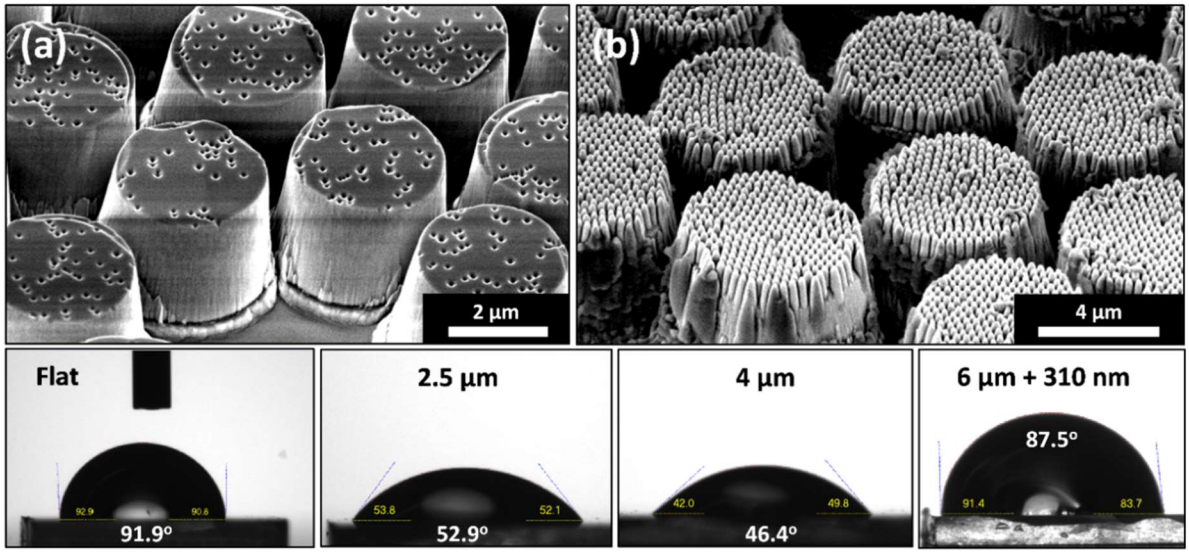

FIG. 7.5. Scanning electron micrographs of GaN surfaces (c-plane GaN on sapphire substrate) patterned with (a) 4 µm diameter silica colloids and (b) hierarchically patterned (6 µm + 310 nm) GaN features, with corresponding sessile drop images and contact angles below, as well as sessile drops of the flat reference and 2.5 µm features (SEMs not shown). The defects seen on the top surface of the GaN frusta in (a) are V-pits induced by threading dislocations during epitaxial growth.

7.3.5 Study limitations

Several improvements in sample processing would allow more rigorous comparison with established wetting models. Firstly, aspect ratios are not constant for the presented size series in Fig. 7.1; while the effects of aspect ratio are expected to become insignificant at submicron scales, the low aspect ratio convolves interactions with the entrenched solid surface. Higher aspect ratios (e.g., 10:1) for all samples would prove useful to discern trends relating to pillar spacing and solid fraction. A second, related limitation is the non-uniformity

in sidewall angle and pillar topography. This stems from the chemical selectivity of the silica mask, as well as its spherical shape that rapidly decreases the flat area atop each pillar as etching progresses. This can be addressed by introducing an additional chemically distinct layer (e.g., photoresist and/or SiO_2) between the mask and Si substrate, forming a less tapered frustum or cylinder. However, as seen in this work, sharper pillar edges may lead to increased contact line pinning, which may in fact hinder the emergence of superhydrophobic behavior. Future work could involve adapting this platform to realize scalable, re-entrant surfaces for repellent properties in a wider suite of liquids [11], and investigating the effect of re-introducing chemical heterogeneities through surface functionalization.

7.4 Summary

We have explored a high dynamic range of wetting states on silicon and GaN surfaces achieved via colloidal patterning. By simply varying the characteristic size of the mask and tuning plasma processing, we were able to access various wetting modes that were dominated by capillary forces (Wenzel) or fractional surface area (Cassie-Baxter). Moreover, exploring the duration of plasma processing steps allowed several distinct superhydrophobic topographies to be achieved. By adding submicron patterning to an inherently Wenzel-wetting topography, we observed a dramatic reversal in wetting characteristics, resulting in nearly superhydrophobic (>146^o) behavior that is tolerant to ambient conditions (contact angle reduction of ~15^o in 20 days). Hierarchical patterning was repeated in GaN, which showed similar wetting trends.

References

1. B. Bhushan, Y. C. Jung, and K. Koch, "Micro-, nano-, and hierarchical structures for superhydrophobicity, self-cleaning and low adhesion," Philos. Trans. R. Soc. A Math. Phys. Eng. Sci. **367**(1894), 1631–1672 (2009).

2. R. N. Wenzel, "Resistance of solid surfaces to wetting by water," Ind. Eng. Chem. **28**(8), 988–994 (1936).

3. F. L. Gonzalez and M. J. Gordon, "Bio-inspired, sub-wavelength surface structures for ultra-broadband, omni-directional anti-reflection in the mid and far IR," Opt. Express **22**(11), 12808 (2014).

4. L. Chan, A. Ghoshal, E. A. Decuir, Y. P. Chen, D. E. Morse, M. J. Gordon, L. Chan, and D. E. Morse, "Fabrication and optical behavior of graded- index , moth-eye antireflective structures in CdTe," J. Vac. Sci. Technol. B **011201**(Jan/Feb 2017), (2017).

5. C. D. Pynn, L. Chan, F. L. Gonzalez, A. Berry, D. H. Wang, H. Wu, T. Margalith, D. E. Morse, S. P. DenBaars, and M. J. Gordon, "Enhanced light extraction from free-standing InGaN / GaN light emitters using bio-inspired backside surface structuring," Opt. Express **25**(14), 15778–15785 (2017)..

6. W. L. Min, B. Jiang, and P. Jiang, "Bioinspired self-cleaning antireflection coatings," Adv. Mater. **20**(20), 3914–3918 (2008).

7. K. H. Tsui, Q. Lin, H. Chou, Q. Zhang, H. Fu, P. Qi, and Z. Fan, "Low-cost, flexible, and self-cleaning 3D nanocone anti-reflection films for high-efficiency photovoltaics," Adv. Mater. **26**(18), 2805–2811 (2014).

8. A. Lafuma and D. Quéré, "Superhydrophobic states," Nat. Mater. **2**(7), 457–460 (2003).

9. T. Darmanin and F. Guittard, "Superhydrophobic and superoleophobic properties in nature," Mater. Today **18**(5), 273–285 (2015).

10. T. S. Wong, S. H. Kang, S. K. Y. Tang, E. J. Smythe, B. D. Hatton, A. Grinthal, and J. Aizenberg, "Bioinspired self-repairing slippery surfaces with pressure-stable omniphobicity," Nature **477**(7365), 443–447 (2011).

11. N. Vogel, R. A. Belisle, B. Hatton, T. S. Wong, and J. Aizenberg, "Transparency and damage tolerance of patternable omniphobic lubricated surfaces based on inverse colloidal monolayers," Nat. Commun. **4**(2176), (2013).

12. I. Yilgor, S. Bilgin, M. Isik, and E. Yilgor, "Tunable wetting of polymer surfaces," Langmuir **28**(41), 14808–14814 (2012).

13. T. Liu and C.-J. Kim, "Turning a surface superrepellent even to completely wetting liquids," Science **346**(6213), 1096-1100 (2014).

14. F. L. Gonzalez, L. Chan, A. Berry, D. E. Morse, and M. J. Gordon, "Simple colloidal lithography method to fabricate large-area moth-eye antireflective structures on Si , Ge , and GaAs for IR applications," J. Vac. Sci. Technol. B **32**(5), 051213 (2014).

15. P. Tsai, Y. Yang, and Y. Lee, "Fabrication of Hydrophobic Surfaces by Coupling of Langmuir-Blodgett Deposition and a Self-Assembled Monolayer," Langmuir **22**(13), 5660–5665 (2006).

16. S. A. Jewett, M. S. Makowski, B. Andrews, M. J. Manfra, and A. Ivanisevic, "Gallium nitride is biocompatible and non-toxic before and after functionalization with peptides," Acta Biomater. **8**(2), 728–733 (2012).

17. S. P. DenBaars, D. Feezell, K. Kelchner, S. Pimputkar, C. C. Pan, C. C. Yen, S. Tanaka, Y. Zhao, N. Pfaff, R. Farrell, M. Iza, S. Keller, U. Mishra, J. S. Speck, and S. Nakamura, "Development of gallium-nitride-based light-emitting diodes (LEDs) and laser diodes for energy-efficient lighting and displays," Acta Mater. **61**(3), 945–951 (2013).

18. U. K. Mishra, P. Parikh, and Y. F. Wu, "AlGaN/GaN HEMTs - An overview of device operation and applications," Proc. IEEE **90**(6), 1022–1031 (2002).

19. F. Wu, E. Stark, P. C. Ku, K. D. Wise, G. Buzsáki, and E. Yoon, "Monolithically Integrated μLEDs on Silicon Neural Probes for High-Resolution Optogenetic Studies in Behaving Animals," Neuron **88**(6), 1136–1148 (2015).

20. B. Bhushan and M. Nosonovsky, "The rose petal effect and the modes of superhydrophobicity.," Philos. Trans. A. Math. Phys. Eng. Sci. **368**, 4713–4728 (2010).

21. L. Feng, Y. Zhang, J. Xi, Y. Zhu, N. Wang, F. Xia, and L. Jiang, "Petal effect: A superhydrophobic state with high adhesive force," Langmuir **24**(8), 4114–4119 (2008).

22. A. Fernández, A. Francone, L. H. Thamdrup, A. Johansson, B. Bilenberg, T. Nielsen, M. Guttmann, C. M. Sotomayor Torres, and N. Kehagias, "Design of Hierarchical Surfaces for Tuning Wetting Characteristics," ACS Appl. Mater. Interfaces **9**(8), 7701–7709 (2017).

23. M. T. Alameda, M. R. Osorio, J. J. Hernández, and I. Rodríguez, "Multilevel Hierarchical Topographies by Combined Photolithography and Nanoimprinting Processes to Create Surfaces with Controlled Wetting," ACS Appl. Nano Mater. **2**(8), 4727–4733 (2019).

8

Outlook and future directions

Several potential research directions building on this dissertation work are outlined, and initial findings are provided as a starter for the brave of heart.

8.1 Deep-ultraviolet reflecting diatom surfaces

Deep ultraviolet light (UVB/UVC: 200-320 nm) is useful in a variety of venues, including photolithography, disinfection, and water remediation. LED-based UV sources have recently begun to achieve sufficiently low dislocation densities where single and even double-digit external quantum efficiencies are feasible [1]. However, Mg-doped p-AlGaN does not provide high enough hole concentrations, given the increasingly insurmountable hole activation energy barrier; as a result, p-GaN is still conventionally used, which is a highly absorbing layer that reduces device external quantum efficiency (EQE) through absorption and Joule heating, leading to high thermal loads. Additionally, very few materials transmit UVC light, especially below 225 nm. Therefore, introducing electrical and optical layers that efficiently extract light is highly desirable.

The current state-of-the-art UV LED device configuration is the thin-film flip-chip (TFFC) configuration, which features a thin light-emitting chip with a backside metal mirror, plenty of heat-sinking sub-mount bond metal, and top (n-side) surface roughening. While

backside metal mirrors can afford ~70% reflectivity, increasing this to over 90% would dramatically improve commercial performance and speed up rapid deployment of UV LEDs. One promising route for achieving this is to deposit dielectric or epitaxial DBRs, but these are thick and may reduce thermal sinking, counteracting any light-extraction gain. Another promising alternative lies in the diatom-like high-contrast grating (introduced in Chapter 3).

While only a few materials do not appreciably absorb UVC light, a combination of AlN supported by MgF_2 appears to be a promising combination. Preliminary computational studies have shown tunable, >90% reflectances across the majority of the UVC wavelength range; it remains to be seen whether such a structure is realizable, as the AlN layer is only ~100 nm in thickness. The ideal HCP structure and cursory optical behavior envisioned is shown in Fig. 8.1 below, calculated with a rectangular unit cell with similar configuration as the fully-defined refractive index sensor geometry (Ch. 4). Several questions remain about the grating's angle-dependent reflectance, tolerance to imperfections, and optimal device integration routes.

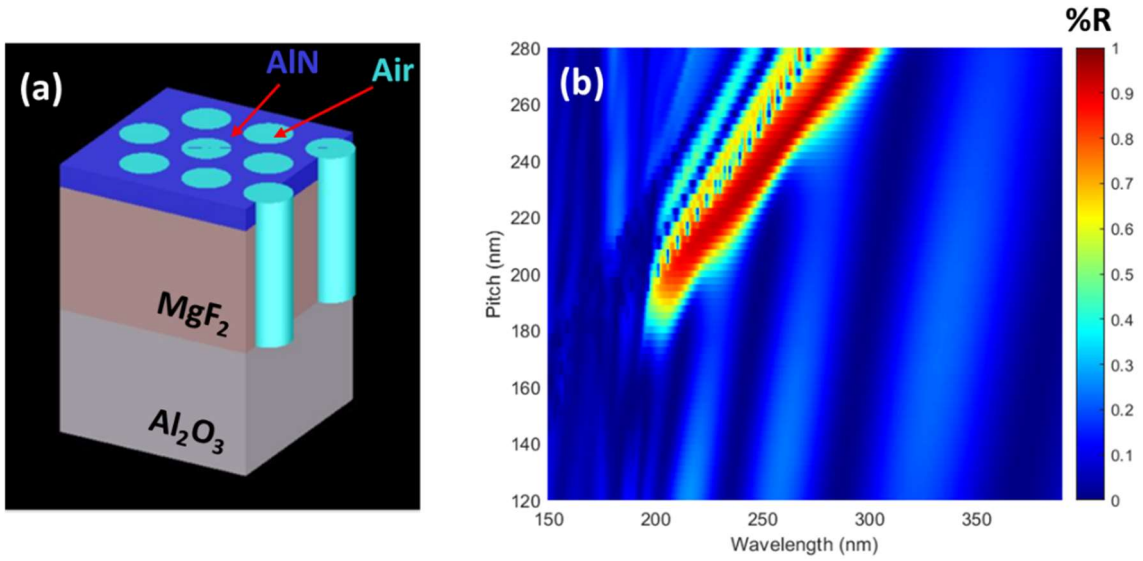

FIG. 8.1. (a) Schematic depicting several unit cells of a UVC AlN-based diatom grating reflector, with hexagonally arranged holes drilled through the MgF_2 underlayer supporting it. (b) Reflectance contour map of varying grating period (pitch) with thickness scaled to maintain a ratio of ~0.4 (pitch:thickness). >90% reflectivity at normal incidence is achieved for the majority of the UVC range. Images courtesy of Abhiram Devata.

8.2 Long-wavelength microLEDs via semipolar RIBs

While we showed quite extensive relaxation in the semipolar RIBs patterned at micron and submicron length scales, the more commercially relevant size for near-eye displays in AR/VR applications is 1-5 μm. Accordingly, it would be interesting to extend the patterning size to 5 microns and probe how large of a relaxation can be achieved, as well as gauge the luminescence redshift at problematic longer wavelengths (> 525 nm). Developing a fabrication process to electrically address these devices would also be an important step in extending this promising avenue.

8.3 Light-emitting diatoms for efficiency benefits

The vivid diffuse color obtained from the TiO_2 diatom structures in Chapter 3 arose from a unique resonant coupling of thin-film interference and broadly distributed guided modes that quickly leaked the low-order Fano-resonant mode out of the structure. A question follows: would it be possible to extract light emitted from within a p-i-n LED (Light-Emitting Diatom) in the same way? Moreover, is the slight disorder inherent to the colloidal patterning method in fact beneficial for this extraction? In prior work, Yue *et al.* computationally studied "deep-hole" photonic structures, where holes were etched into a standard LED on sapphire; however, while the structure under consideration was too thick for low-order thin-film resonances, an increase in light output power was found with amorphous and correlated structures relative to a perfectly ordered hole array [2].

Preliminary FDTD simulation work was conducted to reproduce the base case of Yue *et al.*, and reasonable agreement was found (Fig. 8.2), indicating that a relatable and consistent computational workflow has been developed. This workflow was extended to the ideal case of a floating, perforated slab, where the orientation of the emitting dipole played an important role. When the main emission lobe was in the plane of the structure, disorder dramatically increased the surface-normal emission intensity (Fig 8.3). However, little to no extraction increases were observed with a surface-normal dipole, the likes of which dominate the emission in c-plane quantum wells.

Further process and idea development is necessary to realize a "light-emitting diatom." As seen in Chapter 3, high-index structures are sensitive to the identity and extent of material present in their vicinity. As such, porosification or selective undercut etching

could be used to encourage efficient modal extraction by lowering the refractive index of the underlayer, increasing the likelihood of a high-contrast effect. Further, if a process were developed, PL/EL can be used to probe the peak emission wavelength prior to patterning, and design for optimum extraction of the signal during the processing cycle. While the amount of exposed emitter sidewall area is quite substantial given the small hole size necessary, recent work by Ley *et al*. showed an elimination of surface-based efficiency losses in blue devices, which is promising for high-resolution patterning of InGaN emitters [3].

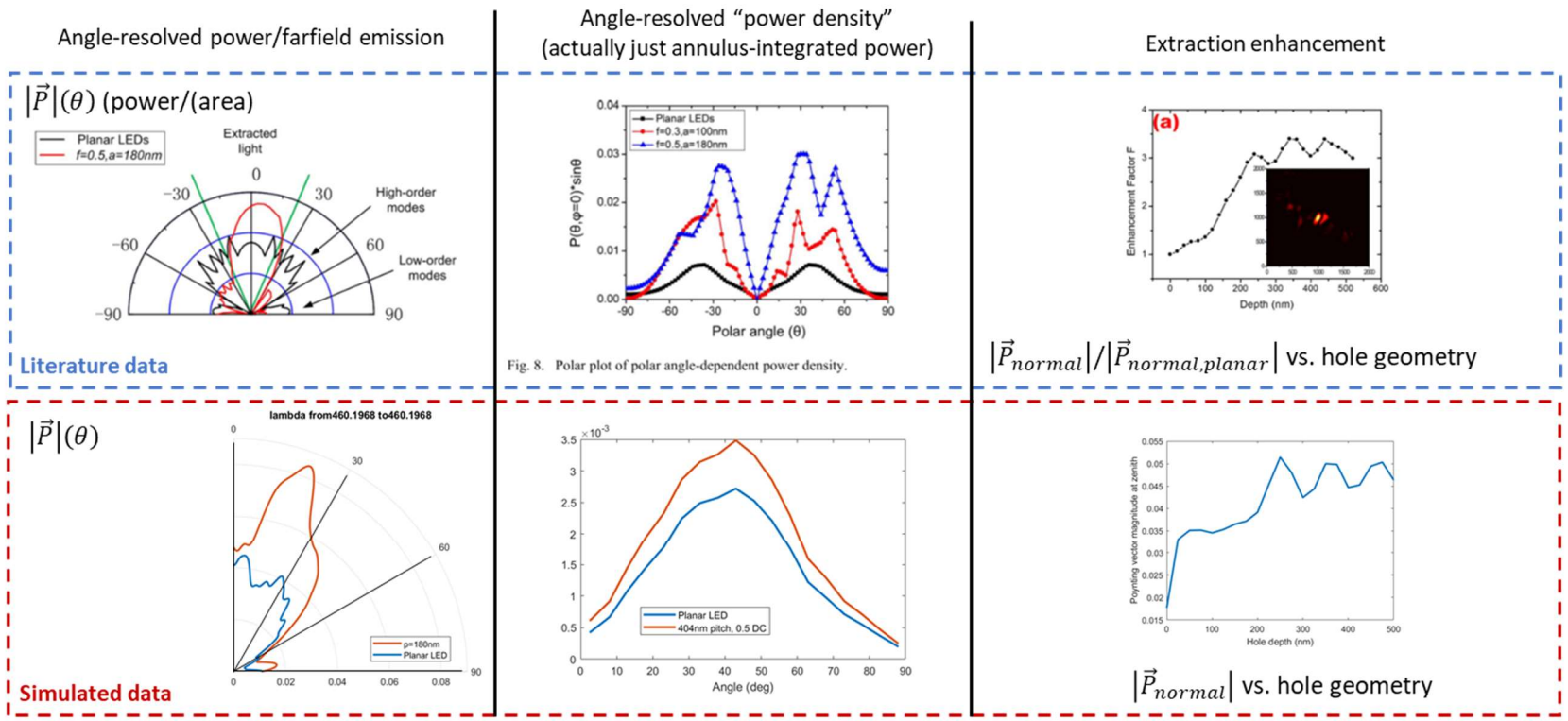

Fig. 8. Polar plot of polar angle-dependent power density.

FIG. 8.2. Angle- and geometry-resolved extraction metrics for deep hole arrays etched into a standard GaN/InGaN LED structure. Top row: plots from Yue *et al*. [2]. Bottom row: data generated from an in-house computational workflow via the monitor-box module in Lumerical FDTD software, initialized with nearly identical geometry as in [2]. Top panel adapted and reprinted with permission. © 2014, IEEE.

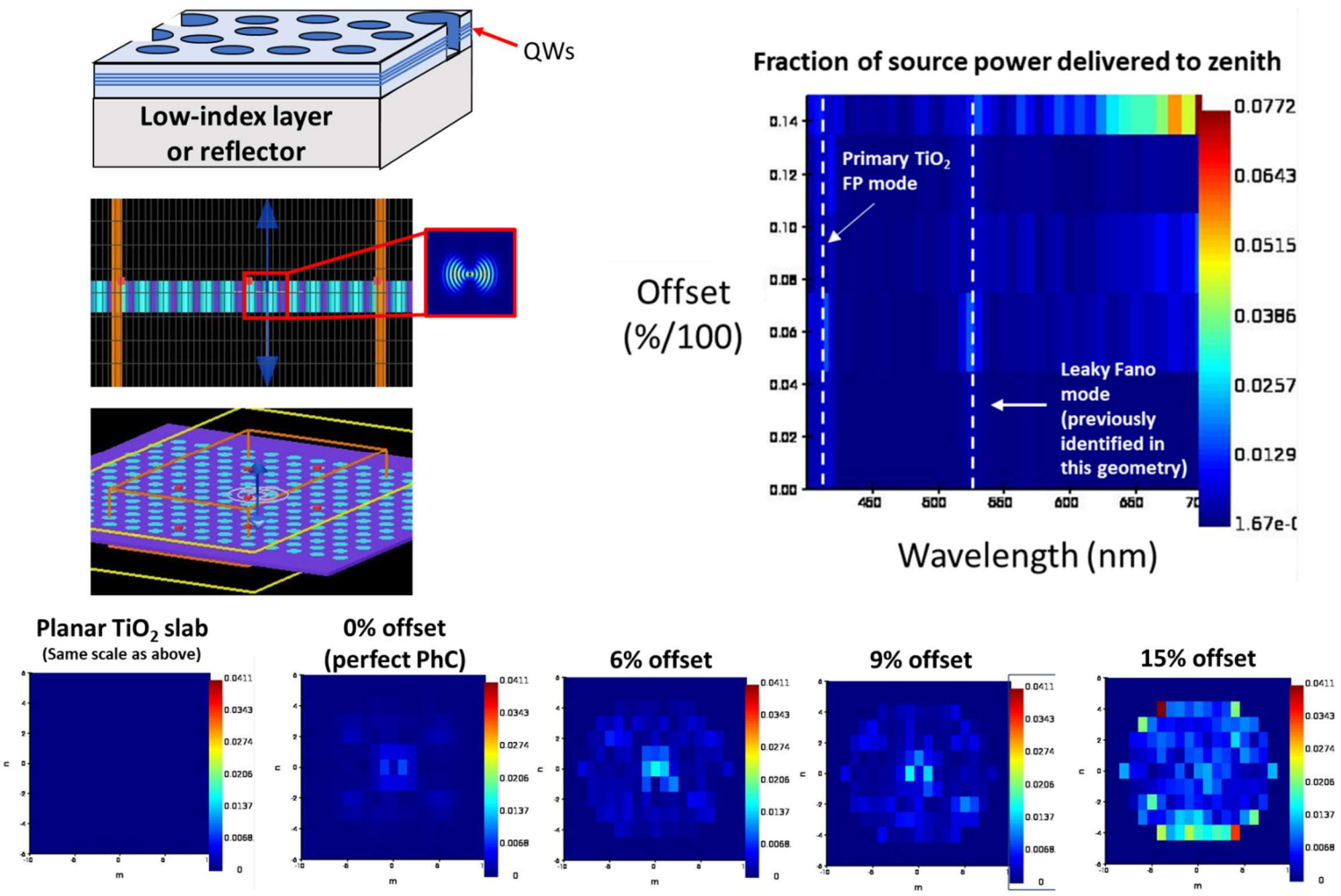

FIG. 8.3. FDTD simulations for floating, light-emitting GaN hole arrays, with an dipole emission lobe radiating in the plane of the structure. At right: spectral response of the emission delivered to the zeroth grating order (normal-incidence, directly above structure) with increasing translational hole disorder. Bottom row: fractional power delivered to each captured grating order within the top hemisphere of the hole-array structure with increasing translational hole disorder. Color scale is identical for all plots.

References

1. Y. Zhang, Z. Jamal-Eddine, and S. Rajan, "Recent progress of tunnel junction-based ultra-violet light emitting diodes," Jpn. J. Appl. Phys. **58**(SC), (2019).

2. Q. Yue, K. Li, F. Kong, J. Zhao, and Q. Ding, "Analysis on the light-extraction efficiency of GaN-based light-emitting diodes with deep-hole amorphous photonic crystals structures," IEEE/OSA J. Disp. Technol. **10**(12), 1070–1077 (2014).

3. R. T. Ley, J. M. Smith, M. S. Wong, T. Margalith, S. Nakamura, S. P. Denbaars, and M. J. Gordon, "Revealing the importance of light extraction efficiency in InGaN/GaN microLEDs via chemical treatment and dielectric passivation," Appl. Phys. Lett. **116**(25), (2020).